The University of Ottawa

A practical approach to the erodibility of cohesive soils

by
Hicham Salem

Thesis submitted to the
Office of the Vice-Provost, Graduate and Postdoctoral Studies
in partial fulfillment of the requirements for
Ph.D. degree in Civil Engineering

Department of Civil Engineering
Faculty of Engineering
University of Ottawa

Ph. D. Program, Civil Engineering

Foreword

The field of hydraulic engineering is quite vast and diversified. It covers aspects such as harvesting hydraulic energy (power generation, heavy lifting, etc.), containing forces induced by fluid motion and pressure (design of structures, vessels, etc.), and fluid interaction with loose boundaries, mostly affecting land conservation (erosion, deposition, flooding, etc.), to list a few.

The forces induced by fluids in motion and their effects on loose soil boundaries, combined with the non-homogeneous nature of such boundaries, can be very complex, and almost appear to be random. As scientists and researchers approached erosion problems over the years in an attempt to model mathematically the behavior of eroding soils, these models evolved into more and more complex formulations in an attempt to increase the prediction accuracy. It is in the Author's opinion that the natural spatial and geographical variations in the properties of soils, especially cohesive soils, and variations in the experimental methods used by researchers, resulted in unnecessary complexities in contemporary formulations and solutions considered as state-of-the-art in today's practice.

One of the main objectives of this study is to revisit the subject of cohesive soil erosion using new experimental and analytical procedures and to develop simple and practical models to predict and quantify soil erosion.

Some devices were developed during the course of this research and are being considered for patent registration, therefore, this thesis and review process shall be treated as confidential.

Acknowledgements

I wish to express tremendous gratitude to Dr. Colin Rennie for his valuable input and guidance, and for his patience and the supervisory flexibility which allowed me to conduct this extensive research around my busy work schedule. I would also like to thank my wife Jewel and my kids Joseph and Liliane for their patience and support over the years of studying and research work. Many thanks to Mr. Mark Lapointe for his valuable assistance throughout this research. I would also like to offer many thanks to the City of Ottawa, and Ms. Darlene Conway for supporting the project. Thanks to Nicholas Zorn, Benjamin Lambert, Alain Kayitaba, Andre Smith, Derek Eden, Carlo Zaro Custodio, and Guillaume Dreysse for assisting in field and laboratory work.

Abstract

A set of solutions to the cohesive soil erosion problem were developed through this study.

A first device, the Erosionometer, was developed to perform a quick and reliable test to determine the critical shear stress of soils. The Erosionometer is based on physical shearing of the soil surface and has been calibrated through comparison with piston flume measurements of critical shear stress for entrainment of various fluvial bed sediments. This device is portable, easy to deploy in the field and in the laboratory and allows engineers and researchers to cover a sizeable terrain by performing many tests in a short timeframe, with immediate results. A modification to the Erosionometer was made to allow for subjecting the soil sample to a pressure differential while testing for critical shear stress. The added functionality is intended for investigating the effect of pressure gradient on the erodibility of cohesive soils by allowing for the erosion test to be conducted under a high pressure head while the other face of the sample (away from the flow) is maintained at zero head. Testing demonstrated that a positive pressure gradient on the eroding side (high pressure on flow side) can significantly increase the critical shear stress of cohesive soils, which is in line with other research available in the literature. The results show a simple linear relation between pressure differential and critical shear stress. Practical implications of these results are discussed.

A second device, the Erosion Rate Meter, or ERM, was developed to test cohesive soil samples to determine the rate of erosion under various levels of bed shear stress. This device, while being portable and fast to setup and run, is a very realistic simulation of the flow-bed interaction and allows for a direct measurement of bed shear stress on the soil sample and a precise measurement of the erosion rate. An obvious outcome of using the ERM is the easy development of erosion rate vs. bed shear stress relationships or models to characterize the different soils for design projects or further research. Of the 16 tested cohesive soils, all but two demonstrated a linear relation between erosion rate and bed shear stress.

The testing systems and methods developed in this research provide a comprehensive solution to the erodibility of cohesive soils from investigation to design. Significant improvements are achieved over existing systems in the speed, reliability, accuracy, and cost of estimating the erodibility of cohesive soils.

Table of Contents

Appendices:

List of figures

List of tables

List of symbols

B	dimensionless log-velocity factor dependent on the shear Reynolds number
b_0, b_1	Wilson's model fitting parameters
c'	Effective cohesion strength of soil (geotechnical parameter)
C_d	drag coefficient
d	diameter of soil particle or cluster
e	Combined erosion rate for all sediment grain sizes
E	erosion thickness
E_o	empirical parameter reflecting the ease of erosion, similar to k and k'
ERM	erosion Rate Meter
E_y	yield force (peak) in Erosionometer pull
F_d	drag force in the flow direction
F_L	lift force perpendicular to the flow direction (upward)
g	gravity acceleration = 9.81 m/s^2
H, h	height of water column (head)
i	seepage hydraulic gradient
k, k'	empirical constants reflecting the ease of erosion of the soil material
k_a	area constant ($d \times k_a$ = particle surface area)
k_d	detachment distance parameter
K_d	dimensionless hydraulic drag parameter
K_e	parameter to account for additional time to remove surrounding particles
k_f	ratio of projected area of drag force to that of lift force
K_L	proportional constant between drag and lift coefficients
K_n	defined as a "combination of particle and fluid factors", $K_n = K_t K_d k_r$
k_r	ratio of volume to area constants (k_v/k_a)
K_s	roughness height
K_{st}	seepage parameter due to the exchange time of a particle
K_t	empirical factor applied to the drag force to account for "the cumulation of instantaneous fluid forces"
k_v	volume constant ($d \times k_v$ = particle volume)
M	mass of eroded material
M_c	Sum of all moments of friction and cohesion forces resisting detachment

m, n	empirical exponents
r^2	coefficient of determination
R_h	hydraulic radius
S, S_o	slope of the sediment bed
T	transport stage = (τ/τ_c -1)
U	time-averaged flow velocity
UC	Unconfined compressive strength characteristic of the soil
V_b	near-bed vertical velocity
W_s	buoyant weight of a soil particle
ΔFF_i	mass fraction finer than d, also fraction of bed area covered with particles of size d
C_v	coefficient of variation for the EVT1 statistical model
ϕ'	effective angle of internal friction of soil (geotechnical parameter)
$\emptyset$	ratio of the height of the drag force point of application to the roughness height
κ	Von Karman constant (about 4.0
μ	dynamic viscosity of the fluid (water)
ρ	density of the fluid
ρ_s	the density of a soil particle
σ'	effective stress
τ	shear stress applied to the soil surface by the fluid flow
τ_{b0}	bed shear stress
τ_c	critical shear stress characteristic of the soil
τ_{c0}	critical shear stress for particle entrainment without seepage
τ_u	undrained shear strength characteristic of the soil
τ^*	dimensionless bed shear stress $= \tau/g\ (\rho_s - \rho)d$
$\bar{\tau}$	average bed shear stress
ω	average particle settling velocity

1. INTRODUCTION

The Author's interest in the erodibility of cohesive soils arose from personal experience with sensitive Champlain sea clay, which is common in many regions of Eastern Canada, even dominant in many areas stretching from Perth, ON to Saguenay, QC, where entire hills and river basins are standing with marginal stability. A slow continuous erosion of the creek and riverbanks reduces the regional stability in some areas triggering retrogressive mud flows, sometimes catastrophic (for example, Locat et al., 2017). In many cases, the thick deposits of marine clays are underlain by sandy tills or weathered bedrock just below the creek or river basins, and in other cases, sand and silt lenses are sandwiched into the clay deposit, forming miniature aquifers in which infiltrated water finds a less resistant path to flow down the hills into the ravines and floodplains. In such cases, seasonal and intermittent artesian conditions can be observed near the toe of the slopes and at the creek banks which sometimes lead to cavities and caverns undercutting the banks and slopes where artesian water pipes through the clay surface. These factors combined with the natural erosion of the banks due to water flow in ravines and creek basins create major instability problems in many communities. It is therefore critical to understand the mechanisms of cohesive soil erosion to quantify and attenuate the problem.

There are several interrelated erosion mechanisms contributing to the sedimentation and loss of soil in hillslopes and streambanks. While major research in past decades significantly advanced our understanding of these mechanisms, research is still needed to understand the complexities of erosion mechanisms, especially the effects of subsurface water (pressure, seepage, piping, etc.).

Mass failure of streambanks can contribute up to 85% of the sediment yield (Simon and Darby, 1999). These include:

- Geotechnical failures where a slope reaches limit equilibrium and relatively large amounts of soil and debris slide into the stream along a characteristic failure surface and
- Gravitational failures, including cantilever failures where an overhanging block collapses into the stream.

While the above-mentioned mass failure mechanisms are distinct and well recognized, in most cases they are caused by surface flow erosion or seepage piping or “pop-out” erosion undercutting soil blocks or the toe of the slope. It is important to note that seepage erosion, where cohesive soil blocks at the face of the streambank pop-out due to a buildup of seepage pressure behind the surface, often occur during a rapid lowering of water levels (Anthony, 2001; Chu-Agor et al., 2008; USDA-NRCS, 2012; UNESCO, 2017). These combined mechanisms are complex and extremely difficult to study or replicate in a laboratory setting. It is therefore important to address the progressive erosion leading to mass failures, and to develop robust methods for studying and understanding such complex processes.

2. PROBLEM STATEMENT

Looking into the current standards in the industry and the knowledge base in the research community with respect to the erosion behavior of cohesive soils, it is evident that additional research is required to address this problem. There is an urgent demand for inexpensive methods to assess quickly the erodibility of cohesive soils across vast terrains and long reaches of watercourses. Currently available methods and processes to assess and model the erodibility of cohesive soils are complex, lengthy, and produce results with high uncertainty.

Due to the challenges faced in directly testing for soil erodibility, a significant research effort has been directed towards correlating the erosion behavior of cohesive soils to other characteristics such as strength, classification, density, porosity, compressibility, etc., so far with no tangible success. This is best expressed by Raudkivi (1976). Since these characteristics are determined by more precise and accessible test methods established and used by other disciplines (geology, geotechnique, etc.), the attractiveness of establishing correlations between the different characteristics is understandable. To reiterate, bulk and strength characteristics of a material are not necessarily indicative of the stability of its surface against fluid abrasion.

As the comparisons between the simple cohesive soil erosion models and test data show a large scatter and inconsistency, the research community is gravitating towards more complex mechanistic models in the hope of getting closer agreements. The simple explanation is that, as researchers try to match scattered data with mathematical models, those models tend to adopt a relatively high level of sophistication and a number of empirical constants to match a specific set of test data. Subsequent research then builds up on the same models, adding new parameters or modifying old ones to match a new set of data, increasing the overall sophistication of the models even further. This is not necessarily an improvement if the data are obtained with inaccurate testing methods and procedures.

Furthermore, in contrast with granular cohesionless soils, cohesive soils can be practically impervious and can sustain a pressure differential across the bed. It is therefore important to investigate the effect of such gradient on the erodibility of a cohesive bed. The erosion due to piping through the bed has been fairly investigated by Fox et al. (2007), Chu-Agor et al. (2008), Fox and Wilson (2010), Midgley et al. (2013), and many others, especially in the discipline of dam engineering; however, very few references can be found on the effect of pressure differential across the bed on the erodibility of the cohesive soil surface by overland flow. Simon and Collison, 2001, discussed the effect of seepage pressures on the erodibility of cohesive beds, backed by *in situ* measurements of pore pressures below stream beds in midwestern USA where pore pressure decreases with depth and becomes negative 10 to 15 cm below the bed due to overconsolidation. Nouwakpo et al. (2010) went further and showed experimentally, using a special flume setup, that the critical shear stress in cohesive soils decreased when the subsurface hydraulic gradient was increased from negative gradients (drainage conditions) to positive gradients (seepage conditions). They also showed that the rill erosion rate under seepage condition was 5.64 times higher than that under drainage condition. Nouwakpo and Huang (2012) later produced more detailed

relationships between subsurface hydrology and the erodibility of a specific cohesive soil used in an elaborate large-scale hillside model. While the above-mentioned researchers presented excellent research quantifying the intensity and duration of differential pressures and seepage forces and measuring the erodibility of the soil surface under such conditions, such measurements are still a challenge and require advanced and elaborate experimental setup.

In summary, researchers and engineers in the industry could benefit tremendously from practical testing devices and methods that can provide fast and reliable information and design parameters related to the erodibility of cohesive soils under a variety of conditions.

For the purpose of this research, the term soil will imply cohesive soil unless explicitly stated otherwise. The term "erodibility" of soils used in this document refers to the general characteristics of the soil's behavior such as entrainment threshold (critical shear stress), rate of erosion under specific shear stress levels, ease of erosion, etc.

3. OBJECTIVES AND NOVELTY

One of the objectives of this research is to develop fast and efficient techniques to directly test for cohesive soil erodibility as an independent characteristic. The goal is to develop new testing devices, tools, and procedures to accelerate the advancement of cohesive soil erosion research. One such device (the Erosionometer) is developed as part of this research work, and a prototype is tested, verified, and published, as will be described later in this document. The novelty in this part of the study is that this device is, to the Author's knowledge, the first to measure directly an accurate critical shear stress of the soil near-instantaneously. The device also requires little test setup time in the field; usually one to five minutes, depending on the terrain and ease of mobility.

Further upgrades to the Erosionometer allow for evaluating the effect of subsurface hydrology on surface erosion, which is sill an under-researched topic. Specifically, influence of gradient in pore pressure on critical entrainment shear stress is tested.

To complete the exploration process, another tool is designed to measure the rate of entrainment of cohesive soils as a function of the fluid shear stress. The new tool is the "Erosion Rate Meter", or ERM for short, and its main objective is to provide data at a fast pace to assess existing erosion rate models and to assist in developing more reliable relationships between bed shear stress and erosion rate in cohesive soils. Several models already exist in literature, some more complex than others (Partheniades, 1965; van Rijn, 1984; Wilson, 1993a and 1993b; Hanson and Cook, 1997; Winterwerp et al., 2012; Al-Madhhachi et al., 2014; Walder, 2016). In all cases, however, and even though the models have been fitted to test data with empirical constants, the correlations between these models and test data still make a good case for more research on the subject. Another objective of this study is to use the newly developed tools to reassess the different erosion rate models and identify the ones that best reflect

cohesive soil behavior. The ultimate goal is to simplify the approach to cohesive soil erosion with methods to increase the accuracy and reliability of predictions and practical designs.

4. LITERATURE REVIEW

The proposed research aims to reassess multiple aspects of the cohesive soil erosion process with the objective of providing the industry and researchers with more efficient tools to evaluate and predict soil erosion. The literature survey is organized into three major topics corresponding to the Author's research objectives. The work developed as part of this study is presented in later sections following the same order as the following literature review topics:

1. Critical bed shear stress: The erodibility threshold of cohesive soils, or the critical fluid bed shear stress (critical shear) that would initiate soil entrainment. The research will include developing new tools and procedures for quick and accurate determination of the critical shear stress. The criteria are to produce accurate data while covering large geographical areas in a relatively brief time, ease of mobility, ease of setup, and ease of testing.
2. Differential pressure effects on erodibility: The newly developed tools can be used to assess the effect of other environmental characteristics such as differential pressure on the threshold of erosion.
3. Erosion rate measurement: The rate of erosion of cohesive soils with varying bed shear levels and other conditions. Once again, the criteria are accurate data, mobile setup, and fast testing.
4. Erosion rate models: Using the developed test methods to investigate and improve existing mathematical models for computing cohesive soil erosion rates and provide practical means to develop new ones for more consistent and reliable predictions.

4.1 Critical shear stress and erosion rate determination

Both the erosion threshold (critical bed shear stress) and the erosion rate of cohesive soils are not yet well determined characteristics despite the substantial amount of research conducted and the development of a multitude of test devices for such purpose. There are many variables affecting the erodibility of cohesive soils, including mineral composition (grain size and shape), soil structure, cohesion, shear strength, porosity, water content, roughness, consolidation, etc. (Raudkivi, 1980; Ternat et al., 2008, and others). As such, it is common to find a wide variation in erodibility potential over relatively short stretches of a watercourse under study. As a result, the need arises for a practical method to map the critical shear and erodibility characteristics across a study area with a reasonable duration and effort in order to model accurately the morphodynamics of a watercourse. Many researchers have studied the erodibility of cohesive soils and several devices and methods are currently in use, both in laboratory setting and in the field, but many drawbacks and challenges still exist, as will be explored in this study.

The most popular and commonly used devices and test methods for determining the critical shear stress characteristic of cohesive soils will be reviewed below, namely, flume test, pinhole test, flow pump test,

rotating cylinder test, and submerged jet test. Another test tool, the Permeameter, is mentioned in some publications as a tool for erosion testing; however, this tool is mainly used to determine the hydraulic head necessary to cause a piping failure through a soil sample and is not for testing erodibility by surface flows.

4.1.1. **Flume test**

Flume tests are the most direct method for determining the erodibility of cohesive soils as they provide the means of mimicking the actual flow.

In erosion studies, piston flumes in different shapes and forms have been designed and used to introduce a soil sample into the bed of the flume subjecting it to the flow. Piston flumes can be closed-conduit such as the EFA (Erosion Function Apparatus) by Briaud et al. (1992) (see Figure 1), the SERF (Sediment Erosion Rate Flume) by Crowley et al., (2014) (see Figure 2), and the SEDflume (Sediment Erosion at Depth flume) by McNeil et al. (1996). Other piston flumes, such as the Flume-Tunnel by Kamphuis and Hall (1983), can be converted and used as both closed-conduit and open-channel type (see Figure 3). Open-channel piston flumes are also common, like the tilting flume by Gaskin et al. (2003) (see Figure 4), Haralampides and Rodgriguez (2006), and the soil box flume by Al-Madhhachi et al. (2014) (see Figure 5).

Regardless of their type, piston flumes allow for the soil sample surface to be maintained flush with the bed, with some form of measuring the quantity of eroded or entrained material, be it by physical measurement, optical methods, or by measuring the concentration of solids in the discharge (by optical backscatter or traditional filtration and weighing). While the amount of entrained soil can be quantified with fair accuracy by any of the above-mentioned methods, the corresponding shear measurement remains a major challenge. Many of the flume devices, some of which are explicitly listed herein, use some form of a shear measuring device. For example, the SERF piston-type flume used by Crowley et al. (2014) includes a shear sensor placed upstream from the piston soil sample. Though not many details are given for the shear sensor, it is a mechanical device and the reported shear is based on the hydraulics of the flow in the flume tube, independent of the soil sample characteristics such as roughness and mobility. It will be argued later in this research that such shear measurement is not representative of the shear stress at the soil-water interface. Rankin and Hires (2000), and Barnes et al. (2007), introduced metallic shear plates flush with the flume bed secured on flexible supports with force sensors to measure the shear induced by wave and swash action assuming the same shear stress acts on the moveable sediment bed. While the shear plates are an improvement to shear estimation from pure hydraulics, the plate surface should match the sediment bed in roughness and general resistance to the flow in order to produce realistic measurements of bed shear stress.

Other researchers use a form of the law of the wall (Yalin, 1992 and others), with velocity measurements, to express the bed shear stress at the soil-water interface. While in theory this method would give an approximation of the bed shear stress, it has several drawbacks, including the following:

- The sample is usually too short for full development of the proper logarithmic velocity profile corresponding to the sample roughness. Kirkgöz and Ardiçlioğlu (1997) showed that the length required for the flow in an open channel to be fully developed ranges between 25 and 75 times the flow height, which is significantly longer than the dimensions of any practical piston sample in a flume.
- Kirkgöz and Ardiçlioğlu (1997) also showed experimentally that the boundary layer along the centerline of the channel develops up to the free surface for a flow aspect ratio $b/h \geq 3$, that is provided if the flow is fully developed. Therefore, the velocity must be measured within the logarithmic velocity distribution zone (inner region), which is hard to determine. Using velocity measurements at random depths may induce errors in the calculated shear. This issue will be discussed in more detail in Section 5.3.2.
- The effective roughness height, which is required for evaluating the law of the wall from a velocity measurement at a single point, is not easy to determine in fine-grained cohesive soils. Even if the size of the scars left by detached soil clusters is used as a roughness height, the frequency and distribution of such scars is random, which will introduce an undetermined error in the effective roughness height determination. In addition, the number of scars will dynamically increase throughout the experiment, starting from a smooth surface, while a constant number is often used for the effective roughness throughout. Furthermore, scars are formed below the general bed surface rather than protruding into the flow, and there is no evidence that they can be used directly as roughness in the law of the wall.

Measuring the velocity profile throughout the depth may resolve many of the problems discussed above; however, this is difficult to achieve without affecting the flow and requires advanced precision instruments. That said, there are ways to determine more accurately the bed shear stress on the flume sample, as will be shown later in this research, and piston flumes with proper setup and calibration can still be some of the most reliable devices for assessing the erodibility of cohesive soils.

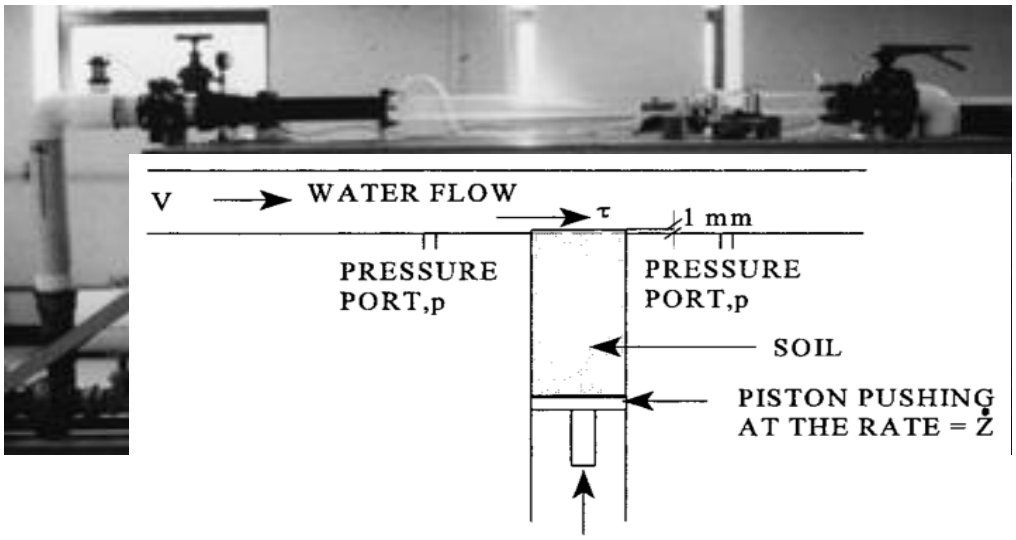

Figure 1. Lab flume (Piston-type), EFA, Briaud et al. (1992)

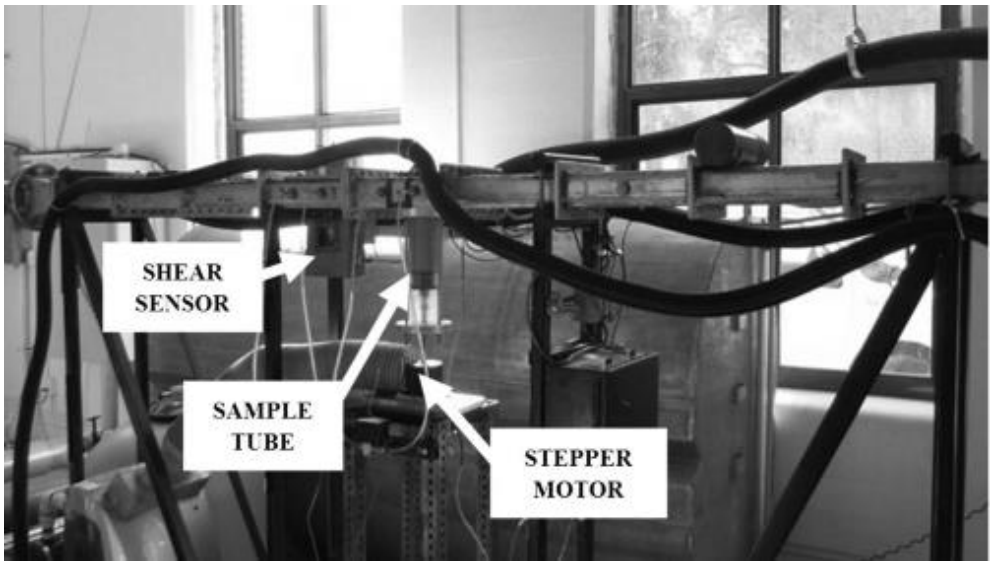

Figure 2. Lab flume (Piston-type), SERF, Crowley et al. (2014)

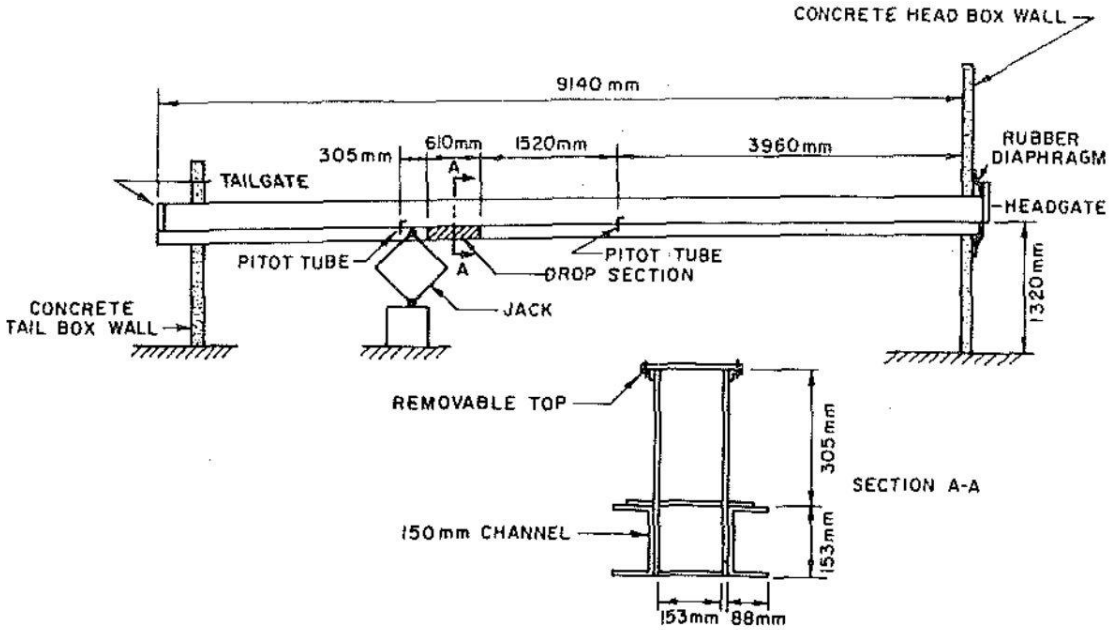

Figure 3. Lab flume (Pison-type), Flume-Tunnel, Kamphuis and Hall (1983)

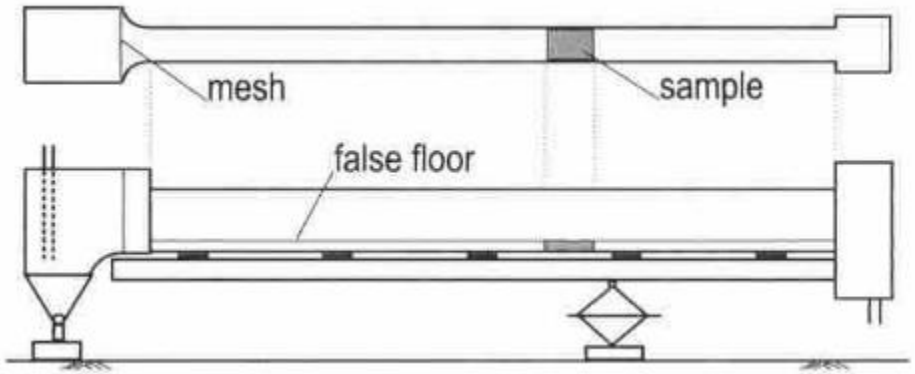

Figure 4. Lab flume (Pison-type), Gaskin et al. (2003)

Figure 5. Lab flume (Pison-type), Al-Madhhachi et al. (2014)

Building a flume test *in situ* is a significant undertaking and impractical when it comes to testing multiple locations across a watercourse; however, some portable flumes have also been developed for *in situ* testing, such as the Sea Carousel benthic annular flume (Amos et al., 1992) and the NIWA (National Institute of Water & Atmospheric Research) benthic *in situ* flume (Aberle et al., 2003, Debnath et al., 2007). Photos of these flumes are shown in Figure 6 and Figure 7, respectively. These flumes are equipped with advanced instrumentation. The Sea Carousel for example consists of an annular conduit, 2 m in diameter, in which rotating paddles in the lid create a circular flow. Bed shear is estimated from flow velocity (using a "laboratory produced algorithm") and the entrained sediments are measured by three optical backscatter sensors measuring the suspended sediment concentration in the flow. An obvious drawback of this device is that the same fluid is continuously recirculated, which implies higher sediment concentrations in the flow with time, which is shown to influence the erosion capacity of the flow (Kamphuis, 1983).

NIWA flumes work the same way as the Sea Carousel, except that the flow is linear, induced by a suction motor, and the fluid is not recirculated. Bed shear is also calculated from flow velocity, and either measured Reynolds stresses or roughness parameters from literature.

While the advanced measurement devices may lead to reliable erodibility measurements, *in situ* flumes can be complex to setup and difficult to deploy in the field. Laboratory flume tests are more practical but require extensive work and preparation to provide reliable results, as will be discussed later. A simpler device for measuring the erodibility of cohesive soils would go a long way in advancing erosion research.

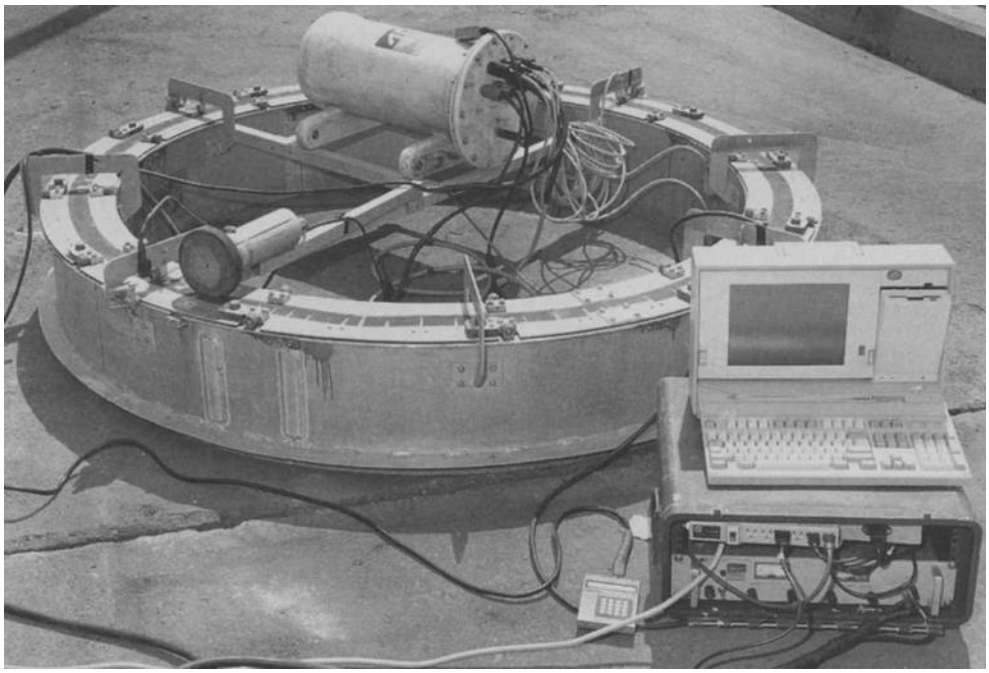

Figure 6: *In situ* flume, Sea Carousel benthic annular flume, Amos et al. (1992)

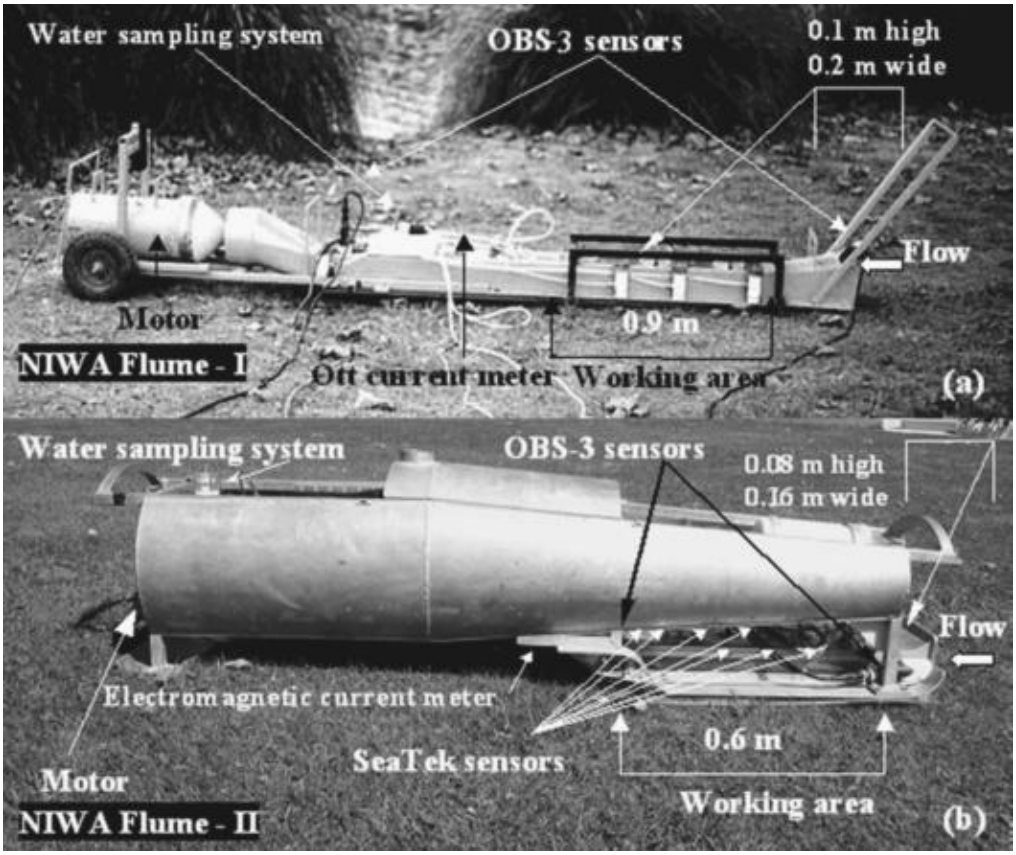

Figure 7: *In situ* flume, NIWA, Aberle et al., 2003; Debnath et al. (2007)

4.1.2. **Pinhole test**

A " Pinhole test" (Sherard et al., 1976; Nadal-Romero et al., 2011) and a similar one known as the "Flow pump test" (Reddi et al., 2000) are used for assessing the erodibility of cohesive soils. These tests consist mainly in running a distilled water flow at a gradually varying hydraulic gradient through a small hole made into a soil sample until dispersive sediments are observed in the discharged water. Although this test is intuitively simple, the eroding surface can be significantly affected by the handling and hole punching and may not represent the actual soil surface in the field. Furthermore, this test assumes homogeneous soil conditions throughout the thickness of the sample and may not be representative of the behaviour of surface soils. This test is illustrated in the schematic (Nadal-Romero et al., 2011) and photo (Walder, 2016) presented in Figure 8.

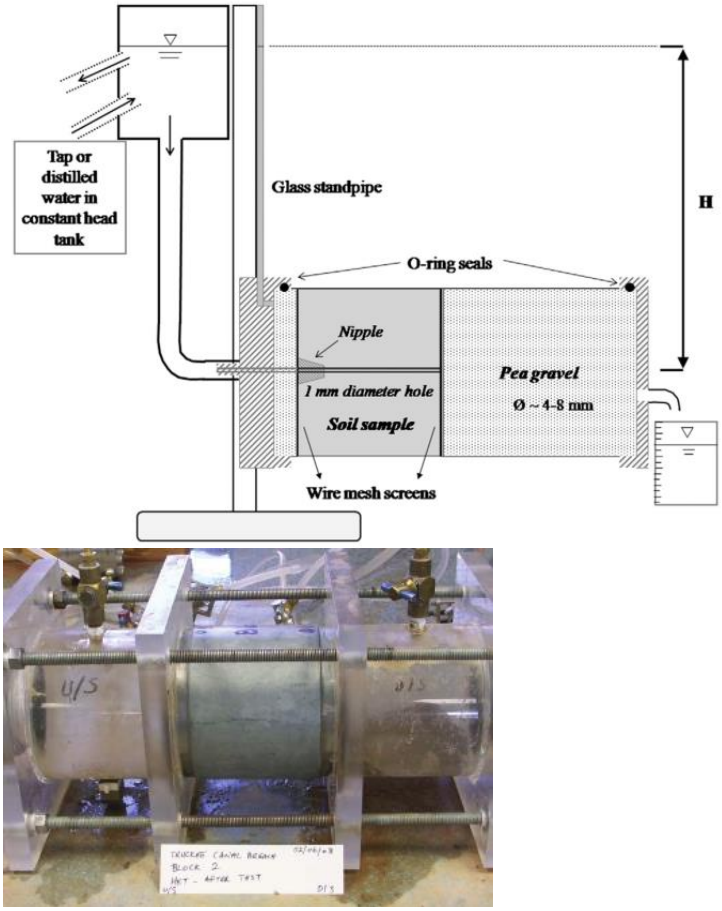

Figure 8: Pinhole test, schematic (Nadal-Romero et al., 2011), photo (Walder, 2016).

4.1.3. **Rotating cylinder test**

The "Rotating cylinder test" (RCT) is used for determining the critical shear and the rate of erosion of cohesive soil samples. The RCT was first developed by Moore and Masch (1962) and has been subjected to several improvements (Lin and Khalili, 2009, and others). In this test, a cylindrical soil sample is mounted between two plates, and suspended by a central shaft in a clear cylinder filled with water. The

shear stress is applied to the lateral surface of the soil by spinning the outer cylinder and the contained water relative to the soil cylinder. The shear is quantified by measuring the torque required to keep the soil sample stationary against the spinning water and the resulting erosion is physically observed and measured. Although this device may provide a close simulation of actual water flow against the soil surface, it presents several limitations as the soil sample is subjected to significant manipulation during the preparation and setup, which may affect its behavior when sheared. Furthermore, as can be seen in Figure 9, delicately carving and mounting the sample is expected to render the test somewhat time consuming. In addition, some softer and/or less cohesive soils cannot be formed and mounted as required in this test setup. Another important drawback of this device is that the increase in sediment concentration in the swirling recirculated fluid may influence the entrainment capacity of the fluid with time and therefore affect the erosion rate (Kamphuis, 1983). Lastly, the eroded surface being vertical introduces an important variable (gravity) in applying the results to field conditions. This test is illustrated in the schematic (Moore and Masch, 1962) and photo (Lim and Khalili, 2009) presented in Figure 9.

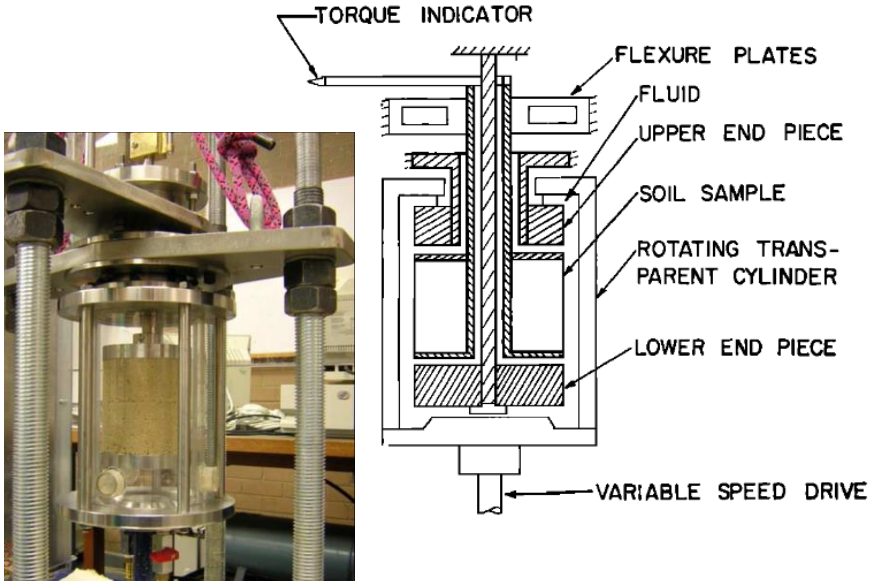

Figure 9: Rotating Cylinder Test (RCT), photo (Lim and Khalili , 2009), schematic (Moore and Masch, 1962).

4.1.4. **Submerged jet test**

The most frequently encountered test in recent literature is known as the "submerged jet test". This type of test was historically used by many researchers to assess the erodibility of cohesive soils (Hollick, 1976; Hanson, 1991; Mazurek et al., 2001). Hanson and Cook (2004), introduced, in detail, an improved version of a portable submerged jet test apparatus, which is currently widely used to determine the erosion rate and critical shear of cohesive soils, both *in situ* and on extracted samples. They also introduced the mathematics required for interpreting the test results along with software in spreadsheet form for simplifying the task.

The submerged jet device (Jet) uses a constant head reservoir discharging through a standard size circular nozzle (6.4 mm dia.) mounted at its base. The jet nozzle is mounted such as to discharge vertically or at a slight incline inside an enclosed cylinder filled with water (submerging the jet), impinging onto the soil surface at the base of the cylinder. The thickness of soil scoured under the impinging jet is determined at regular time intervals using a point gauge which temporarily blocks the jet flow during the measurement. The rate of erosion is determined based on the change in depth measurements of the scour hole. Jet impingement theory is then applied to determine the maximum tractive shear stress (parallel to the soil, also known as wall shear) on the soil surface as a decreasing function of the increasing distance between the jet and the soil, or indirectly, the depth of the scour hole. In theory, the critical shear is specifically defined as the calculated tractive shear stress when equilibrium is achieved, and no further scour is caused by the jet; however, such a point is rarely reached within a reasonable scour depth, and a method is provided (Hanson and Cook, 2004) to extrapolate a theoretical asymptotic value of the wall shear as the critical shear stress. It should be noted that the soil must be assumed homogeneous throughout the scour depth and beyond, with the only variable being the wall shear for such theory to be valid.

As presented by Hanson and Cook (2004), Figure 10 illustrates the operating principle and equations of the impinging jet apparatus and Figure 11 shows a functioning apparatus in the field.

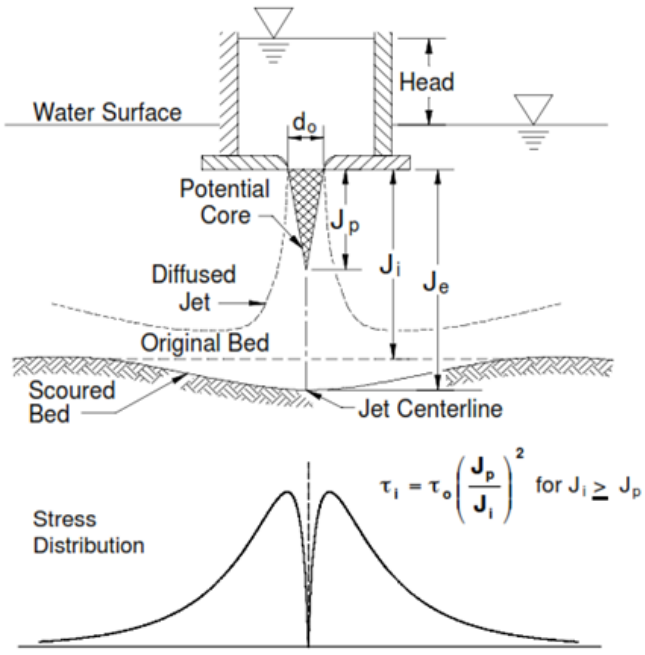

$$\tau_i = \tau_o \left(\frac{J_p}{J_i}\right)^2$$

$$J_p = C_d\, d_o \qquad \tau_o = C_f\, \rho\, U_o^2 \qquad U_o = \sqrt{2gh}$$

τ_i	=	initial peak boundary stress prior to scour
τ_o	=	the maximum stress due to the jet velocity at the nozzle
J_p	=	the potential core length
J_i	=	the initial jet orifice height
C_d	=	the diffusion constant = 6.3
d_o	=	the nozzle diameter
C_f	=	the coefficient of friction = 0.00416
ρ	=	the fluid density
U_o	=	the velocity at the jet nozzle
g	=	the gravity acceleration constant
h	=	the differential head measurement

Figure 10: Illustration of the impinging jet: principle and formulation (Hanson and Cook, 2004)

Figure 11: The original Jet apparatus deployed in the field, Hanson and Cook (2004)

As can be seen in Figure 10, the maximum stress τ_o due to the jet velocity at the nozzle is computed as a function of the exit velocity, U_o, water density, ρ, and an empirical constant (coefficient of friction C_f). The tractive lateral shear, τ_i, at the impinging point (perpendicular to the jet direction), at impact depth J_i below the nozzle, can then be computed as a function of τ_o, J_i, and the length of the cone formed by the jetted water where the velocity within the cone is equal to the velocity at the nozzle, which is in turn a function of the nozzle diameter. These are well-known relationships for a submerged impinging jet on a flat surface, predating the Jet device.

Despite its wide use for soil characterization, both in research and in the industry, the phenomena involved in the Jet are still subject to significant research and critique. The Jet apparatus has provided significant advantages in terms of reducing the time and effort required to determine the erodibility of cohesive soils, especially *in situ*; however, there are significant drawbacks to the Jet test method:

- It is important to note that cohesive soil erosion can be very slow, especially near the critical shear, and becomes very difficult to observe when determined by a rough point gauge probe. Also, depending on the initial tractive stress at the start of the test, reaching equilibrium may require a long time, and a deep scour hole, which may distort the test. Therefore, the equilibrium value (critical shear stress) is usually determined by extrapolation, which introduces a potentially significant uncertainty in the accuracy of the interpretation.

- The analytical methods developed by Hanson and Cook for interpreting the Jet test results are based on the shear stress distribution induced by an unconfined submerged impinging jet. Ghaneeizad and Atkinson (2015) showed that the jet within the apparatus is significantly affected by the confinement imposed by the cylindrical enclosure used to submerge it. They reported a maximum shear stress under the particular confined condition as much as 240% greater than that obtained from unconfined jet theory. Furthermore, Ghaneeizad and Atkinson showed that the confinement also alters the tractive shear distribution, causing the maximum shear to occur closer to the impingement point than in an unconfined jet condition, which magnifies the impinging capability of the jet flow.

- The tractive shear force developed from the impinging jet theory is based on a circular jet impinging on a horizontal flat surface. Considering the confinement effect reported by Ghaneeizad and Atkinson (2015) (see above), a deep scour hole at the impingement point, which introduces further confinement of the jet, is expected to induce even more significant errors in the computed magnitude and distribution of the tractive shear. It is therefore implied that the impingement test should be limited to a wide and shallow scour hole to minimize the confinement effect. Furthermore, it is obvious that the fluid in the scour hole will become more sediment-laden with time, which is expected to change its density and viscosity, hence hindering the impinging potential of the jet going through it, which is not accounted for in the formulation of the Jet tester.

- Many clays and silty clays are sensitive to shear strain and manipulation, as will be discussed later in this document. This implies that the physical characteristics, including strength and erodibility, will change when the soil is subjected to some level of shear. Since the Jet test, by its nature, starts with a high shear that gradually reduces towards the equilibrium value as the scour hole deepens, it mimics the reverse process of natural erosion, which may not be suitable, for sensitive soils.

- In addition to the technical issues discussed above, the Jet test is still somewhat time consuming to perform and interpret in the field.

It is important to mention that it may be possible to improve the Jet test accuracy by modifying the test procedure. The depth of the scour hole can be limited to a couple of millimeters by moving the device and repeating the test at an intact nearby spot with a higher nozzle each time. This way, every tested spot can be a new data point on the shear versus erosion rate chart and the entire dataset will be representative of the same surface soil while the estimated wall shear from the water head will be more accurate as the impingement surface remains quasi-plane. Although the confining effect of the cylindrical enclosure remains, the resulting accuracy is expected to be improved significantly.

Another device, operating on similar principles to the Jet tester, is commercially available as the Cohesive Strength Meter (CSM). The CSM is more portable than the Jet apparatus and has been calibrated by

researchers (Grabowski et al., 2012); however, it is also based on an impinging jet perpendicular to the eroding surface and hence subject to the same limitations as the Jet tester.

Mazurek and Rajaratnam (2003) introduced a horizontal submerged jet test mounted in a laboratory flume tank. As shown in Figure 12, the jet is parallel to the soil surface and the excess water overflows back into the pump tank for recirculation. For the purpose of their experiment, the authors physically measured the size of the scour caused by the jet and computed the shear stress based on the flow velocity (no shear measurement was done). This type of jet is not impinging, but rather similar to a short flume where the flow shear calculations using methods like the law of the wall are not valid due to the complex interaction between the stagnant water in the tank and the jet flow. Furthermore, the limited height of the jet flow makes it difficult to establish a velocity profile to use for shear calculations. The submerged horizontal jet can be improved and made more effective by enclosing the soil impacted by the discharge in a container that is free to move in the direction of the flow and restrained with a force measuring device. The shear could then be measured fairly accurately.

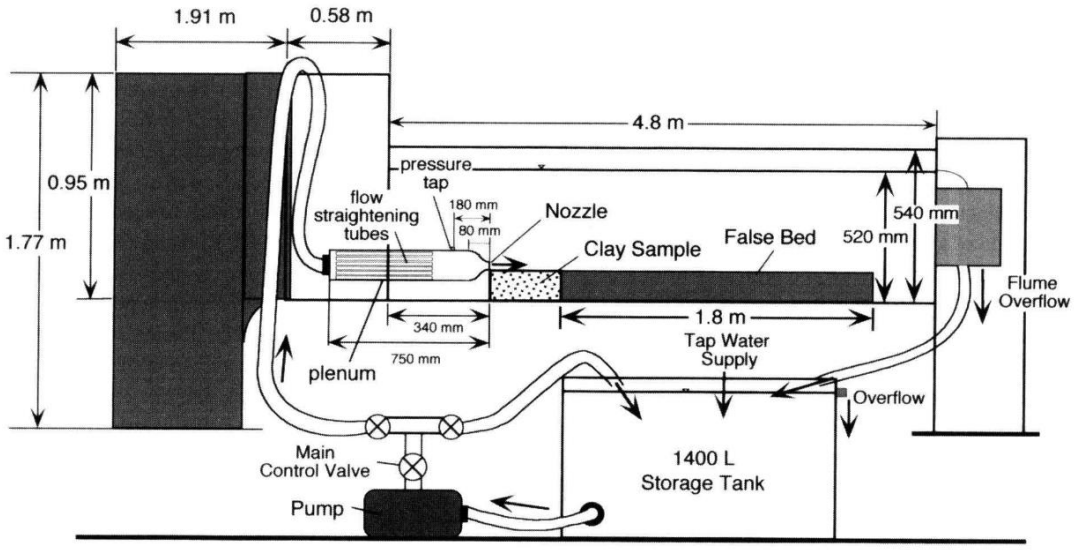

Figure 12. Submerged turbulent plane wall jet, Mazurek and Rajaratnam (2003)

4.1.5. **Permeameter test**

A permeameter test (Kassiff et al., 1965) is used to determine the hydraulic head necessary to cause a piping failure through a soil sample placed on a perforated base. Although the tested failure is due to soil erosion, this test is not suitable as a direct indication of the critical shear of the soil under surface flow for several reasons:

- Although the head upstream of the failure zone is measured, the pressure at the exit, which causes the actual failure, is not easily determined.

- The head buildup within the confined piping path applies a normal pressure on the soil (perpendicular to the piping path) which would help stabilize the soil surrounding the piping conduit against entrainment.
- The geometry of the burst hole is not usually prismatic, therefore it is difficult to quantify the shear stress that caused the failure.

4.1.6. **Other**

Early researchers, and some recent ones, attempted to relate geotechnical characteristics and classes of soil to their erodibility, which was mostly driven by the lack of practical test methods for soil erodibility. Raudkivi (1976), documented early studies in Russia in the 1930's developing charts relating critical shear stress of clays to their void ratio. Others related the erodibility of cohesive soils to their plasticity (Lutz, 1934, and Beasley, 1959). Briaud et al. (2017), used the EFA flume tests to produce "erosion charts" for a number of geomaterials based on their unified soil classification, which lumps a large variety of soil textures and compositions under the same class.

The tendency to relate soil erodibility to geotechnical soil characteristics is driven by the availability of practical test methods for such characteristics (falling cone, Casagrande tools, scale, drying oven, etc.), as opposed to the complex and time-consuming test methods for erosion and bed shear.

As there were wide variations in such correlations between researchers, serious doubts can be cast on their value. This was best expressed by Raudkivi (1976), in regards of shear strength vs. erodibility correlation attempts: "In general, the shear strength of a soil has little bearing on its erodibility. Critical shear stresses have been found to be orders of magnitude lower than corresponding soil shear strength and the same flow conditions may initiate erosion in cohesive soils which differ in shear strength by orders of magnitude".

4.2 **Erosion rate models**

Many researchers have studied and formulated the rate of erosion of cohesive soils, and, not surprisingly, produced a wide spectrum of predictive models with quite a variation in complexity and prediction results. Several erosion rate models have been proposed over the years. Two broad types of models that are mostly used in contemporary research will be discussed in this study. The most widely used one is a simple excess shear stress model, of which different variations are introduced as will be discussed below. Other mechanistic and probabilistic models have been introduced in an attempt to quantify the driving and resisting forces leading to the detachment of a particle or a cluster of particles out of the soil matrix. These models add significant complexities to the erosion problem and will be discussed in depth.

4.2.1. **Excess shear and linear models**

Excess shear models and linear models are simple, easy to apply empirical models tailored to each soil by means of a single proportionality parameter determined from data fitting. In some models where non-linear behavior is suggested, a constant exponent is also determined, though no consensus on a specific exponent is found among the researchers that propose non-linearity.

In general, the Excess Shear model is expressed as:

$$E = k(\tau-\tau_c)^m \qquad \text{for } \tau > \tau_c \tag{1}$$

or in terms of eroded mass:

$$M = k'(\tau-\tau_c)^n \qquad \text{for } \tau > \tau_c \tag{2}$$

Where E is the erosion thickness, M is the mass of eroded material, k and k' are empirical constants reflecting the ease of erosion of the soil material, τ is the shear stress applied to the soil surface by the fluid flow, τ_c is the critical shear characteristic of the soil, and m and n are empirical exponents, which are usually taken as unity implying a linear relationship between erosion rate and shear differential (Partheniades, 1965; Hanson and Cook, 1997). A different variation of the excess shear model has been introduced in an attempt to derive a dimensionless version of the model using the dimensionless differential shear stress, also referred to as Transport Stage Parameter (van Rijn, 1984; Winterwerp et al., 2012):

$$T = (\tau-\tau_c)/\tau_c \quad \text{or, equivalently,} \quad T = (\tau/\tau_c - 1) \tag{3}$$

and

$$E = E_o.T^m \tag{4}$$

Where E is the erosion rate as defined earlier, E_o is an empirical parameter reflecting the ease of erosion of the material, similar to k and k' above, and T is the Transport Stage Parameter.

Some researchers have introduced different values for m; for example, Walder (2016), used values of $m = 1.60$ and $m = 1.72$ to fit data for two different soils. Walder also went further to propose a dimensionless erosion rate:

$$\tilde{\Phi} = \left(\frac{s_d}{s_s}\right)\left(\frac{E}{\sqrt{\tau_c/\rho_w}}\right) = \frac{M}{\rho_s\sqrt{\tau_c/\rho_w}} \tag{5}$$

Where s_d is the dry bulk specific gravity of the soil, s_s is the solid bulk specific gravity, E is the erosion thickness as defined earlier, τ_c is the critical shear stress, ρ_s is the solid density, ρ_w is the water density, and M is the mass of eroded material.

The premise of Walder's transformation is to show a linear relationship between $\log \widetilde{\Phi}$ and $\log T$ of the form:

$$\log \widetilde{\Phi} = \beta_0 + n_0 \log T \quad (6)$$

With β_0 and n_0 as the intercept and slope, respectively. While the relationship in Equation 6 does somewhat fit the data used by Walder, the same fit can be obtained between log E and log T directly, without having to determine the additional parameters.

It is important to note that, with assumed linearity (no exponent), using excess shear or transport stage parameter makes no difference other than using a different multiplier (k) to fit the data.

4.2.2. **Fundamentally based detachment model**

Some fundamentally based mechanistic and probabilistic models (Wilson, 1993a and 1993b; Al-Madhhachi et al., 2014) have been gaining interest in recent years. These models are based on a mechanistic particle detachment analysis and apply probabilistic models to estimate the exceedance of the detachment condition. In this section we examine the model presented by Wilson, B.N., in two articles (1993a and 1993b). This model is intended for assessing the erodibility of cohesive soils, as stated and used by Wilson and others. The premise of this model is that there is some form of erosion occurring at any shear stress level, though very limited below the critical shear level. Al-Madhhachi et al. (2014), built on Wilson's model and provided a modified version to account for seepage effects, which will be discussed in the next section.

Using the illustration shown in Figure 13, Wilson formulated a moment balance at which the incipient motion of a particle of diameter d occurs:

$$l_1 W_s \sin\alpha + l_3 F_d + l_4 F_L = l_2 W_s \cos\alpha + M_c \quad (7)$$

It should be noted that, while the schematic in Figure 13 appears to represent granular soils as opposed to fine-grained cohesive ones, the model is explicitly described to apply to cohesive soils. This method of representing the structure of the soils is one of the fundamental issues casting doubt on the validity of this model for cohesive soils.

The terms on the left-hand side of Equation 7 represent the dislodging moments while the right-hand terms represent the resisting or stabilizing moments. Keeping in mind that the moment balance is applied for one grain size at a time, the terms in Equation 7 from left to right represent the following moments

of forces causing rotation of the particle around the lee point of contact with the adjacent grain; l_1 through l_4 being the length of the corresponding moment arm of each force:

1. Component of the buoyant weight (W_s) of the particle parallel to the flow direction where α is the incline of the bed with respect to the horizontal.
2. Drag force (F_d) in the flow direction
3. Lift force (F_L) perpendicular to the flow direction (upward)
4. Component of the buoyant weight (W_s) of the particle perpendicular to the flow direction (downward)
5. Sum of all moments (M_c) of friction and cohesion forces resisting detachment.

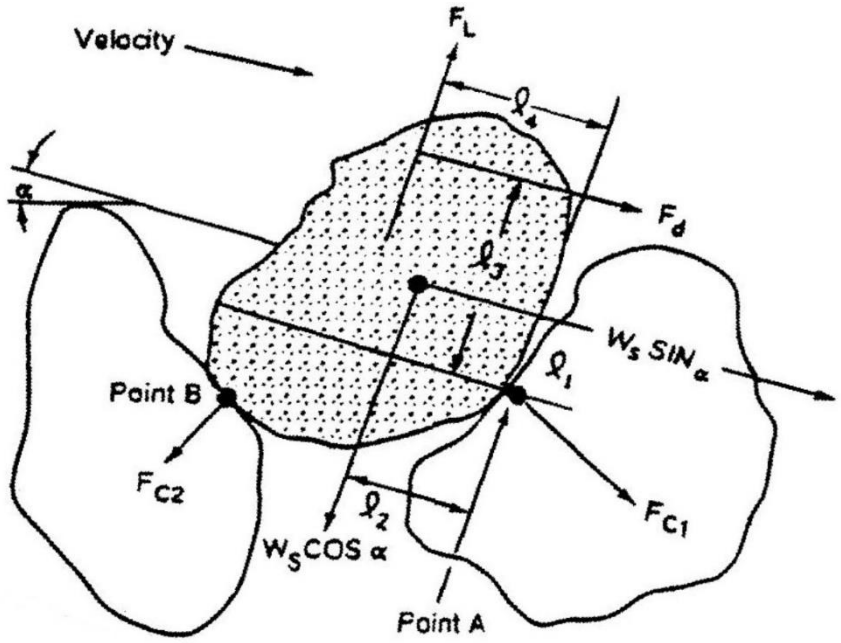

Figure 13. Illustration of moments acting on sediment grain, Wilson (1993a)

After extensive mathematical transformations, adopting relationships from literature, and using the Extreme Value Type 1 (EVT1) probabilistic distribution, the fractional mass detachment (e_i) model is given by Wilson for Soil Fraction "*i*" of particle size *d* as:

$$e_i = \chi_1 \rho_s \sqrt{gd\tau^*} \times \left[1 - e^{-e^{\left(\frac{1.28}{C_v} - 0.5572 - \frac{\chi_2}{C_v \tau^*}\right)}}\right] \quad (8)$$

With

$$\chi_1 = \frac{k_r}{K_e} \Delta FF_i \sqrt{\frac{K_n}{k_d}} \quad (9)$$

$$\chi_2 = \frac{\pi}{\sqrt{6}} \frac{k_r(K_{ls}+f_c)}{K_d}$$

10

Where

ρ_s is the density of the particle

g is the gravity acceleration

d is the i[th] particle size in the soil mix

τ^* is the dimensionless bed shear stress $= \frac{\tau}{g\,(\rho_s-\rho)d}$

C_v is the coefficient of variation for the EVT1 model

k_a is the area constant ($d \times k_a$ = particle surface area)

k_v is the volume constant ($d \times k_v$ = particle volume)

k_r is the ratio of volume to area constants (k_v/k_a)

K_e is a parameter to account for the additional time to remove the surrounding particles such that the underlying particles are no longer protected from the flow

ΔFF_i is mass fraction finer than d, also assumed as fraction of bed area covered with particles of size d

k_d is a detachment distance parameter

K_t is an empirical factor applied to the drag force to account for "the cumulation of instantaneous fluid forces"

$K_n = K_t\,K_d\,k_r$ defined as a "combination of particle and fluid factors"

$K_d = \left[C_d\,k_f\,(\ln(\varphi)\,/\,\kappa + B)^2\right]/2$: Dimensionless hydraulic drag parameter; C_d is the drag coefficient, φ is the ratio of the height of the drag force point of application (z) to the roughness height (K_s), κ is the Von Karman constant (about 4.0), and B is a dimensionless log-velocity factor dependent on the shear Reynolds number

k_r is the ratio of volume to area constants

$K_{ls} = [\cos\alpha\,(l_2 - l_1\,S_0)]\,/\,\left[l_3 + l_4\,K_L/k_f\right]$: S_0 is the slope of the sediment bed (slope of the flow direction), K_L is the proportional constant between drag and lift coefficients and their respective velocities (Chepil, 1959), k_f is the ratio of projected area of drag force to that of lift force (assumed constant)

$f_c = \left[M_c\,/\left(l_3 + l_4\,K_L/k_f\right)\right]/W_s$

This detachment model must be applied to each particle size "*i*" separately, and the different values added to obtain a total detachment rate of the mix. That said, Wilson cautions about adding the rates of

detachment of various particle sizes, rightfully stating that this concept would overlook the interaction between particles of different sizes, i.e. larger particles shielding smaller particles must be entrained first, and vice versa ("selective detachment"). In fact, with truly cohesive soils, geometric representation of force and moment balance on grains of specific grain size is not a viable approach, as the particles and particle assemblies most efficient in resisting entrainment are microscopic, and do not allow free water flow through the pores, in addition to being practically weightless. Wilson (1993b), then proposes a simplified version of the model that would be applied to the sediment mix, lumping selective detachment effects with all other coefficients and parameters as part of the "calibration procedures". He then proposes a modified form consisting of a two-parameter model that is a direct function of the average bed shear:

$$e = b_0 \sqrt{\bar{\tau}} \times \left[1 - e^{-e^{\left(3.0 - \frac{b_1}{\bar{\tau}} \right)}} \right] \quad (11)$$

With

$$b_0 = \rho_s \frac{k_r}{K_e} \sqrt{\frac{K_n}{k_d(\rho_s - \rho)}} \quad (12)$$

$$b_1 = \frac{\pi}{c_v \sqrt{6}} \frac{k_r(K_{ls} + f_c)}{K_d} g (\rho_s - \rho) d \quad (13)$$

Where:

e is the combined erosion rate for all sediment grain sizes

$\bar{\tau}$ is the average bed shear stress

ρ is the density of the fluid

Other parameters are as defined earlier.

It is important to note that the term d in the above expression of the combined model is a "representative diameter" of the sediment mix, which is hard to define for cohesive soils.

At this point, parameters b_0 and b_1 become merely empirical parameters determined by curve-fitting techniques to match experimental data of bed shear versus erosion rate.

A more in-depth critical review of Wilson's model is presented in Appendix 1. The review shows that Wilson's proposed fundamentally based detachment model, while intended as an elaborate attempt to predict the erodibility of cohesive soils based on their physical characteristics, is practically a two-parameter curvilinear representation of the bed shear-detachment rate relationship. This model must

ultimately be calibrated by curve fitting to representative erosion test data, the same as the linear excess shear model. The field data selected by Wilson for demonstrating the model application (see Appendix 1) seems to lend itself to a linear trend with relatively high coefficient of determination (R^2) and the comparisons provided did not show any advantage for using the proposed fundamental model over the commonly used excess shear model in terms of representing actual detachment rate data.

It is in the Author's opinion that the complexities of the fundamental model proposed by Wilson are unnecessary and the model itself provides no real advantages over the simpler excess shear model. One of the main objectives of this research is to develop new tools for fast and accurate assessment of the erosion rate of cohesive soils under varying shear levels. It is therefore anticipated that the excess shear model, or an improved version of it, will be used throughout the continuation of this study.

4.2.3. **Modified mechanistic model**

In recent years, Al-Madhhachi et al. (2014) built on Wilson's model and provided a modified version to account for seepage effects.

Using the illustration shown in Figure 14, Al-Madhhachi formulated a moment balance by adding the seepage-related components (F_s) to Wilson's moment balance, at which the incipient motion of a particle of diameter d occurs:

$$l_1 W_s \sin\alpha + l_3 F_d + l_4 F_L + \underline{l_2 F_s \cos\alpha} = l_2 W_s \cos\alpha + \underline{l_5 F_s \sin\alpha} + M_c \quad (14)$$

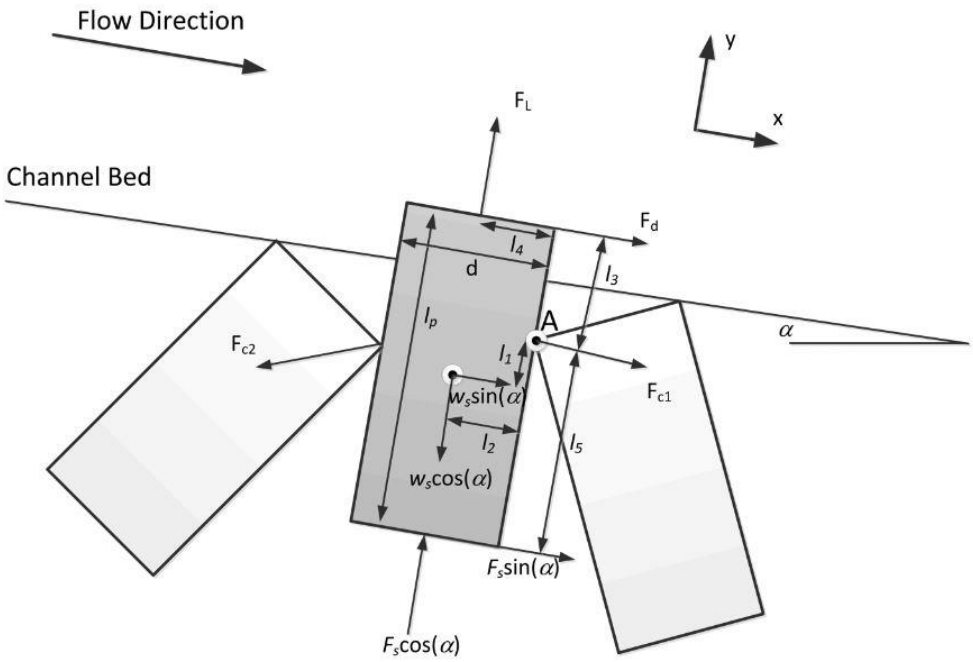

Figure 14. Illustration of moments acting on sediment grain, Al-Madhhachi et al. (2014).

With similar derivations to Wilson's, Al-Madhhachi proposes an identical total detachment rate expression to that given by Wilson, with the same two parameters to be determined experimentally (see Eq.15). The only difference between the two expressions are additional components in the definition of the two parameters related to the seepage forces (see Eq.16, Eq.17, and Eq.18).

$$e = b_0 \sqrt{\bar{\tau}} \times \left[1 - e^{-e^{\left(3.0 - \frac{b_1}{\bar{\tau}}\right)}}\right]$$

15

With

$$b_0 = \rho_s \frac{k_r}{K_e} \sqrt{\frac{K_n + K_{st}}{k_d(\rho_s - \rho)}}$$

16

$$b_1 = \frac{\pi}{c_v \sqrt{6}} \frac{k_r(K_{ls} - K_s + f_c)}{K_d} g\,(\rho_s - \rho)\,d$$

17

$$K_{st} = \frac{\mu_s g i d \rho}{\bar{\tau}} = \mu_{sr} g i d \rho$$

18

Where:

K_{st} is the seepage parameter due to the exchange time of a particle.

$K_s = [i\rho/(\rho_s - \rho)] \times [\cos\alpha\,(l_2 - l_5\,S_o)] \,/\, [l_3 + l_4\,K_L/k_f]$

i is the seepage hydraulic gradient.

μ_s is the seepage coefficient which is function of soil and fluid characteristics.

$\mu_{sr} = \mu_s/\bar{\tau}$

The rest of the parameters are as defined earlier in Wilson's model. Note that in the absence of seepage, where $K_s = 0$ and $K_{st} = 0$, Equations 15, 16, and 17 revert to Wilson's model presented earlier.

Again, despite the elaborate definitions and multipliers, parameters b_0 and b_1 become merely empirical parameters determined by curve-fitting techniques to match experimental data of bed shear versus erosion rate while seepage is applied to the experimental setup.

4.2.4. **Discussion**

Based on data and discussions presented in later sections in this research, and on the review provided in Appendix 1, it is reasonable to conclude that the simple linear model represented in Equation 3 is a

practical model to represent the rate of erosion as a function of bed shear stress for cohesive soils. Also, with truly cohesive soils, geometric representation of force and moment balance on grains of specific grain size is not viable. As stated above, the particles and particle assemblies that are most effective in resisting entrainment are microscopic, and do not allow free water flow through the pores, in addition to being practically weightless. Therefore, the only practical parametric representation of the erosion rate vs. shear stress within the limitations of currently available technology is empirical.

4.3 Effect of pressure differential on cohesive bed erodibility

The erosion due to underground seepage and piping through streambanks and beds has been investigated by many researchers such as Fox et al. (2007), Chu-Agor et al. (2008), Fox and Wilson (2010), Midgley et al. (2013), and many others; however, very few references can be found about the effect of pressure differential across the streambed on the erodibility of a cohesive soil surface. Huang and Laflen (1996) and Zheng et al. (2000) showed that positive pore water pressure due to seepage increased cohesive sediment discharge when compared to the drainage condition where the pore water was under tension. They also showed that the sediment load increased as the pore water pressure was increased from negative (drainage) to positive (seepage). Al-Madhhachi et al. (2014a and 2014b) conducted erosion tests using both a piston flume and a miniature Jet tester on silty sand cohesive samples subjected to an injection gradient. The gradient was applied to the underside of the samples via a riser pipe with varying water column height. By conducting such measurements at different gradients, they were able to build on Wilson's mechanistic detachment model (Wilson 1993a and 1993b) and provided a modified version of the model to account for seepage effects by adding seepage-related terms to the model's two parameters: b_0 and b_1. Few or no other techniques are available for rapid assessment of the relation between pore water pressure gradient and critical shear stress of a given cohesive soil, especially in drainage seepage conditions.

Three other publications reporting research that related pore pressure gradient to erodibility are reviewed in more detail in the following subsections.

4.3.1. Simon, A., and Collison., A. J., 2001, Pore-water pressure effects on the detachment of cohesive streambeds - seepage forces and matric suction

In a joint research effort between the USDA Agricultural Research Service (USDA-ARS) and Kings College, London, UK, Simon and Collison (2001), investigated the effect of seepage pressures on the erodibility of cohesive beds in midwestern USA, where pore pressure was found to decrease with depth and in some cases becomes negative 10 to 15 cm below the bed due overconsolidation. The soils were generally of clay materials, with a hydraulic conductivity ranging between 10^{-9} and 10^{-10} m/s. While they discussed the role of seepage forces in increasing or decreasing the erodibility of cohesive soils (depending on the flow direction), the main thrust of the published research was the buildup of pore pressure due to a rise in flow depth and the resulting upward directed seepage forces on the recessional

limb of the hydrograph. By imposing synthetic hydrographs on cores from the cohesive beds, the authors showed significant upward pressure gradients, wherein a resulting net upward seepage force was large enough to contribute to the detachment of cohesive bed material. The soil cores were 5-cm-wide and 15.2-cm long. Three tensiometers were inserted and sealed into the core, 3.5 cm from the top, 3.5 cm from the bottom, and in the middle, 4.1 cm from the top and bottom tensiometers.

As reported by the Authors, the head initially was at zero and negative pore-water pressures were obtained. It was then raised to a base-flow level of 43.5 cm and maintained for 1 to 2 hours. The experiments were conducted with a hydrograph peak of 2.5 m and 5.0 m, slowly reached over 1 to 2 hours and maintained for approximately 1 to 4 hours. The head was then slowly lowered to the base-flow height over 1 to 2 hours. After the head was lowered, tensiometer readings were recorded for the remainder of a 24-hour period. The tensiometer readings were then converted to seepage forces as shown in the typical results in Figure 15.

Simon and Collison proceeded to perform numerical modelling using a commercially available finite-element seepage model SEEP/W, by GeoSlope International, to verify and extend the experimental results obtained with the core samples, particularly the magnitude of the seepage forces.

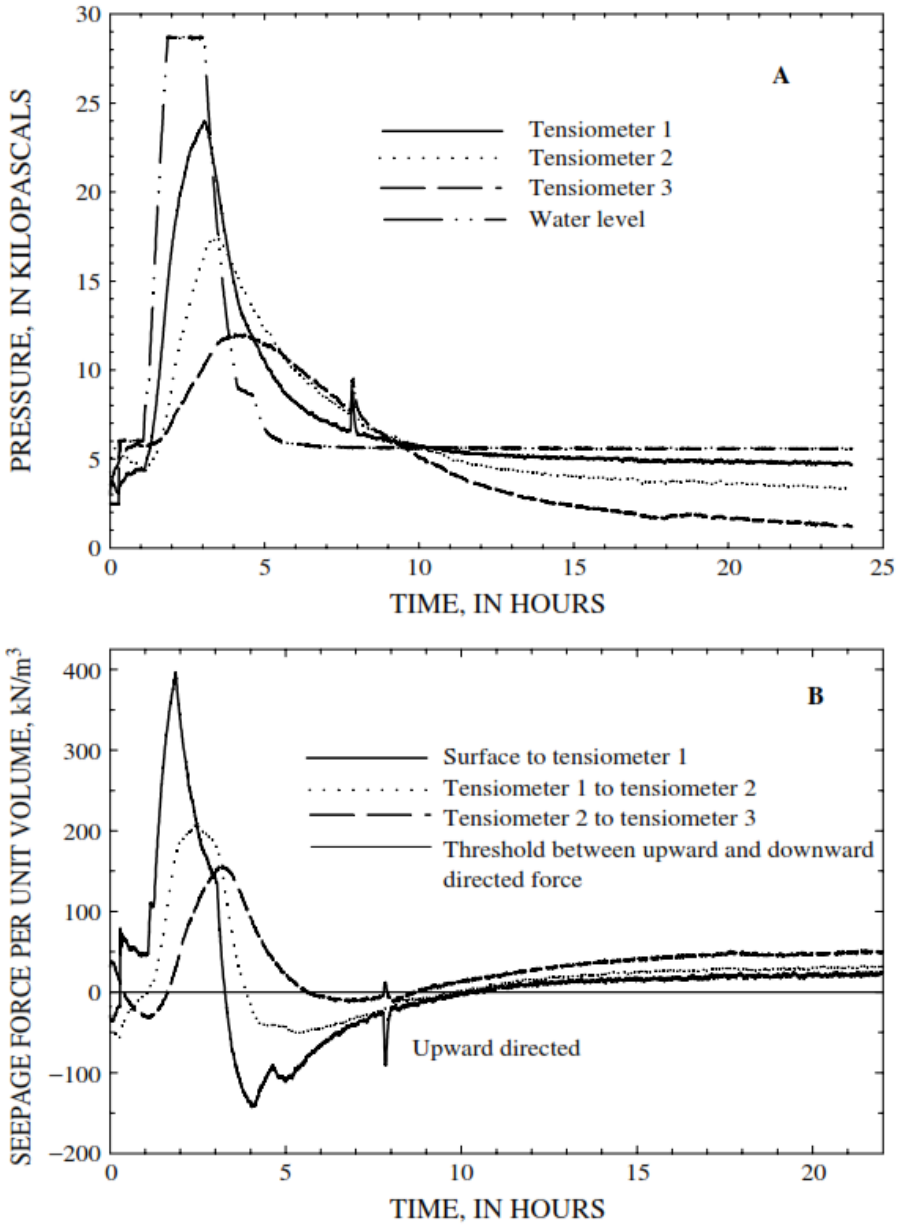

Figure 15. Example results from a test core taken from West Tarkio Creek, western Iowa showing temporal changes in pore-water pressure distributions (A), and associated temporal changes in seepage force per unit volume (B). (after Simon and Collison, 2001)

4.3.1. **Nouwakpo, Sayiro K., Chi-hua Huang, Laura Bowling, and Phillip Owens. (2010). "Impact of Vertical Hydraulic Gradient on Rill Erodibility and Critical Shear Stress."**

Nouwakpo et al. (2010) performed an extensive research study with one of the objectives being to use an empirical approach to measure the change in rill erodibility and critical shear stress in response to a change in the vertical hydraulic gradient within the upper 0.05 m of soil. The soil used in their study was collected in the southern part of Tippecanoe County, Indiana and was mapped as a Crosby–Miami complex (CwB2). It is essentially a loess-derived silt loam with 18% sand, 62% silt and 20% clay. Once

collected, the soil was ground and sieved through a 2-mm sieve before its use in the experiments. The soil was packed 0.05-m deep in a V-shaped mini-flume, 0.5 m long, 0.045 m wide, and 0.13 m deep over 0.08 m of pea gravel. The gravel provided a medium to apply an even hydraulic pressure and water flow to the soil above. At the two ends of the flume, a V-shaped channel matching the shape of the flume and flush with the soil surface was constructed to force the shape of the flow to conform to the shape of the flume. Fine sand was glued to the intake channel to match the roughness of the soil. The hydraulic pressure in the gravel was controlled by a variable head communicating reservoir (Marriott bottle). For the critical shear stress tests, the flow was varied until erosion began, and the corresponding shear stress was calculated using Newton's second law and the balance of forces along the sloping flume.

Five different soil matric potentials (unsaturated) or hydrostatic pressure heads (under positive pressure) were created: −0.10, −0.05, 0, 0.05, and 0.10 m, which, for a soil thickness of 0.05 m, correspond to hydraulic gradients of −2, −1, 0, 1, and 2 m/m, respectively. The positive and negative pressures were set by adjusting the elevation of the Marriott bottle to achieve the desired head above and below the soil surface, respectively. Two different slopes were created, a 5% slope and a 2% slope, and for each slope and each hydraulic gradient studied, three runoff flow rates were applied: 0.57, 1.8, and 2.5 L/min.

The experiments showed that rill erodibility of an oversaturated silt loam soil (seepage condition) was 5.64 times higher than that of the same soil in the presence of infiltration (drainage condition). They also found that the critical shear stress decreased when the subsurface hydraulic gradient was increased from negative gradients (drainage conditions) to positive gradients (seepage conditions). A summary of their main findings with respect to critical shear stress is shown in Figure 16.

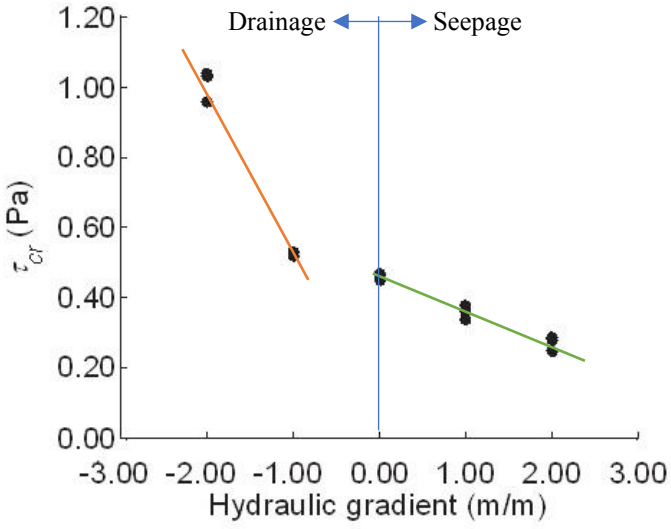

Figure 16. Effects of pore water change from drainage to seepage on critical shear stress (τ_{cr}), Nouwakpo et al. (2010)

The critical shear stress study showed a decrease in the critical shear stress with increasing hydraulic seepage gradient. The Authors also acknowledged more research is needed to fully understand seepage-

induced erosion in the context of cohesive soils and that their study was performed on ground and reconstituted soil, which might not mimic the exact field characteristics.

4.3.2. Nouwakpo, S. K., and C. Huang, 2012, The Role of Subsurface Hydrology in Soil Erosion and Channel Network Development on a Laboratory Hillslope

In a more recent work, Nouwakpo and Huang (2012) conducted an experimental study to build on the 2010 findings, namely, to quantify the effect of soil subsurface hydrology on erosion and concentrated flow channel development at the hillslope level.

To conduct the experiment the Nouwakpo and Huang (2012) built a large hillslope box in the laboratory that was designed to control surface and subsurface hydrologic conditions. The box was 3.66 m wide by 9.75 m long and consisted of two side slopes at 5% separated by a central bed. The slopes and the bed were also sloping in the longitudinal direction at 5%. For modeling the subsurface hydraulic gradient, they installed an array of perforated pipes at the base within a 0.05-m thick sand layer which were used as "water table control tubes". The test soil was packed on top of the sand layer at a constant thickness of 0.3 m, with a geotextile fabric separating the two materials. The illustration shown in Figure 17 shows the general setup of the hillslope box experiment. The soil used was a silt loam with 73% silt, 17% clay, and 10% sand. While the permeability of the silt loam was not reported, the soil composition implies fine grained cohesive soil with low hydraulic conductivity (below 10^{-6} cm/s) .

Variations of both run-on surface water from the top of the hillslope and artificial rain were modeled in combination with subsurface hydrology conditions. A system of high-resolution digital photogrammetry was set up over the box to generate a series of digital elevation maps (DEMs) to measure the erosion and channel formation on the hillslope.

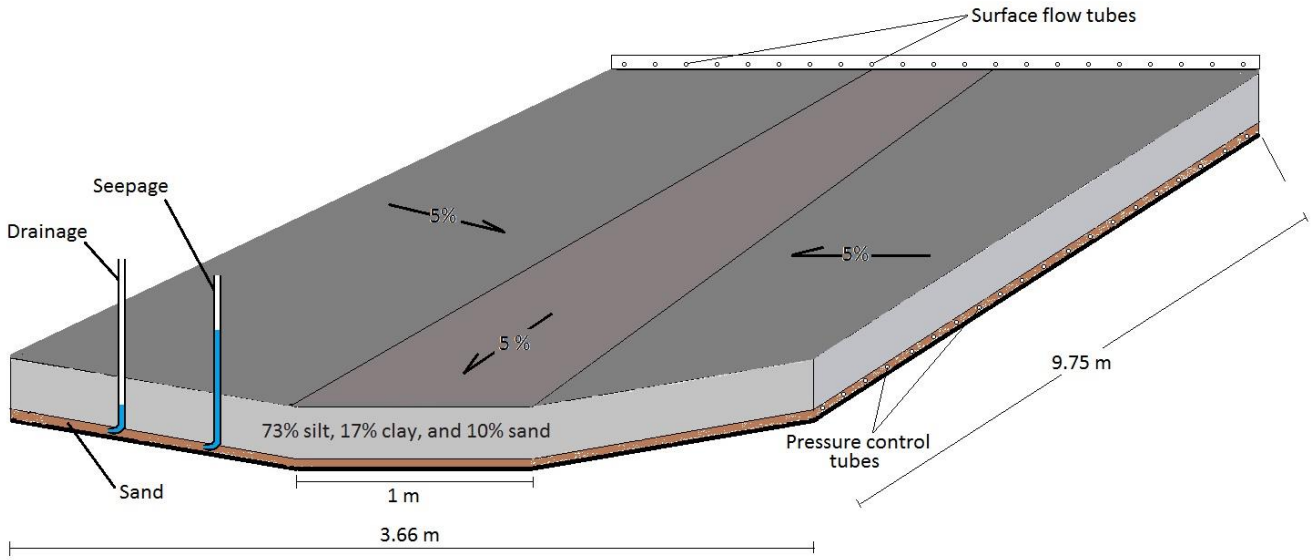

Figure 17. Illustration of the hillslope box elements constructed by Nouwakpo and Huan (2010)

The experiments consisted of a series of rainfall and run-on events in which the soil was kept either under seepage (S) or drainage (D) condition and the surface flow varied between high (H) and low (L) intensities. In the seepage treatment, the water table in the box was kept at the soil surface. To apply the drainage treatment, both the bottom and the top of the soil box were set at atmospheric pressure by disconnecting the tubes joining the water supply pipe to the subsurface pipes. Infiltration was then generated by the downward movement of water from the higher hydraulic potential at the soil surface to the lower potential at the bottom.

In addition to digital photogrammetry, sediment samples were collected in 1-liter bottles (45 bottles per event). The sediments were chemically flocculated and dried overnight for assessing the erosion rates.

The reported experimental results based on direct measurements are summarized in Figure 18. In conclusion, based on sediment samples collected in the direct erosion measurement method, the erosion rates under the seepage condition were 2.1 and 1.6 times higher than those under drainage condition for the high and low rainfall and runoff intensities, respectively. These experimental results show the significant effect of subsurface pressure gradient on the erodibility of cohesive soils.

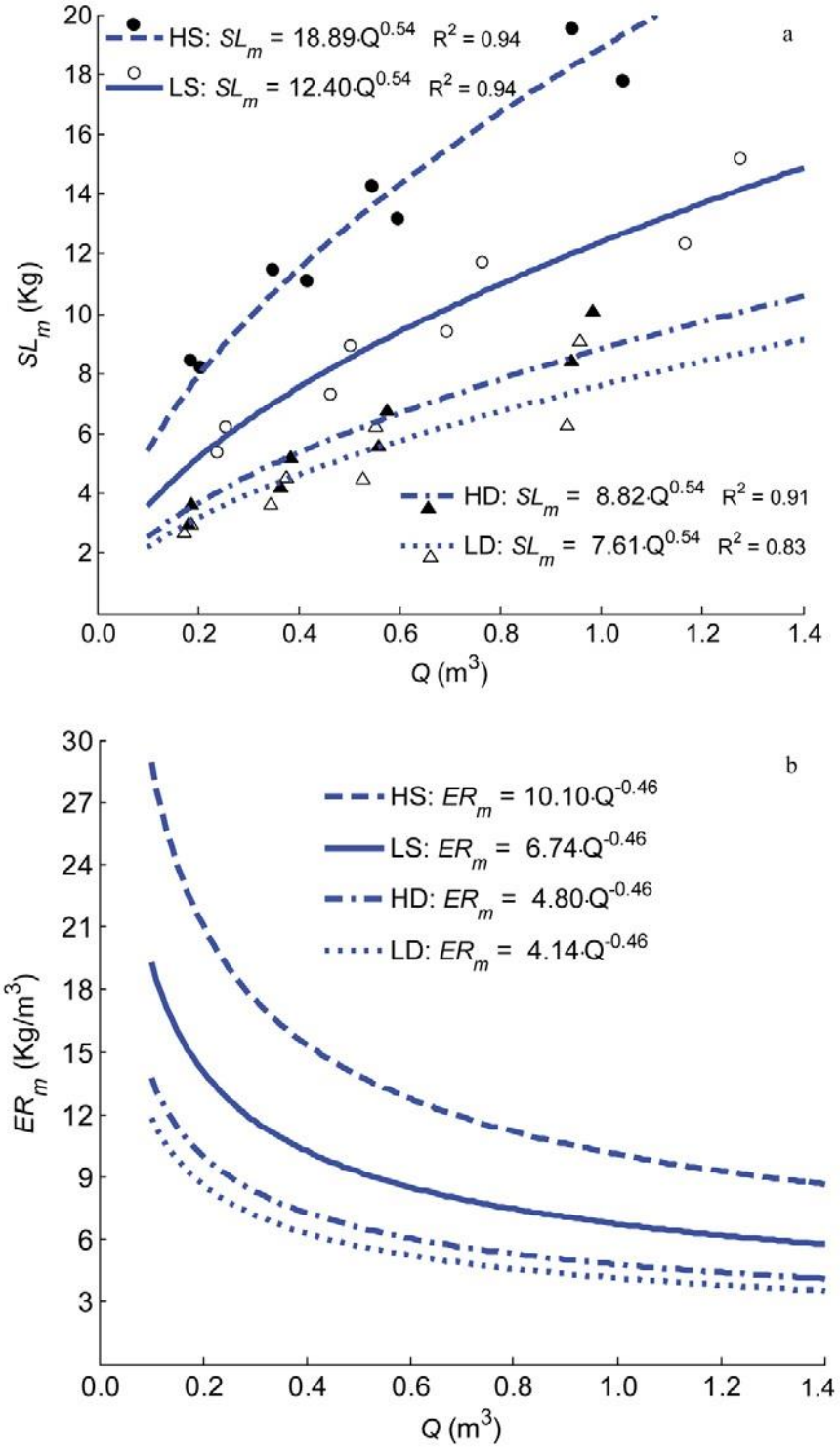

Figure 18. Soil loss, SL_m (a) and erosion rate ER_m (b) derived from sediment samples as a function of the cumulative runoff Q. S represents seepage, whereas D represents drainage, under either high (H) or low (L) surface flow conditions (Nouwakpo and Huang, 2012)

4.3.3. **Discussion**

It was shown that differential pressure caused by flow level fluctuations or subsurface seepage has a very important effect on cohesive soil erosion by overland flow (Simon and Collison, 2001; Nouwakpo and Huang, 2012). Especially important is the pressure left below the bed during and after the receding limb of the hydrograph which has the potential of dislodging and eroding blocks of soil even without the contribution of the flow. This effect, also known as "pop-out" erosion mode (Anthony, 2001; Chu-Agor et al., 2008; USDA-NRCS, 2012; UNESCO, 2017) is magnified in the case of structured cohesive soils such as Leda clays. While these clays are somewhat protected from surface flow effects by a polished slippery surface and sealed weakness planes, they are left vulnerable to back pressure with not much resistance to block dislodging along weakness planes.

Despite the proven importance of differential pressures translating into substantial seepage forces within the cohesive soil structure (Simon and Collison, 2001), very few publications can be found in literature addressing this issue. We can speculate on reasons for the relative scarcity of such research, one of which is the inherent difficulty in setting up practical experiments to replicate field conditions. For example, Valentin et al. (2005) pointed out that the lack of adequate research tools to address the complex processes involved in gully erosion hinders research progress in understanding this erosion pathway. Another possible reason could be that many researchers erroneously associate seepage pressures through soils with the seepage flow rate or velocity, and therefore discount the importance of seepage pressures in cohesive soils. That said, there is obviously a research vacuum on this topic, which is essential to the advancement of the study of cohesive soil erosion, and practical experimental tools are a key requirement. Despite the significant research work by Simon and Collison (2001) showing the transition of seepage forces in practically impervious soils and pointing out the potential effect on erosion by backpressure, they had no means of quantifying the effect of subsurface seepage pressure on the erosion by overland flow. The complexity and cost of the experimental setup by Nouwakpo and Huang (2012) to assess a single soil sample can be prohibitive.

In closing, there is an obvious need for simple practical tools to advance the research into the effect of seepage pressure on cohesive soil erodibility, which makes for a prime research objective.

4.4 Literature review summary

Literature pertaining to the measurement and modeling of the erosion of cohesive soils has been examined. This review is intended to summarise the research deficiencies in this domain and to highlight the need for further research.

Starting with data collection with various experimental setups, the target data boils down to two essential quantities: bed shear stress and corresponding loss of soil material through detachment and entrainment.

Identifying the start of erosion and quantifying the detachment of soil particles for a specific duration, while challenging at times, can be reasonably streamlined to obtain reliable measurements. Several

methods were used by researchers in various experimental setups, including visual observation, physical measurements, acoustics, light scatter, lidar, etc. These methods, while satisfactory, are often part of experimental setups that have significant limitations or ones that are complex, expensive, and require significant setup effort and time.

Many different theories on ways of measuring or computing bed shear have been suggested by various researchers, many of whom relied on hydraulic formulae for calculating bed shear, independently from water-soil interaction. Some used sensors to measure shear stress on an artificial surface placed within the flow and assumed the same shear stress is applied to the soil; this can be an improvement from the theoretical shear calculations, but unless the texture, shape, and size of the artificial surface, where the shear is measured, mirror those of the soil specimen throughout the test stages, the measured shear would be a rough estimate. Very few experimental setups are adapted for measuring shear force on the soil sample and they are limited to stationary laboratory flumes. The RCT device does measure the stress on the sample rather accurately but has other drawbacks (see Section 4.1.3).

The lack of consistent agreement between test data and actual observations has led to the development of many theories in shear and erosion measurements and varying views on representative entrainment models (see Section 4.2). Furthermore, the lack of practical and rapid testing methods has led to many attempts to link entrainment to measured geotechnical parameters of soils such as shear strength, bulk density, void ratio, plasticity, cohesion, etc., without much consistent success.

The literature review did not reveal any consistent methods or procedures for practically dealing with the erosion of clays and other cohesive soils. Some of the most popular measurement methods or devices for cohesive soil erodibility (Jet tester, mini Jet, RCT, etc.) have been criticized by many reviewers. It follows that the search for a model representing the erodibility of cohesive soils becomes a challenge as the selected model is as good as the data validating it. Further research is therefore needed in two principal areas:

1. New testing methods for relating bed shear and erosion threshold and rate. The methods must be fast, easy to deploy and perform, and sufficiently accurate to produce reliable data for both engineering design and further research. One of the criteria for the new testing systems, in addition to accuracy, would be to cover a large site area or many soil samples in a relatively short time.

2. Assess existing erodibility models using newly acquired data and possibly develop a representative model based on findings from novel testing methods.

In addition to measuring and modelling the erosion behavior of various soils, a robust system will allow researchers to investigate the effect of physical phenomena and different natural conditions on the erodibility of these soils. It is important, for example, to assess the effect of climate change on the erodibility of such soils, including frequent freeze-thaw cycles, desiccation and wetting cycles, flash

flooding and fast-receding water in drainage channels, etc. Investigating these conditions can be made more efficient with faster and more accurate testing methods.

5. RESEARCH WORK

5.1 Soil samples and sampling sites

A number of soil samples, 49 in total, were used for device calibrations and testing throughout this research work. The soils were acquired from basins of rivers and creeks across eastern Ontario, but mostly from the Ottawa region.

5.1.1. General surficial geology in the Ottawa region

The geology in the Ottawa-Carleton region is described in great detail in Schut and Wilson (1987). The following description pertains to the surficial geology at the main sampling sites for the soils sourced in this research and is based on Schut and Wilson's work. The bulk of the soil samples used in this research are taken from the basins of three drainage creeks in north-west Nepean near the boundary of Kanata in the Greater Ottawa area, formerly known as the Regional Municipality of Ottawa-Carleton (see Appendix 2).

The surficial geology west of the City of Ottawa is a combination of clay plains and bedrock uplands which is due to faulting. The thin veneer of material is mostly glacial drift subjected to modification due to subsequent marine inundation following glacial retreat. The Champlain Sea marine inundation resulted in deep water deposits, shallow water or near shore deposits, and shoreline or beach deposits influenced by tidal fluctuation (Richard et al., 1977). The deep-water deposits generally consist of blue-grey clay and silty clay. These deposits are also referred to as Leda clay and are usually non-calcareous and non-fossiliferous in the upper metre, and slightly calcareous and fossiliferous at lower depths. Bands of silt and very fine sand commonly occur amongst the clay deposits, especially in areas where the marine clays are adjacent to till knolls. The upper clay layer was deposited in a more freshwater environment associated with the late stages of the Champlain Sea and the early stages of the ancestral Ottawa River. The deeper, finer, slightly calcareous and fossiliferous clays were deposited during the earlier stages of the Champlain Sea in a salt to brackish water environment.

The main surficial soils sampled consist of varying combinations of glacial till deposits, marine clay deposits, and fluvial or estuarine sand and silt deposits with intrusions of organic materials and roots. A mapping of the surficial geology in the general sampling area is shown in Appendix 2, adapted from Shut and Wilson (1987) and Richard et al. (1977).

5.1.2. **Collected soil specimens**

As stated earlier, the test soils were collected from various river and creek basins across Ontario, namely: Bear Brook (1 sample), Black River (1 sample), Feedmill Creek (12 samples), Green's Creek (2 samples), Muddy Creek (2 samples), Orillia Waste Water Treatment Plant (1 sample), South Nation River (1 sample), Stillwater Creek (22 samples), Watts Creek (5 samples), and West Branch Scotch River (2 samples). The locations of all sampling sites are shown in Appendix 2, courtesy of Google Earth, and coordinates measured by GPS are provided in Appendix 3.

The samples were collected by pushing the 150-mm diameter thin-walled stainless steel cylinders into the ground surface, within the stream banks and bed, and extracting them with as little disturbance as possible. In many cases, the cylinders were easily inserted in the soft sediments with minimal effort. In some cases where the flow had incised into virgin overconsolidated clayey strata, the cylinders had to be driven in by hammering on a special bulky steel bracket distributing the impact on the entire rim of the sampling cylinder. Visual observation showed no appreciable effect of the sampling on the soil consistency beyond the interface with the inner surface of the sampling cylinders. One exception was observed when sampling structured Champlain sea clay where an abundance of fissures and planes of weakness were observed, and the soil exhibited a brittle behavior when sampled. In such cases, *in situ* tests were relied upon where possible.

It should be noted that the samples were extracted from saturated ground near the water line or from a submerged surface. This is illustrated in Figure 19 showing typical sampling procedures. The samples are then wrapped in plastic to maintain saturation. Soil samples that were not tested shortly after collection were placed in plastic containers and submerged.

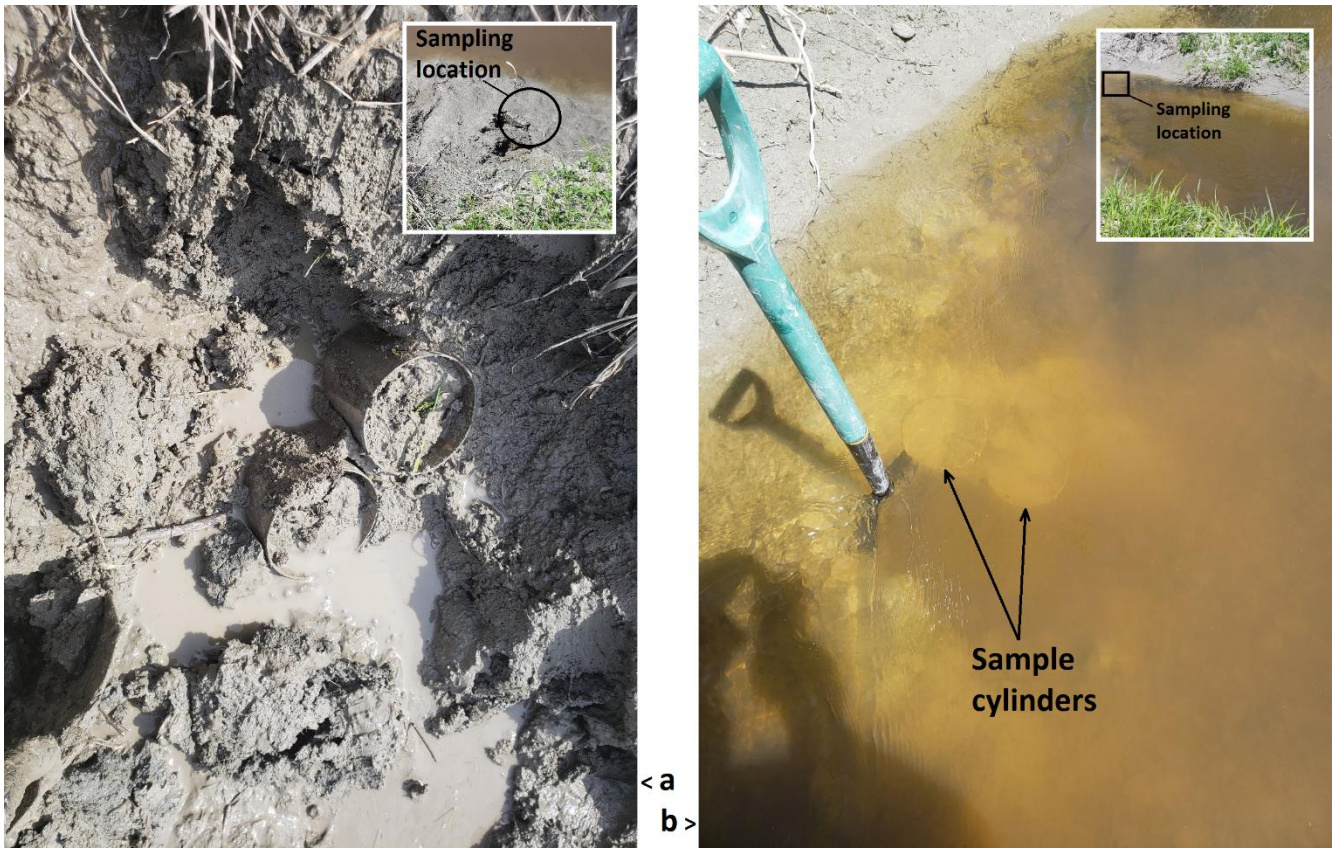

Figure 19. Sampling locations: (a) Green's Creek; (b) Muddy Creek

A primary collection consisting of ten (10) different soils were collected from the basins of Stillwater Creek (5 soils) and Watts Creek (5 soils). These will be referred to herein as the core soils and are used in the various testing and calibration of new devices introduced in this research. The other soils were sampled from various locations across eastern and western Ontario, including additional samples from Stillwater Creek, and used along with the core samples for further improving the calibration accuracy and validation of novel testing devices. These additional soils are hereafter referred to as supplemental soils.

The core soils are subjected to more rigorous classification and strength tests than the supplemental soils, mainly for investigating the effect of geotechnical parameters and grainsize characteristics on the erodibility of the soils. The various tests performed on the core soils and supplemental soils are described in the following section.

5.1.3. **Classification, strength, and other testing**

Results of all laboratory tests and the tests performed as part of the research work on the collected samples are summarised in two master tables placed at the beginning of Appendix 3: Table A3-1 (core soils) and Table A3-2 (supplemental soils).

5.1.3.1. **Soil classification tests**

All of the core soils and many of the supplemental soils were subjected to Atterberg classification testing using a 30º falling cone (Campbell, 1976; Al-Dahlaki and Al-Sharifi, 2008). The results of the classification tests (Atterberg limits and moisture content) can be found in the tabulated test summaries in Appendix 3. The graphical classification results are shown in the plasticity charts in Figure 20 through Figure 23 for the different groups of soils used throughout the research work.

The classification data shows a wide variation in soil characteristics (fines portion) ranging from medium to very high plasticity silty clays and clayey silts with varying proportions of fine to medium sand and organic content.

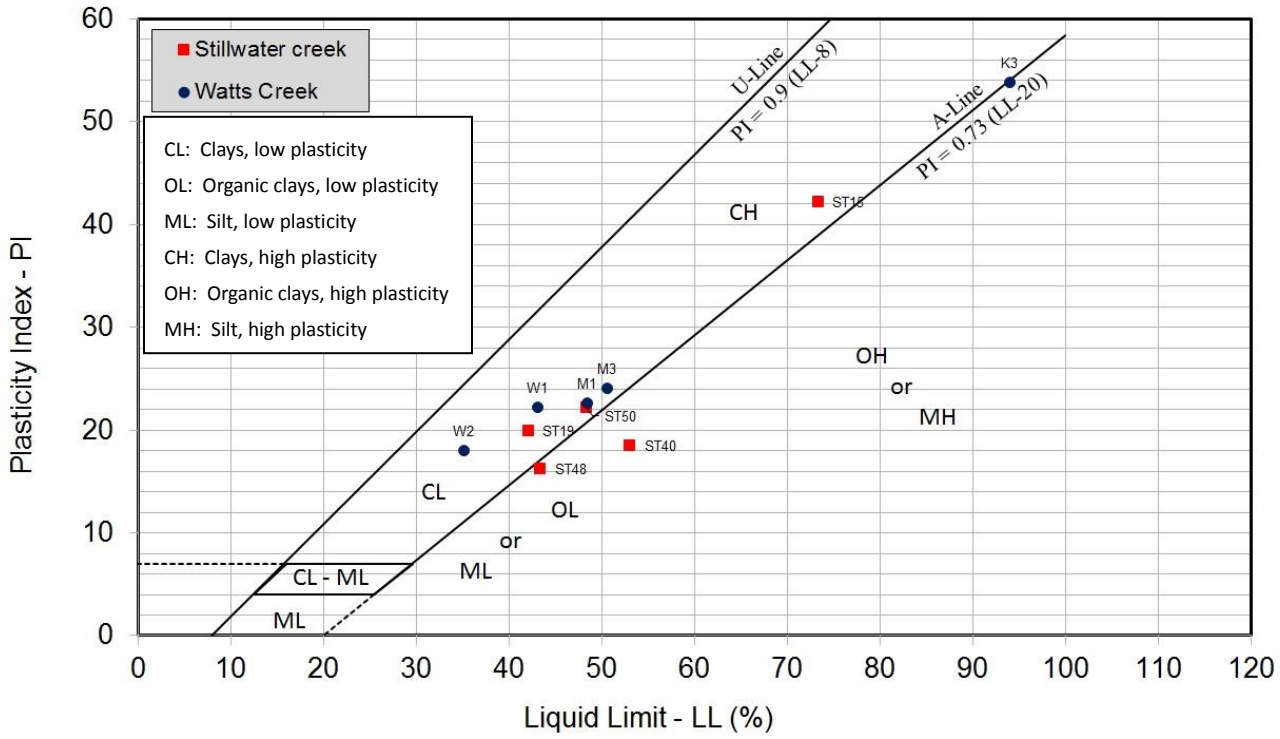

Figure 20. Plasticity data, core soils.

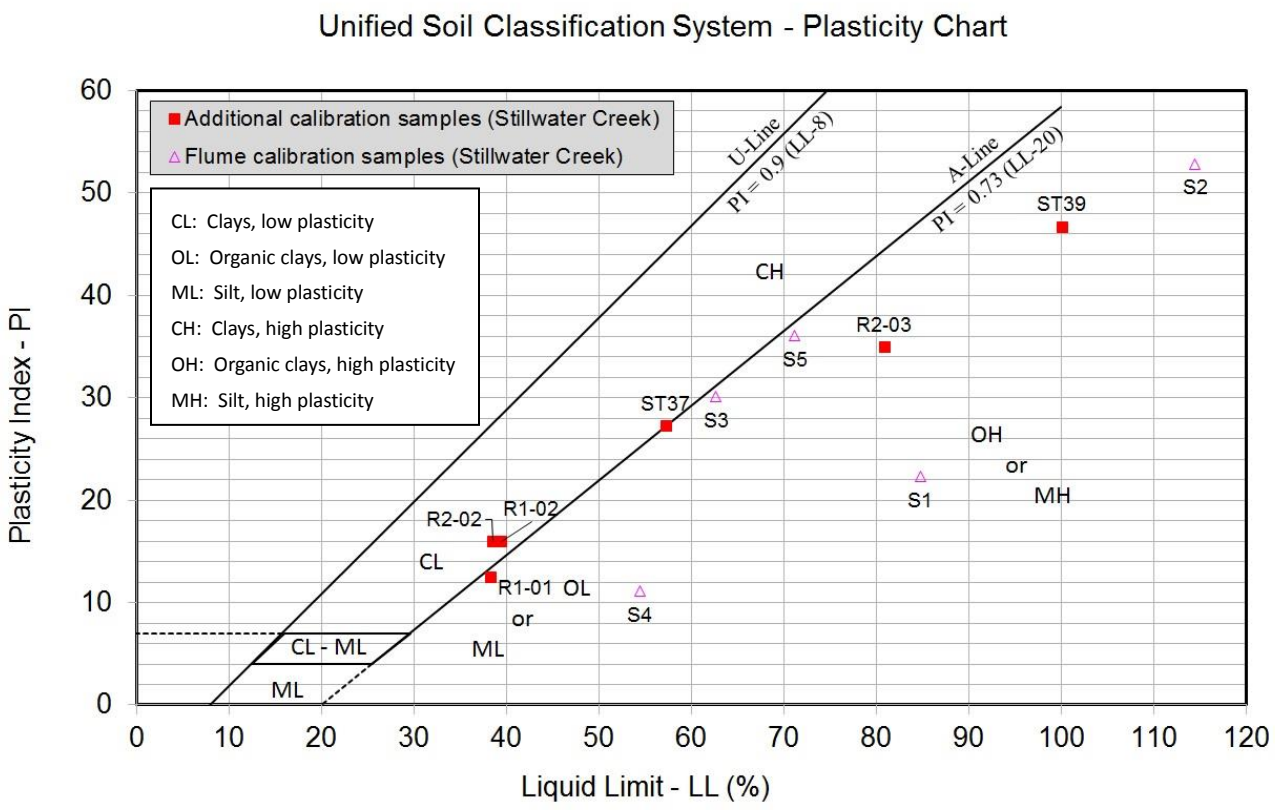

Figure 21. Plasticity data, supplemental soils from Stillwater creek

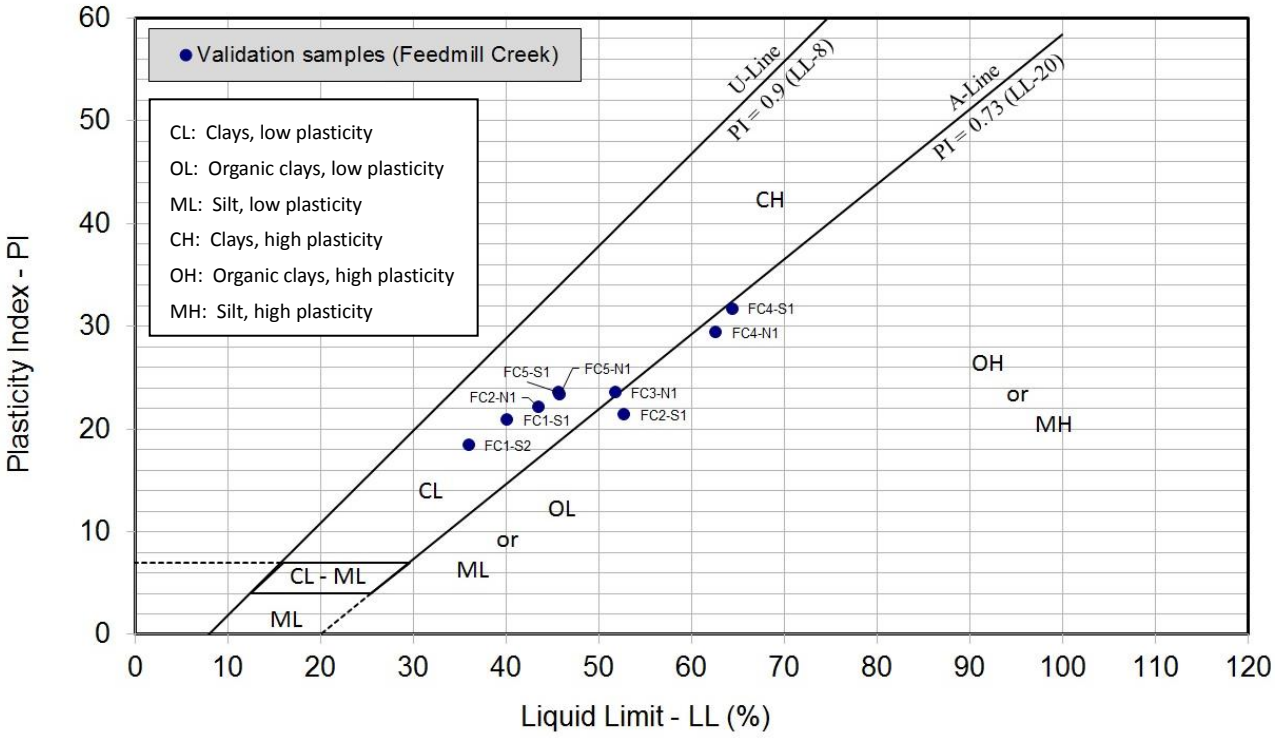

Figure 22. Plasticity data, Feedmill Creek soils

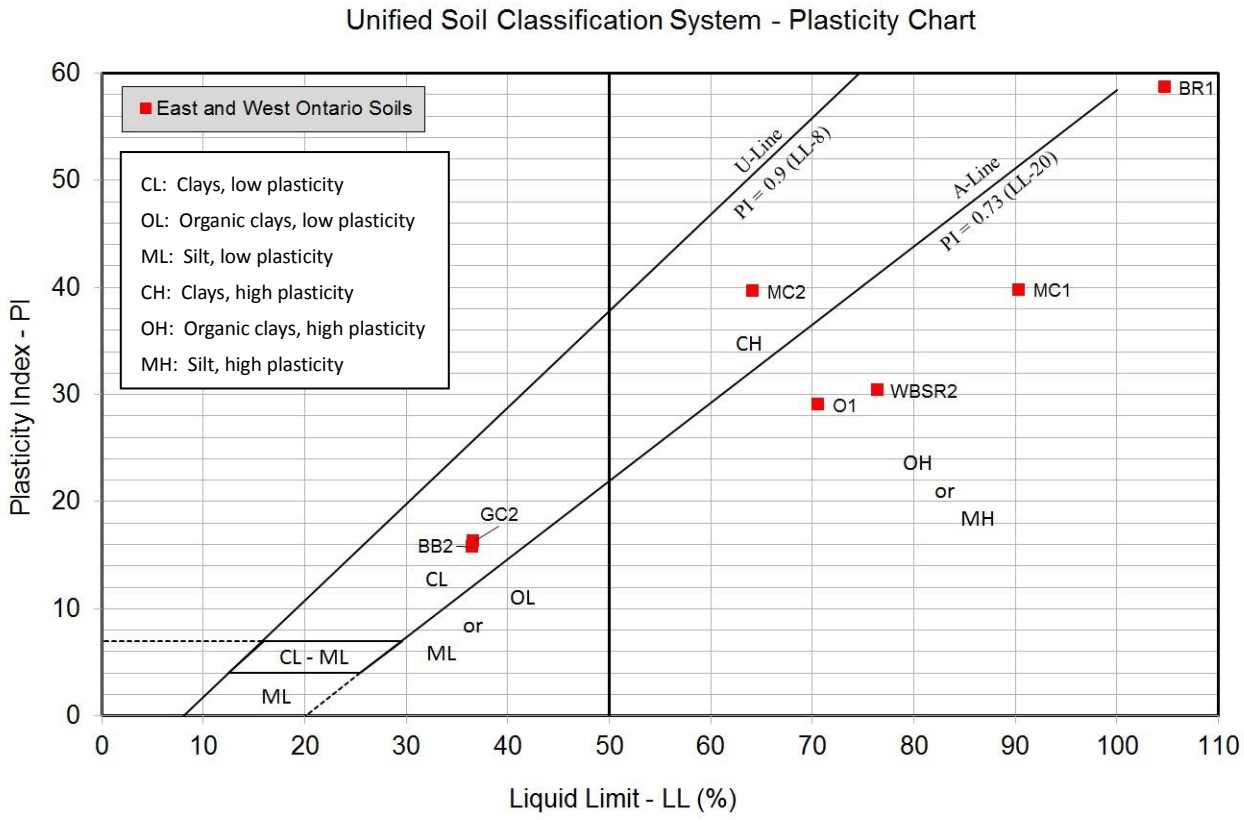

Figure 23. Plasticity data, supplemental soils from East and West Ontario

5.1.3.2. **Grain size analyses**

In addition to the Atterberg classification tests, the core soils and some of the supplemental soils were subjected to grain size analysis using a standard 152H Hydrometer. The gradations of the tested soils can be found in the tabulated test summaries in Appendix 3 as sand, silt and clay composition for each tested sample. The grain size analyses show a similar range of soil composition as indicated by the Atterberg classification.

5.1.3.3. **Strength tests**

The core soils were subjected to consolidated drained direct shear testing to determine their effective cohesion (c') and effective angle of internal friction (φ'). A direct shear testing device developed by AATech Scientific Inc., shown in Figure 24 was used for the testing. The device accepts cylindrical samples, relatively undisturbed. The test specimen is collected in a stainless-steel cylinder with an internal diameter of 63 mm and mounted through the fixed cylinder of the device. The specimen is then partially pushed down into an identical specimen cylinder section mounted within the gliding cylinder on a bed of clean sand for even support and drainage. The gliding cylinder is then filled with water to submerge the shear plane between the upper and lower specimen cylinders.

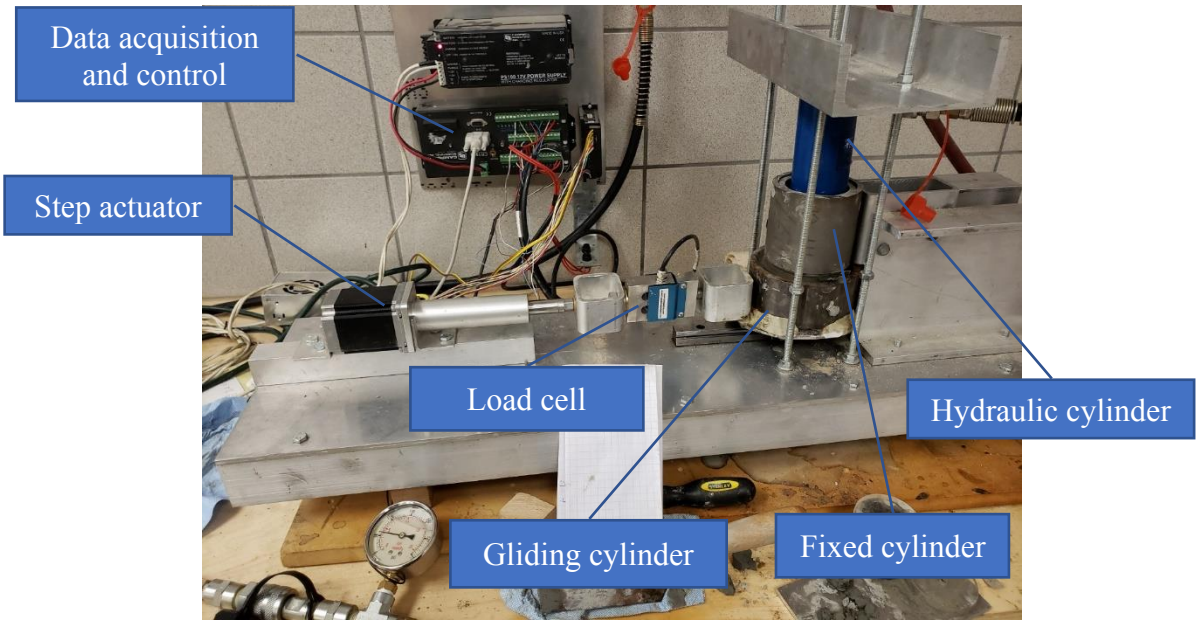

Figure 24. Direct shear test device, AATech Scientific Inc.

The specimen is sheared along the plane of interface between the upper and lower cylinder by setting the actuator to pull the gliding cylinder forward at a rate of 0.05 mm/min. At first, the specimen is sheared with no normal pressure. Subsequently, the sheared lower portion of the specimen is removed and replaced by pushing another portion of the specimen into the lower cylinder. The hydraulic jack on top of the specimen is then pressurized to apply an equivalent of a 50 kPa normal stress onto the specimen, which is left to consolidate for over 8 hours. The pressure is maintained constant by means of pneumatic to hydraulic pressure exchanger. With the thin lower portion of the specimen drained on a sand bed, and with special spacers creating a gap of about 0.5 mm between the upper and lower specimen cylinders, the bulk of the excess pore water pressure is expected to dissipate within the eight hours for an acceptable level of consolidation. The specimen is then sheared (as per the previous cycle) while the normal pressure is maintained on the specimen. The same process is repeated again with a consolidation and normal pressure of 100 kPa to establish a third shear failure point. The maximum measured shear stress from each of the three tests are plotted against their corresponding normal stress (0 kPa, 50 kPa, and 100 kPa), and the resulting linear relationship is used to determine the effective cohesion (intercept) and the effective angle of internal friction (inverse tangent of the slope). A sample direct shear test data and analysis is shown graphically in Figure 25; similar results for all 10 core soils as well as a tabulated summary consisting of effective cohesion (c') and effective angle of internal friction (φ') for each soil can be found in Appendix 3. The effective cohesion of the core soils ranged from 1.38 kPa through 9.36 kPa. The effective angle of internal friction of the core soils ranged from 22.3° through 37.4°.

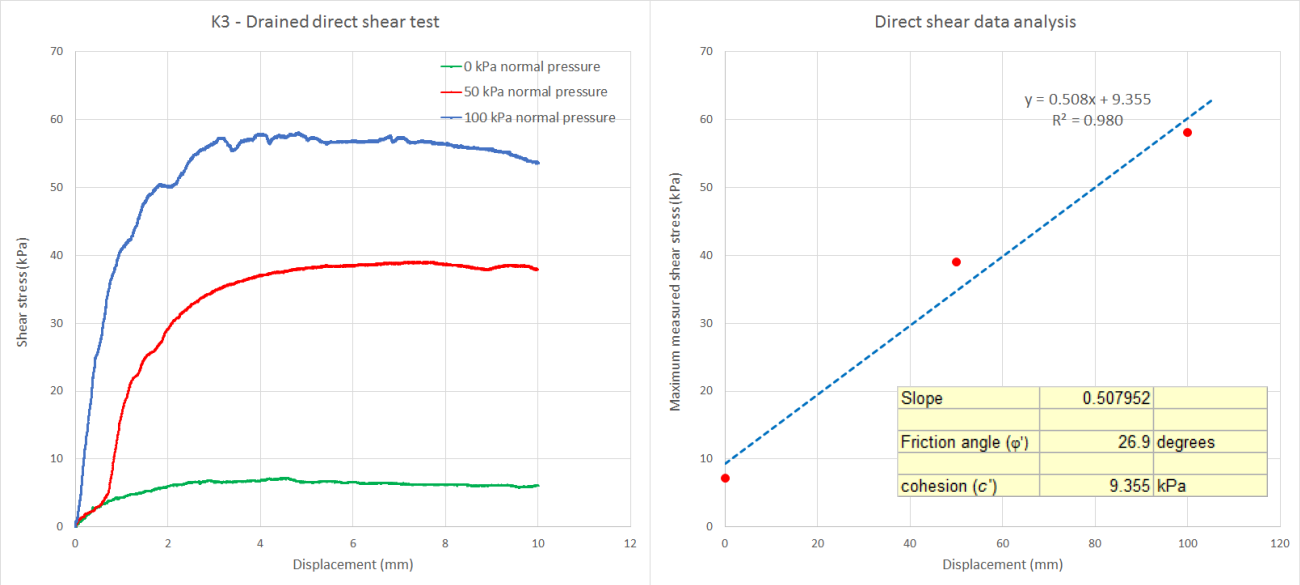

Figure 25. Typical direct shear test data and analysis

5.1.3.4. **Hydraulic conductivity tests**

The hydraulic conductivity of the samples from Muddy Creek, and Green's Creek were determined using a falling-head permeameter. The test results showed a hydraulic conductivity of 8.2E-7 cm/s, and 1.5E-8 cm/s, respectively. Detailed soil test results can be found in Appendix 3.

5.2 Critical shear determination

In looking to conduct intensive studies on the erodibility of cohesive soils, one of the objectives of this research was therefore to develop a new method that can be adapted for use in the field to quickly determine the critical shear of soils with good accuracy. A new apparatus, termed the Erosionometer, was developed by the author, in collaboration with Dr. Colin Rennie of the University of Ottawa, as part of this Ph.D. Research, and will be presented herein.

5.2.1. The development of the Erosionometer

The Erosionometer was developed to measure the critical shear by measuring the soil's resistance to surface shear induced by a special probe. The surface shear probe is a specially fabricated stainless-steel plate equipped with protruding machine screws in a grid formation, 10 mm on center: six rows along the direction of shearing and four across (see Figure 19). The screws protrude 5 mm past the face of the plate.

The probe is positioned on the soil (sample or *in situ*) by applying a steady normal pressure until a near full penetration of the pins into the soil is observed, leaving a slim space between the plate and the soil surface. The probe is then pulled at a set rate of displacement by a software-controlled step motor. The present tests and calibration presented herein were performed using a set rate of probe displacement of

0.5 mm/s. The displacement rate is selected to avoid generating a dynamic shear resistance (high speed) while remaining fast enough to reflect the flow action. That said, doubling the drag speed to 1.0 mm/s did not show any tangible effect on the results. A braided flexible steel wire diverted around a fixed pulley close to the soil surface level pulls the probe horizontally along the surface of the test soil and slightly upward as the probe advances. This interaction induces a complex combination of drag, uplift, and rotation forces against the soil. For laboratory applications, a plexiglass submerging cell is added at the base of the device where a soil sample contained in a cylindrical steel tube, 150 mm in diameter, can be inserted, submerged, and tested in the same manner. The applied tractive force is constantly measured by a resistive inline load cell and the probe displacement is measured by a linear potentiometer while the thrust is maintained until a visible yielding of the soil surface is observed. The resulting load-displacement relationship is inspected to determine the yield point representing the peak tension force in the wire, which is in turn calibrated to indicate the critical shear of the tested soil surface.

Figure 26 shows an illustration of the Erosionometer device and probe, as designed and built for the above-mentioned purposes. As stated earlier, the setup illustrated in Figure 26, with the submerging cell, is the one adapted for laboratory testing on extracted soil samples. For field testing, the submerging cell is removed, and a pulley mounted on a bracket at the base of the Erosionometer is used instead to drag the probe at ground level. The photo in Figure 27 shows the Erosionometer's surface shear probe set up on a clay bank and on a cylindrical extracted soil specimen. Typical Erosionometer data are shown in Figure 28; the peak force reached during the test is calibrated to indicate the critical shear characteristic of the tested surface.

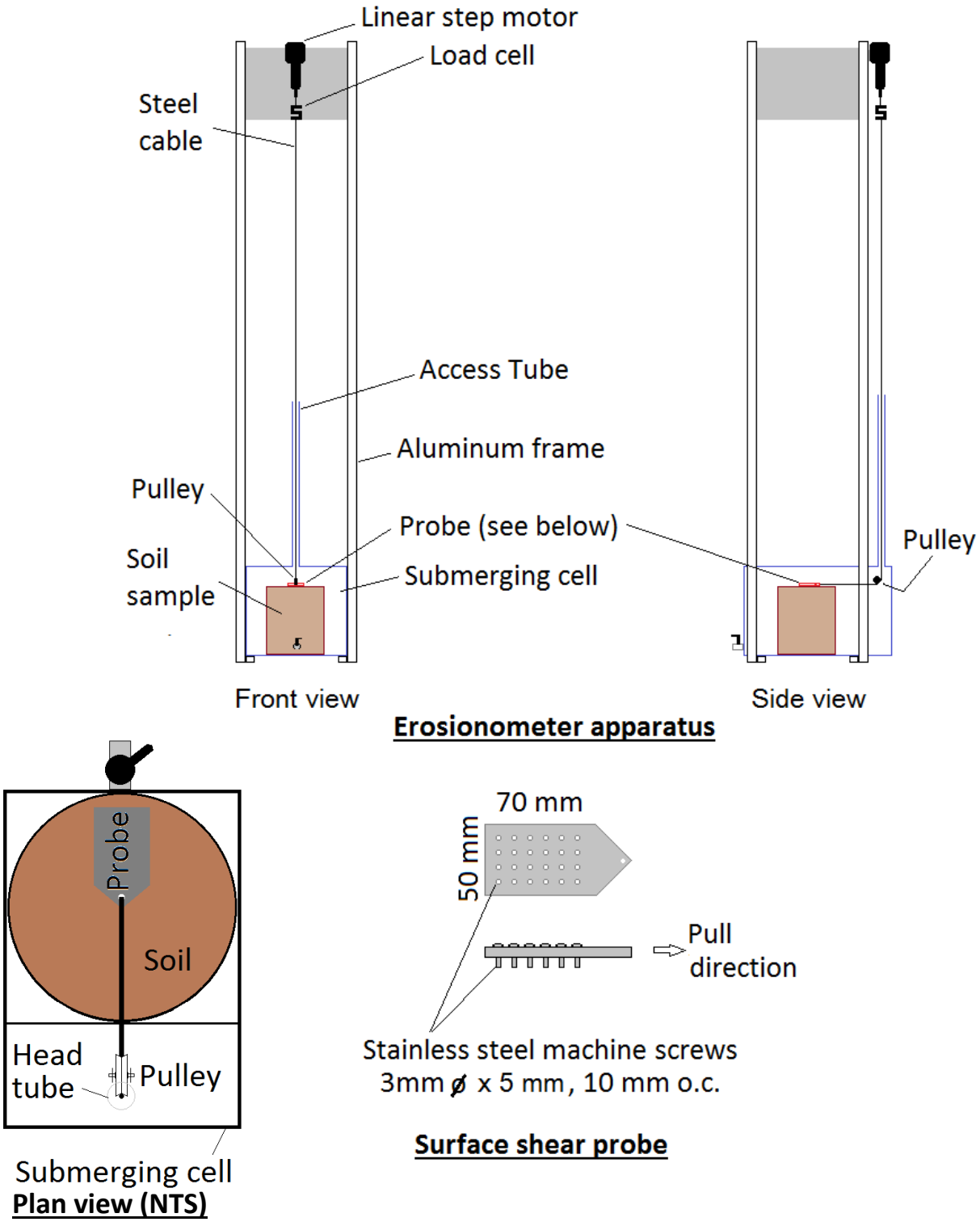

Figure 26. Illustration of the Erosionometer device

Figure 27. Erosionometer probe deployed in the field and in the laboratory

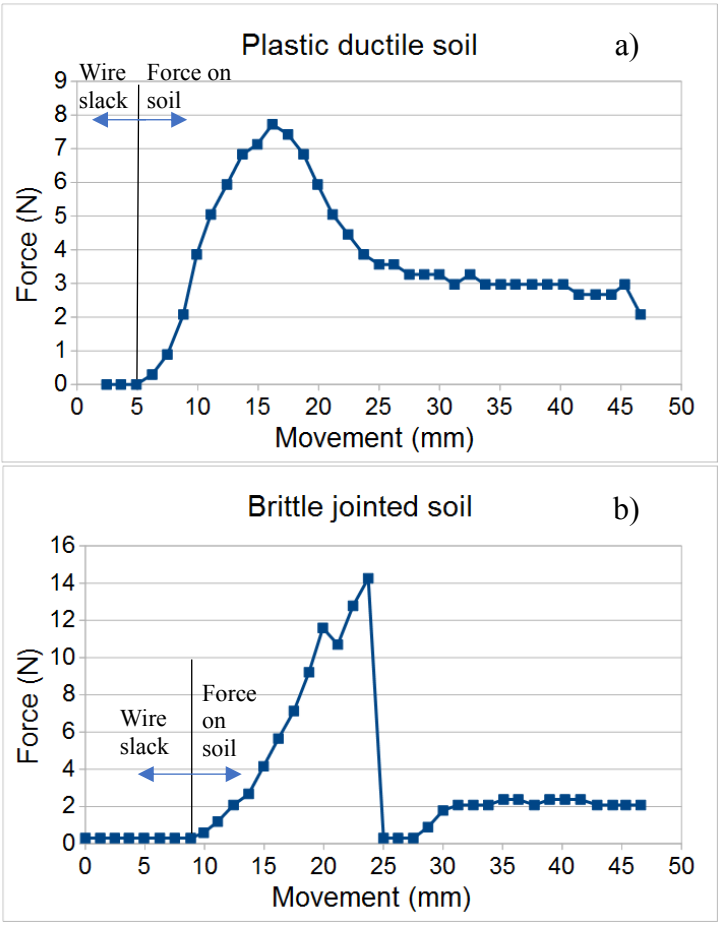

Figure 28. Typical Erosionometer data: a) Plastic ductile soil, b) brittle soil. The slack length in the wire varies between setups (movement at 0 force). The force at the peak is considered the yield value

5.2.1.1. **Probe action – Failure modes**

As the Erosionometer probe is pulled across the sample (See Figure 29), it progresses towards a complex failure process as the soil yields. As the probe is installed floating in the soil, it is not expected to provide any reinforcement or confinement to the soil. Furthermore, as it is pulled forward, the probe will seek the path of least resistance, which is to gradually pull out of the soil. This complex interaction with the soil makes it a unique testing tool producing a mode of failure similar to that produced by turbulent water flow. The different modes of failure produced simultaneously by the moving Erosionometer probe consist of:

- Pins flowing through the soil
- Tension as the probe uplifts soil clusters gripped around and between the pins
- Shear between the base soil and the bottom of the pins and soil clusters trapped between the pin formations

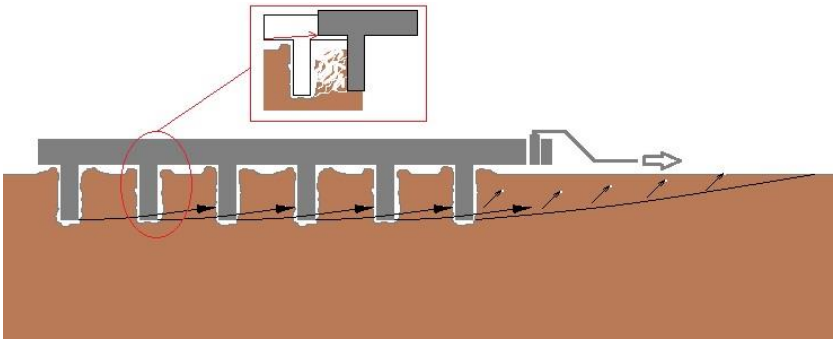

Figure 29. Probe failure modes

5.2.1.2. **Calibration process**

A total of 23 soil samples taken from different sites along Stillwater Creek, its tributary E1, and Watts Creek, all in Ottawa, Canada, were tested with the objective of calibrating the test apparatus. Following development of the calibration equation, 15 additional samples collected from Feedmill Creek, also in Ottawa, Canada, were used for independent validation of the calibration relation. The approximate sampling locations of all test samples are shown on satellite images, courtesy of Google Earth, placed in Appendix 2. Using a piston flume (see Section 4.1.1), the critical shear, which is the fluvial shear stress applied to the soil surface at the initiation of erosion, was determined for each sample. The samples were extracted in 150 mm outer diameter (o.d.) stainless steel cylinders, with a wall thickness of about 1.5 mm, and a height of 150 mm. The upper surface of the soil was subjected to the water flow in the flume. The piston flume used in this research and the process of determining the critical shear in the flume is described in more detail in later sections.

The same soil sample tested in the piston flume was sheared with the Erosionometer for correlation. As mentioned earlier, the rate of displacement of the probe was set at 0.5 mm per second throughout this phase of the research, including calibration and validation. The yield force (peak force attained) determined from the Erosionometer test was correlated with the flume results (critical shear). With the relatively large number of diversified samples and a wide range of determined critical shear values, a reliable correlation function was determined between the critical shear and Erosionometer yield values. Please note that the correlation function is specific to the probe and drag speed of 0.5 mm/s and may not apply if the probe was altered or a different speed is used for testing. Once the apparatus is calibrated, other samples or *in situ* soil surfaces can be tested with the Erosionometer to determine its critical shear without the need for flume testing. It should be emphasized that in addition to replacing the flume tests, the calibrated Erosionometer can be deployed in the field to run *in situ* tests, therefore eliminating the effects of sample disturbance associated with extraction and transport. Furthermore, the Erosionometer can test competent soils which cannot be easily eroded in a moderately sized piston flume.

Test samples

As stated earlier, a total of 23 samples from multiple locations along different creek basins in Ottawa, Canada, were tested. Many of the collected samples had a duplicate (two samples collected from each spot); occasionally Erosionometer tests were performed on both samples to verify consistency, while the flume test was performed on one of the samples. It should be noted that the surface of the sample subjected to the water flow was trimmed to eliminate the flow effects prior to the Erosionometer test.

As noted above, following the calibration of the Erosionometer, it was used to assess the critical shear of 15 silty clay and clayey silt samples taken from five locations along the banks of Feedmill Creek, in the west end of Ottawa, Canada. The same soils were also tested in the flume to validate the Erosionometer calibration. The five locations covered a reach of about 1,150 m along the creek. The field and laboratory work were conducted from July 2015 through October 2015.

The approximate sampling locations of all test samples are shown on satellite images, courtesy of Google Earth, placed in Appendix 2. The samples were collected by pushing the 150-mm diameter thin-walled stainless steel cylinders into the ground surface, within the stream banks and bed, and extracting them with as little disturbance as possible. In many cases, the cylinders were easily inserted in the soft sediments with minimal effort.

Most of the calibration samples and all the validation samples were subjected to Atterberg classification testing using a 30º falling cone (Campbell, 1976; Al-Dahlaki and Al-Sharifi, 2008). Furthermore, the 10 core soils were subjected to drained and undrained strength testing as well as grainsize analysis (Hydrometer testing). Some of the supplemental soils were also subjected to Hydrometer testing. For more information on the tested soils, including laboratory test results, please refer to Section 5.1 above.

The classification data show a wide variation in soil characteristics ranging from medium to very high plasticity silty clays and clayey silts with varying fine to medium sand and organic content.

5.2.2. **Flume measurements**

An open-channel piston flume (Kamphuis and Hall, 1983; Gaskin et al., 2003; Al-Madhhachi et al., 2014), specially constructed at the University of Ottawa hydraulic laboratory, was used to test for the critical shear of the samples. The flume is 30 cm wide by 20 cm high, made of aluminum channel sections with a tilt adjustment at one of the supports to change the slope of the channel. The total length of the flume is 4.86 m, and 3.6 m from the inlet to the sample location where a sleeve is provided for inserting the sample cylinder through the bottom. The flume is illustrated in Figure 30

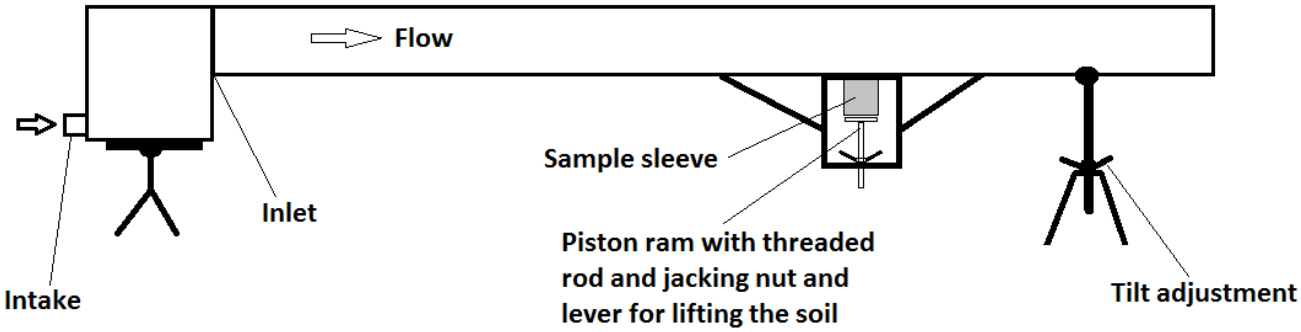

Figure 30. Specially constructed piston flume, hydraulic laboratory, University of Ottawa

The flume slope was set at 1.5% for some of the early samples tested, then increased to 3% throughout the remainder of the testing to raise the limit on the available bed shear stress. The sample cylinder was inserted through the special opening at the bottom of the flume then pushed up and trimmed flush with the flume base and subjected to a gradually increased flow. The trimming of the samples was done as cleanly as possible using a fine tensioned steel wire, and any resulting loose particles were allowed to wash out before the actual test was started.

In cases where the sample surface was left exposed during handling before flume testing, a gate at the end of the flume (discharge point) was raised to maintain a stagnant water level until surface saturation was achieved. The flume was then drained, and the gate was fully opened to allow for a free unrestricted discharge.

The soil surface was subsequently subjected to a gradually increasing water flow while visually observing the surface of the sample to identify the initiation of erosion. Initially, the fluid bed shear stress was computed using the depth-slope product, which is derived from the balance of forces on a free body of water on an inclined plane, using Newton's second law:

$$\tau = \rho . g . R_h . S$$

Where τ = fluid bed shear stress (N/m^2), ρ = water density = 998 kg/m^3, g = gravitational acceleration = 9.81 m/s^2, R_h = Hydraulic radius (m), S = Flume slope (0.015 or 0.03). Equation 19 assumes steady and uniform open-channel flow where boundary friction balances gravitational forcing and estimates the shear on a boundary surface similar in roughness to the typical channel boundary. Given that the sample surface had different roughness than the aluminum flume, the use of Equation 19 is expected to induce an error in the shear estimation (see Section 4.1.1). Another issue to overcome was the short distance between the flume intake and the sample, which may prevent a fully developed open-channel flow at the sample location, especially at high flows where a highly non-uniform flow can be observed at the intake. The lack of fully developed flow, along with the abrupt change in roughness at the sample location, complicated the use of measured velocity profiles for bed shear stress estimation (see Section 4.1.1, as well as Section 5.3.2) It was therefore necessary to derive a more accurate estimate of the flow shear that takes into consideration the contrast in roughness between the sample surface and the general flume surface, and the proximity of the sample to the intake, in addition to the usual scaling issues. A shear plate apparatus was then constructed to measure directly the shear stress across the sample surface and relate it to the depth of flow at the sample location. The shear plate measurement setup consisted of replacing the sample cylinder with a shallow circular dish mounted on a very flexible spring allowing it to move freely in the direction of the flow. A thin steel wire connected to a small pin at the centre of the dish was run upstream along the base of the flume and redirected vertically around a small bearing pulley to a load cell mounted above the flow inlet. The details of the shear measurement setup are shown in Figure 31. The collage of photos shown in Figure 32 illustrate the setup and measurements.

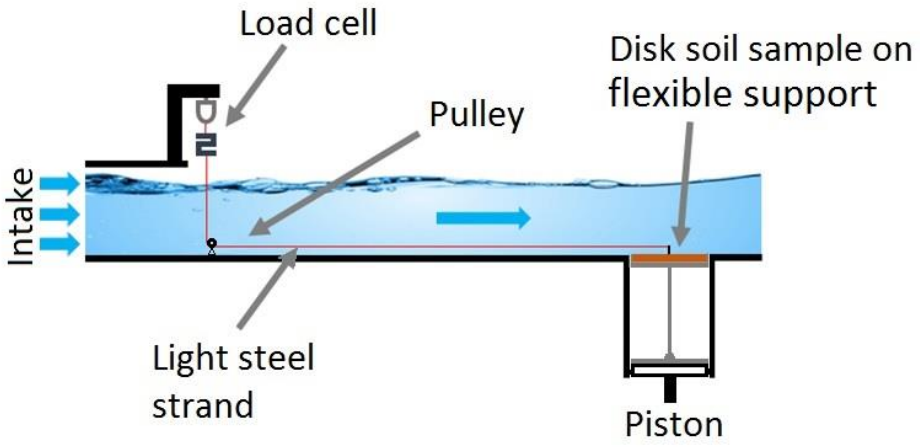

Figure 31. Flume shear measuring system

Five different soil samples, a sheet metal disc, and a 120-grit sandpaper disc, were tested in the shear plate apparatus to assess the sensitivity of the flow-shear relationship to the roughness of the soil sample. The soil samples were selected from the Stillwater Creek group of samples to cover a wide range of visually assessed roughness. The sheet metal disc and the sandpaper were used as end-member reference points to establish a tangible roughness scale. The five samples were subjected to classification testing (see Appendix 3).

The sample dish was filled with a slice of a sample of cohesive soil and the steel wire connecting it to the load cell was tensioned. As the flow depth was gradually increased in the flume, the additional tension in the wire was measured at 1 Hz frequency and recorded along with the measured flow depth. Each level of flow depth was maintained for about one minute and the recorded drag forces were averaged to capture the turbulent response. The shear measurements were performed at two different slopes of the flume: 1.5% and 3%. It should be noted that in all cases, the flow intensity was increased beyond the critical shear of the soil to map the full range of flow depth-shear correlation, until large clusters of soil were eroded, or the soil surface deviated from plane bed consistency. Subsequently, the dish was immobilized by a metal wedge downstream, and the flow was varied again to assess the drag forces on the wire and pulley system, which were subtracted from all the measurements. An example of the measured drag force can be seen in the raw measurements shown in Figure 33 (3% flume slope)

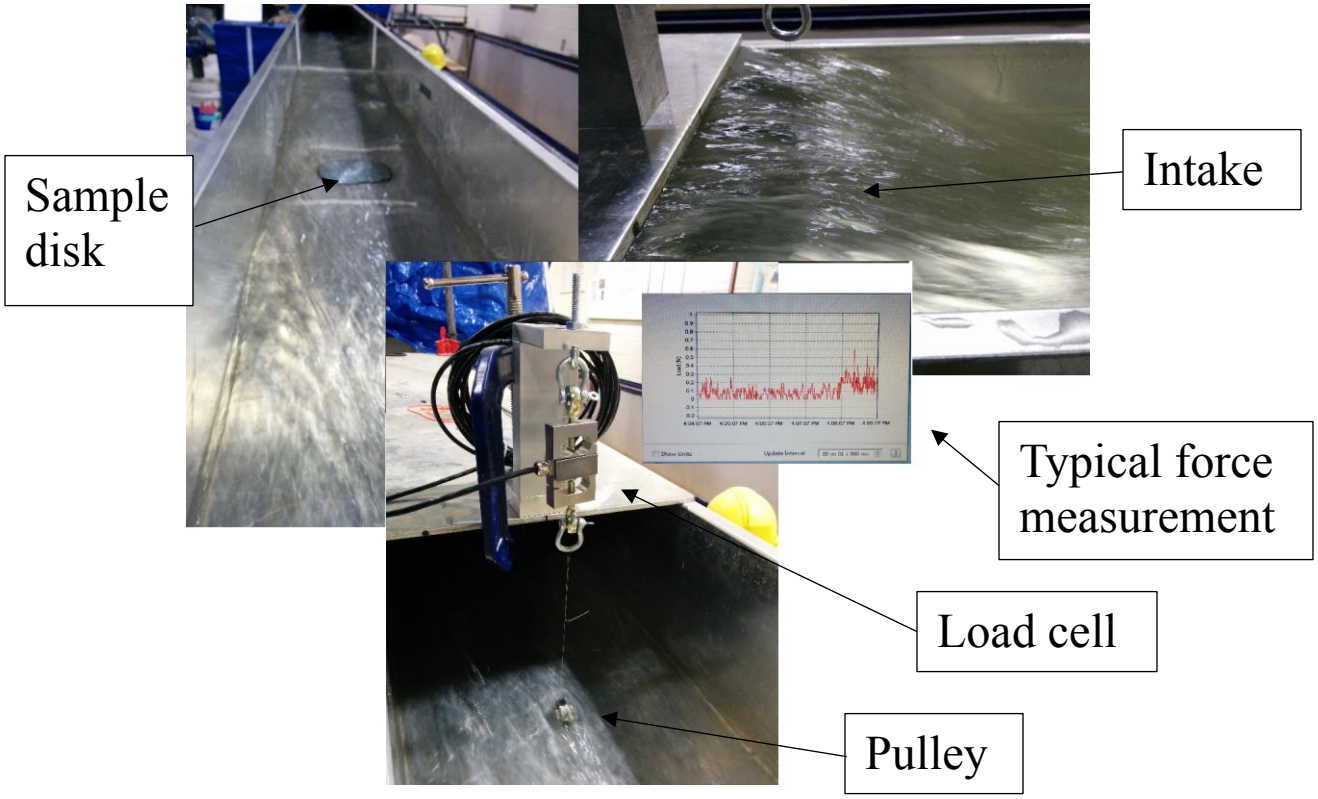

Figure 32. Specially constructed piston flume, hydraulic laboratory, University of Ottawa

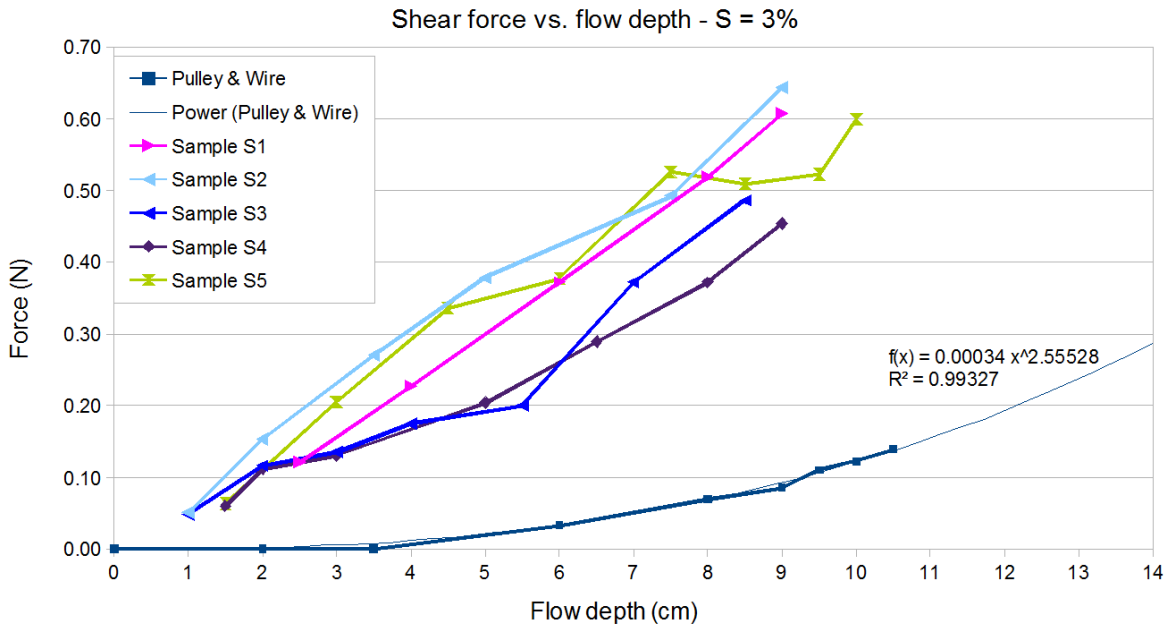

Figure 33. Raw shear plate measurements with drag force on pulley and wire system

The net shear results for individual samples at 1.5% flume inclination, including those of the sheet-metal and sandpaper discs, are shown in Figure 34, along with the theoretical shear calculations (using Equation 19). The results in Figure 34 show a clear trend for each sample and suggest that the tested samples represent a wide range of surface roughness varying from that of a smooth sheet-metal surface to near that of a 120-grit sandpaper. It is safe to conclude that such a range covers the cohesive soils of interest for this research. The net shear results for individual samples at 3.0% flume inclination are shown in Figure 35.

As the surface roughness of the cohesive soils of interest is relatively low, it is difficult to separate the effects of soil texture and surface quality of the sample on the resulting shear force. Furthermore, it was decided to use all recorded points as one response space and obtain a single calibration relationship for the flume in terms of net shear stress versus flow depth. This was done mainly to avoid having to calibrate the Erosionometer for every sample roughness and having to classify the roughness of each sample to be tested. In other words, this proposed procedure involves accepting an intentional error in order to simplify and speed up the test procedure. As can be seen in the graphics of Figure 34 and Figure 35, the average of the depth versus shear stress from all five soil samples is still a significant improvement over the theoretical curve (Equation 19). The final set of net values of the shear stress versus flow depth from all samples, at a flume slope of 1.5% and 3.0%, are shown graphically in Figure 36 and Figure 37, respectively.

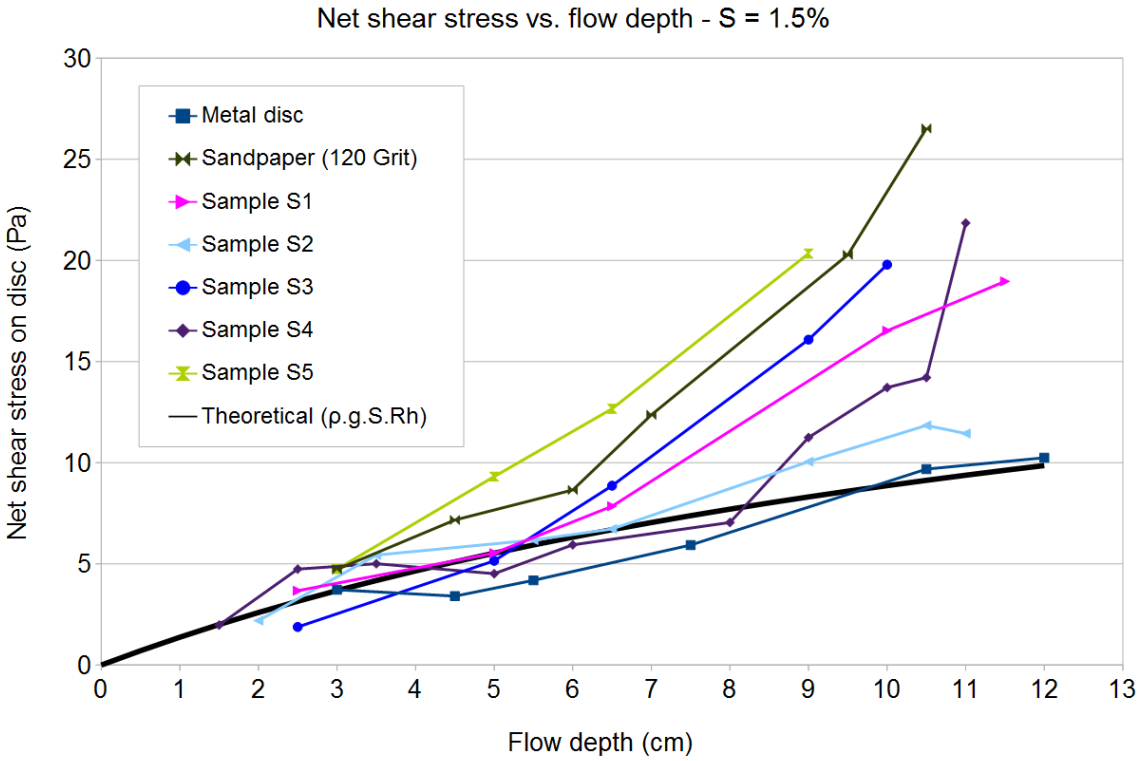

Figure 34. Flume shear measurements for individual samples at a flume slope of 1.5%

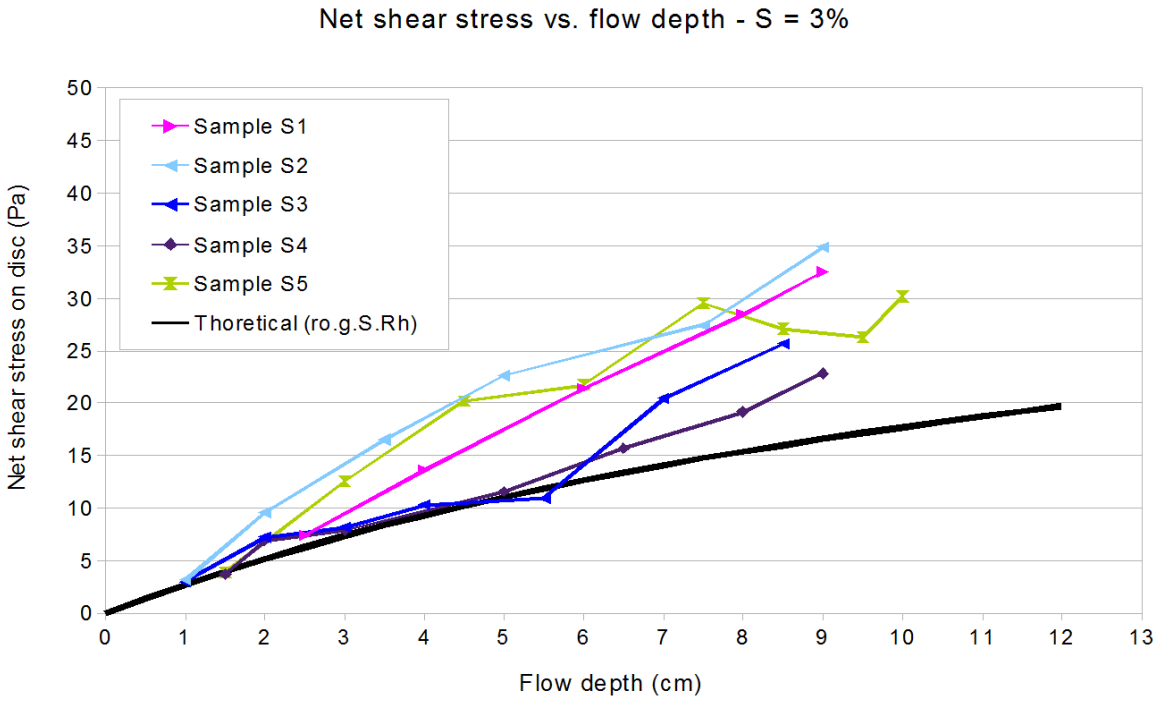

Figure 35. Flume shear measurements for individual samples at a flume slope of 3.0%

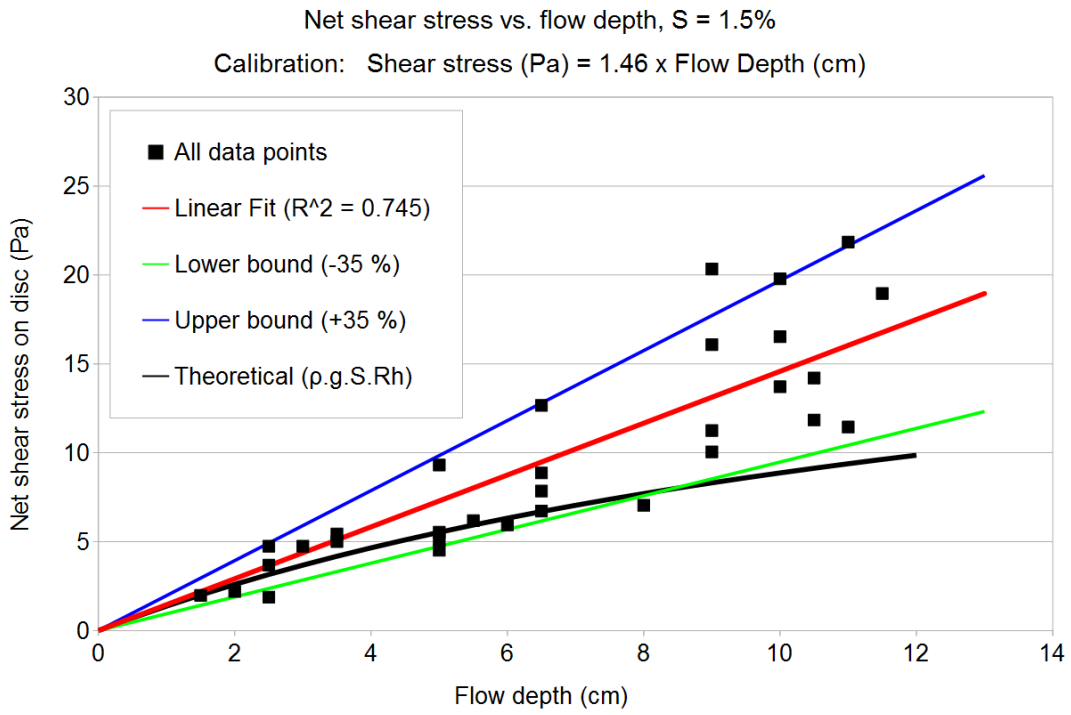

Figure 36. Flume shear calibration data at 1.5 % slope

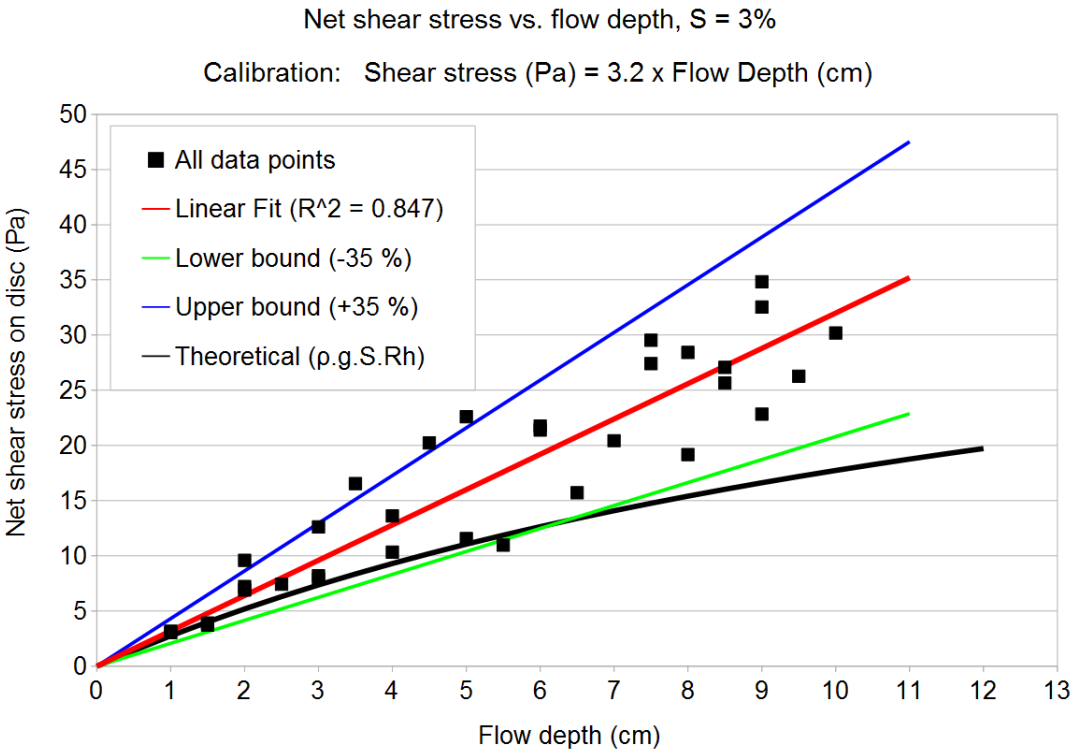

A linear regression trend line computed from the lumped data from all five tested soils yields the following relationships between the depth of water flow in the flume, measured in cm, and the induced shear on cohesive soil samples:

$$\tau = 1.42 \times D_{1.5} \quad (20)$$

And

$$\tau = 3.2 \times D_{3.0} \quad (21)$$

Where τ = fluid shear (N/m^2), $D_{1.5}$ = depth of water flow, in cm, at 1.5% flume slope, and $D_{3.0}$ = depth of water flow, in cm, at 3% flume slope.

The displayed lines representing the -35% to +35% uncertainty range (determined visually) around the trend lines appear to encompass the bulk of the measured values. As stated earlier, for practical purposes, the estimate of bed shear stress induced on the soil was simplified by lumping the response of all tested soils and textures and plotting a single best fit calibration curve (see Figure 36 and Figure 37). During subsequent sample testing, this calibration curve was used to estimate critical bed shear stress at the flow depth that was observed to induce the initiation of particle entrainment. The simplicity of this approach outweighs the required effort and the uncertainty that would be induced by attempting to classify the texture and roughness of each soil sample being tested.

Note that in all cases, the measured shear is higher than the theoretical shear computed from the depth slope product (Equation 19). This is particularly true at higher flows, which is expected since the flow is constantly accelerating between the flume intake and the free-falling discharge, including at the sample location.

5.2.3. **Erosionometer calibration**

The 23 soil samples from the different sites were tested in the piston flume and the critical shear at the observed initial entrainment was computed using Equations 20 and 21 accordingly, based on the flume inclination at the time of testing. Subsequent Erosionometer tests were performed on the same samples and the yield values were plotted against the corresponding critical shear measured in the flume. The correlation appeared to be linear and a regression analysis performed on the 23 points produced the following relationship with a coefficient of determination (r^2) of 0.83:

$$\tau_c = 0.57\ E_y - 0.65 \quad (22)$$

Where τ_c = critical shear of the soil (N/m^2), and E_y = yield force (peak) measured by the Erosionometer (N); 0.57 (m^{-2}) and 0.65 (N/m^2) are the slope and intercept of the correlation, specific to the Erosionometer probe.

The calibrated relationship between the Erosionometer yield force and the critical shear of the soil is shown graphically in Figure 38.

The small negative intercept in Equation 22 may represent a viscous drag resistance in soft sediments that are susceptible to suspension at any level of fluid motion (τ_c near zero). In other words, sediments already in suspension, i.e. zero critical shear (light mud), would still exert some resistance to the moving probe by surface tension, viscous damping forces, etc. Also shown in Figure 38 are lines representing -35% and +35% deviation from the linear correlation, which appear to contain most of the data points. It is important to note that since a simplifying error of ±35% was adopted for the critical shear stress measurements in the flume (Y-values in Figure 38), then, statistically, the error in the correlation is minimal, and can be reasonably neglected.

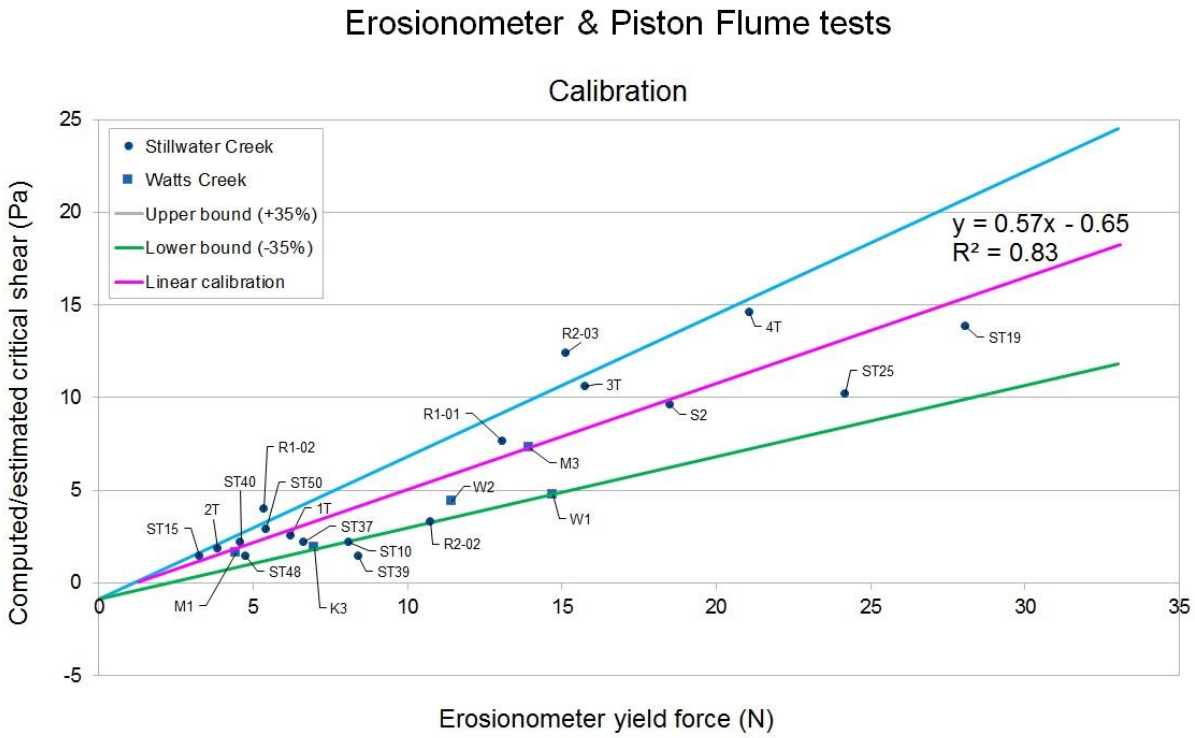

Figure 38. Erosionometer calibration data

5.2.4. **Validation**

Following the calibration of the Erosionometer, it was used to assess the critical shear of silty clay and clayey silt samples taken from five general locations along the banks of Feedmill Creek, in the west end of Ottawa, Canada. The five locations covered a reach of about 1,150 m along the creek (See

Appendix 2). A total of 17 spots were sampled in the vicinity of the five locations as the soil appeared to vary between the north bank, the south bank, and the bed, as well as along the creek alignment. A specimen from each of the 17 spots was subjected to classification testing; see Section 5.1 for further details and classification data..

The approximate locations of the five test sites along the Feedmill Creek basin are shown on the corresponding map placed in Appendix 2. Some of the samples were not subjected to flume or Erosionometer testing due to difficulties in sampling and handling of the soil (extremely loose or soft organic soil, excessive wood fragments and root content, etc.). A total of 15 Erosionometer and flume test sets were performed for the validation. In three of the cases, the Erosionometer tests were performed *in situ* and compared to flume test results on extracted samples. In the remainder of the cases, both the Erosionometer and flume tests were performed on the same extracted sample.

The tests were performed following the same methodology described earlier, as applied to the samples used in the calibration process. The measured yield force was plotted against the observed critical shear in the flume test and compared to the established calibration line as shown in Figure 39.

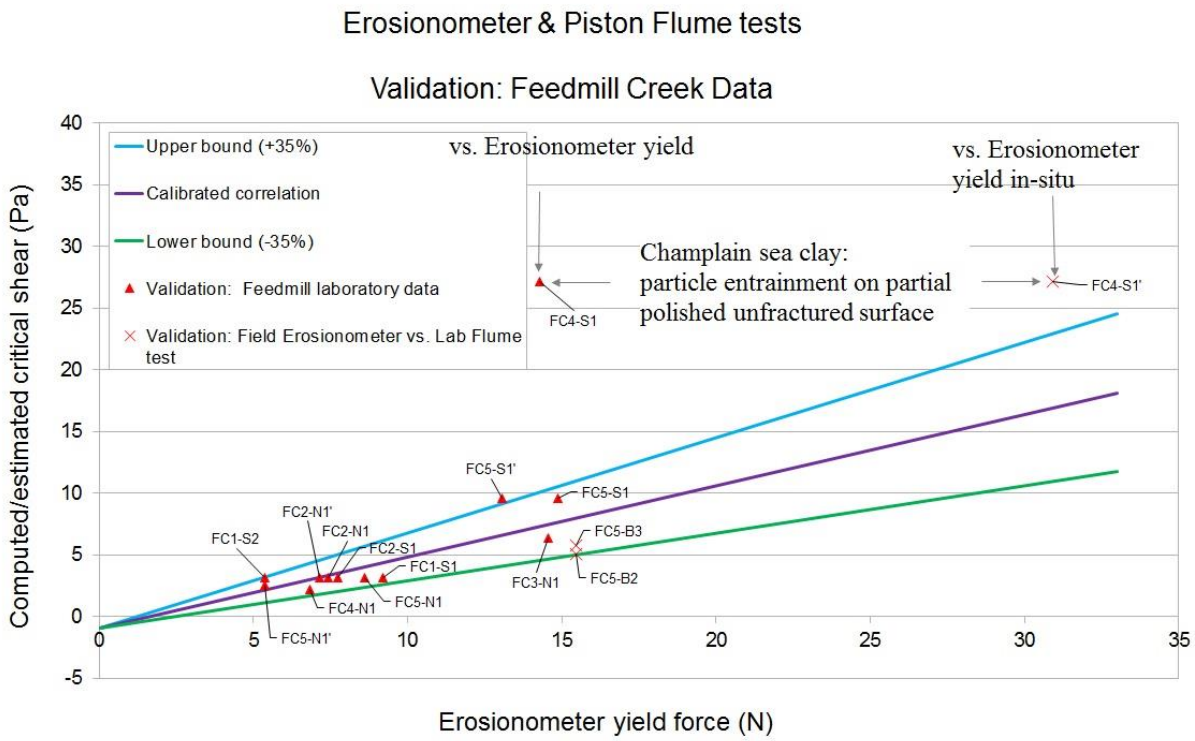

Figure 39. Erosionometer validation data

The Erosionometer and flume test data for both calibration and validation are provided in Table 1.

Table 1. Erosionometer and flume test data

Sample No.	Flow depth	Flume slope (%)	Calibrated shear stress (Pa)	Erosionometer yield force (N)
Calibration data: Stillwater Creek, Tributary E1				
1T	1.75	1.5	2.56	6.23
2T	1.25	1.5	1.83	3.85
3T	7.25	1.5	10.59	15.74
4T	10.00	1.5	14.60	21.09
R2-02	2.25	1.5	3.29	10.75
R1-02	2.75	1.5	4.02	5.34
R1-01	5.25	1.5	7.67	13.06
R2-03	8.50	1.5	12.41	15.14
Calibration data: Stillwater Creek, multiple locations along main bed				
ST10	1.50	1.5	2.19	8.11
ST15	1.00	1.5	1.46	3.26
ST19	9.50	1.5	13.87	28.07
ST25	7.00	1.5	10.22	24.19
ST37	1.50	1.5	2.19	6.62
ST39	1.00	1.5	1.46	8.41
ST40	1.50	1.5	2.19	4.59
ST48	1.00	1.5	1.46	4.74
ST50	2.00	1.5	2.92	5.43
Calibration data: Watts Creek, multiple locations along main bed*				
M1-1	1.20	1.5	1.75	4.44
M1-2	1.00	1.5	1.46	4.44
M3-1	5.50	1.5	8.03	13.96
M3-2	4.50	1.5	6.57	13.96
K3	1.30	1.5	1.90	6.98
W1-1	3.00	1.5	4.38	14.70
W1-2	3.50	1.5	5.11	14.70
W2	3.00	1.5	4.38	11.43

Sample No.	Flow depth	Flume slope (%)	Calibrated shear stress (Pa)	Erosionometer yield force (N)
Validation data: Feedmill Creek, five general sampling zones				
FC1-N1	1.00	3.0	3.20	5.35
FC1-S1	1.00	3.0	3.20	9.21
FC2-N1	1.00	3.0	3.20	7.43
FC2-N1'	1.00	3.0	3.20	7.13
FC2-S1	1.00	3.0	3.20	7.72
FC3-N1	2.00	3.0	6.40	14.56
FC4-N1	0.70	3.0	2.24	6.84
FC4-S1	8.50	3.0	27.20	14.26
FC4-S1'	8.50	3.0	27.20	30.91**
FC5-N1	1.00	3.0	3.20	8.61
FC5-N1'	0.80	3.0	2.56	5.35
FC5-S1	3.00	3.0	9.60	14.86
FC5-S1'	3.00	3.0	9.60	13.07
FC5-B2	1.60	3.0	5.12	15.46**
FC5-B3	1.80	3.0	5.76	15.46**

*: Some of the samples from Watts Creek were tested twice in the flume, the average critical shear and a single data point from the two tests are shown in the calibration plot

**: *In situ* Erosionometer data compared to flume data on a sample from the same location

Two categories of validation tests are shown in the plot in Figure 39 as stated in the legend:

1. Laboratory (lab) data representing flume tests and Erosionometer tests performed on the same sample surface in the lab.
2. Field Erosionometer versus lab flume test, whereby the *in situ* Erosionometer tests were compared to the flume tests performed on samples extracted from the same location

All but one sample (from the south bank of Site 4) showed a very close agreement with the established relationship. It is worth noting the range in measured critical shear (3 N/m^2 to 32 N/m^2) along this short reach, which demonstrates the need for a rapid and practical testing device.

The material at the south bank of Site 4 is a brownish gray Champlain sea clay, which, as mentioned earlier, is heavily structured with a dense web of fissures and weak planes. This clay exhibits a firm consistency with a brittle behavior, making it sensitive to manipulation. The wet surfaces appear polished

and slick (oily-like surface) which blends the joints and gives the soil the appearance of a single homogeneous mass. Due to the brittle nature of this soil, it was obvious that the sampling process significantly affected the characteristics of the soil in terms of strength and integrity. This can be clearly seen in the photo shown in Figure 40, taken during sampling. Consequently, *in situ* Erosionometer tests were conducted for this site, which showed a yield force of more than twice the value measured for an extracted sample in the lab (see Figure 39). Furthermore, the high value of critical shear (flume test) was based on observed erosion of a polished partial surface of the sample, since it was not feasible to obtain a complete clean-cut flush with the flume base. Other parts of the sample surface showed a rugged texture as clusters of soil detached along the weak planes (see Figure 41). These parts were eroded at a much lower flow/shear. This mode of erosion may be more representative of field conditions in such clays, as reported by Gaskin et al. (2003). The result of such erosion in clusters or blocks is often observed in the form of aggradation downstream by patches of rounded clay stones (Terwindt et al., 1968). It is the authors' opinion that the lower critical shear reflected by the Erosionometer test on such clays is more realistic than particle-level erosion observed in the flume on partial patches of smooth horizontal planes. This may represent a significant advantage of using the Erosionometer as macro-erosion of channel features made up of such clays, with underlying weakness zones, is very difficult to replicate in the laboratory. Furthermore, due to the sensitivity of this clay to manipulation, using a Jet test for several minutes at higher than critical shear may induce an error in prediction when extrapolating for the critical value.

Figure 40. Distressed brittle Champlain sea clay during sampling

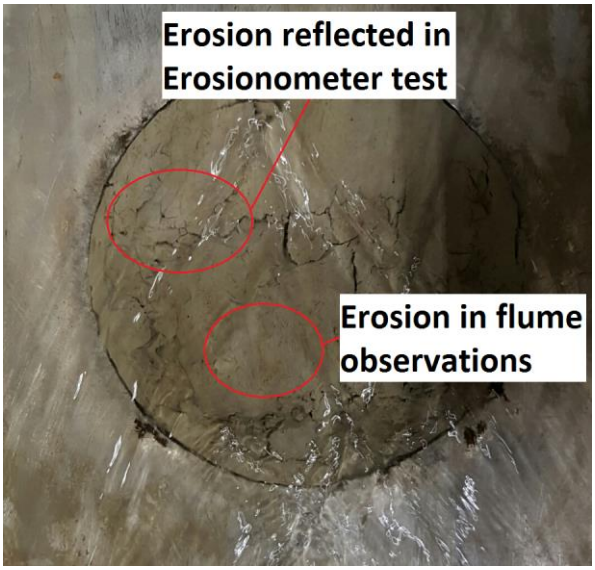

Figure 41. Champlain sea clay sample in the flume

5.2.5. **The concept of seepage**

Seepage through a porous medium is a well-known scientific concept. A review of this principle is presented herein as an introduction to the next section where the effect of seepage on the erodibility of cohesive soils is investigated. The following simplified review is adapted from part of a lecture published by the Melbourne School of Engineering in the public domain.

According to Bernoulli's equation:

$$h_t = [p/(\rho g)] + [v^2/2g] + [h_e] \quad (23)$$

Where h_t is the total head, p is the water pressure, ρ is the water density, g is the gravitational acceleration, v is the flow velocity, h_e is the elevation head above a selected datum. The three elements enclosed in brackets in Equation 23 represent, from left to right, the pressure head, the velocity head, and the elevation head. In seepage problems the velocity of flow is very small, and the velocity head is negligible in comparison with the pressure and elevation heads, therefore, the total head referenced in this section is the sum of pressure head and elevation head.

To better understand the seepage principle, the simplified setup illustrated in Figure 42 will be used throughout this section. The setup consists of a symmetrical U-shaped tube in which a soil column of length L (applies to any soil type) is mounted in the right side, a short distance below the top of the tube as shown. Initially, the entire tube is full of water: water level in the left section is at Point A, and the water level in the right section is maintained at the top of the tube throughout the experiment. The initial profiles of effective stress (σ') and pore water pressure along the depth of the soil column are represented in the blue graph lines in the pressure diagrams to the right of the tube illustration in Figure 42, as shown. The initial profiles are labelled as "A", which corresponds to the position of the free water surface in the left tube section. The pore water in the soil is under hydrostatic pressure at this stage so no water flow is occurring, and the total head is constant throughout the soil depth. The datum has been arbitrarily chosen to coincide with the underside of the soil.

If the water level in the left side of the tube is lowered by a distance h to Point B. The pressure head at the underside of the soil is reduced by h. The pressure head at the top of the soil remains unchanged, therefore the effective stress at the top of the soil remains unchanged.

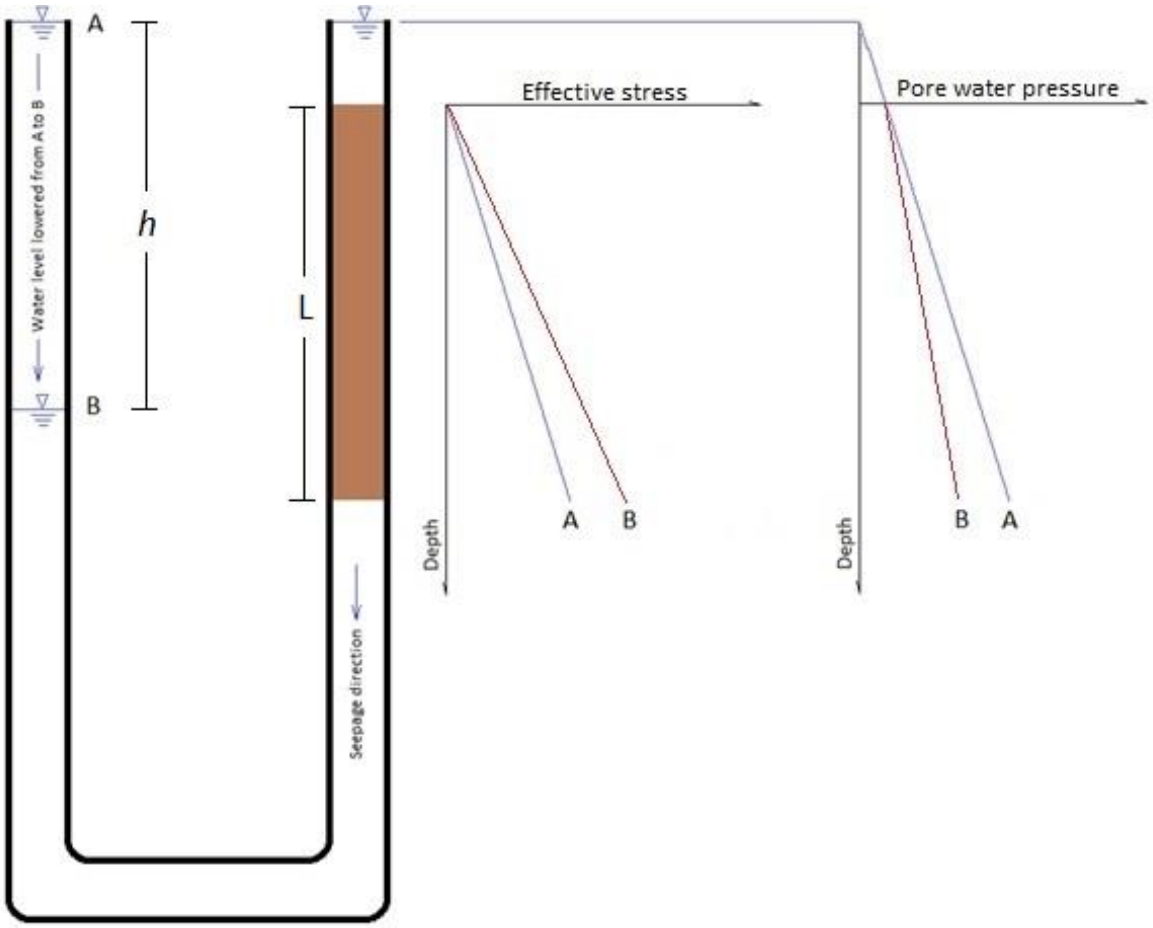

Figure 42. Illustration of the seepage experiment – Not to scale

The elevation head between the two cases (water at A and water at B) remains unchanged throughout the soil column as the soil is stationary, therefore, the total head loss between the top and bottom of the soil between Case A and Case B is equal to the loss of pressure head h. This implies that the gradient of total head loss, i, across the soil column can be expressed as:

$$i = h/L \qquad 24$$

It should be noted that in a homogeneous soil at steady-state condition, the gradient (total head loss with distance) is the same between any two points along the seepage path.

The total vertical stress at any point in the soil column remains unchanged, and equal to the weight of the saturated soil above the point plus the weight of water above the soil. Therefore, as the pore pressure at the bottom of the soil column has decreased by $\rho g h$, then the effective stress at the bottom of the soil column had increased by the same amount, and substituting the value of h in Equation 24:

$$\Delta\sigma' = \rho g i L \qquad 25$$

As the effective stress at the top of the soil column remains unchanged, the increase in effective stress throughout the soil is represented by the difference between Lines A and B in the effective stress diagram in Figure 42 and is directly proportional to the total head gradient. In other words, the increase in effective stress at a depth d below the top of the soil column ($\Delta\sigma'_d$) can be expressed as

$$\Delta\sigma'_d = \rho g i d \qquad 26$$

It is important to note that seepage laws apply to any porous medium, regardless of the permeability of the material. The only difference between high and low permeability soil is the time they require for reaching the steady-state seepage condition, which should not be confused with the time water requires to travel through the soil.

The implications of the seepage pressures (effective stress increase) on erodibility is significant.

To illustrate, consider a cylindrical sample of cohesive soil, 30-mm thick, placed in a steel sleeve, and subjected to Pressure A at its top surface, and Pressure C at its underside, which is maintained constant; this can represent a higher-permeability soil underneath which can accept the slow seeping water from the cohesive soil above it without any meaningful increase in pressure. Figure 43 illustrates the case setup and the water pressure profile. The only change in the system's boundary conditions considered in this case is a rise in the water level at the surface raising the head at the surface of the soil to Pressure B. The pressure distribution with depth shown in Figure 43 represents steady-state profiles before and after the rise in water level.

Consider a soil cluster or block at the surface that would potentially be detached and entrained, for example a 10-mm thick block of reasonable lateral dimensions. The objective of this discussion is to investigate the effect of the rise in surface pressure on the erodibility of the cluster. Therefore, for clarity, the flow shear, and the traditional resisting forces such as the weight of the block, the cohesion between the block and the soil matrix, etc., will not be discussed as they are common to both cases (before and after the rise in pressure head). The balance of vertical water pressures that the block is subjected to is illustrated in Figure 43; these pressures being the surface pressure B acting downward and pressure b1 acting upward. It should be noted that the lateral water pressure is not represented in the balance of forces for clarity, as it acts equally on opposite sides of the block. It is obvious that the rise in surface water pressure would result in an added downward force on the surface block. This added net force will continue to act on the upper surface of the block as long as pressure B and pressure C are maintained at the top and bottom surfaces of the soil specimen, respectively. While the represented case is at steady-state condition, it can be easily shown that a higher net downward force originally acts on the top surface of the block immediately after the surface pressure is raised to pressure B, and gradually declines with time as the pressure profile approaches steady-state. The time it takes for the steady-state condition to be reached is dependent on the characteristics of the soil. Such transient conditions can be predicted by a well-calibrated numerical model or determined experimentally by advanced instrumentation and

labour-intensive experimentation setups. The important point to make is that at any time, while a higher pressure is applied at the surface in this setup, the surface clusters are assisted against detachment/entrainment by a net downward hydraulic force. This stabilizing effect can be measured by the Erosionometer as a change in the critical shear stress, which is the threshold flow shear required to initiate the detachment and entrainment of surface clusters of the specific soil. As shown earlier, since the seepage pressure acts as effective stress on the soil, it is inherent that cohesive soils will also commence a process of consolidation (reduction in void ratio) under the imposed seepage pressures, which is expected with time to further increase the soil's resistance to detachment as the consolidated soil will be more competent.

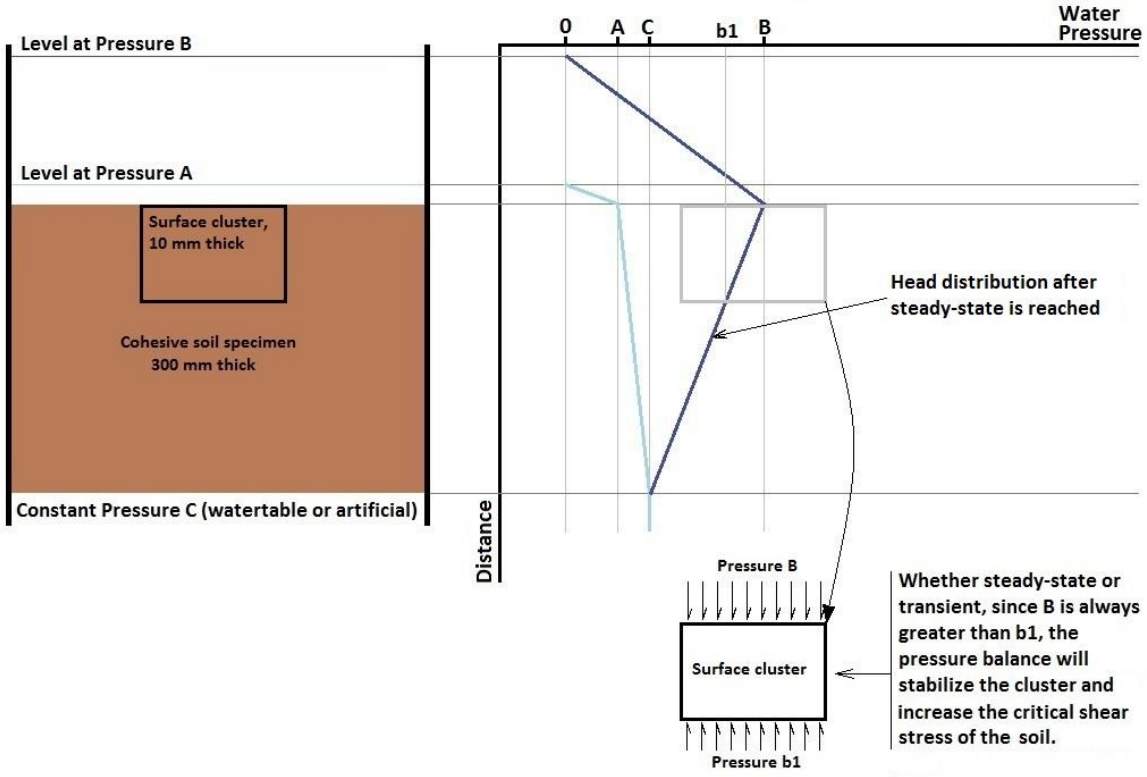

Figure 43. Seepage forces applied to a cohesive soil cluster.

5.2.6. **Influence of pressure gradient on critical shear stress**

Part of the difficulty in simulating the effect of water flow on cohesive samples is the near impossibility to replicate field conditions, namely, the constantly varying pore water pressure within the soils in response to changing flow depth, changing groundwater conditions and resulting seepage pressures, and other variations both with distance and time at study sites. Unlike granular soils, which adopt the new hydraulic conditions in a relatively short time, cohesive soils tend to take considerable time to reach steady state under new imposed conditions, and often do not reach such state before the hydraulic conditions change again. One obvious example is flood level flow which imposes a higher hydraulic head on the soil for a relatively short time period before receding back to usual flow level. Julian and

Torres (2006) enumerated a multitude of such difficulties and used statistical methods to relate the entrainment of cohesive riverbanks to peak flow intensity, duration, and silt-clay content of the soils, which in a way reflects the cyclic variation in pore pressure within the bed and bank materials. In addition, the slow rate of erosion and the fact that cohesive soils erode mainly in clusters of random size and shape, as opposed to individual grains in the case of granular soils, adds another layer of difficulty to the research.

Simon and Collison (2001), investigated the effect of "seepage pressures" on the erodibility of cohesive beds in midwestern USA, where pore pressure was found to decrease with depth and in some cases becomes negative 10 to 15 cm below the bed due overconsolidation (see Section 4.3.1). The soils were generally of clay materials, with a hydraulic conductivity ranging between 10^{-9} and 10^{-10} m/s. They discussed the role of seepage forces in increasing or decreasing the erodibility of cohesive soils (depending on the gradient direction), but mainly highlighted the "upward directed seepage forces on the recessional limb of the hydrograph" and showed significant upward pressure gradients, "great enough to contribute to detachment of cohesive bed material". While they showed by measurements and numerical modelling the progression of differential pressures and resulting seepage forces, they did not test the effect of such forces on the critical shear stress of the soils.

Nouwakpo et al. (2010) found that rill erodibility of an oversaturated silt loam soil (seepage condition) was 5.64 times higher than that of the same soil in the presence of infiltration (drainage condition). They also found that the critical shear stress decreased when the subsurface hydraulic gradient was increased from negative gradients ("drainage conditions") to positive gradients ("seepage conditions"). In a more recent work, Nouwakpo and Huang (2012) conducted a complex experimental study, using a large-scale laboratory hillslope model (see Section 4.3.2), to build on the 2010 findings, namely to quantify the effect of soil subsurface hydrology on erosion and concentrated flow channel development at the hillslope level. They were successful in relating the critical shear stress and the erosion rate of the soil packed in the hillslope model to the subsurface gradient varying from drainage to seepage conditions.

To investigate the change in critical shear stress with subsurface gradient, the Erosionometer apparatus introduced in Section 5.2.1 was modified to create a fluid pressure differential between the surface and the base of the soil sample. The modifications to the original Erosionometer system (Figure 26) are limited to the submerging cell, while the rest of the apparatus remains the same. As shown in Figure 44, a sub-chamber (backpressure chamber) is created within the submerging cell. The backpressure chamber is vented and drained to the outside to maintain zero relative pressure inside while holes drilled through the cap of the chamber allow the water seeping through the soil sample to drain into the chamber. The steel cylinder housing the soil sample is shortened and sits on top of the backpressure chamber on an annular rubber seal, maintaining zero relative pressure connection between the bottom of the soil sample and the backpressure chamber. The cover of the submerging cell is extended vertically via a 19-mm diameter acrylic tube allowing a water head in the cell of up to 1,500 mm (15 kPa water pressure).

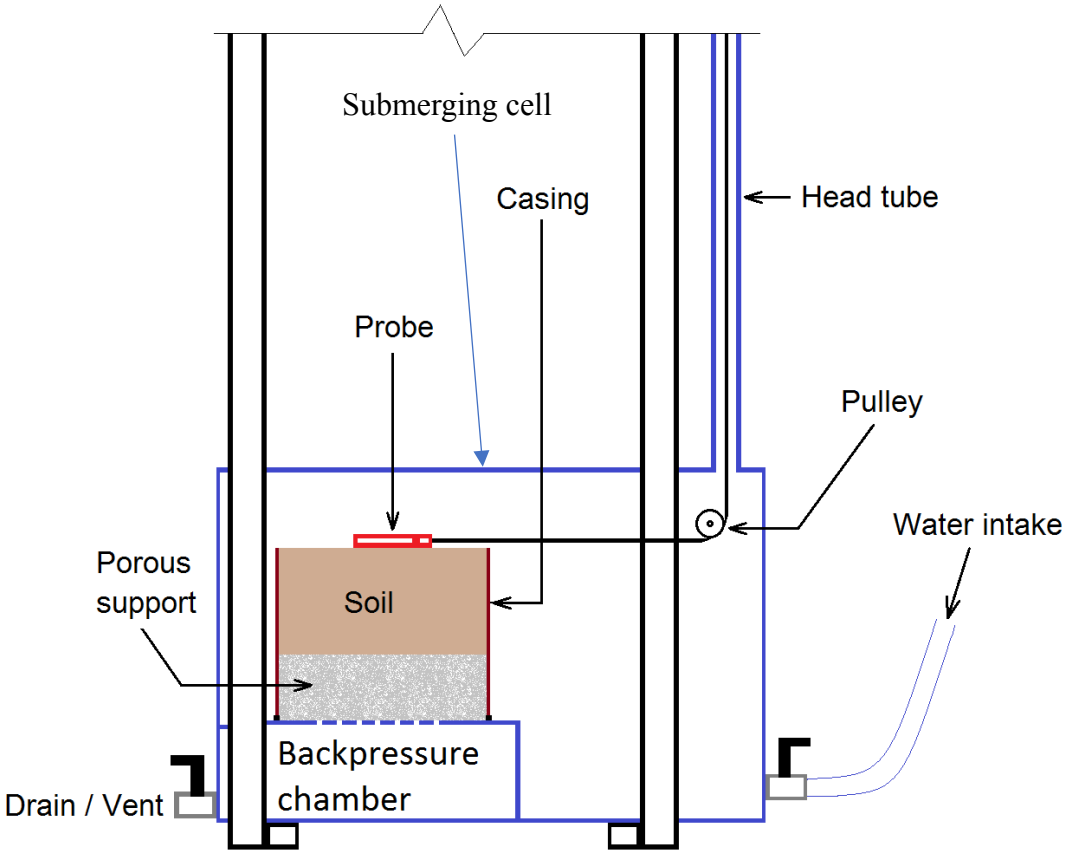

Figure 44. Erosionometer modifications with a backpressure chamber

5.2.6.1. **Test procedure**

As stated earlier, the Erosionometer was developed to measure the critical shear by measuring the soil's resistance to surface shear induced by a special probe (see Section 5.2.1).

For differential pressure experiments, the sample cylinder is adapted with a 50-mm thick reinforced screen material cut to size to fit inside the steel cylinder. A filter fabric is also cut to fit inside the sample cylinder between the screen and the soil to prevent the soil from sinking or crumbling into the screen under pressure. The sample cylinder setup is shown in Figure 45. A layer of clean sand can be placed between the filter and the soil sample to control the sample thickness for gradient calculations.

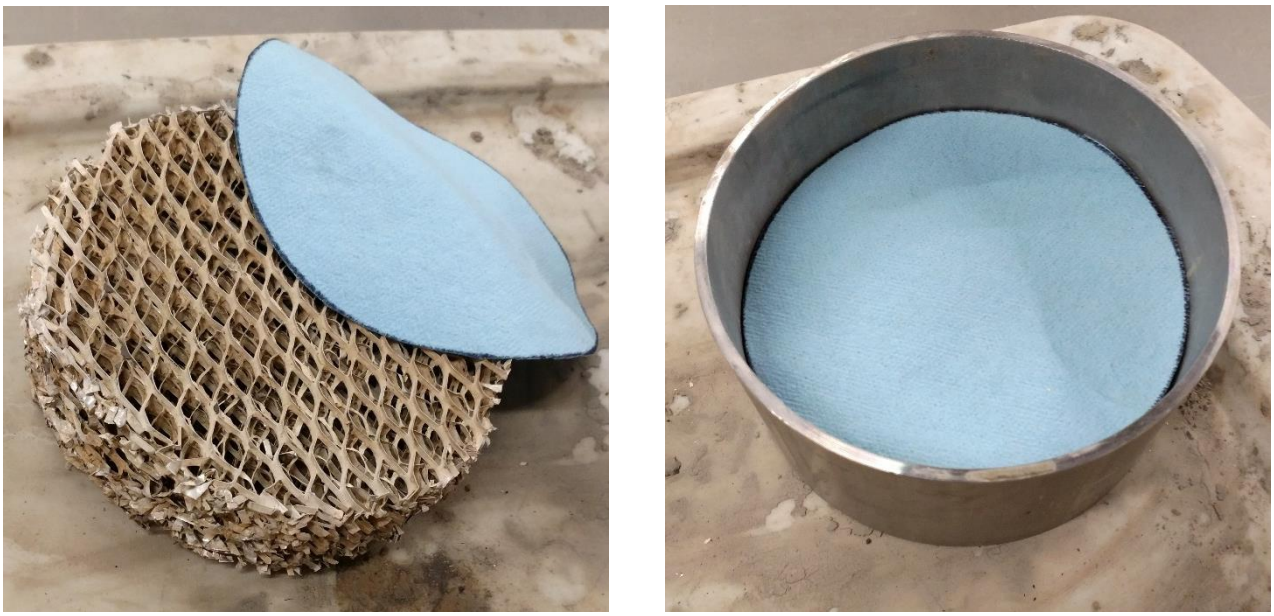

Figure 45. Sample cylinder and screening/drainage insert

For the purpose of this research, only drainage gradient will be tested whereby the water head at the upper surface of the sample is varied between 0 kPa and 15 kPa, while the underside of the sample is kept at 0-head by draining the backpressure chamber and keeping it at ambient atmospheric pressure at all times. The reverse gradient (seepage condition) can be established by injecting water in the backpressure chamber at a higher pressure head than the one at the upper surface of the sample (not performed in this research).

The four supplemental soils listed in **Error! Reference source not found.** were tested with the b ackpressure chamber completely drained. As these soils have very low hydraulic conductivity (see Appendix 3), it is reasonable to expect that they will remain saturated throughout the duration of the experiment.

Table 2. Supplemental cohesive soils subjected to Erosionometer testing under varying gradient

Sampling location	Sample #	Description
Green's Creek	2	Bluish grey soft silty clayey fine sand, medium plasticity
Muddy Creek	2	Champlain sea clay, soft, grey, structured, high plasticity
South Nation River	1	Brown silty clayey sand
West Branch Scotch River	1	Greyish brown silty clay, stiff, black organic content, high plasticity

The first sample is tested at zero gradient, i.e. free water surface just above the soil surface. A similar sample is then tested with a specified pressure head over the soil surface while the backpressure head is controlled against the underside of the sample cylinder to remain close to the sample surface level. Both tests are conducted by first placing the sample in the pressure cell, with the probe installed on the soil surface and connected with the drag line. The submerging cell cap, which is extended with the head tube, is then placed over the cell on a neoprene gasket and clamped in place. Once the cap and head tube are

secured, the valve of the constant head tank is opened to flood the submerging cell. In the first test, the intake valve is closed as soon as the water level in the cell covers the surface of the soil to maintain zero gradient. In the subsequent experiments, the valve of the constant head tank remains open and the tank is moved up or down to control the head applied at the upper surface of the sample. The setup of the Erosionometer for testing under drainage gradient is shown in Figure 46.

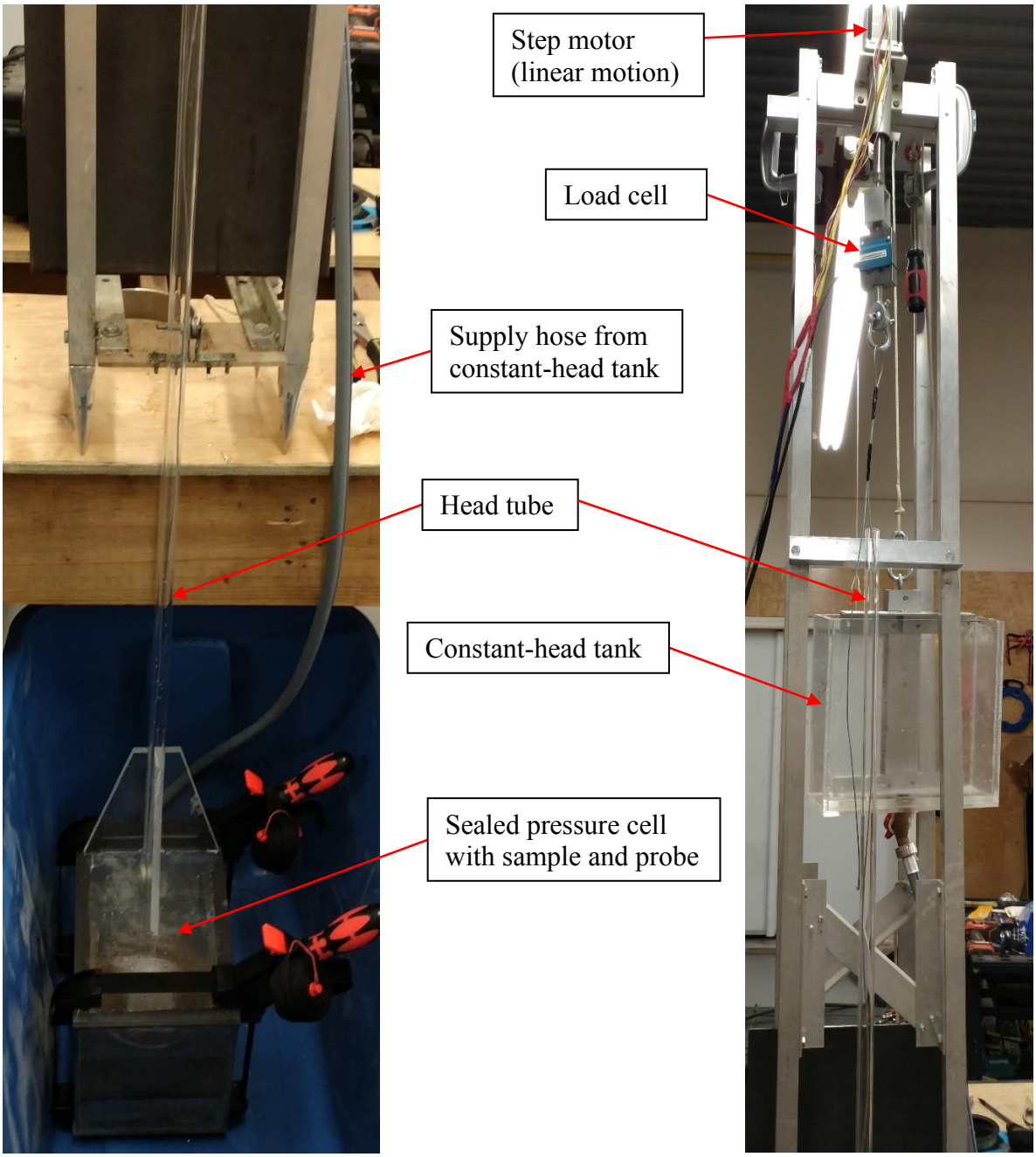

Figure 46. Erosionometer setup for drainage gradient testing

With the water head maintained just above the surface of the saturated soil sample, the Erosionometer test yields the critical shear stress of the soil without drainage gradient effect. With a water head in the acrylic riser tube higher than the elevation of the soil surface, and with the relative pressure on the

underside of the specimen maintained at zero, the test indicates the critical shear of the soil under a drainage gradient i such that:

$$i = \frac{h}{t} \qquad 27$$

Where i is the drainage gradient across the soil sample, h is the head of water above the soil surface (head differential through the sample thickness), and t is the thickness of the soil specimen.

Following the testing of the supplemental soils, the Erosionometer was upgraded with a flexible riser tube connected to the backpressure chamber. By controlling the height of the backpressure riser tube, the head against the underside of the sample can be controlled. The core soils were subsequently tested while the head in the backpressure chamber was maintained roughly at the level of the sample surface. It should be noted that by raising the height of the backpressure riser tube above the head in the submersion chamber riser tube, a reverse gradient (upward) can be achieved and the soil can be tested for critical shear under a seepage gradient. Such test, however, is beyond the scope of this research and can be an important topic for future research.

Another important upgrade to the Erosionometer was done before testing the core soils. It consisted of adding a second rigid riser tube connected to the lid of the submerging chamber, right over the initial position of the probe. This upgrade allowed access to push the probe into the soil at any time, especially after applying the differential head to the soil. This modification provided for more flexibility in conducting the tests and added more versatility to the device:

1. Inserting the probe in the soil after applying the differential pressure eliminates any doubt that the water pressure is acting on the underside of the probe, preventing friction between the soil surface and the probe face.

2. As the pins of the probe pierce the surface of the soil, they provide a shortcut for the hydraulic head to penetrate beneath the soil surface and undermine the soil's resistance to the probe's movement, therefore, the test is time sensitive and must be performed on thin fully saturated samples to ensure that the hydraulic gradient is established in a short time. This also implies that only soils with low hydraulic conductivity can be properly tested. Installing the probe into the soil surface after the gradient is established expands the test to include higher permeability soils such as clayey sand and silt loams.

3. The option to pierce the soil surface with the probe later in the test allows for testing the effect of time-dependent consolidation of the soil by the differential head. Therefore, the Erosionometer can now be used as a falling-head permeameter, and samples can be tested for critical shear at different stages of consolidation. Such test, however, is beyond the scope of this research and can be an important topic for future research.

The added upgrades to the Erosionometer are shown in Figure 47.

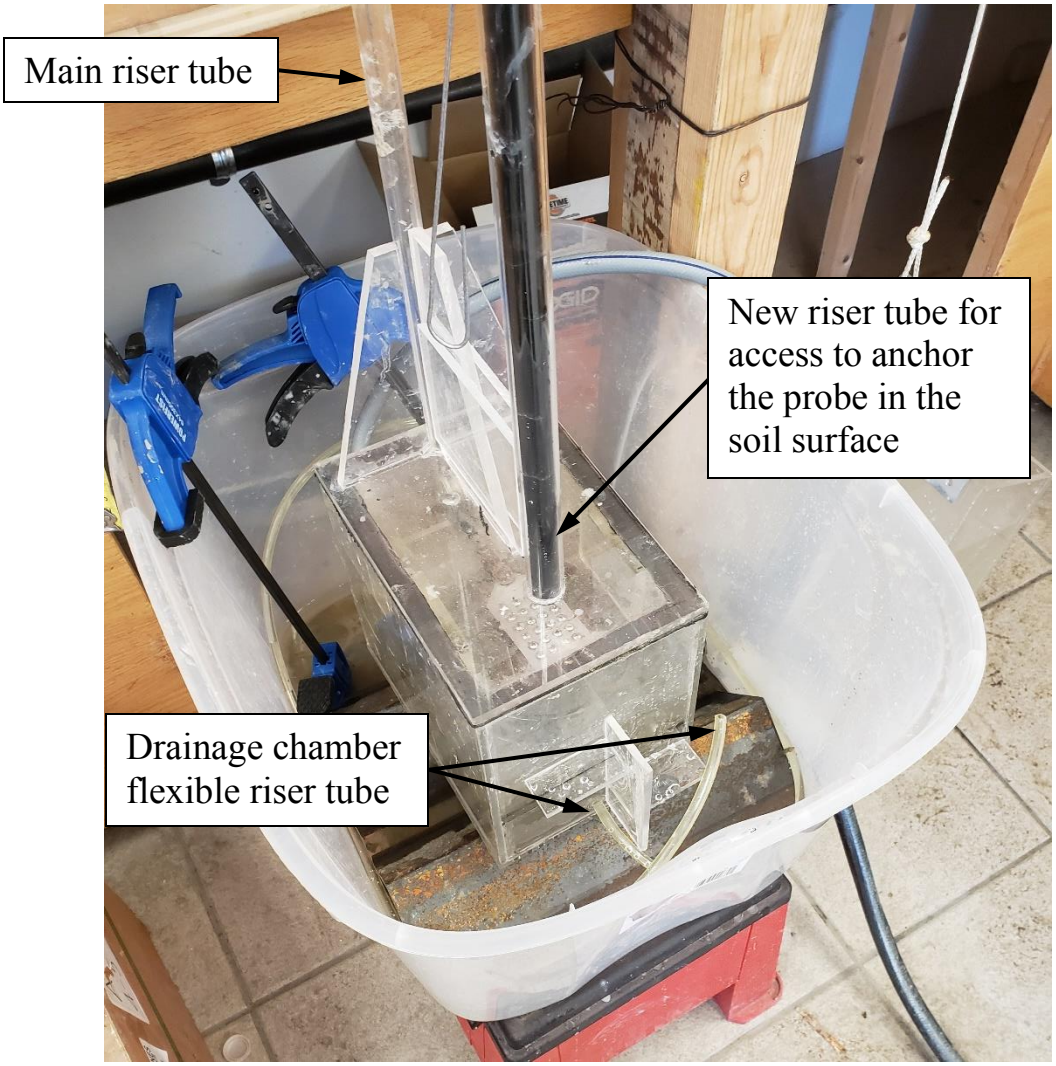

Figure 47. Further Erosionometer upgrades

5.2.6.2. **Test results**

The test specimens were sliced from larger samples collected in a 150-mm diameter stainless steel cylinder, as shown in Figure 48.

Figure 49 shows the specimen from South Nation River #1 sample after the zero-gradient test.

Figure 48. Specimen preparation – South Nation River #2

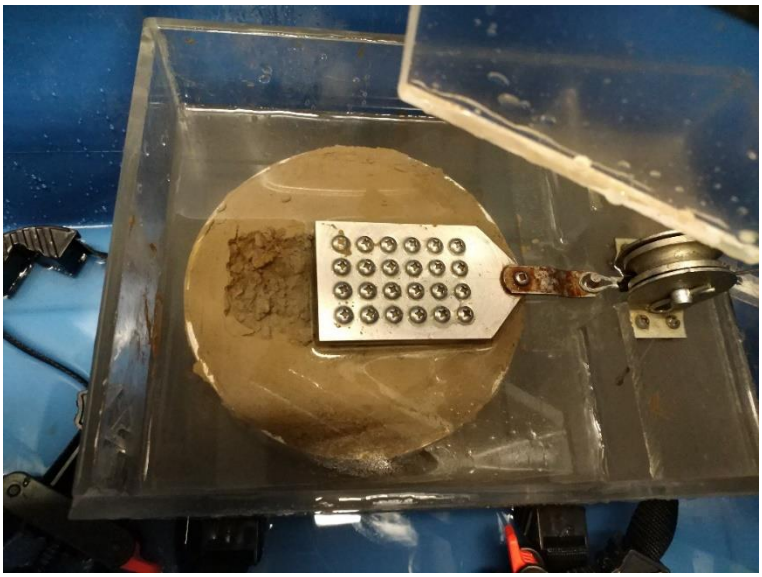

Figure 49. South Nation River #1 specimen after the Erosionometer test is concluded.

The specimens from South Nation River and West Branch Scotch River were tested only at zero head and 1,500 mm head, with a specimen thickness of 35 mm, which results in downward gradients of 0 and 43 m/m, respectively. The Erosionometer test results for both soils are shown in Figure 50 and Figure 51, respectively. Each figure shows, for the corresponding soil sample, the raw Erosionometer measurements of traction force against the step motor piston movement, which includes the displacement required to eliminate the slack in the wire connecting the probe to the load cell and the step motor piston (movement at near zero force), as well as the probe's displacement with respect to the soil it is embedded in. Also stated on the graphical data are the yield force measured by the Erosionometer, and the conversion to critical shear stress in accordance with Equation 22. As shown in the graphical data for both soils, the response of the soil to the probe's advancement under drainage gradient is much stiffer and shows a much higher yield force than in the case of zero gradient. In fact, both soils show almost double the yield force under a downward gradient of 43 m/m. Furthermore, once the initial failure occurs, the data show that the soil resistance in the remolded state with the downward gradient is similar to the virgin resistance at zero gradient, which is expected as the surficial soil clusters are fully or partially detached from the soil mass and are subjected to the same water pressure all around (zero gradient). This shows that the drainage gradient significantly increases the critical shear stress of cohesive soils. The test results are summarized in Table 3. The change in critical shear stress of the two soils and the apparent relationship with the downward gradient is illustrated in Figure 52. Note that a linear relationship is assumed. To further assess the relationship, soil specimens from the Green's Creek and Muddy Creek sites were tested at multiple gradients.

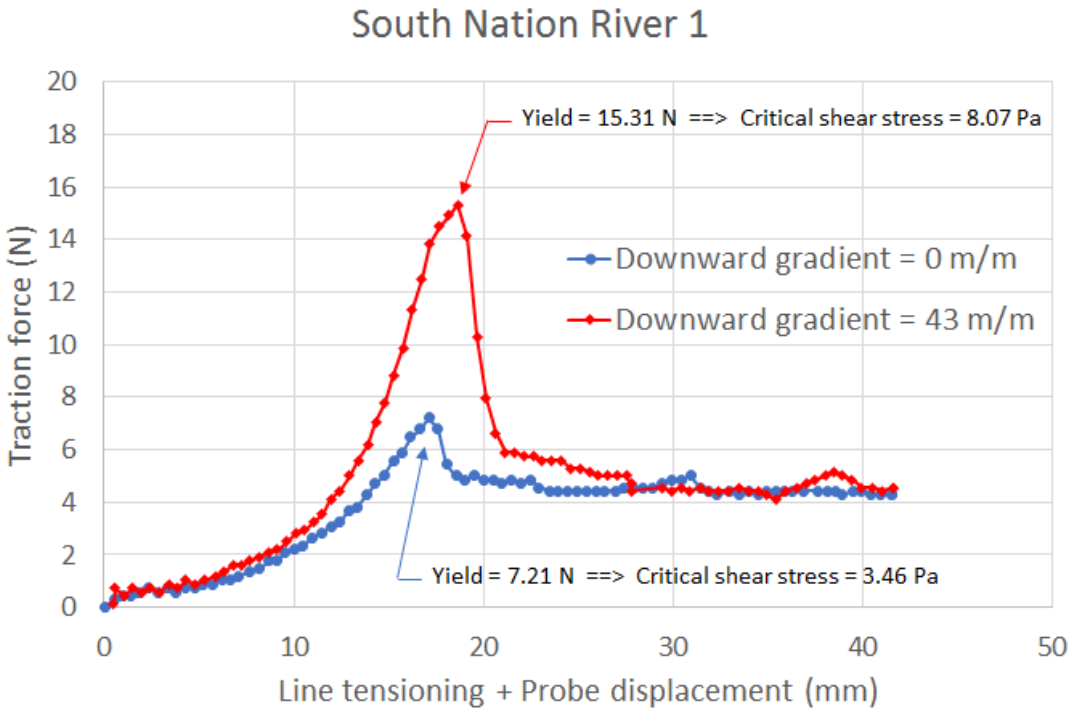

Figure 50. Erosionometer test results, specimens from South Nation River

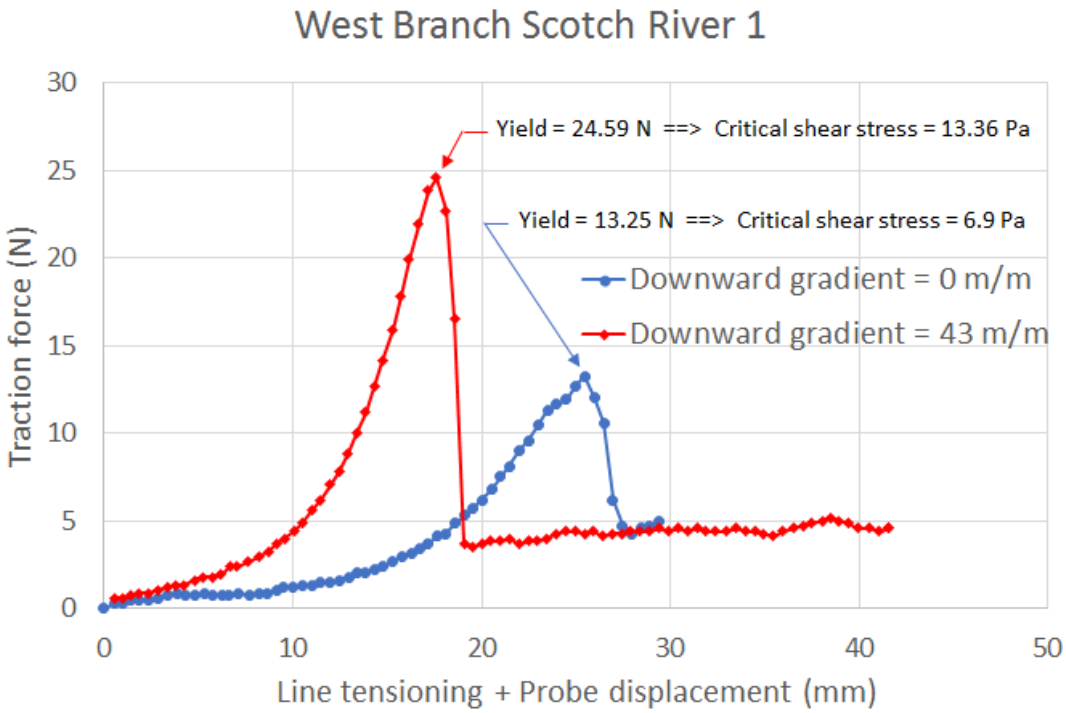

Figure 51. Erosionometer test results, specimens from West Branch Scotch River

Table 3. Summary of Erosionometer test results for critical shear stress (τ_c) under drainage gradient

Sampling location	τ_c at 0-m/m Gradient (Pa)	τ_c at 43-m/m Gradient (Pa)
South Nation River	3.46	8.07
West Branch Scotch River	6.90	13.36

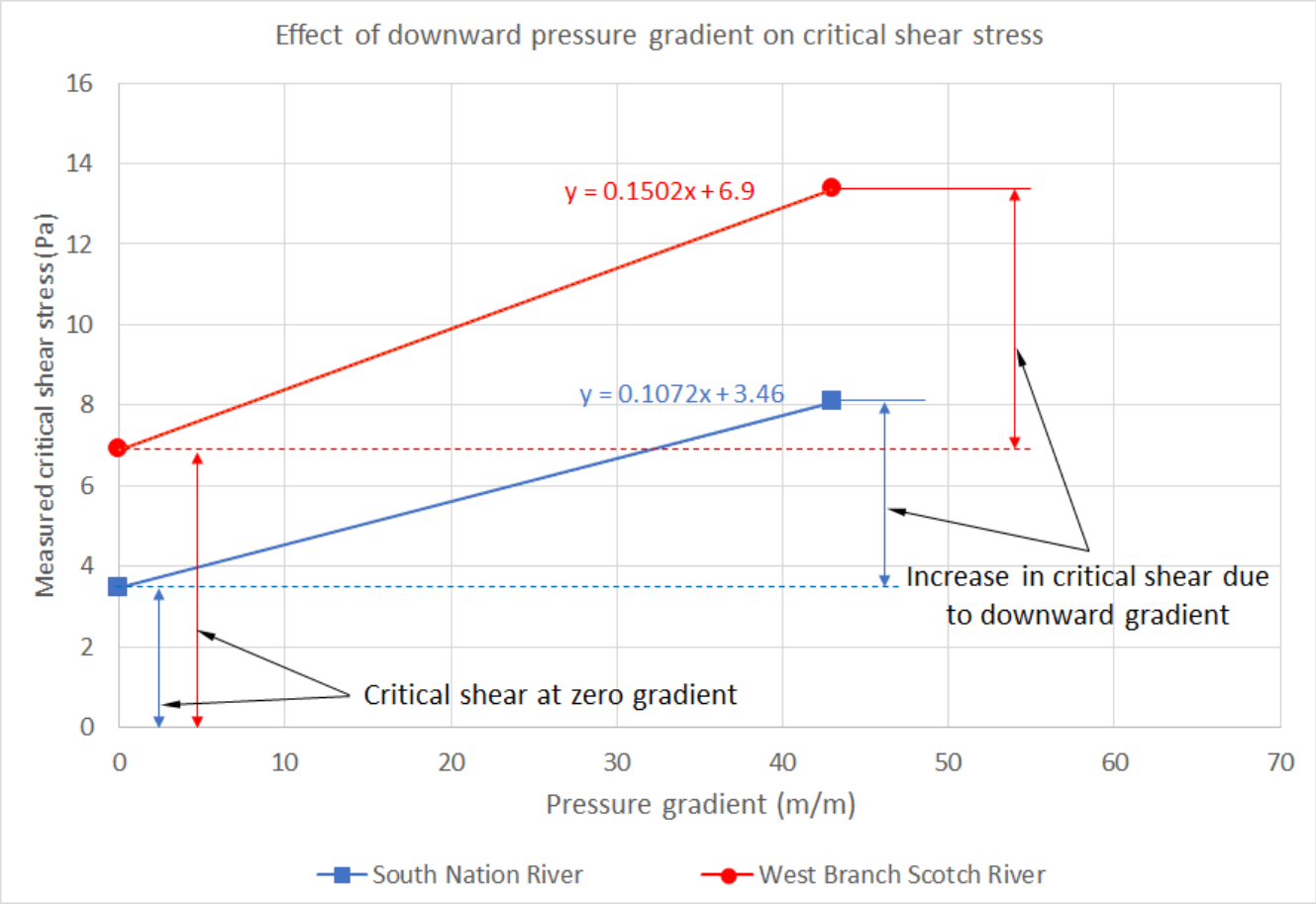

Figure 52. Graphical compilation of critical shear tests under varying gradient

Five different tests were performed on Green's Creek soil specimens with a differential pressure head of 0, 700, 1040, 1150, and 1520 mm applied across the sample, which corresponds to pressures of 0, 7, 10.4, 11.5, and 15.2 kPa respectively. The specimens were sliced about 43-mm thick, resulting in a corresponding gradient of 0, 16.3, 24.2, 26.7, and 35.3 m/m, respectively. The Erosionometer test results for Green's Creek soil at different downward gradients are shown in Figure 53 and summarized in Table 4. Note that the test at zero differential pressure was repeated since the first test did not show a distinct peak at failure, but rather a constant limit resistance with displacement. The second test showed a clear peak followed by a similar drag resistance as the first test.

The resulting relationship between the downward gradient and the critical shear stress is shown in Figure 54. While a second order polynomial shows a slightly better fit to the experimental data, the linear fit shown in Figure 54 is still a viable representation of the correlation with an R^2 value of 0.93.

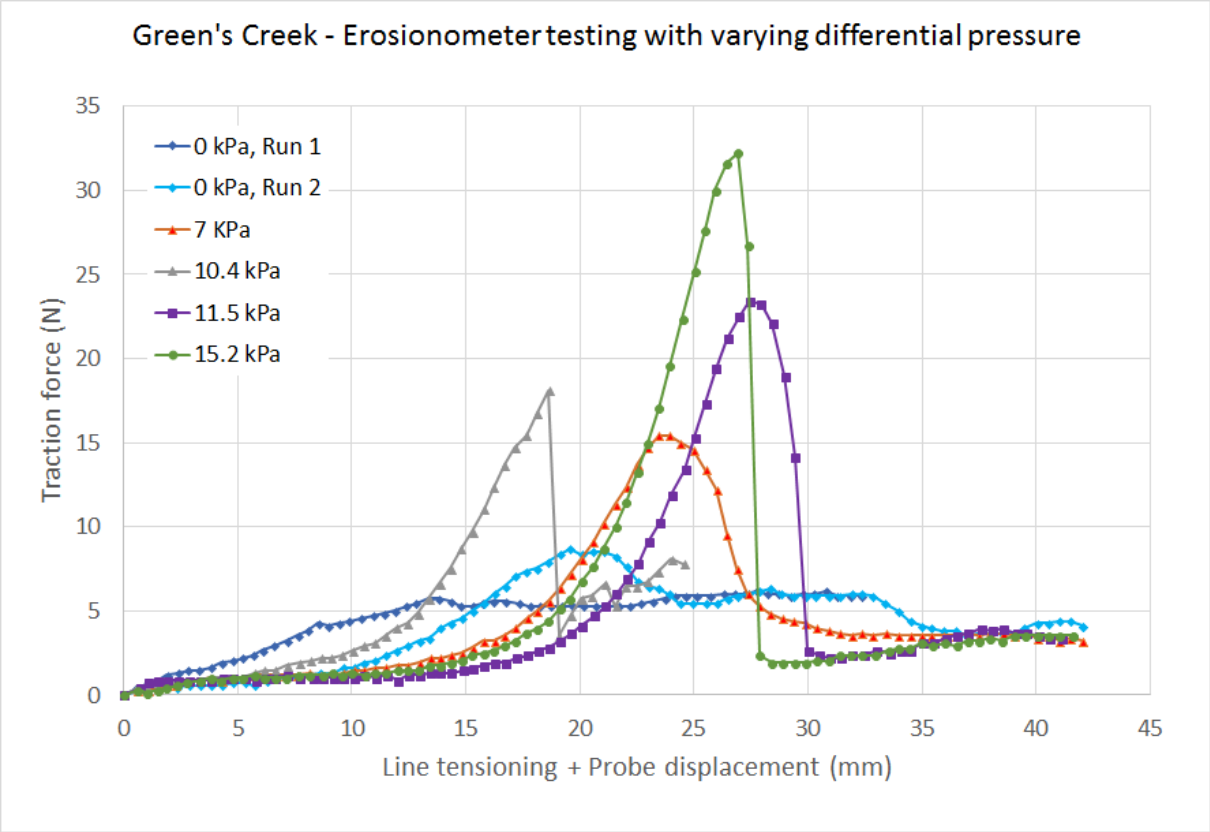

Figure 53. Erosionometer test results for Green's Creek soil under varying differential pressures

Table 4. Green's Creek, summary of Erosionometer testing with downward pressure gradient

Sample thickness (mm)	Differential head (mm)	Gradient (m/m)	Erosionometer Yield force, *EY* (N)	Computed critical shear stress, τ_c * (Pa)
43	0	0.00	6.18	2.87
43	0	0.00	8.69	4.30
43	700	16.28	15.45	8.16
43	1040	24.19	18.10	9.67
43	1150	26.74	23.40	12.69
43	1520	35.35	32.23	17.72

*: Determined from Erosionometer calibration (τ_c = 0.57 *EY* - 0.65)

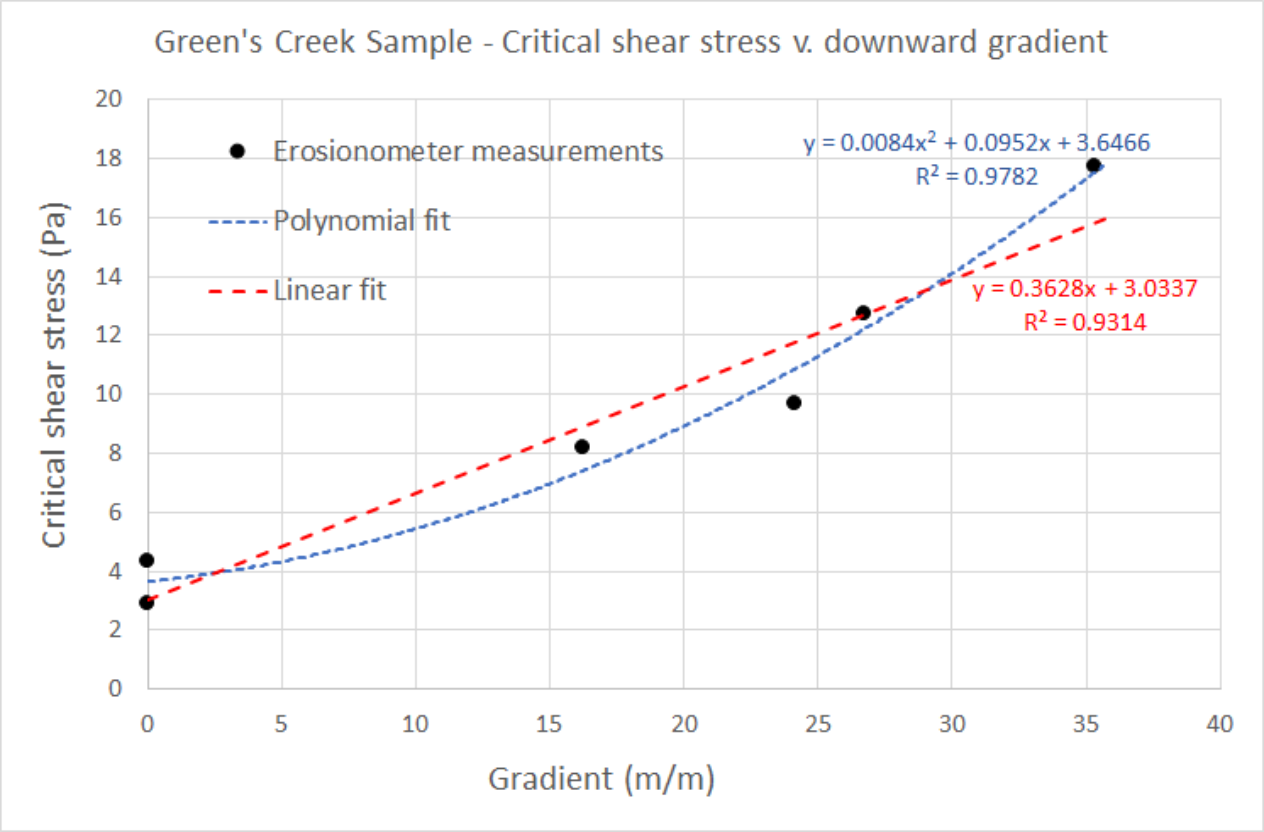

Figure 54. Critical shear stress versus downward gradient, Green's Creek

Similarly, five different tests were performed on Muddy Creek soil with a differential head of 0, 800, 1100, 1300, and 1540 mm applied across the sample, which corresponds to pressures of 0, 8, 11, 13, and 15.4 kPa respectively. The specimens were sliced about 43-mm thick, resulting in a corresponding gradient of 0, 18.6, 25.6, 30.2, and 35.8 m/m, respectively.

Results of the Erosionometer tests for Muddy Creek are shown graphically in Figure 55. Note that the test at zero and 15.4 kPa differential pressures were repeated to confirm the results as they showed gradual failure. The test results are summarized in Table 5.

The resulting relationship between the drainage gradient and the critical shear stress is shown in Figure 56. While a second order polynomial shows a slightly better fit to the experimental data, the linear fit shown in Figure 56 is still a viable representation of the correlation with an R^2 value of 0.97.

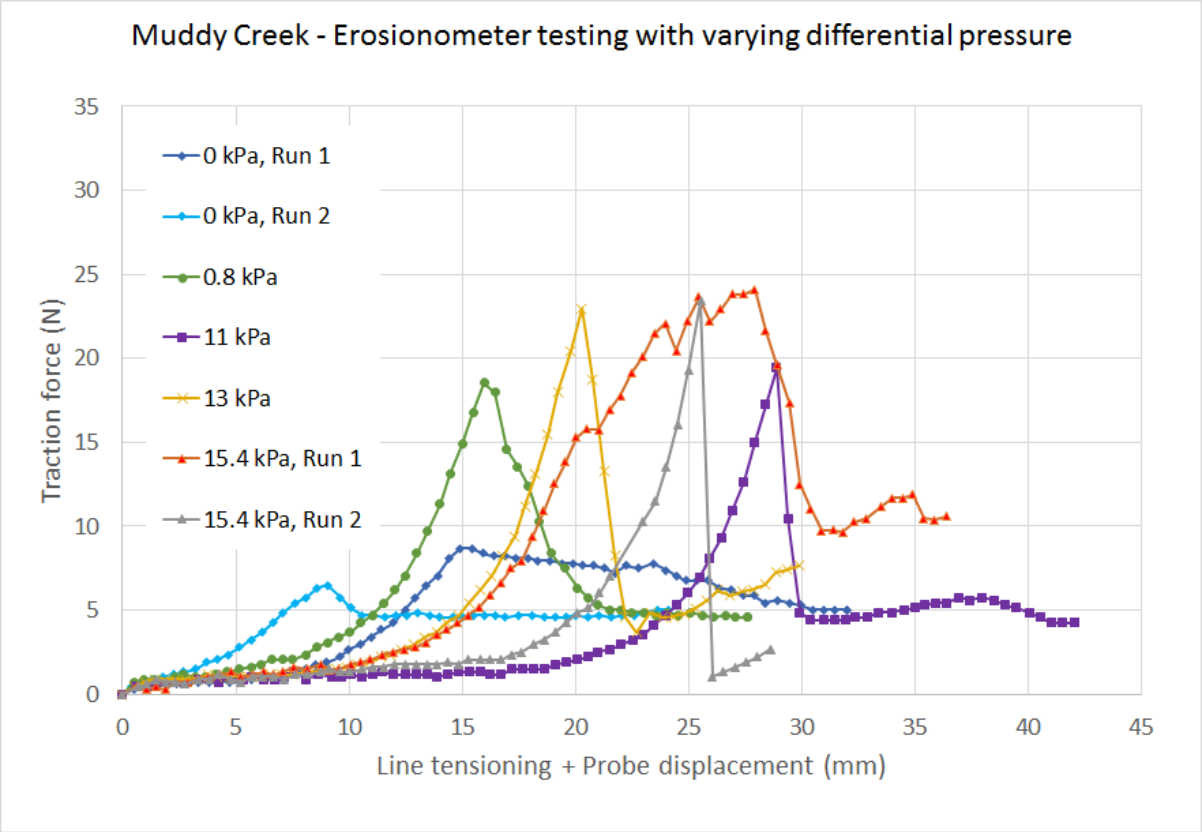

Figure 55. Erosionometer test results for Muddy Creek soil under varying differential pressures

Table 5. Muddy Creek, summary of Erosionometer testing with downward pressure gradient

Sample thickness (mm)	Differential head (mm)	Gradient (m/m)	Erosionometer Yield force, *EY* (N)	Computed critical shear stress, τ_c * (Pa)
43	0	0.00	8.69	4.30
43	0	0.00	6.48	3.04
43	800	18.60	18.54	9.92
43	1100	25.58	19.43	10.43
43	1300	30.23	22.96	12.44
43	1540	35.81	24.11	13.09
43	1540	35.81	23.41	12.69

*: Determined from Erosionometer calibration ($\tau_c = 0.57\ EY - 0.65$)

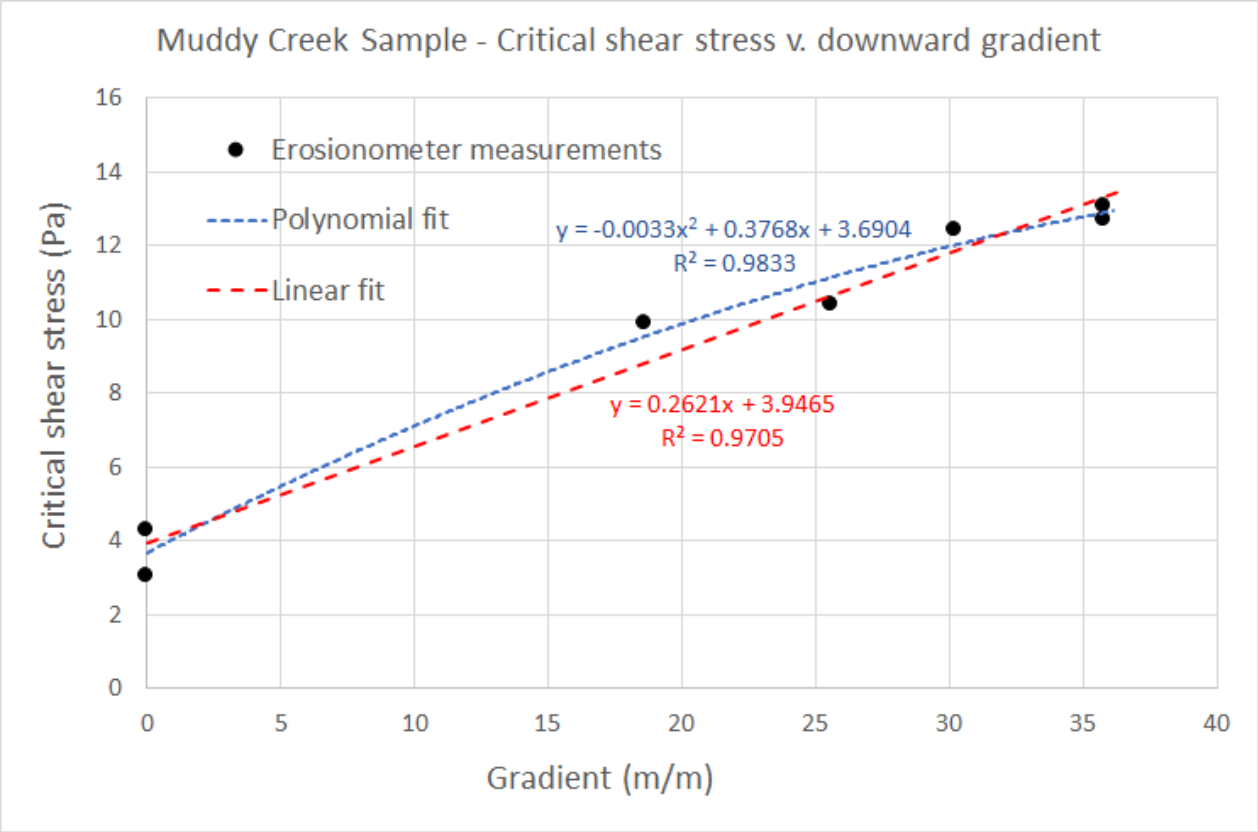

Figure 56. Critical shear stress versus downward gradient, Muddy Creek

Furthermore, the general critical shear of the soil can be expressed as a linear function of the saturated critical stress (at zero-gradient), and the gradient across the soil surface as:

$$\tau_c = \tau_{c0} + \Gamma \times i \qquad 28$$

Where τ_c is the general critical shear stress of the soil, τ_{c0} is the saturated critical shear stress at zero gradient, i is the hydraulic gradient, and Γ is an empirical factor calculated as the slope of the correlation between the measured critical shear stress and the applied gradient as shown in Figure 54 and Figure 56.

Furthermore, when the high gradient was eliminated to remove the soil sample following the Erosionometer test, the surface of the sample appeared fluidized, and in the case of the Leda clay (Champlain sea clay), the surface appears to be littered with clusters of the clay structures outside the footprint of the probe (Figure 57); this was not observed in the sample of this soil tested at zero pressure gradient. This suggests a reversed gradient due to residual pore pressures below the surface which exceed the receding surface pressure. These observations are in line with the findings of Simon and Collison (2001).

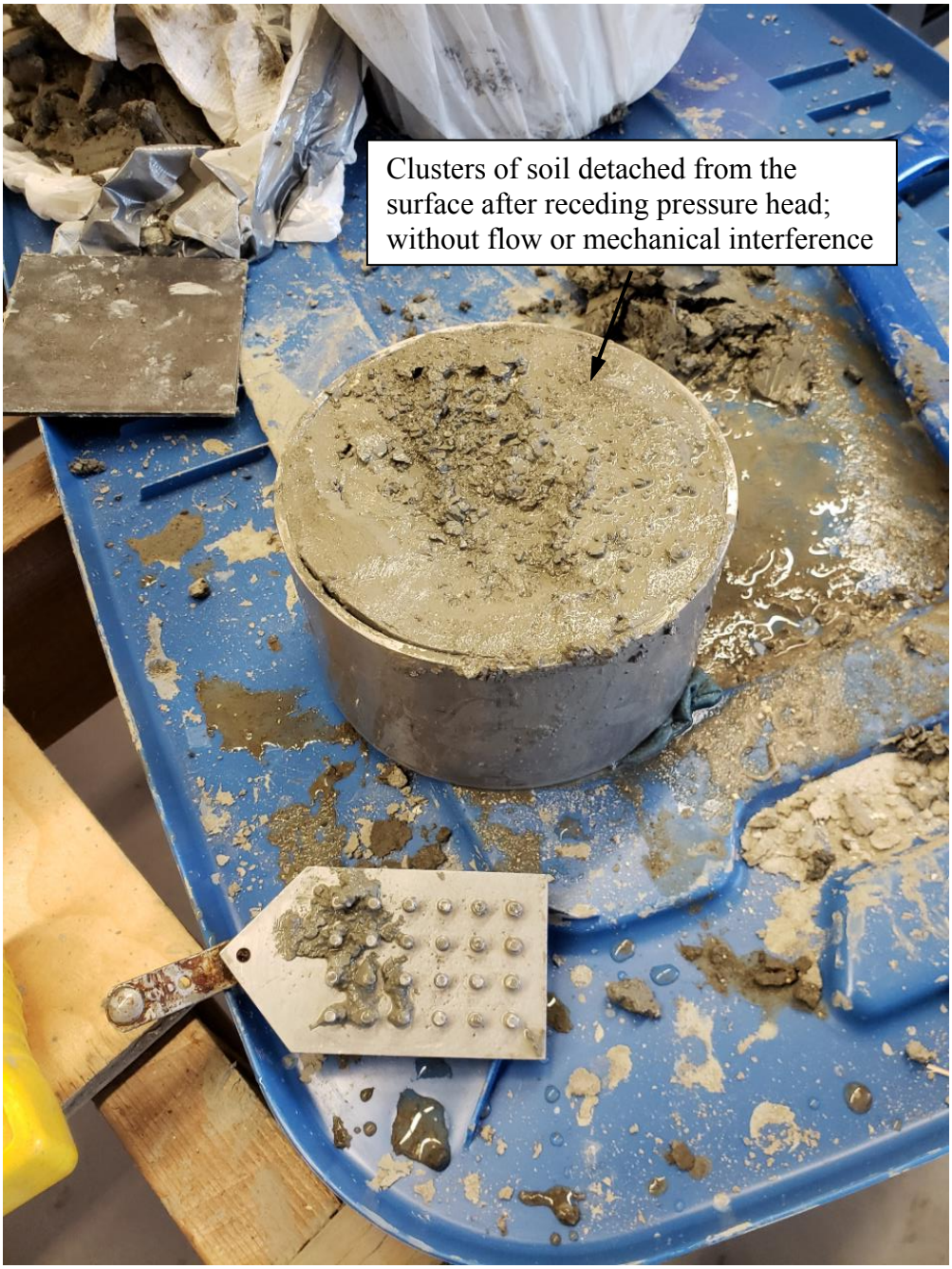

Figure 57. Detached clusters due to upward pressure gradient (arrow)

As stated earlier, the Erosionometer device was subsequently upgraded with a backpressure riser tube and probe insertion riser tube and the 10 core soils (refer to Appendix 3 for further information) were then tested at varying head differentials. As such, the core soils were tested while the backpressure head is near the soil surface and the underside of the sample remains submerged. Also, the time lag between the breach of the soil surface by the probe pins and running the test is reduced significantly. The remainder of the testing procedure is similar to the one used to test the supplemental soils earlier. The graphical results of the core soils tests are shown in Figure 58 through Figure 77. For each soil, the first figure shows the recorded Erosionometer traction force profiles; the next figure shows the computed

critical shear for each run plotted against the corresponding gradient as well as the linear and polynomial fit, as done for the supplemental soils. The results for the core soils are also summarised in Table 6.

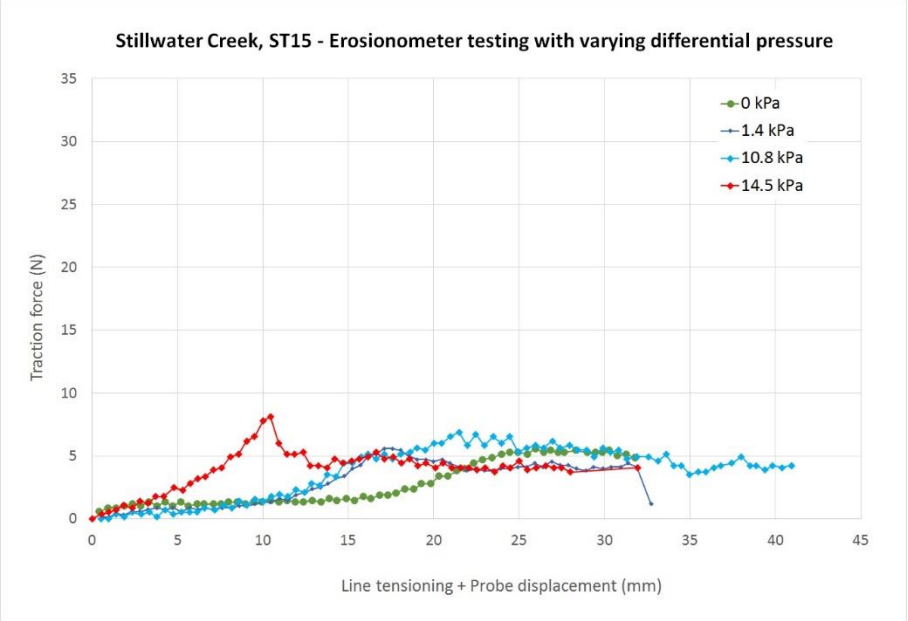

Figure 58. Erosionometer test results for ST15 soil under varying differential pressures

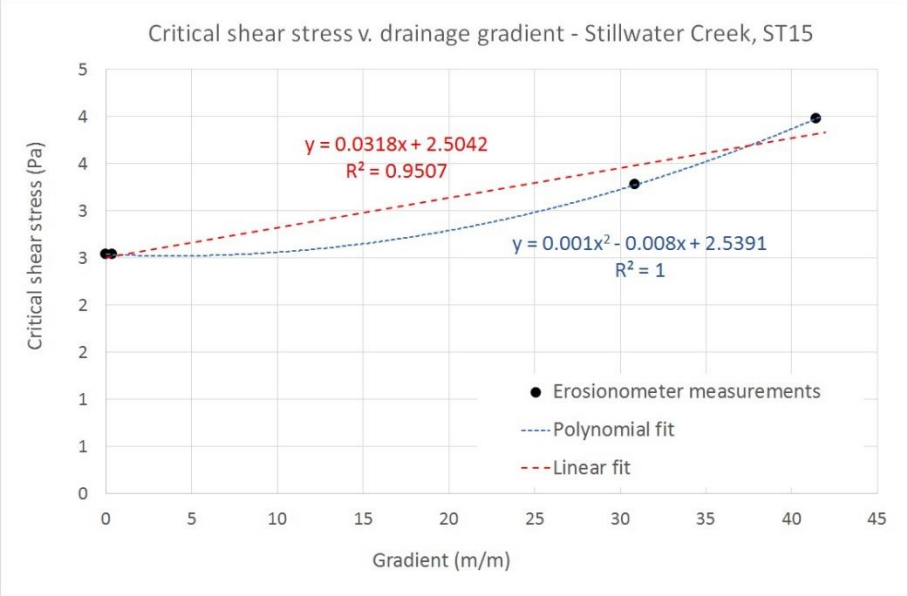

Figure 59. Critical shear stress versus downward gradient, ST15

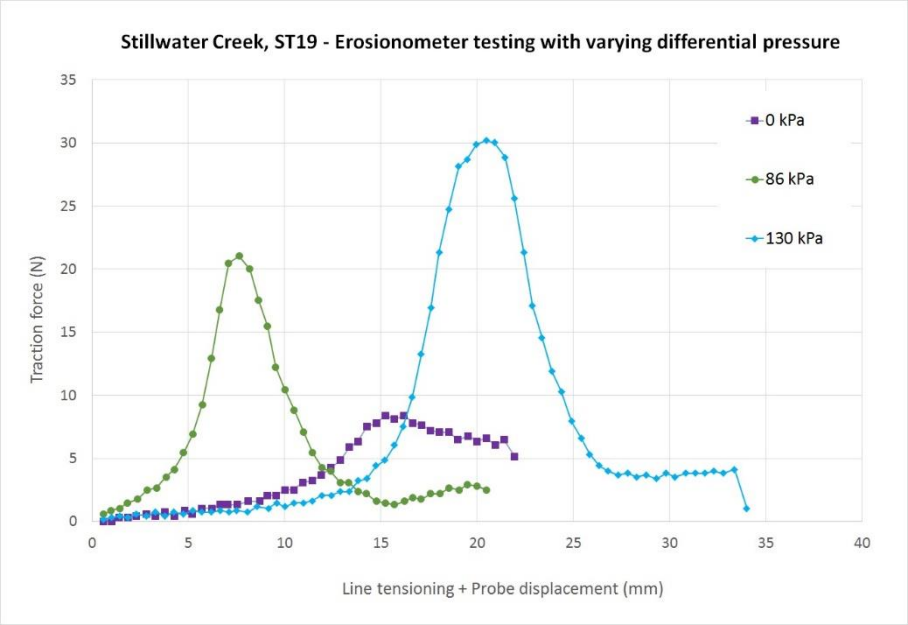

Figure 60. Erosionometer test results for ST19 soil under varying differential pressures

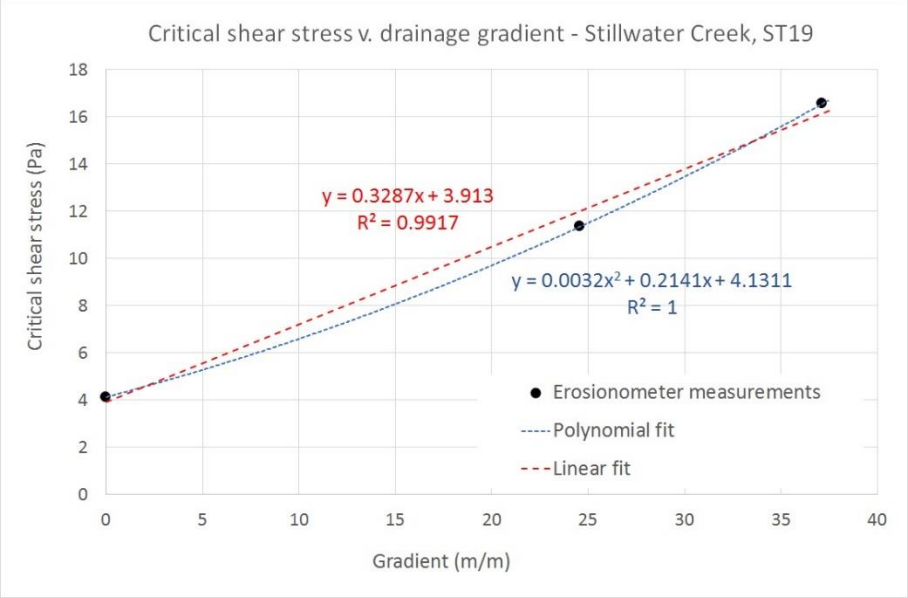

Figure 61. Critical shear stress versus downward gradient, ST19

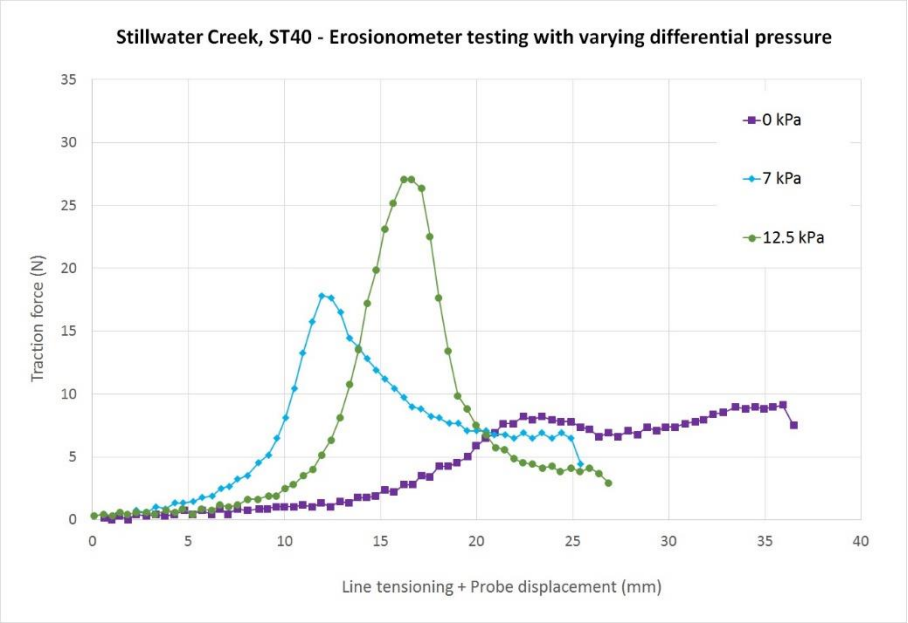

Figure 62. Erosionometer test results for ST40 soil under varying differential pressures

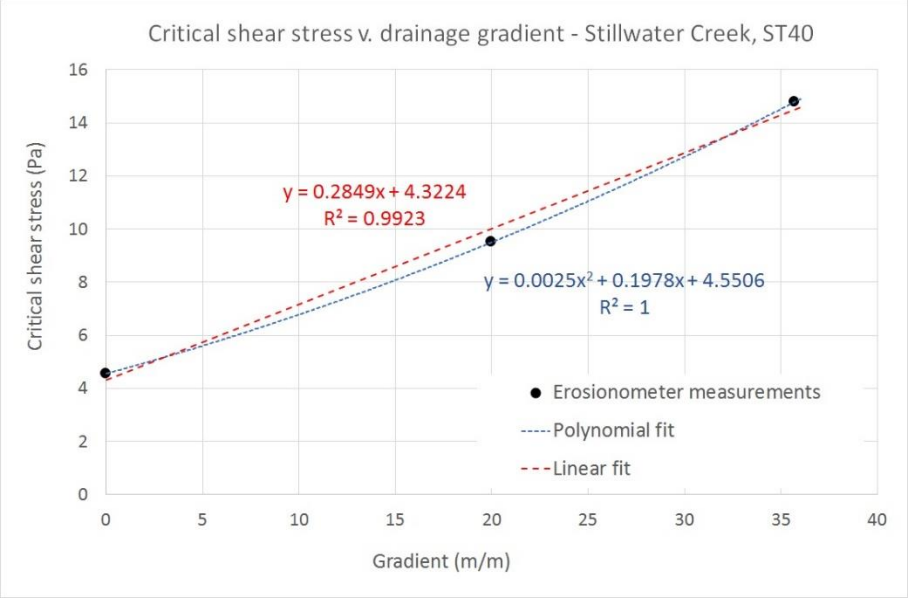

Figure 63. Critical shear stress versus downward gradient, ST40

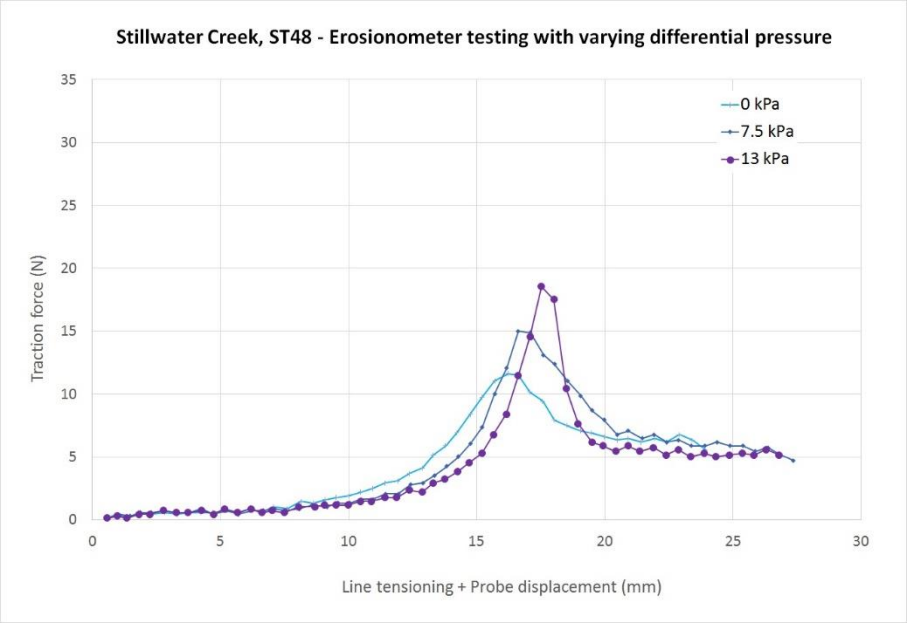

Figure 64. Erosionometer test results for ST48 soil under varying differential pressures

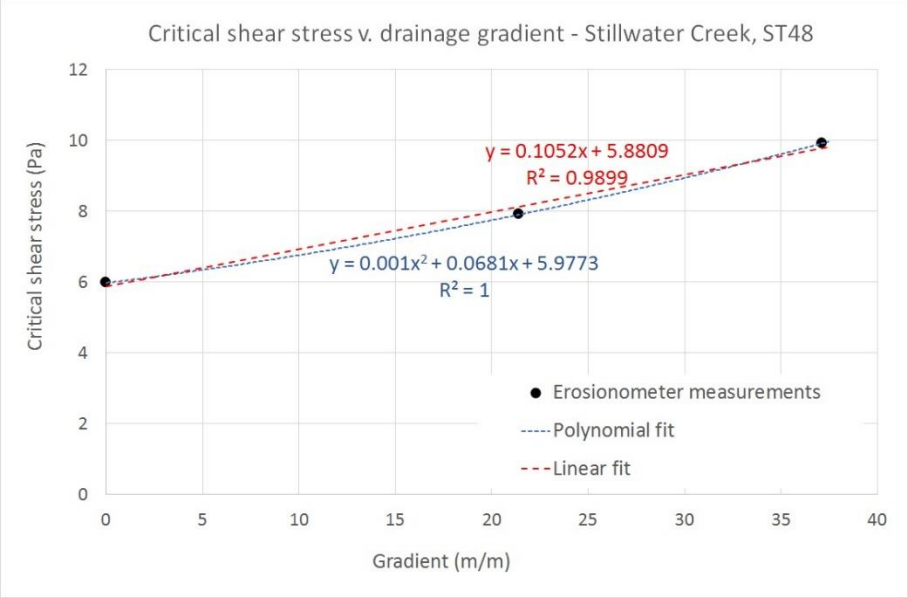

Figure 65. Critical shear stress versus downward gradient, ST48

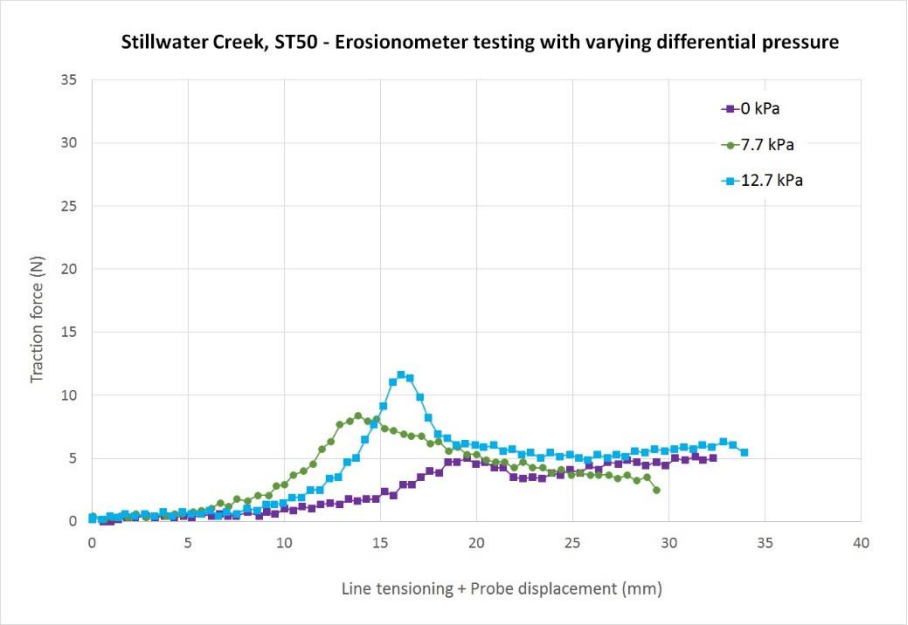

Figure 66. Erosionometer test results for ST50 soil under varying differential pressures

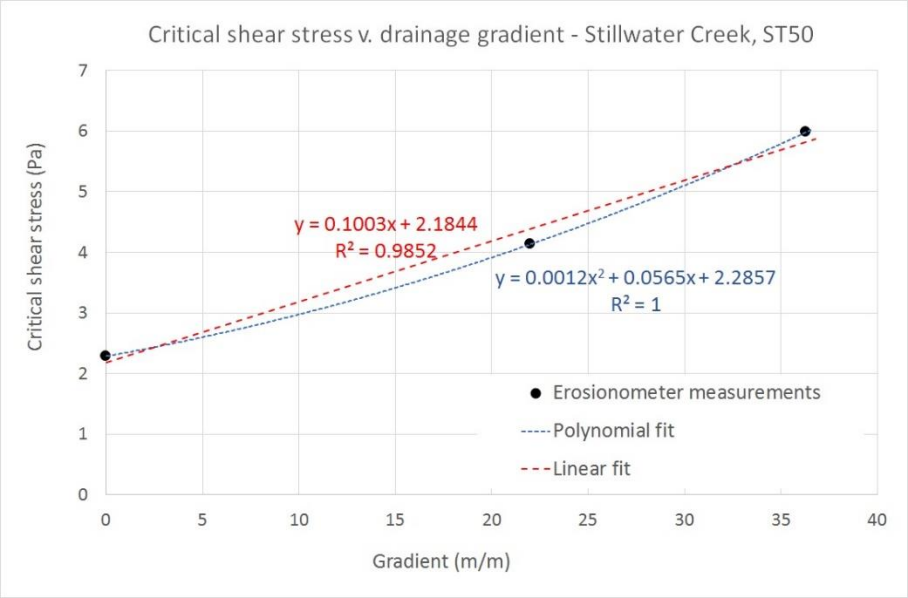

Figure 67. Critical shear stress versus downward gradient, ST50

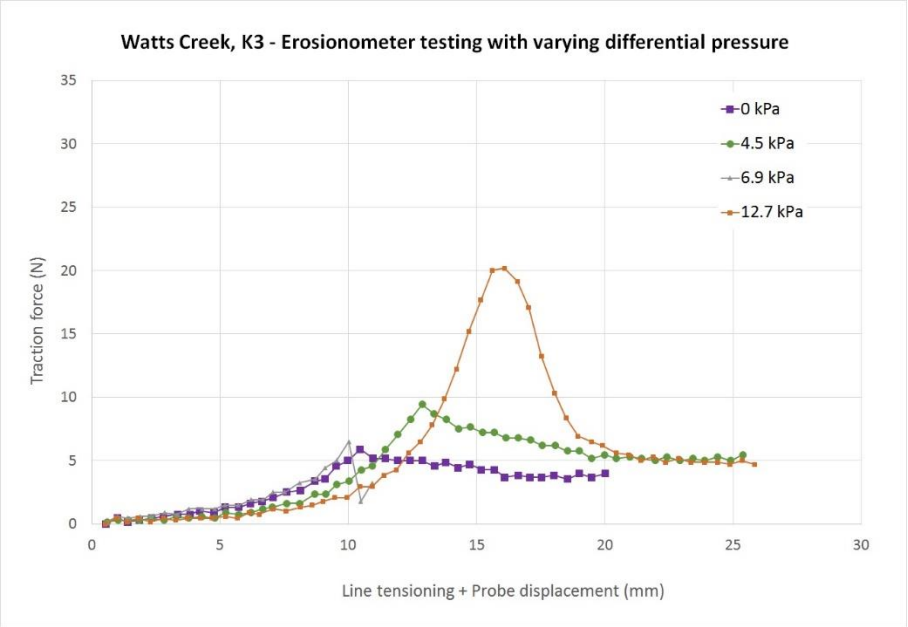

Figure 68. Erosionometer test results for K3 soil under varying differential pressures

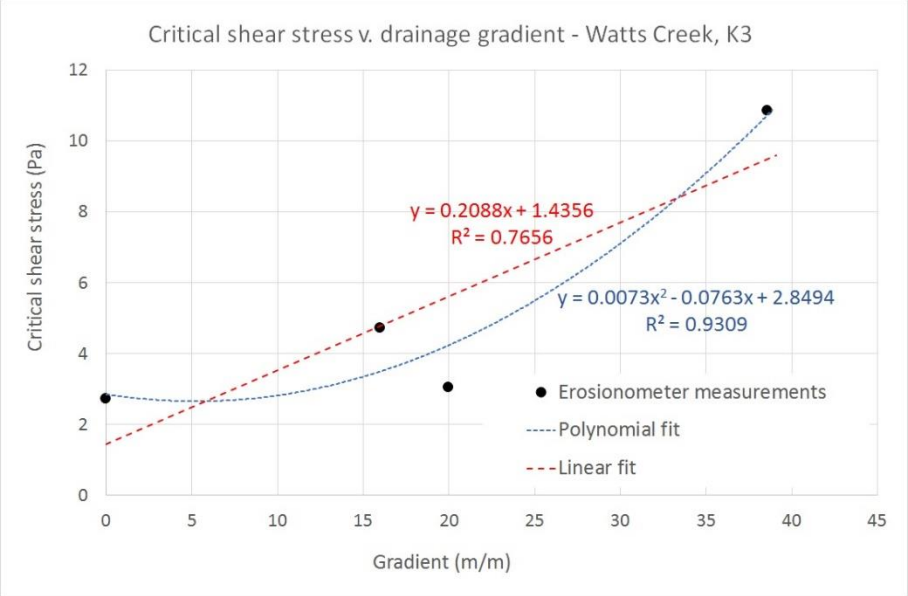

Figure 69. Critical shear stress versus downward gradient, K3

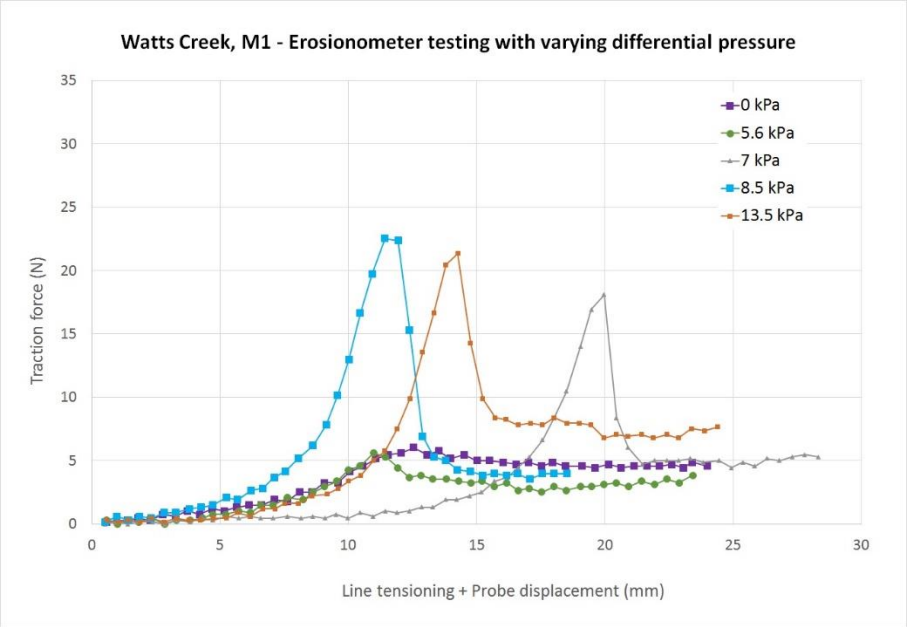

Figure 70. Erosionometer test results for M1 soil under varying differential pressures

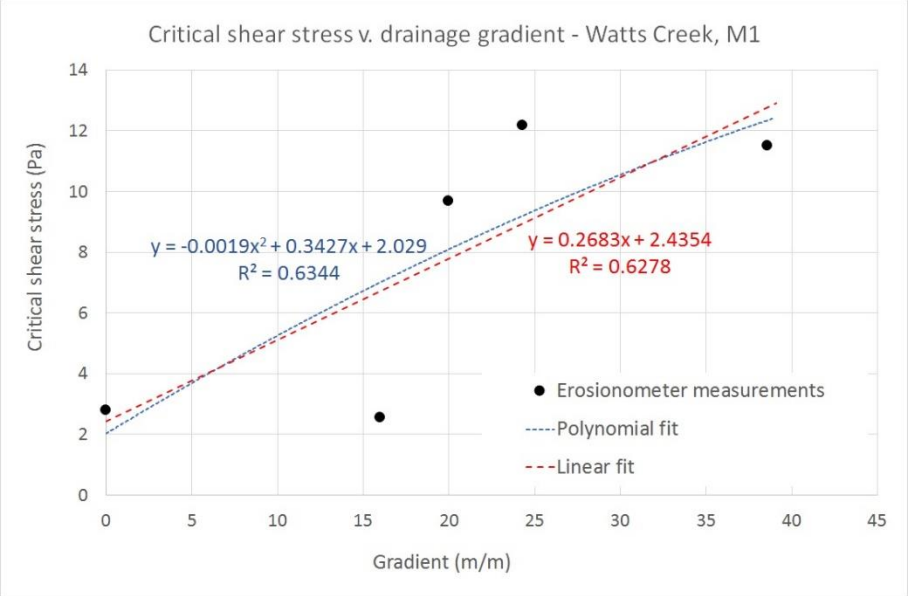

Figure 71. Critical shear stress versus downward gradient, M1

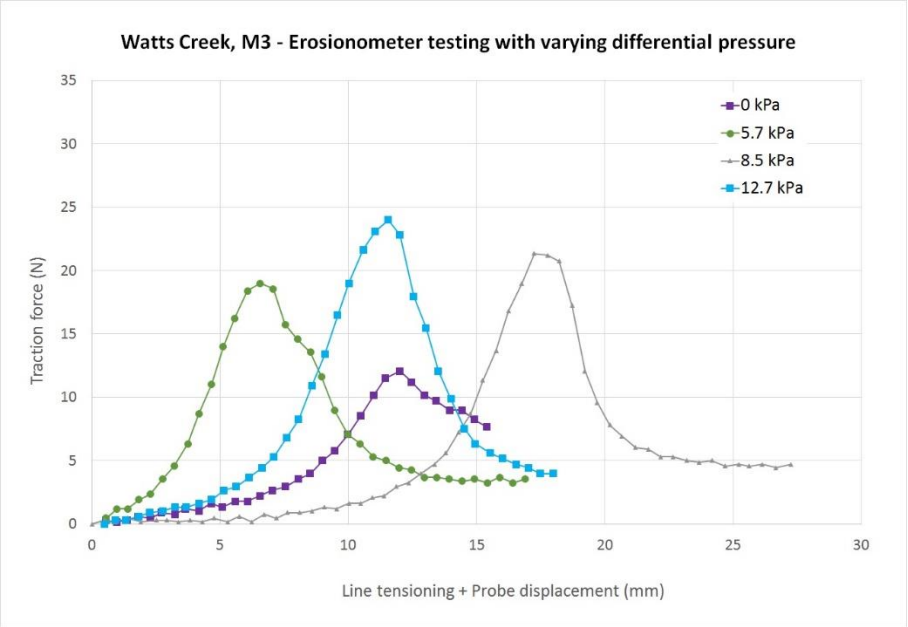

Figure 72. Erosionometer test results for M3 soil under varying differential pressures

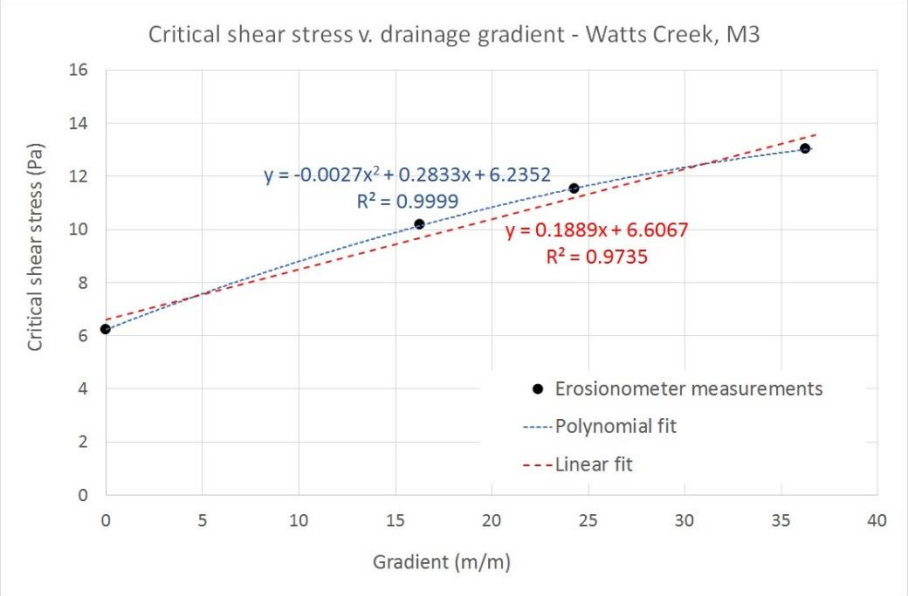

Figure 73. Critical shear stress versus downward gradient, M3

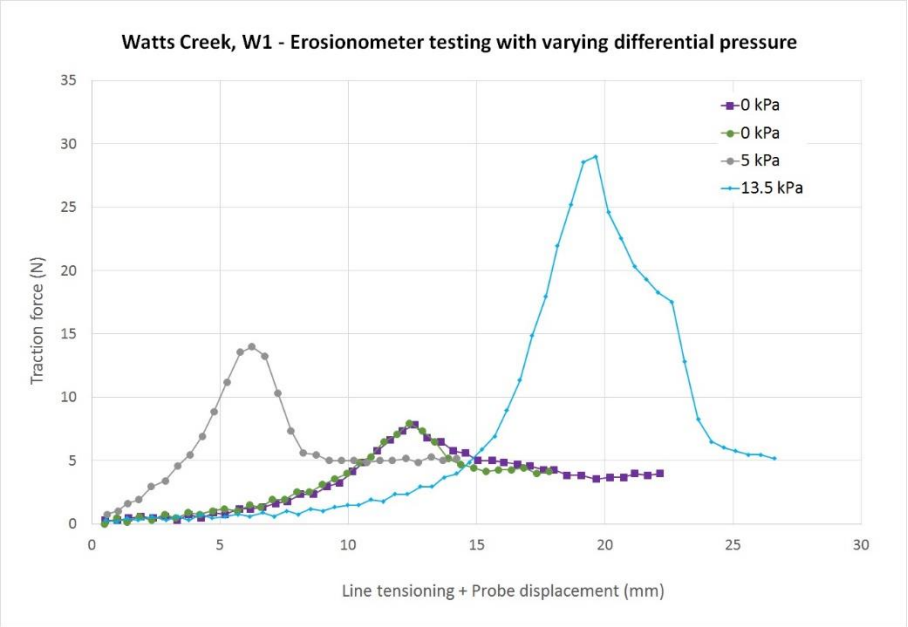

Figure 74. Erosionometer test results for W1 soil under varying differential pressures

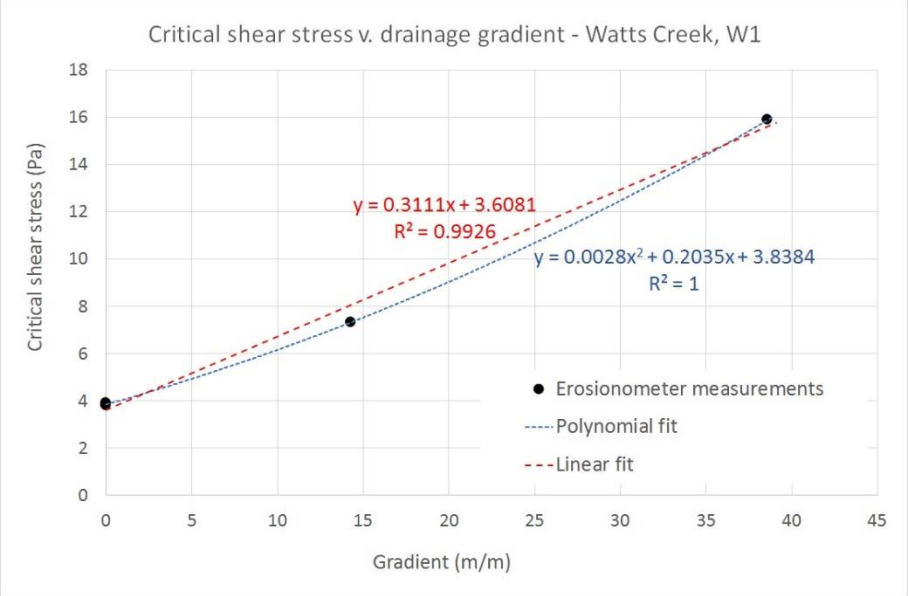

Figure 75. Critical shear stress versus downward gradient, W1

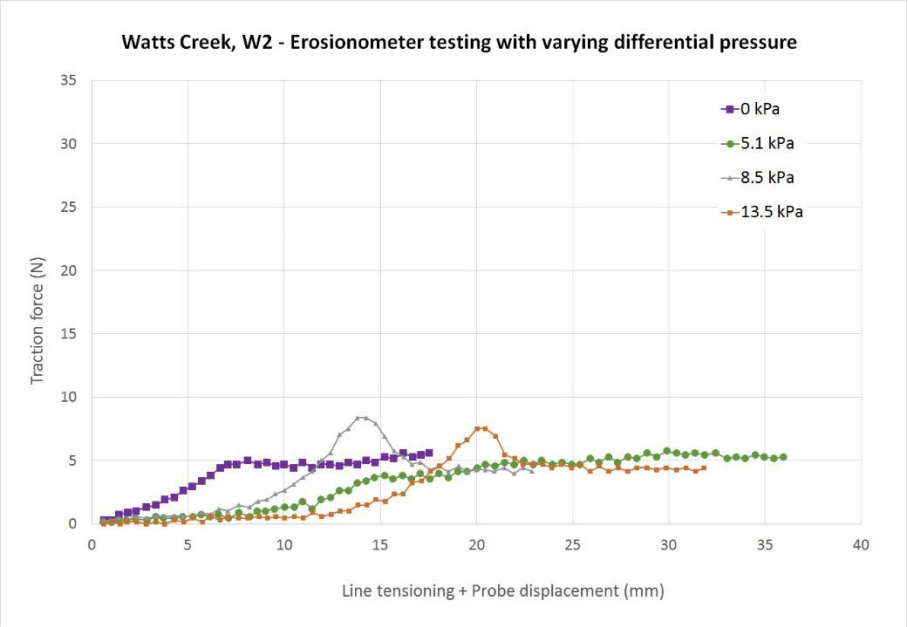

Figure 76. Erosionometer test results for W2 soil under varying differential pressures

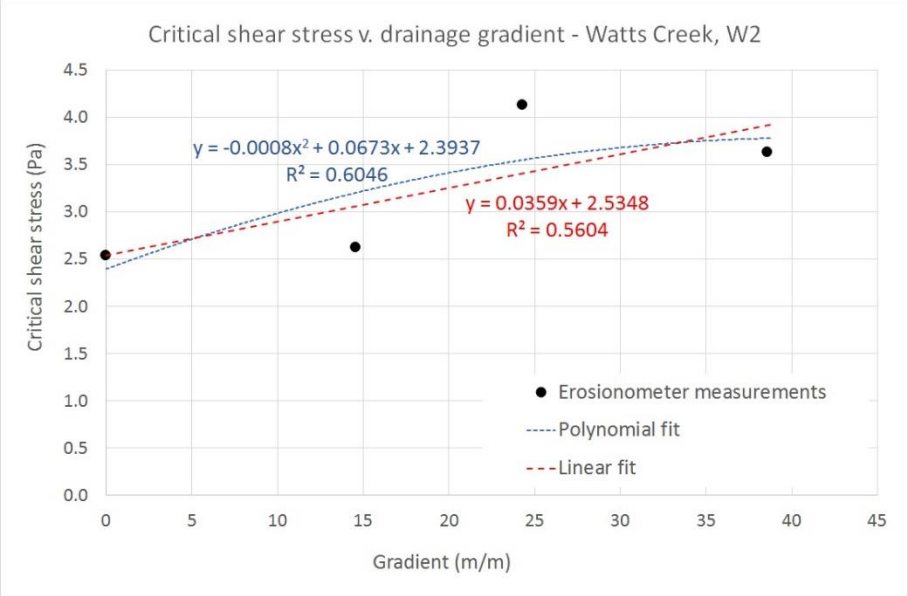

Figure 77. Critical shear stress versus downward gradient, W2

Table 6. Core soils - summary of Erosionometer testing with downward pressure gradient

Sample number	Sample thickness (mm)	Differential head (mm)	Gradient (m/m)	Erosionometer Yield force (N)
ST15	35	0	0.00	5.59
	35	14	0.40	5.59
	35	1080	30.86	6.89
	35	1450	41.43	8.12
ST19	35	0	0.00	8.39
	35	860	24.57	21.05
	35	1300	37.14	30.17
ST40	35	0	0.00	9.12
	35	700	20.00	17.81
	35	1250	35.71	27.08
ST48	35	0	0.00	11.63
	35	750	21.43	15.01
	35	1300	37.14	18.54
ST50	35	0	0.00	5.15
	35	770	22.00	8.39
	35	1270	36.29	11.63
K3	35	0	0.00	5.89
	35	560	16.00	9.42
	35	700	20.00	6.48
	35	1350	38.57	20.16
M1	35	0	0.00	6.03
	35	560	16.00	5.59
	35	700	20.00	18.10
	35	850	24.29	22.52
	35	1350	38.57	21.34
M3	35	0	0.00	12.07
	35	570	16.29	18.99
	35	850	24.29	21.34
	35	1270	36.29	23.99
W1	35	0	0.00	7.80
	35	0	0.00	7.95
	35	500	14.29	13.98
	35	1350	38.57	29.00
W3	35	0	0.00	5.59
	35	510	14.57	5.74
	35	850	24.29	8.39
	35	1350	38.57	7.51

*: Determined from Erosionometer calibration (τ_c = 0.57 EY - 0.65)

As shown in the test results, a linear relationship can be closely fitted for all core soils relating the critical shear stress to the applied hydraulic gradient, similar to the results obtained for the supplemental soils tested previously. It should be emphasized that, while the core soils were used earlier in the

Erosionometer calibration, the Erosionometer test at zero gradient was repeated for this part of the research as a different batch of samples was used for testing with hydraulic gradient. The linear relationships established for all soils are shown in Figure 78.

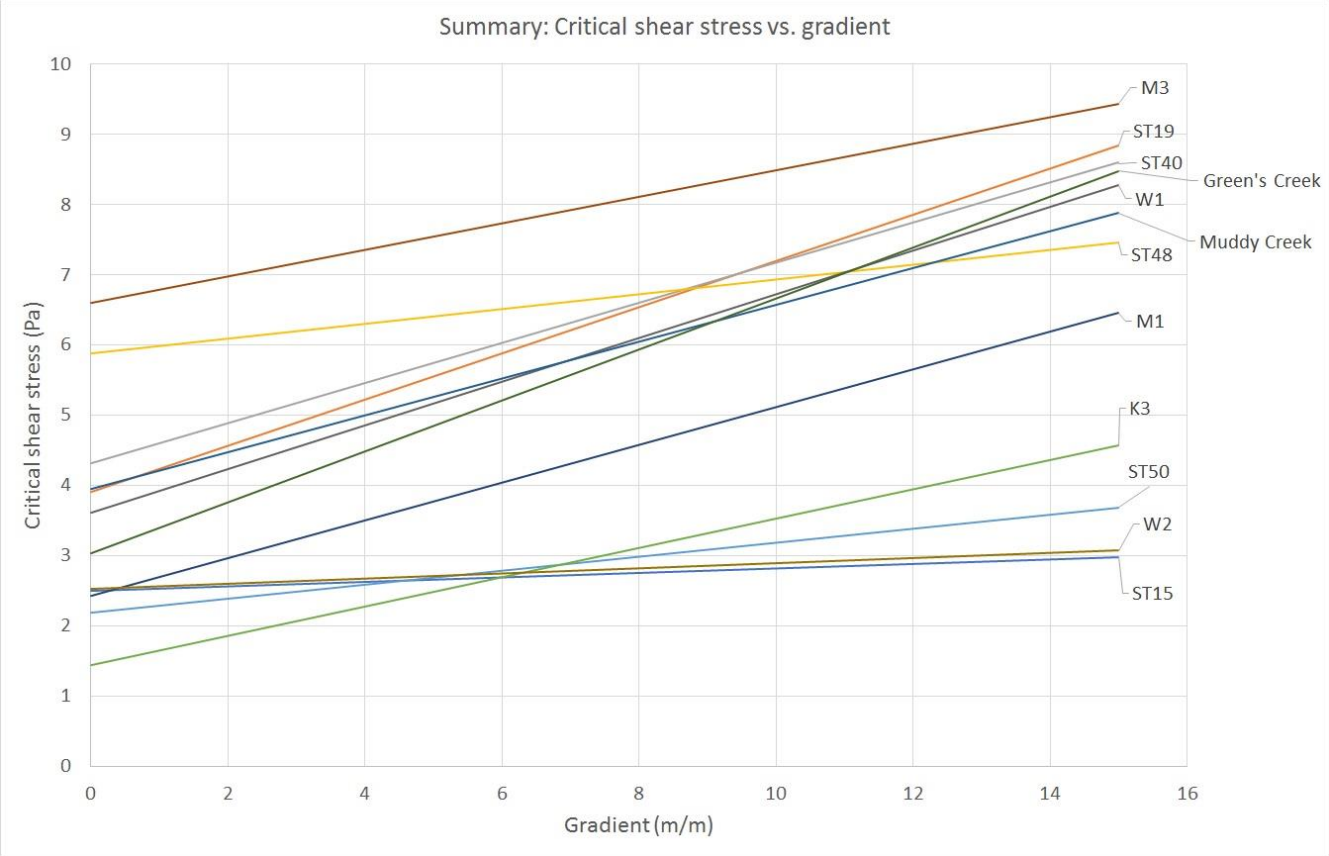

Figure 78. Critical shear versus gradient – Linear fit from all tests

The experimental results confirm the effect of hydraulic gradient on the critical shear stress of cohesive soils. These results are in line with the effects reported by other researchers (Simon and Collison, 2001; Nouwakpo et al., 2010; Nouwakpo and Huang, 2012).

5.2.7. **Practical applications**

The relationship determined by Erosionometer testing coupled with gradient distribution in the zone of interest as determined by field measurements or modern numerical analysis can provide a more realistic determination of soil erodibility in the presence of pressure gradients within the soil. This is especially important where flow level and/or groundwater fluctuations are dominant, or in banks with significant wave action such as navigation waterways and coastal regions. A good example of such cases is the Saint Lawrence riverbanks near Montreal which are subjected to both water level fluctuations and significant wave action due to shipping traffic. An annual loss of as much as 3 m of the structured clay riverbanks was documented (Gaskin et al., 2003), which could not be explained by simple flow shear erosion.

Another important use of the Erosionometer is for better understanding the effects of groundwater fluctuations on gulley erosion and hillside stability, which spans across engineering disciplines. Many other applications can benefit from Erosionometer testing including the effect of highly overconsolidated soils on surface erosion, the effect of freeze-thaw cycles, desiccation, and so on. One obvious application is the design of clay-lined artificial channels with a drained base. Using the Erosionometer, a combination of flow depth and liner thickness (controlled gradient) for a stable design can be established with minimal time and effort and an optimized stable channel can be built.

5.2.8. **Discussion**

A new device is presented, referred to as the Erosionometer, permitting fast and accurate determination of critical shear stress in cohesive and semi-cohesive soils. The device was rigorously calibrated and verified to produce a realistic measure of the critical shear of cohesive soils. The Erosionometer is also portable and easy to deploy in the field for obtaining a large number of data values across a reach of a water course, which helps addressing the variability of soil conditions over short distances, typical of cohesive soil basins.

Furthermore, the Erosionometer showed an additional advantage when it comes to soils with underlying weaknesses below the surface, including sensitive soils. The probe emulates the shear effect at a short distance below the surface, thus exposing potential cluster entrainment under flow intensities that would not normally erode the soil surface at particle level. This would overcome a serious disadvantage of the Jet test which may destabilize such underlying weaknesses during early stages of the test as discussed earlier.

Following is a discussion of the improvements introduced by the new device in contrast with the drawbacks of the leading method currently in use (the Jet tester).

While the Jet tester can be an excellent tool for assessing the erodibility, it suffers from several disadvantages when it comes to determining the critical shear stress:

- As stated earlier the Jet test consists of collecting data points of wall shear versus eroded thickness as it impinges deeper into the soil, assuming the soil characteristics do not change throughout the scour depth. The critical shear is then estimated by fitting a hyperbolic trend to the data with the asymptotic value representing the critical shear or projected equilibrium condition. There is an inherent uncertainty in the Jet test erosion rate data, which could deviate by as much as 100% from the rate determined in the flume (Al-Madhhachi et al., 2013; Al-Madhhachi et al., 2014; Hanson and Cook, 2004). While such uncertainty in measured data is within the traditionally accepted margin in morphodynamics, extrapolating the data trend may not produce a reliable outcome. In contrast, The Erosionometer measures the critical shear directly, and within the top 5 mm of the surface. Furthermore, repeating the test at different depth intervals after carefully scraping the surface can produce a profile of the critical shear with depth as opposed to the Jet

test which produces a single value for the entire scour thickness assuming similar soil characteristics throughout.

- Many clays and silty clays are sensitive to shear and manipulation. This implies that the physical characteristics, including strength and erodibility, will change when the soil is subjected to some level of antecedent shear. Since the Jet test, by its nature, starts with a high shear that gradually reduces towards the equilibrium value as the scour hole deepens, it mimics the reverse process of natural erosion, which may not be suitable for sensitive soils. In contrast, the Erosionometer probe shears the soil along the tips of the pins with minimal prior disturbance.
- The tractive shear force developed from the impinging jet theory is based on a circular jet impinging on a horizontal flat surface. It is therefore implied that the impingement test should be limited to a wide and shallow scour hole to minimize the confinement effect; however, impingement scour holes as deep as 8 cm have been reported (Al-Madhhachi et al., 2014). Assuming the effect of gradually increasing confinement on the erosion rate is not excessive, extrapolating the data trend to simulate an even deeper scour condition may not represent the characteristics of the surface soil.
- Despite its versatility, the Jet test is still somewhat time consuming to perform and interpret in the field.

Additionally, a modification to the submersion chamber allowed the application of different pressures on each side of the soil sample. Using the modified chamber, the effect of subsurface hydrology on soil erosion was investigated and a linear relationship was established between the applied downward gradient and the critical shear of the soil. This is similar to test results reported by Nouwakpo et al. (2010) using a large-scale hillside model (see Section 4.3.1).

5.2.1. Limitations of the Erosionometer

There are some limitations associated with the current version of the Erosionometer in terms of the types of soils that can be tested adequately. Based on the size and details of the probe, it is obvious that soils with structures or erodible clusters larger than 1 cm in dimensions would not test properly as the clusters would not flow through the pins of the probe. While a larger probe with double the dimensions and the pin spacing of the existing one is already prepared, it was not tested for the current research.

Furthermore, non-cohesive soils were also not tested for this work

5.3 Erosion rate determination

In previous sections the development of the Erosionometer was introduced as a fast and effective way to determine the threshold of erodibility of cohesive soils. The follow up objective of this research is to develop an alternative method to determine the rate of erosion of cohesive soils at varying levels of shear

stress applied to the soil surface by the fluid (water in this case). A new apparatus, termed the Erosion Rate Meter (ERM), was developed by the author in collaboration with Dr. Colin Rennie of the University of Ottawa, as part of this Ph.D. Research. In addition to meeting its research objective, the ERM helped shed some light on current misconceptions in many aspects of cohesive soil erosion, as will be presented herein.

5.3.1. **Introduction**

The relation between fluid shear stress and soil erosion has been subject to exhaustive research, yet when it comes to cohesive soils, such as clays and clay-silt-sand mixtures, research is still in its infancy. Furthermore, the concept of bed shear stress does not seem to be interpreted consistently between various researchers. It is therefore important to address the concept of bed shear before embarking on erosion rate determination.

Due to the complexity and the heterogeneous nature of cohesive soils, the theories using force and moment balance to explain and predict the mechanical processes of detachment do not produce any reliable outcome, as will be addressed in this research work. As such, the bulk of current research on this subject relies heavily on innovative devices that can simulate natural erosion by flowing water, some of which will be discussed herein, as a new testing device will be introduced for assessing both bed shear and erosion rate simultaneously.

5.3.2. **The concept of bed shear**

Most natural flows, and flows in engineering practice, have physically rough boundaries, in which case there is a downstream component of pressure force on the boundary in addition to a downstream component of viscous force.

In fully developed open-channel flows, bed shear can easily be determined using Newton's second law for the balance of forces (free body of fluid on an inclined plane), equating the downslope driving force, caused by the downslope component of the weight of the fluid in the free body, with the resistance force exerted by the planar boundary on the lower surface of the free body. This results in the relationship stated in Equation 19 ($\tau = \rho.g.R_h.S$), between flow and bed shear.

Another way of determining bed shear is by using a form of the law of the wall or log-law for the vertical profile of streamwise velocity in a turbulent shear flow (Yalin, 1992):

$$\frac{U}{u^*} = \frac{1}{\kappa} \ln\left(\frac{z}{k_s}\right) + B_s \;\; ; \;\; \tau_b = \rho u^{*2}$$

29

Where U is the time-averaged velocity, u^* is the shear velocity, κ is the von Karman's constant (=0.41), z is the height above the bed surface where the velocity is measured, k_s is the effective roughness height, B_s is a function of the roughness Reynolds number (= 8.5 for rough flow), and ρ is the fluid density.

The log-law represents a semi-logarithmic relation between time-averaged streamwise velocity and the height above the bed, with one of the parameters, the shear velocity, being a function of bed shear. Therefore, by establishing the logarithmic correlation, the bed shear can be calculated.

That said, the log-law does not necessarily apply throughout the flow depth; Afzalimehr and Rennie (2009) observed in gravel-bed river field measurements that the log-linear region of the profile extended from as little as 22% to as much as 68% of the flow depth above the bed. Only in pure fully developed laminar flows does the velocity follow a logarithmic profile throughout the flow depth. Southard (2006) explains that, in turbulent flows, which are by far the most common flows encountered in engineering problems, the velocity profiles are much more nearly uniform over most of the flow and show a much sharper change in velocity near the boundary, where by the no-slip condition the velocity must go to zero. It is easy to understand qualitatively why this is so: the exchange of turbulent eddies across the surfaces of mean shearing normal to the solid boundaries is much better at averaging velocity differences than is just the exchange of molecules over short distances in laminar flow. But then the velocity gradient near the boundary, where the normal-to-boundary motions of eddies are inhibited by the presence of the boundary itself, must be even sharper than in laminar flow. This is well explained in the illustration by Southard (2006) shown in Figure 79. This illustration shows a comparison of velocity profiles, in both pipes and channels, between laminar and turbulent flows arranged to have the same discharge.

There are several difficulties in using the log-law to determine the bed shear. It is inherently difficult to determine the depth to which the log-law applies in a specific flow. Taking velocity measurements at multiple depth intervals can help determine the velocity profile, and then u^* can be determined from the slope of the observed log-linear region, but this requires either substantial effort or the use of advanced instruments. Furthermore, in non-uniform flow the region of applicability of the log-law can be limited to a short distance above the bed.

While it is possible to establish the logarithmic relationship from a one-point measurement, choosing an arbitrary point outside the logarithmic zone can lead to a significant error in estimating the bed shear. Moreover, using a single point requires an accurate estimate of the effective roughness height (Equation 29), which is not easy to determine in fine-grained cohesive soils. Even if the size of the scars left by detached soil clusters is used as a roughness height, the frequency and distribution of such scars is random, and varies with time while a constant number is used for the effective roughness throughout the experiment. This will introduce an undetermined error in the effective roughness height estimate.

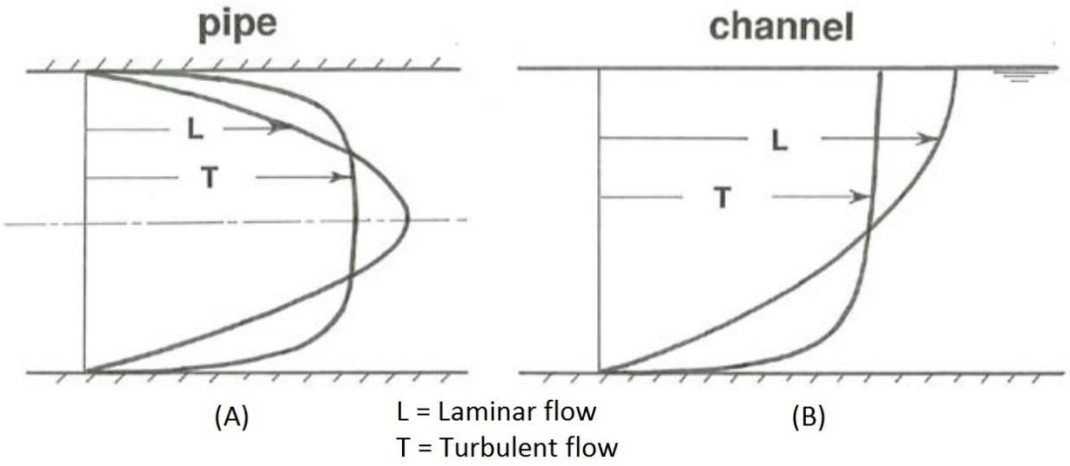

Figure 79. Comparison of laminar and turbulent velocity profiles in steady uniform flow in A) a circular pipe and B) an open-channel flow, Southard (2006)

While the physics of fluid-induced shear stress detailed above are fundamentally correct, they have been, in the Author's opinion, misused when it comes to assessing the shear stress on a soil sample. In open-channel flow, for example, it can be considered that the channel geometry and bed roughness are consistent through a sufficiently long reach to allow a "fully developed" flow to form. The hydraulic radius of the channel responds to the bed resistance and obtains a steady state level, and a consistent velocity profile is established. In other words, for the same flow rate, a higher roughness throughout applies a higher resistance force on the flowing water, thus causing a reduction in velocity and a resulting increase in the cross-section of the flow, hence a larger hydraulic radius. With everything else being the same, namely, flow rate, slope, channel geometry, and water density, a simple application of Newton's second law can be justified, resulting in the relationship stated in Equation 19 ($\tau = \rho.g.R_h.S$) between flow and bed shear. The problem arises when a flume or a fluid circuit of any kind is used to generate a flow over a relatively small soil sample (Briaud et al. 1999; Crowley et al. 2014; McNeil et al., 1996; Hanson and Cook 2004; etc.); while the fluid shear stress in the vessel can be computed from a fully developed flow over the conduit materials (metal, plastic, etc.), the assumption that the calculated shear stress or velocity profile extend to the interface with the soil sample is not necessarily true and Equation 19 in this case is not applicable. Newton's second law, which is at the base of Equation 19, requires that the fluid mass is moving at constant velocity for the balance of forces to apply; while the flow is in steady state over the conduit material, it is in deceleration mode over the rougher sample where Newton's second law no longer applies without introducing the force imbalance and deceleration. It is easy to visualize this effect intuitively as well: if the entire flume was made of the rougher sample material, the same flow rate in the flume would have resulted in a higher flow depth due to lower flow velocity, hence applying Equation 19 would have resulted in a higher bed shear.

It can be argued that measuring the velocity profile within the log-law region over the sample can be representative of the bed shear on the sample surface, which is a reasonable assumption; however, relying on a single-point velocity measurement can be misleading as the velocity at a distance from the bed is affected by the momentum of faster-moving water upstream. See Section 5.2.2 for more details.

That said, there are ways to determine more accurately the bed shear stress on the flume sample, as will be shown later in this research, and piston flumes with proper setup and calibration can still be some of the most reliable devices for assessing the erodibility of cohesive soils.

5.3.3. **Existing methods**

Flume testing is the most direct method for determining the rate of erosion of cohesive soils. As stated in Section 4.1.1., there are several flume setups that can be used to assess the rate of erosion of a soil sample or *in situ*, including: the National Institute of Water and Atmospheric Research (NIWA) benthic *in situ* flume (Aberle et al., 2003; Debnath et al., 2007), the Sea Carousel (Amos et al., 1992), piston flumes (Kamphuis and Hall, 1983), the EFA (Briaud et al., 1999), the SERF (Crowley et al., 2014), the SEDFLUME (McNeil et al., 1996), and many others. Many of these flumes use optical backscatter sensors to measure the erosion rate by comparing sediment measurements upstream and downstream of exposed soil; others rely on physical measurements and visual observations at soil surface level. With respect to shear measurement, many of the flume devices, some of which are explicitly listed herein, use some form of a shear measuring device. For example, the SERF Piston-type flume used by Crowley et al. (2014), includes a shear sensor placed upstream from the piston soil sample. Though no details are given for the shear sensor, it is a mechanical device and the reported shear is based on the hydraulics of the flow in the flume tube, independent of the soil sample characteristics, which was shown to be inadequate. Rankin and Hires (2000), and Barnes et al. (2007), introduced a metallic shear plate on flexible supports with force sensors to measure the shear induced by wave and swash action on a moveable sediment bed. Both plates were installed at the base of a laboratory wave tank. While the shear plates are an improvement to shear estimation from pure hydraulics, the plate surface should match the sediment bed in roughness and general resistance to the flow in order to produce realistic measurements of bed shear stress.

The most widely used portable test is the "submerged jet test". This type of test was historically used by many researchers to assess the erodibility of cohesive soils (Hollick, 1976; Hanson, 1991; Mazurek et al., 2001). Hanson and Cook (2004), introduced, in detail, an improved version of a portable submerged vertical impinging jet test apparatus, which is currently widely used to determine the critical shear and the erosion rate of cohesive soils both *in situ* and on extracted samples. The impinging jet version introduced by Hanson and Cook is described in detail in Section 4.1.4. Basically, the thickness of soil scoured under the impinging jet is determined at regular time intervals using a point gauge that temporarily blocks the jet flow during the measurement. The rate of erosion is determined based on the change in depth measurements of the scour hole. The corresponding shear is obtained by applying the jet impingement theory to determine the maximum tractive shear stress (parallel to the soil, also known as wall shear) on the soil surface as a decreasing function of the increasing distance between the jet and the soil, or indirectly, the depth of the scour hole. It is important to note that the bed shear imposed by the jet is computed from hydraulics laws, without consideration to the soil surface condition throughout the test (roughness, incline, etc.).

The Rotating cylinder test (RCT) is used for determining the rate of erosion as well as the critical shear of cohesive soil samples. Detailed information about this device is provided in Section 4.1.3. In brief, the way the RCT operates involves a cylindrical soil sample placed vertically between two horizontal platens in a larger concentric cylindrical tank. As the wall of the tank is rotated, the water spins around the sample which is held stationary by a torque-measuring device, thus measuring the soil drag on the surface of the sample. While the RCT does account for the actual shear imposed on the soil surface, it has some drawbacks, such as the difficulty in setting up the exposed sample between the platens, the difficulty in measuring the entrainment, and the sediments added to the spinning water in the tank during the test that change the experiment's conditions as it progresses.

5.3.4. **The development of the Erosion Rate Meter (ERM)**

As stated earlier, one important objective of this research is to develop an efficient method to measure the rate of erosion as it varies with applied fluid shear beyond the critical shear stress. Logically, a flume with robust means of measuring the shear at the water-soil interface, and the level of the bed surface at any moment in time, is the ideal setup for quantifying the erosion rate versus shear stress. Based on this premise, the Erosion Rate Meter (ERM) was developed.

The ERM device and its various elements are illustrated in Figure 80. It consists of a 100-mm diameter standing acrylic tube (head tube) sealed against a base plate. The base plate hosts a circular opening, 12.5 mm in diameter connected to a small acrylic tube of the same diameter, extending vertically down, and ending with a 90º elbow (nozzle). The discharge elbow is to be placed just over the surface of the soil to be tested where the discharged water would flow over the soil surface causing entrainment scour, similar to a miniature flume effect. A linear potentiometer is mounted on the side of the head tube and extended with a thin probe to reach the base level of the elbow, about 25 mm beyond the discharge point. The purpose of the potentiometer and probe is to measure and record the scour depth caused by the discharge. The tip of the probe is rounded and smoothed to minimize the damage to the soil surface, potentially altering its scour resistance. Also incorporated in the base plate of the head tube is a resistive piezometer to measure and record the height of water in the tube (head) at any time. All mounted instruments are connected to a CR1000 measurement and control datalogger, manufactured by Campbell Scientific Inc. (CSI), and can be read simultaneously.

The base plate is mounted on four acrylic "feet", for the lack of a better word, with tapered ends, extending about 100 mm below the discharge elbow. The feet are designed to be planted in the soil being tested, if the device is used *in situ*, and would be inserted sufficiently to align the discharge nozzle with the ground surface while maintaining vertical stability of the device.

Water is pumped into the head tube through a conduit mounted through the base plate. The conduit is also equipped with an outflow valve to regulate and stabilize the water level in the head tube to provide a continuous discharge through the nozzle under constant-head gradient.

The operating principle of the ERM is that there is a direct correlation between the gradient corresponding to a specific water head in the tube and the characteristics of the flow through the discharge nozzle in terms of velocity and flow rate. These characteristics can be easily measured and correlated to the water head; however, such calibration is not necessary for the operation and use of the device, in fact it could be misleading as will be explained later on. The initial intent was in fact to calibrate the water head to directly indicate the amount of shear induced at the interface with the soil surface, in an analogous manner to the calibration of the lab flume discussed in Section 5.2.2. As will be shown later, the intended calibration proved impractical while revealing an important characteristic of fluid-soil interaction. Subsequently, the ERM had to be upgraded with a capability to measure the induced shear at the soil surface directly and in real time during the test.

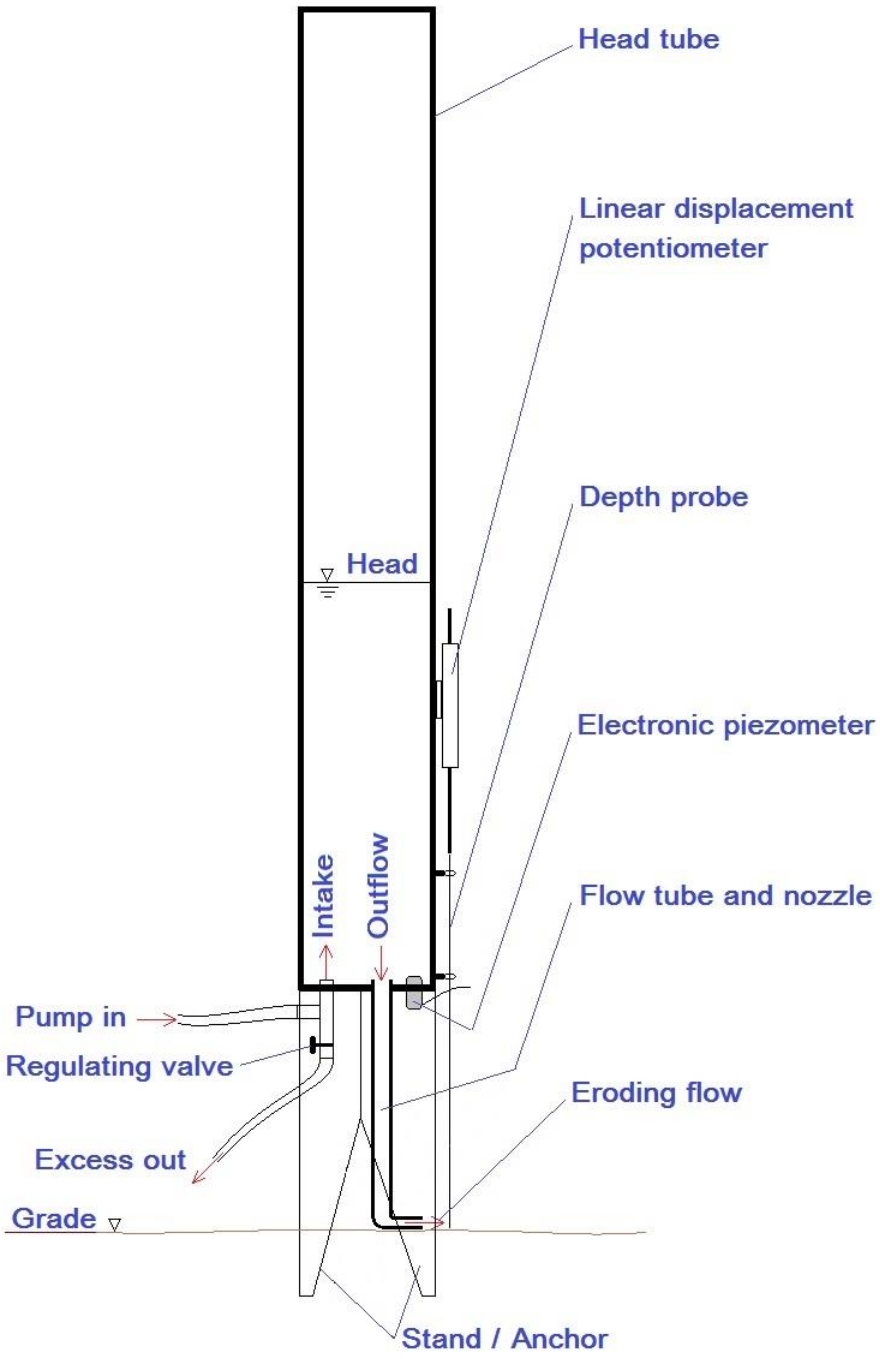

Figure 80. Illustration of the ERM device as used in the field (not to scale)

In order to provide the capability to directly measure the induced shear stress at the fluid-soil interface, special accessories are constructed as shown in Figure 81.

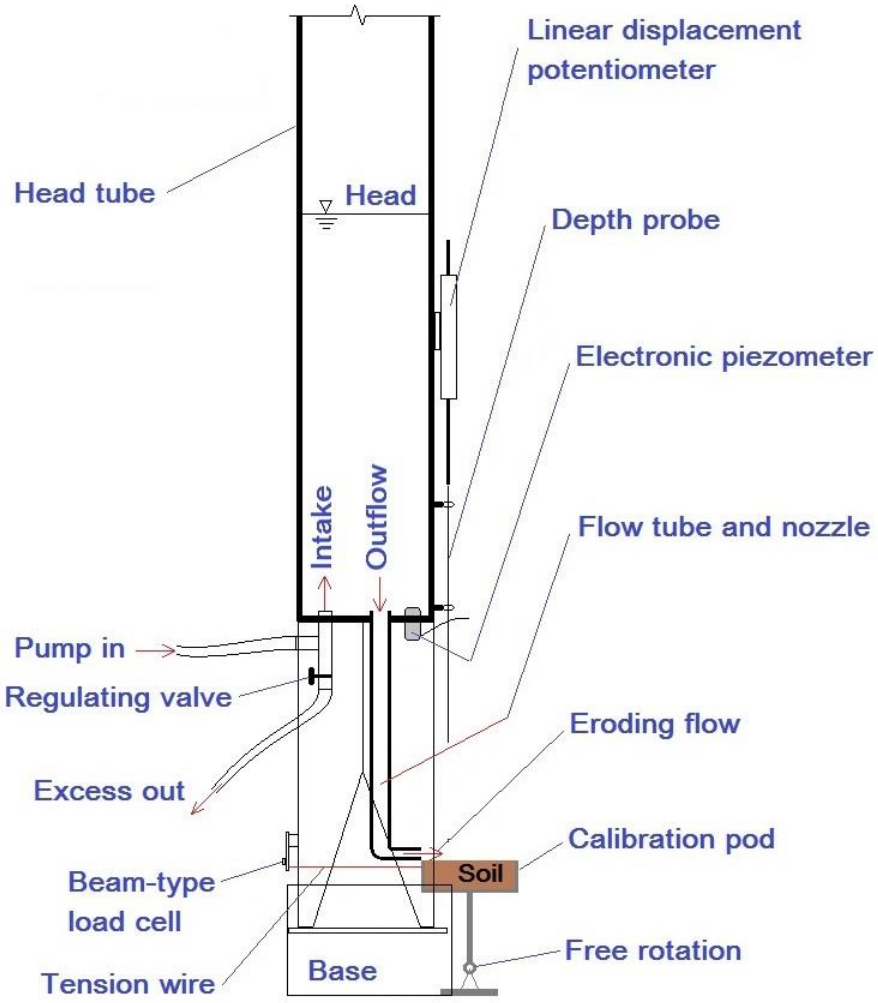

Figure 81. Illustration of the ERM device with calibration setup accessories (not to scale)

An acrylic pod of specific dimensions is built to accommodate a small soil sample. The pod is supported on a thin acrylic rod connected to a pivot support at the base to eliminate any resistance to a small movement of the pod in the direction of the flow. The pod is tied back to a miniature beam-type resistive load cell. With the pod's mechanical resistance to small motion eliminated, any net increase in the lateral pull load measured by the load cell is due entirely to the shear force transferred to the pod as the soil interacts with the flow from the nozzle. The walls of the pod parallel to the flow are tapered to a sharp edge to minimise their drag and hence their contribution to the measured force. With the known surface area of the impacted soil, the shear stress imposed on the soil can be calculated by dividing the measured force by the surface area of the soil sample. A photo showing the actual ERM is presented in Figure 82.

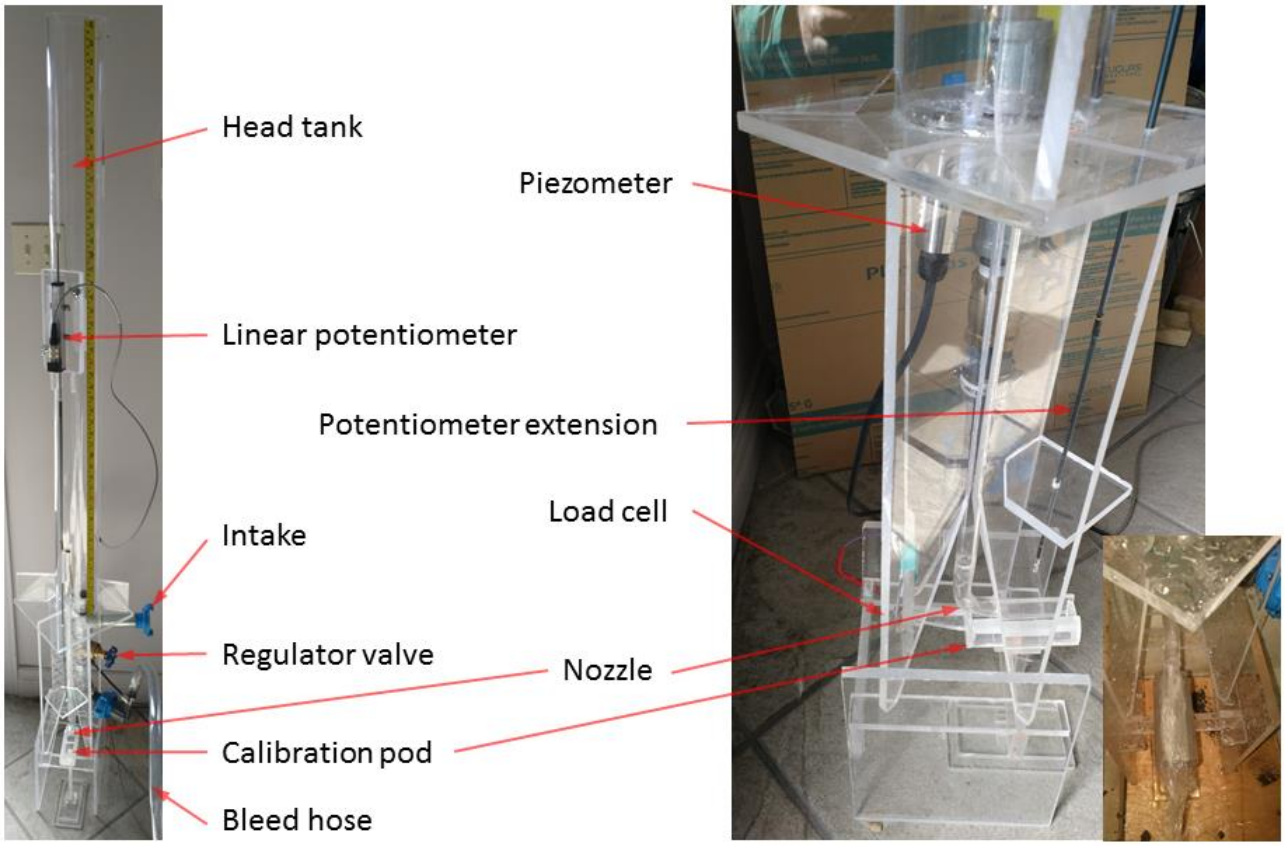

Figure 82. Erosion Rate Meter (ERM)

5.3.5. **Initial measurements**

The initial measurements were performed on soil samples in the test pod with the load cell connected. No measurement of the thickness of entrained soil was done at this stage (potentiometer disconnected). The purpose of these measurements was to establish a relationship between the water head in the tube and the shear stress at the surface of the soil samples. As the trial runs were performed on different soil samples and with the water head in the tube varied at different rates, it became obvious that the shear stress cannot be reduced to a simple function of the water head or the flow characteristics, especially when the induced shear exceeds the critical shear stress of the soil. In other words, the induced shear was found to be greatly affected by the change in soil surface characteristics due to entrainment. Figure 83 shows the results of tests performed on a silty clay sample from Orillia, Ontario. While the data can be collected at any desired frequency, a standard frequency of 10 samples per second is used to collect data for this research. Two sets of data were acquired from testing two identical samples. In both cases, the water head was increased from zero to about 1,100 mm and reduced back to zero while the force (stress) was recorded at 10 Hz. The difference between the two tests was the rate at which the water head was increased/decreased: the "slow" test is characterized by a dense collection of data points, while the

sparse data reflects the "fast" test. These tests, and several others on different clay samples revealed an important characteristic of soil fluid interaction for erosion testing. By examining the fast test data in Figure 83, it is obvious that the shear stress-head relationship is linear; in other words, the shear stress is proportional to the water head, both during the loading and unloading. The slow test data, however, shows a different trend: as time progressed, the proportionality coefficient between shear stress and water head increased, resulting in a polynomial relationship. This complex interaction continued through the unloading cycle as well in a way that could be described as displaying hysteresis, wherein shear stress for a given head increases due to increasing soil roughness as the test progresses. A tangent to the polynomial relationship at the early stages of the slow loading is parallel to the fast loading trend, proving that the change in behavior is time dependent. Photos of the sample surface at the start and end of each test are also shown in Figure 83.

It is clear from these data that the changes to the soil surface characteristics caused by the sustained flow resulted in an increase in the soil's resistance to the flow, thus increasing the shear stress against the soil surface. This effect is more pronounced at higher shear levels.

Following the initial tests, it was obvious that a straight calibration of the device at relatively high shear stresses is not practical and could be misleading; therefore, testing on extracted soil samples placed in the pod would be more accurate and controlled. It was also observed in the initial test data that the shear stress induced by flows at lower water head (between 0 and 30 mm) is irregular and increases quickly with the water head due to a vortex forming at the intake of the flow tube (partial flow) causing intermittent bursts at the nozzle. In order to achieve lower shear stress at full pipe flow, the opening of the pipe was constricted by suspending a string of metallic obstructions extending from the intake to shortly above the nozzle. Results of a slow test on the same Orillia clay with restricted flow is shown in Figure 84. Note that with reduced and less eroding flow, the shear stress remains more or less proportional to the water head throughout the reduced stress range, even during the slow test. It should be noted that with the added restrictions, the flow remains irregular at low water head, although the threshold of proportional correlated flow is reduced from a 30 mm head to a 20 mm head, approximately, and the lowest correlated shear for this specific soil was reduced from 30 Pa to 20 Pa. The correspondence between the threshold values of head in mm and minimum correlated shear in Pa in this case is thought to be coincidental and should not be taken as an empirical correlation at this point.

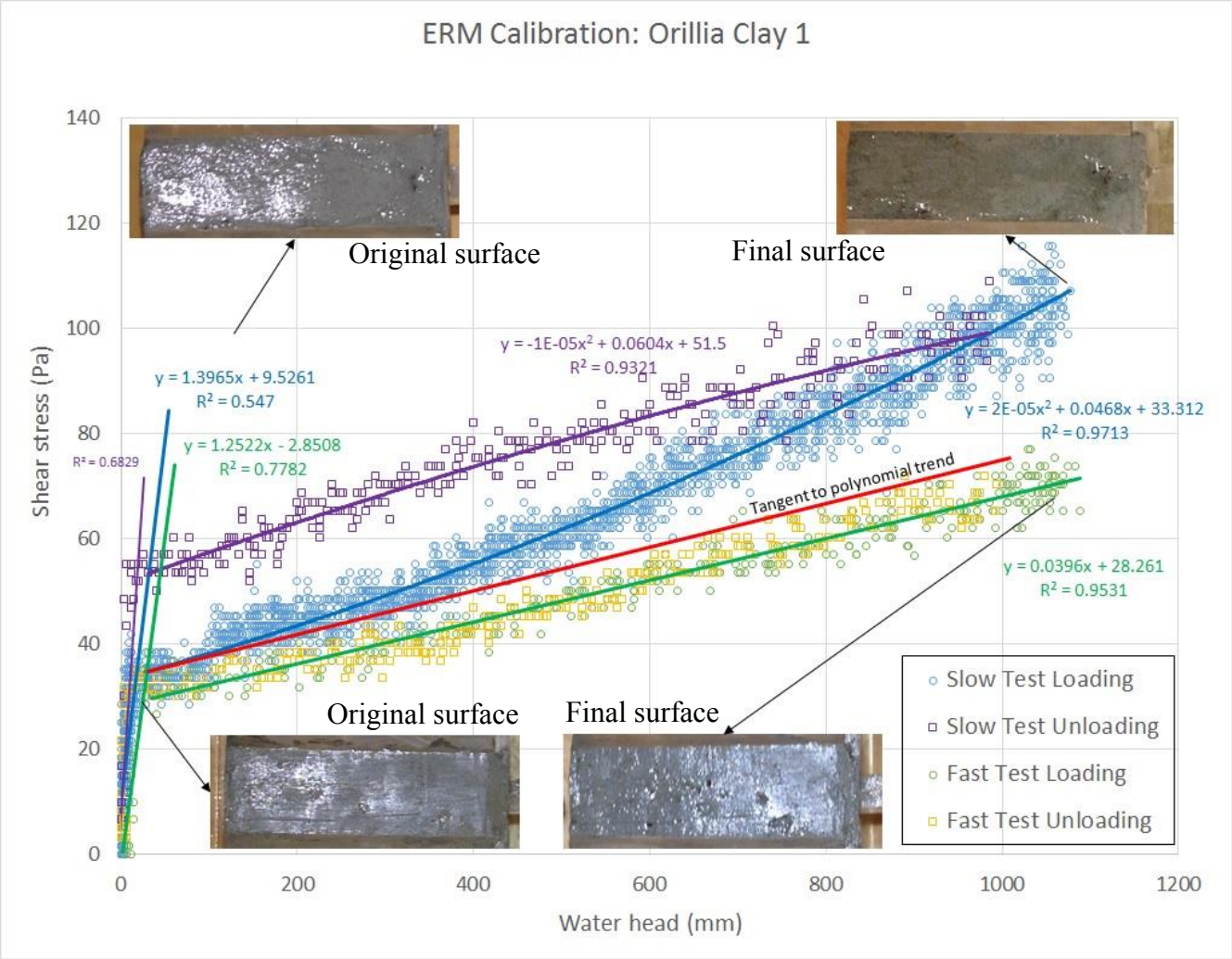

Figure 83. Fast and slow ERM tests on a clay sample from Orillia, Ontario

The flow restriction was kept in the device for the remainder of the testing throughout this research work. It is important to note that by using the pod sample and force measurement, the effect of any flow restriction is automatically accounted for in the measurements and does not need to be quantified. Furthermore, it is possible to calibrate the device for specific soil types at relative stress levels where the shear stress remains proportional to the head in the tube, and therefore allowing it to be used *in situ* on an exposed (i.e., unsubmerged) riverbed with reasonable accuracy. Note that no direct shear measurements can be done *in situ*.

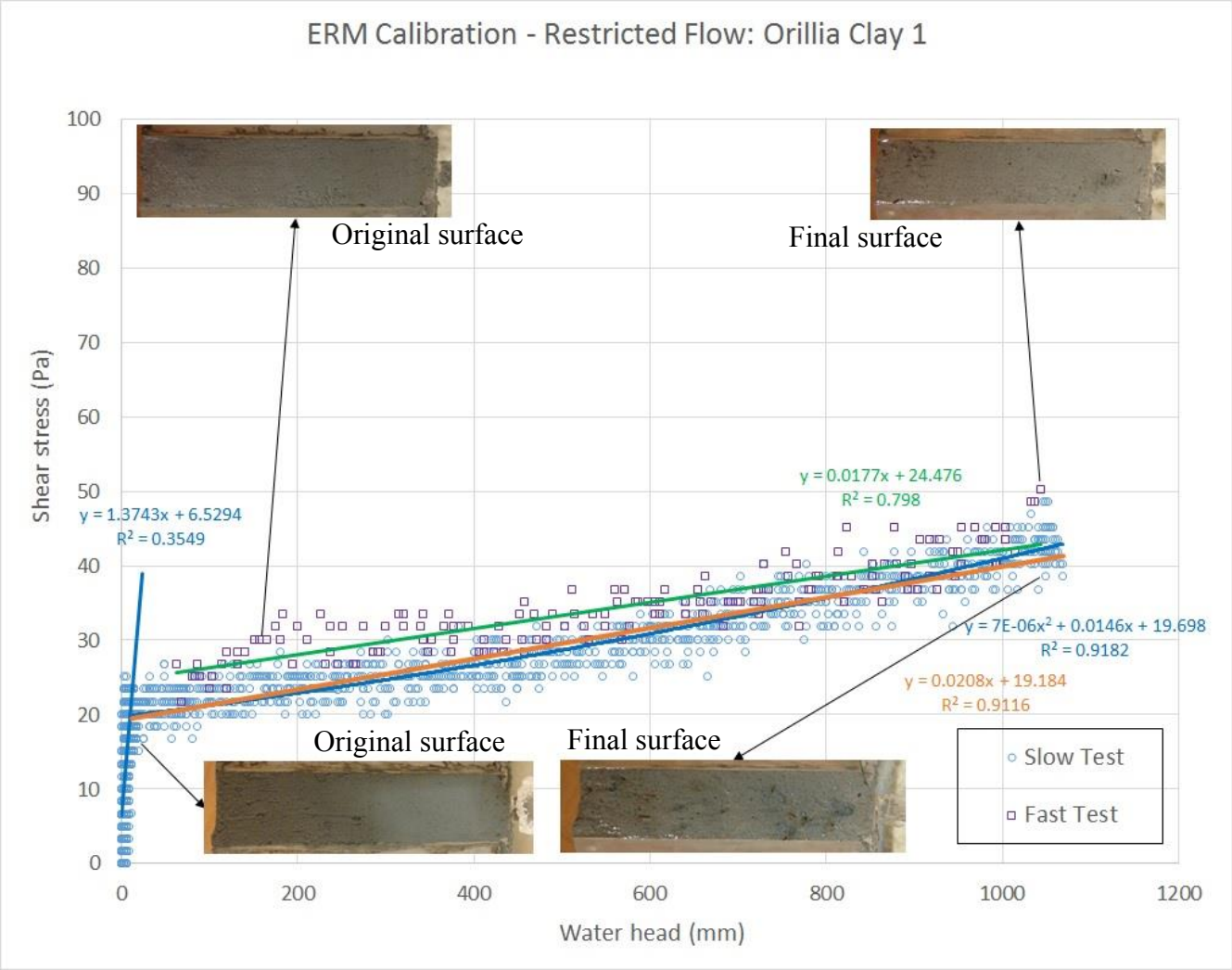

Figure 84. Slow ERM test with restricted flow on a clay sample from Orillia, Ontario

5.3.6. **Erosion measurements**

As discussed earlier, the erosion measurements were performed using the pod sampler and the restricted flow in the nozzle tube. A first set of six cohesive soil samples from several sites in Ontario, Canada, (supplemental soils) were tested as described in Table 7. The locations of the sampling sites are indicated and labelled on maps enclosed in Appendix 2 (courtesy of Google Earth). All tested samples were subjected to Atterberg classification tests using a 30° falling-cone device, which showed the samples as silty clay and clayey silt, medium to high plasticity. One sample (Bear Brook) showed a relatively high content of fine sand. Refer to Appendix 3 for more information on laboratory testing on soil samples.

Table 7. Supplemental cohesive soil samples subjected to ERM testing

Sampling location	Sample #	Description
Bear Brook	BB2	Grey clay-fine sand-silt mix, some organics, medium plasticity
Black River	BR1	Grey sensitive clay (Champlain Sea), stiff, high plasticity
Muddy Creek	MC1	Champlain sea clay, soft, grey, structured, high plasticity
Orillia	O1	Grey silty clay, soft, high plasticity
West Branch Scotch River	WBSR2	Greyish brown silty clay, stiff, black organic content, high plasticity
Green's Creek	GC1	Bluish grey soft silty clayey fine sand, medium plasticity

In addition to the classification tests, the hydraulic conductivity of the samples from Black River, Muddy Creek, and Green's Creek were determined using a falling-head permeameter. The test results showed a hydraulic conductivity of 9.8E-7 cm/s, 8.2E-7 cm/s, and 1.5E-8 cm/s, respectively (see Appendix 3). Two of the samples tested by the ERM, namely the Muddy Creek and Green's Creek samples, were also subjected to hydrometer testing (see Appendix 3 for gradation).

The samples were packed in the pod and the top sliced flush with the top of the pod's walls. The test starts by taking a distance measurement from a reference position (zero position) to the surface of the sample prior to any water flow. This distance is the reference for subsequent measurements to determine the thickness of eroded soil at any point during the test. The flow is then started at a low water head and sustained for about 1 to 2 minutes, depending on the competence of the soil. A distance measurement is then made just before raising the head to a higher level. This process is repeated until a head of about 1.1 m is reached or until a sizeable portion of the sample surface is entrained (sample failure).

Figure 85 through Figure 90 show the head, shear stress, and distance measurements for the five samples, respectively. Note that the Bear Brook sample (Figure 85) could not sustain the full range of water head and started to disintegrate at head of about 600 mm, and an average shear stress of about 30 Pa. Also note that for each distance measurement, the bottom-most green circle represents the distance (mm x 10) to the soil surface from the reference level at that time step

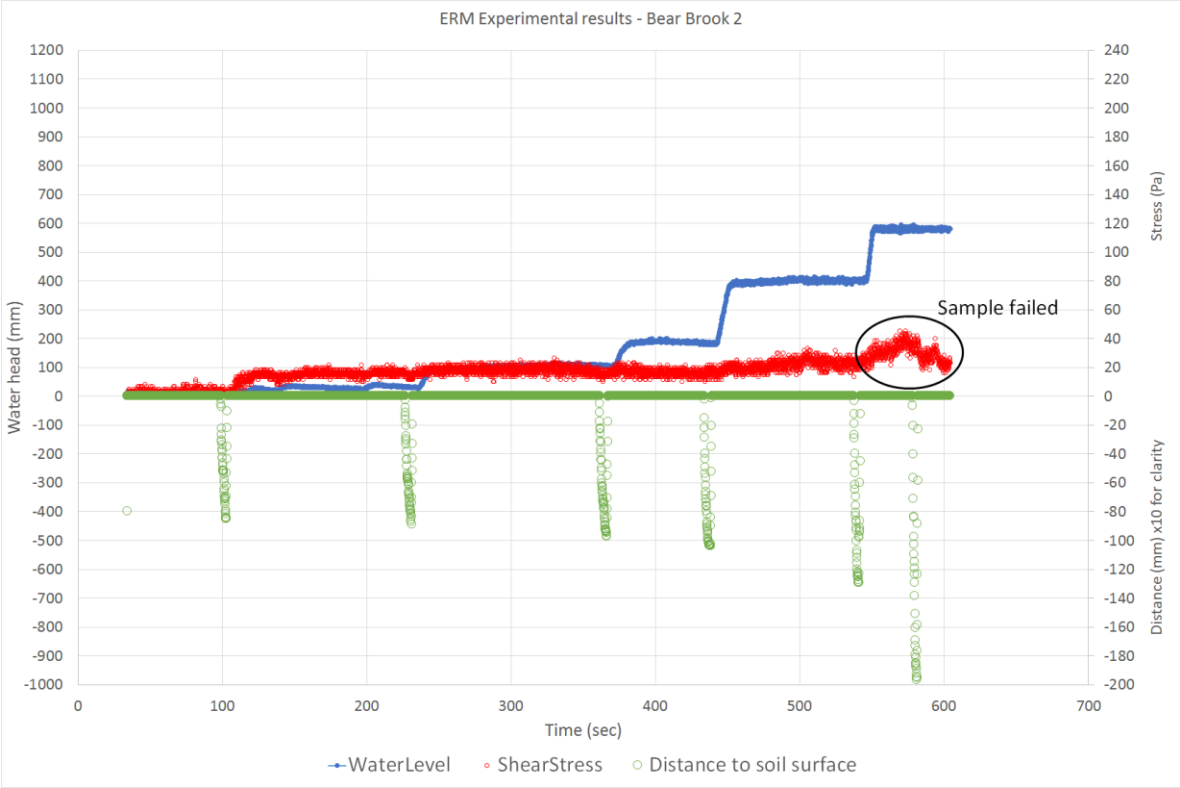

Figure 85. Bear Brook sample, head, shear stress, and distance measurements.

Figure 86. Black River sample, head, shear stress, and distance measurements.

Figure 87. Muddy Creek sample, head, shear stress, and distance measurements.

Figure 88. Orillia sample, head, shear stress, and distance measurements.

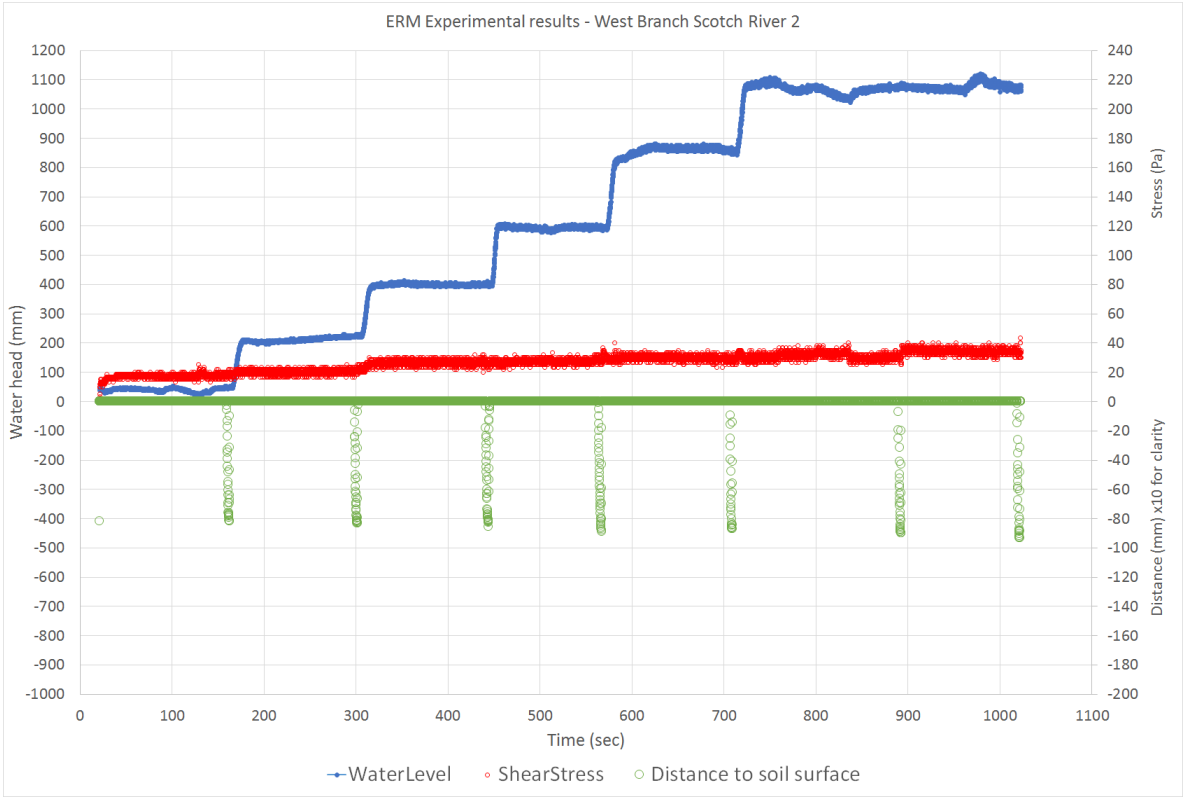

Figure 89. West Branch Scotch River sample, head, shear stress, and distance measurements.

Figure 90. Green's Creek sample, head, shear stress, and distance measurements.

The measurement data are treated in a specially developed spreadsheet to find the incremental loss of soil (thickness) and the average shear stress between distance measurements. The spreadsheet also calculates the rate of erosion between measurements. The resulting compilations are plotted as erosion rate versus average shear stress as shown in Figure 91 to Figure 96, respectively. A linear regression fit is applied to each compilation, and the resulting equation and the coefficient of determination (R^2) are shown on the corresponding plot. It should be noted that a few data points were deemed as not representative; these are mostly at low flow at the start of the test, which could be due to the presence of loose material at the surface from sample preparation, or near the end of the test where the sample begins to deteriorate (fail). Such points are reported as outliers and plotted as hollow square markers. Theoretically, the trend of erosion rate versus bed shear stress should intersect the x-axis at the critical shear stress value. To supplement the results of the ERM, the critical shear stress of each soil used in the tests was independently determined using the Erosionometer device introduced in Section 5.2.1. The Erosionometer critical shear results are plotted with the ERM data for comparison.

As can be seen in the compiled data in Figure 91 to Figure 96, the erosion rate appears to reasonably follow a linear correlation with the shear stress, which is averaged over the same representative time period. Furthermore, the critical shear stress measured using the Erosionometer is in good agreement with the ERM measurements; in fact, in cases like the Bear Brook soil where the number and spread of data points are not sufficient to draw an accurate trend, the Erosionometer measurement adds confidence to the data by correcting the trend.

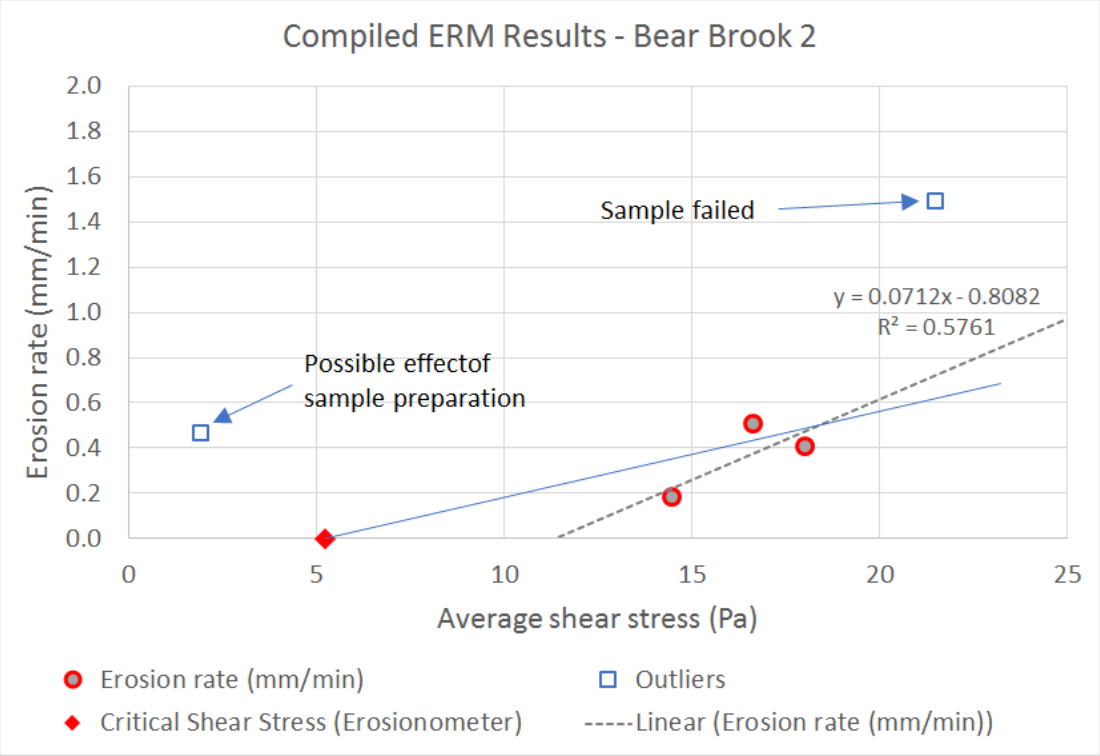

Figure 91. Bear Brook, compiled ERM results

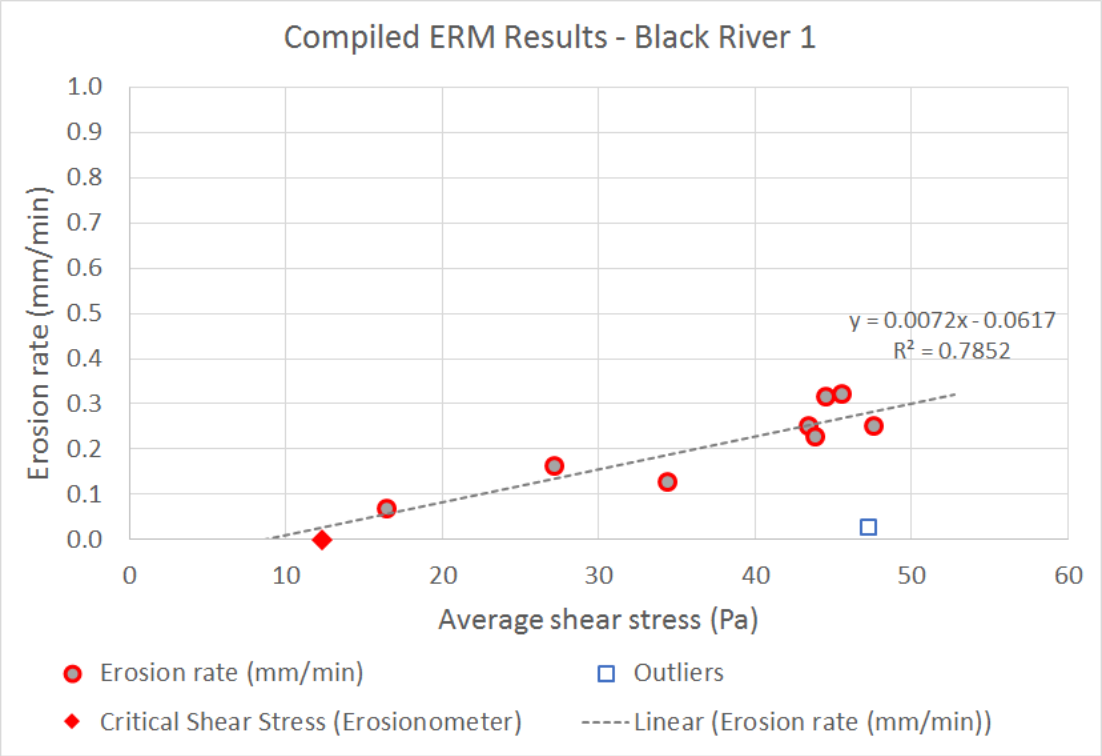

Figure 92. Black River, compiled ERM results

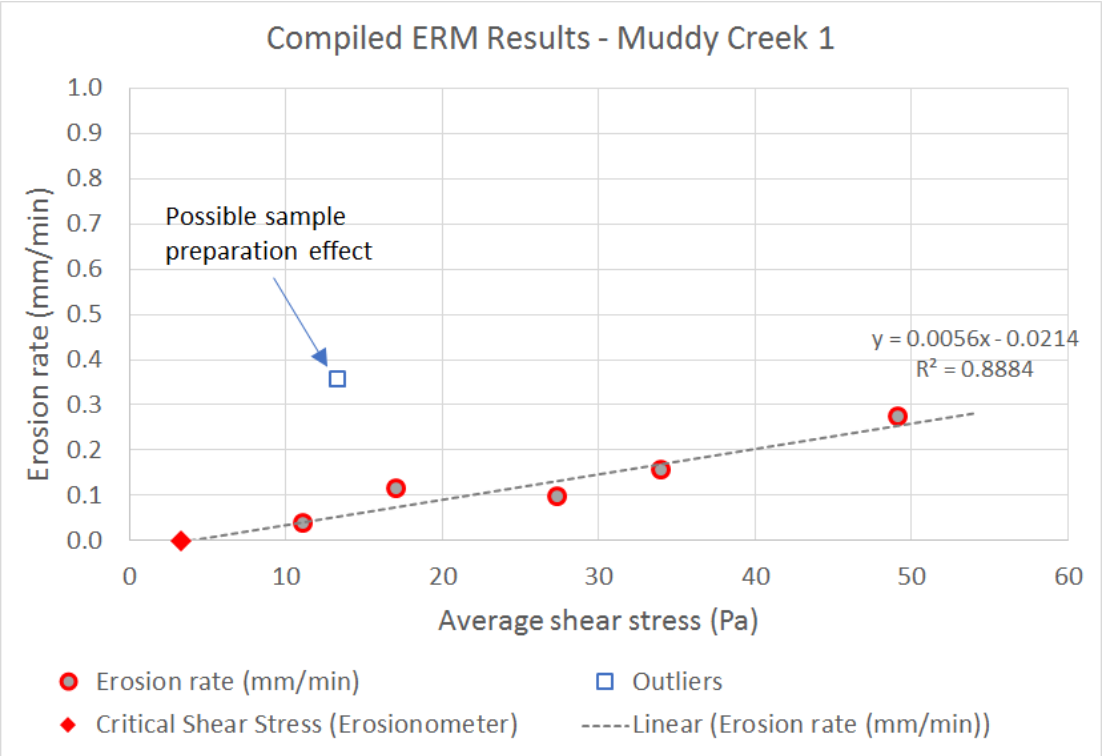

Figure 93. Muddy Creek, compiled ERM results

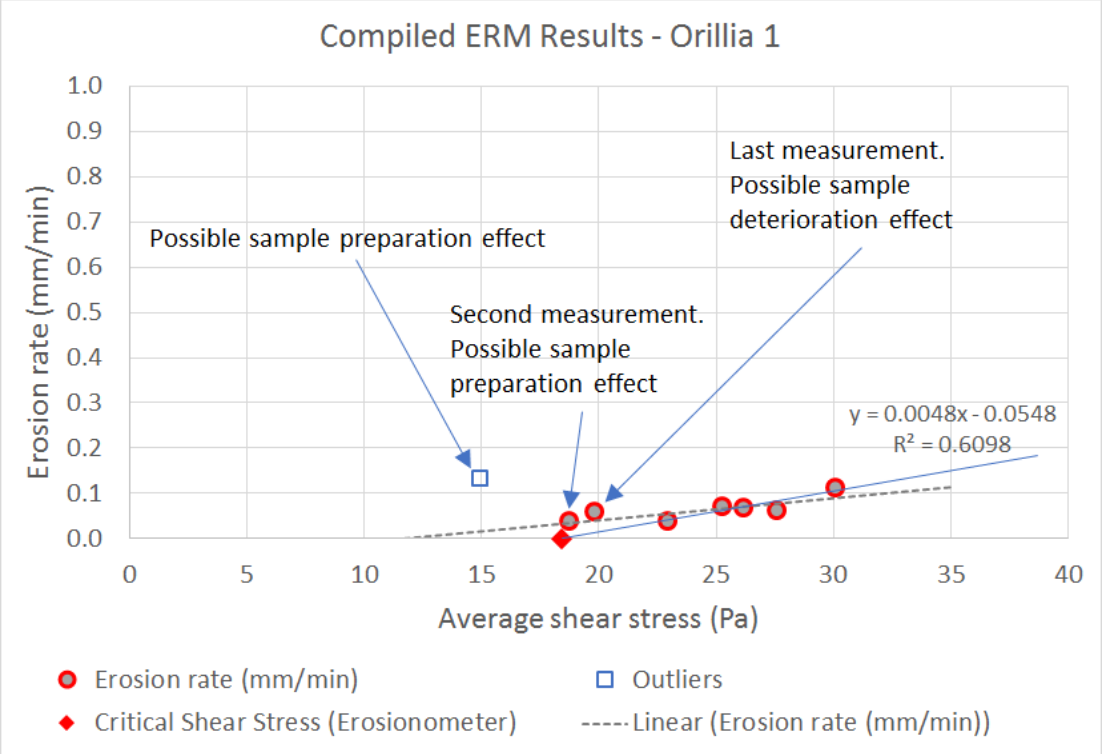

Figure 94. Orillia, compiled ERM results

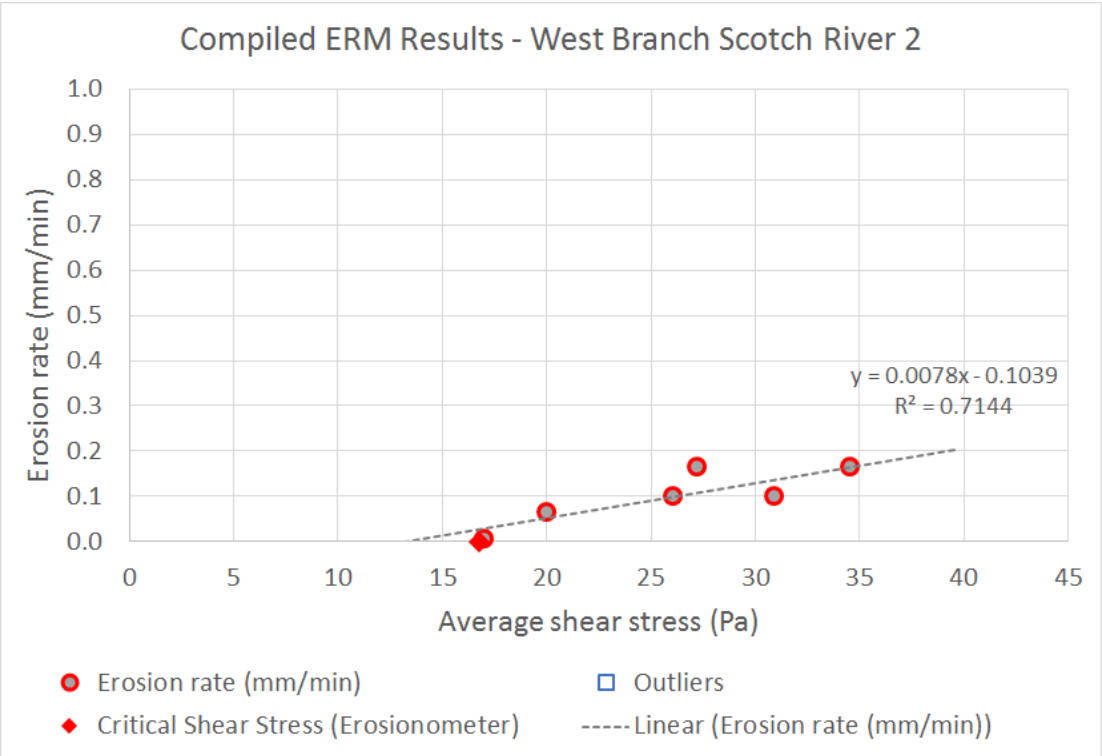

Figure 95. West Branch Scotch River, compiled ERM results

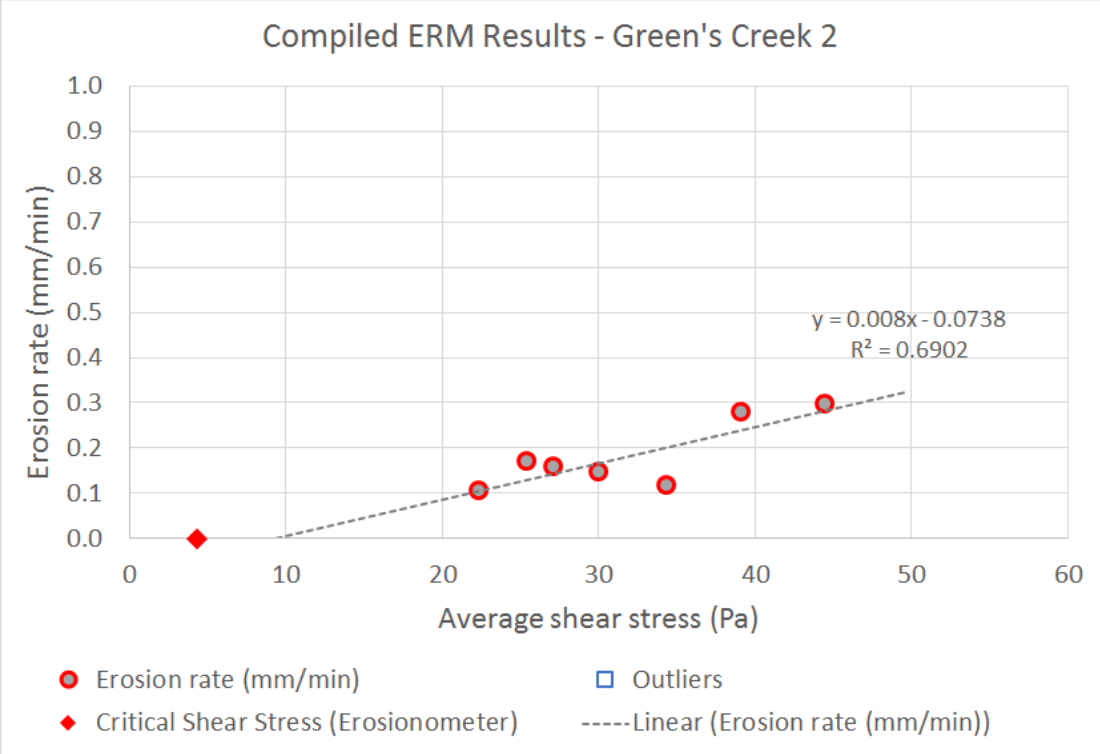

Figure 96. Green's Creek, compiled ERM results

The sample from Orillia was the only one tested while the water head was drawn down. As shown in Figure 94, the second measurement point, which may still have an effect from the sample surface disturbance, and the last measurement point after the drawdown seems to deviate from the general trend by showing a higher erosion rate. The last measurement point may be an indication that subjecting the soil surface to high shear flow for an extended length of time may reduce its ability to resist entrainment at lower shear for a brief time, at least until the affected thin surface layer is entrained; however, the single observation is insufficient to draw any conclusive interpretation and could have been just a soil cluster at the measuring point that was ready to dislodge. It is important to remember that the measured intervals of entrained soil thickness in this experiment are normally a fraction of a millimeter. By eliminating the two data points flagged in Figure 94, a much stronger agreement between the ERM and Erosionometer data is obtained, as shown in Figure 97. That said, it is difficult to justify statistically the removal of these outliers; regardless, keeping the two points in the results would still provide a reasonable and representative model.

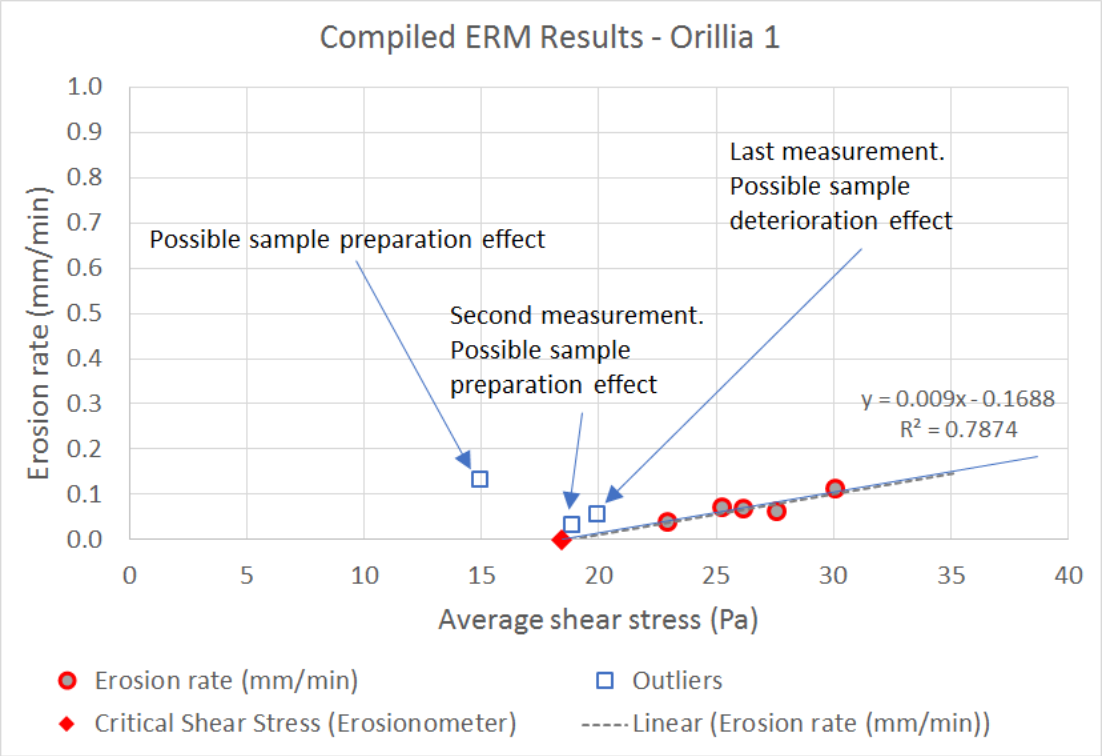

Figure 97. Bear Brook, compiled ERM results with additional eliminated outliers

The soil sample from Bear Brook (Figure 85 and Figure 91) presented a special challenge as it is composed mostly of coarse sand with minor clay content, hence very low cohesion strength. The rough surface of the sample draws a high shear force from the flow which washes the fine content around the grains in a relatively brief time and causes rapid deterioration of the sample, as can be seen in Figure 85. The critical shear measurement added to the data of this sample in Figure 91 proved to be a valuable addition to compensate for such difficulties. This issue can be solved with a lower intensity flow.

A second round of testing was performed for all core soils following the same procedure as the previous tests, except for the piezometer measuring the height of water in the riser tube. The water level was shown to be irrelevant for the test when shear is measured directly, therefore, only shear and erosion will be reported for this group of soils. The graphical results of the core soils tests are shown in Figure 98 through Figure 117. For each soil, the first figure shows the recorded shear and distance to soil surface with time; the next figure shows the computed average shear between soil surface measurements versus the computed rate of erosion during the same time interval, as done for the supplemental soils. The results for the core soils are also summarised in Table 8.

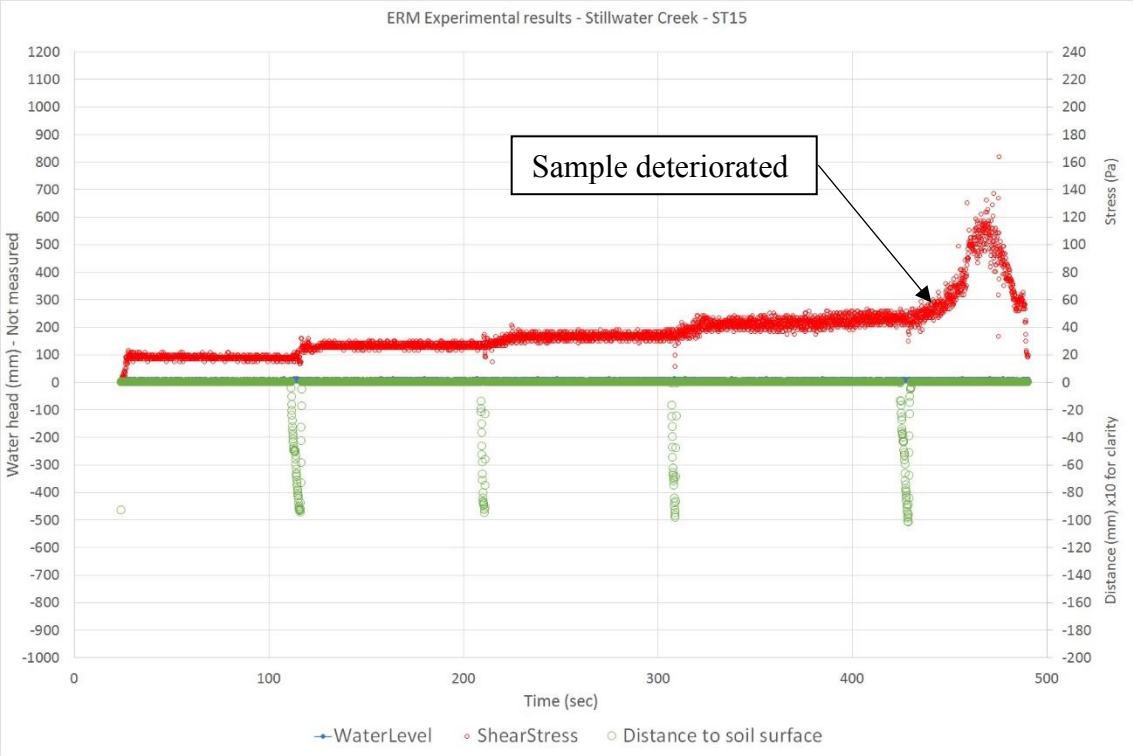

Figure 98. ST15, shear stress and distance measurements.

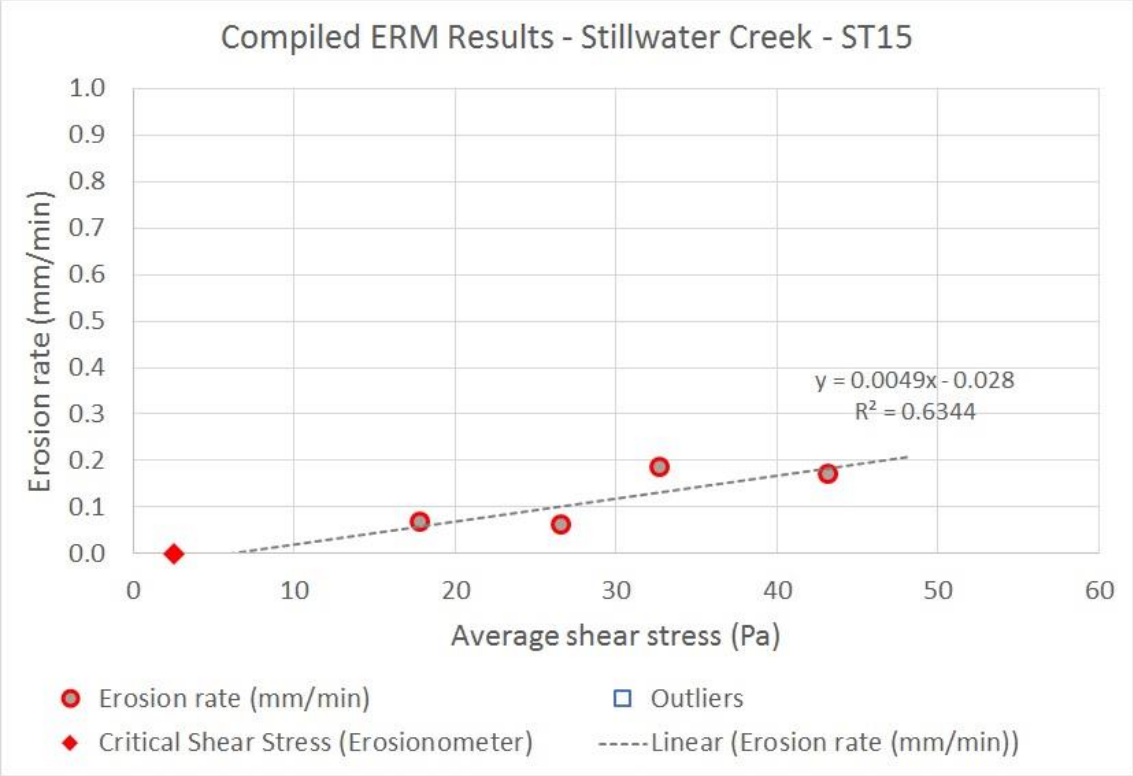

Figure 99. ST15, compiled ERM results

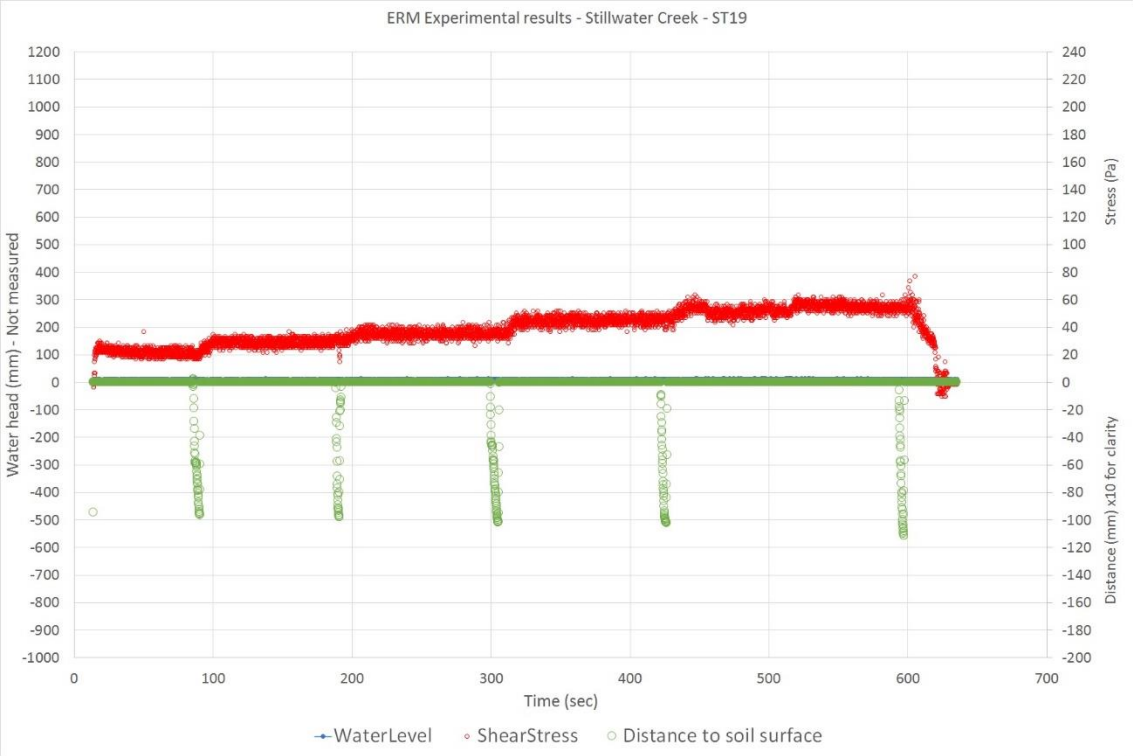

Figure 100. ST19, shear stress and distance measurements.

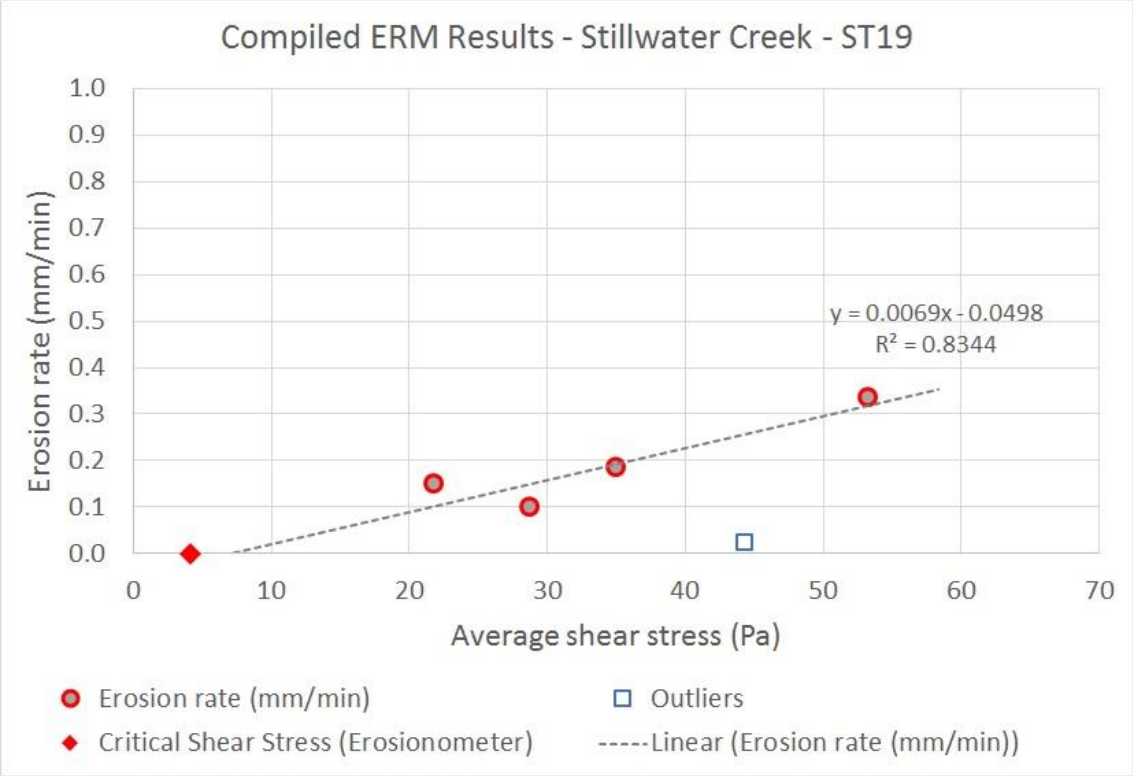

Figure 101. ST19, compiled ERM results with additional eliminated outliers

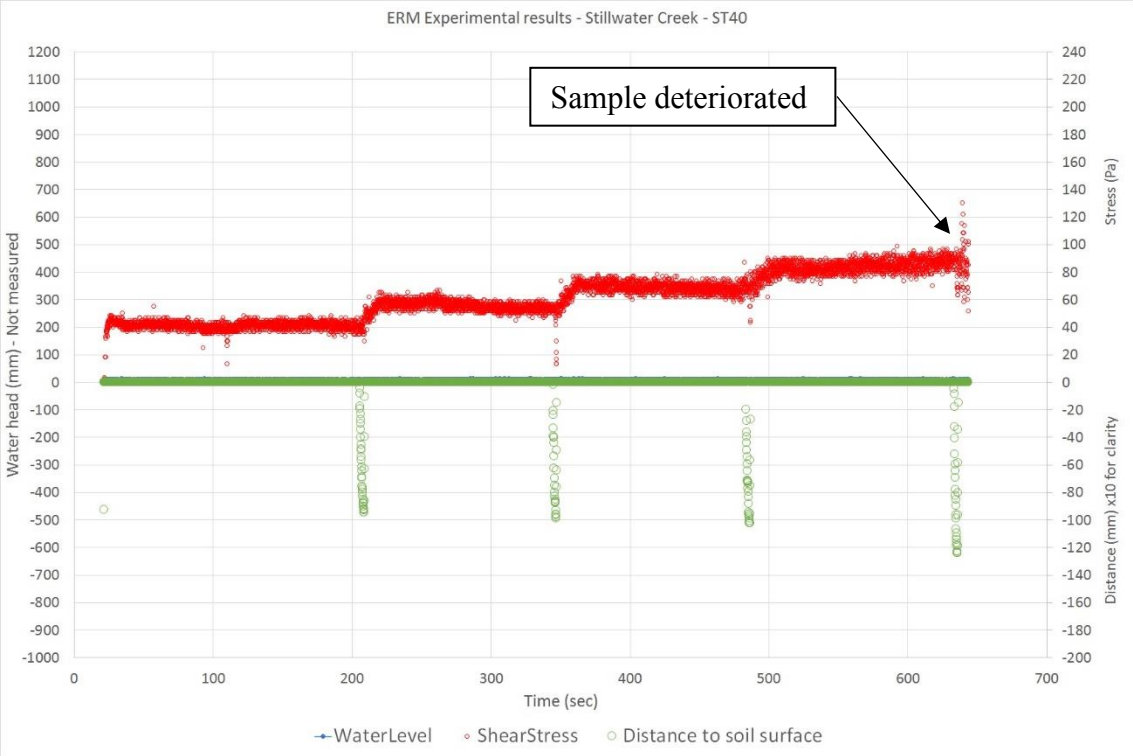

Figure 102. ST40, shear stress and distance measurements.

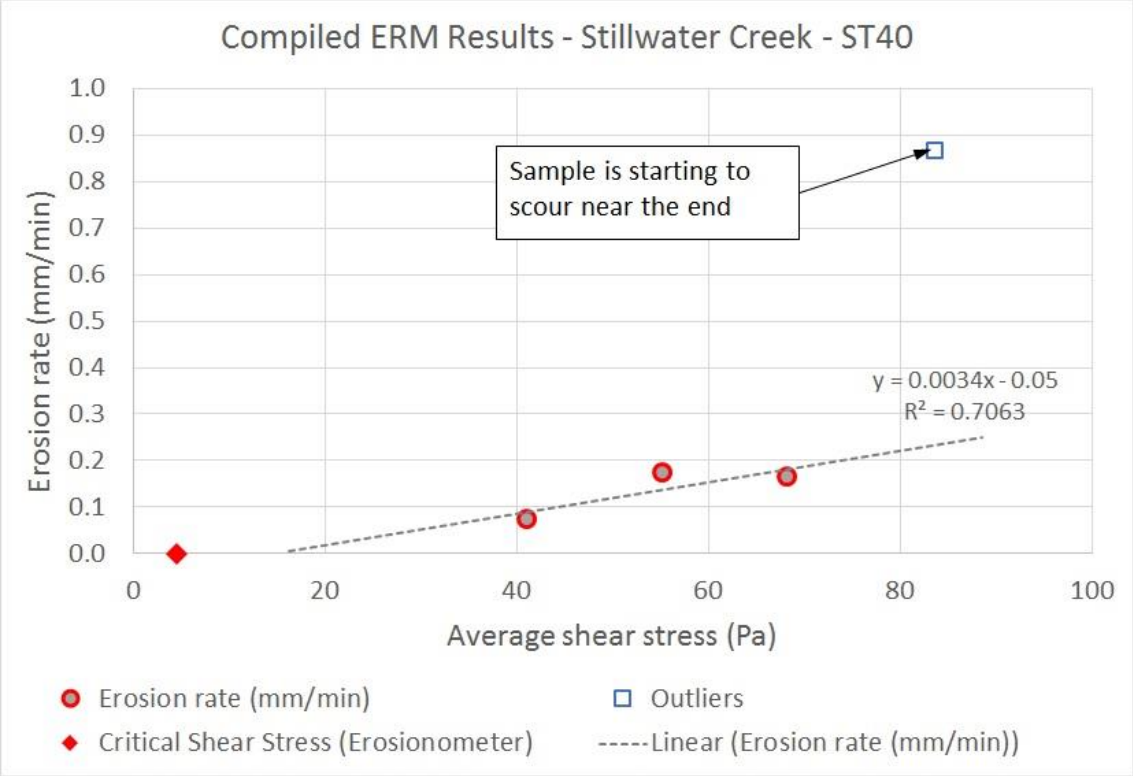

Figure 103. ST40, compiled ERM results with additional eliminated outliers

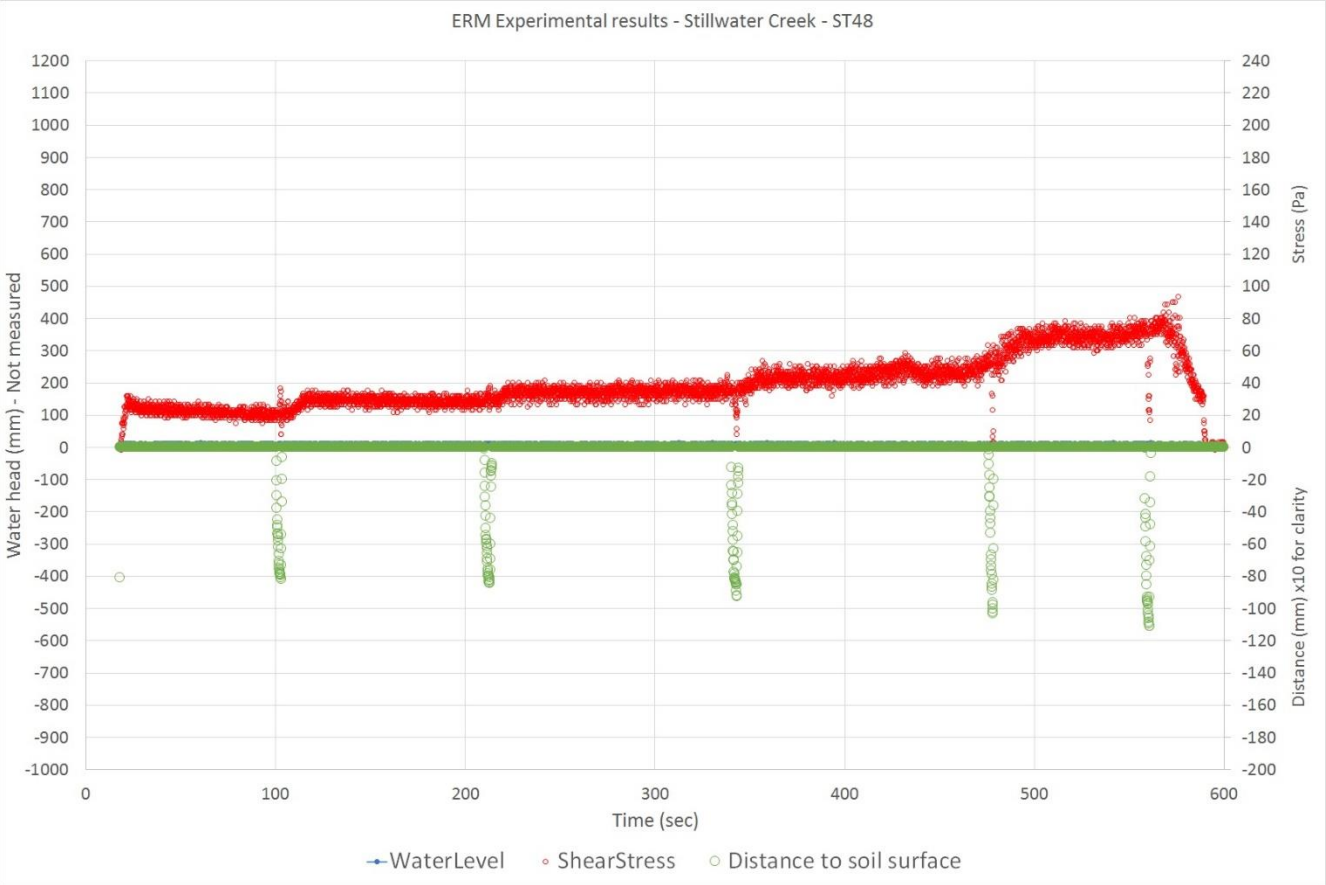

Figure 104. ST48, shear stress and distance measurements.

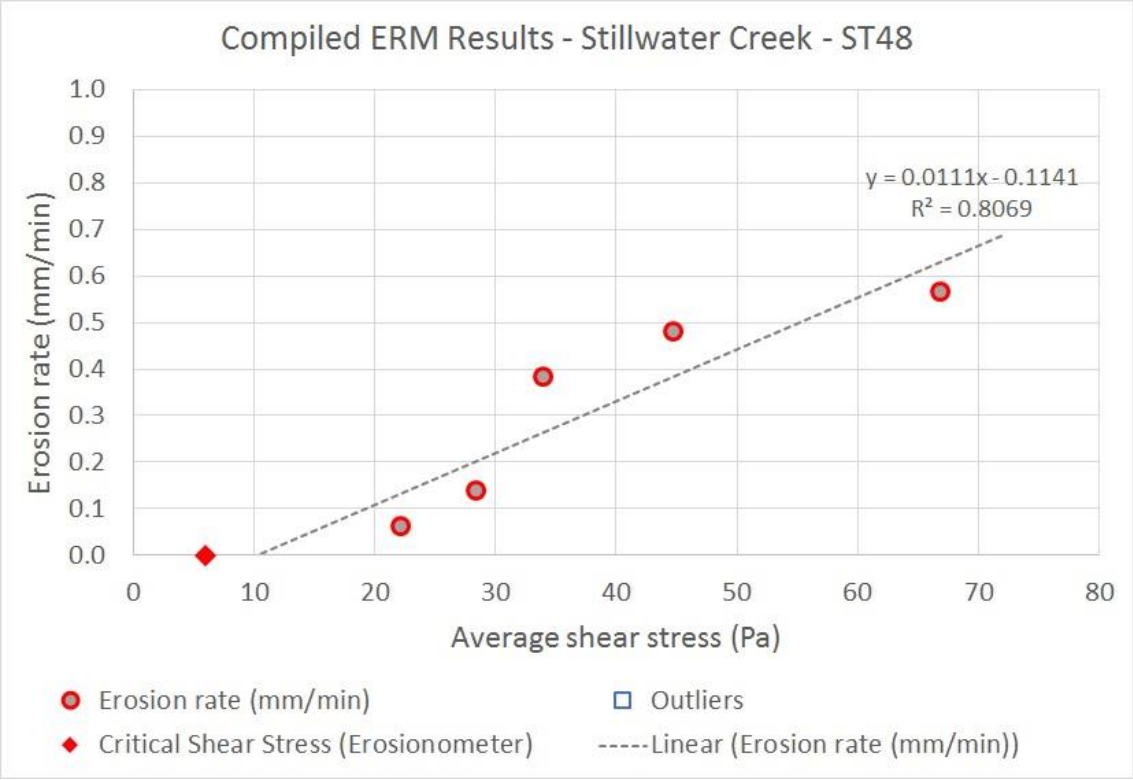

Figure 105. ST48, compiled ERM results.

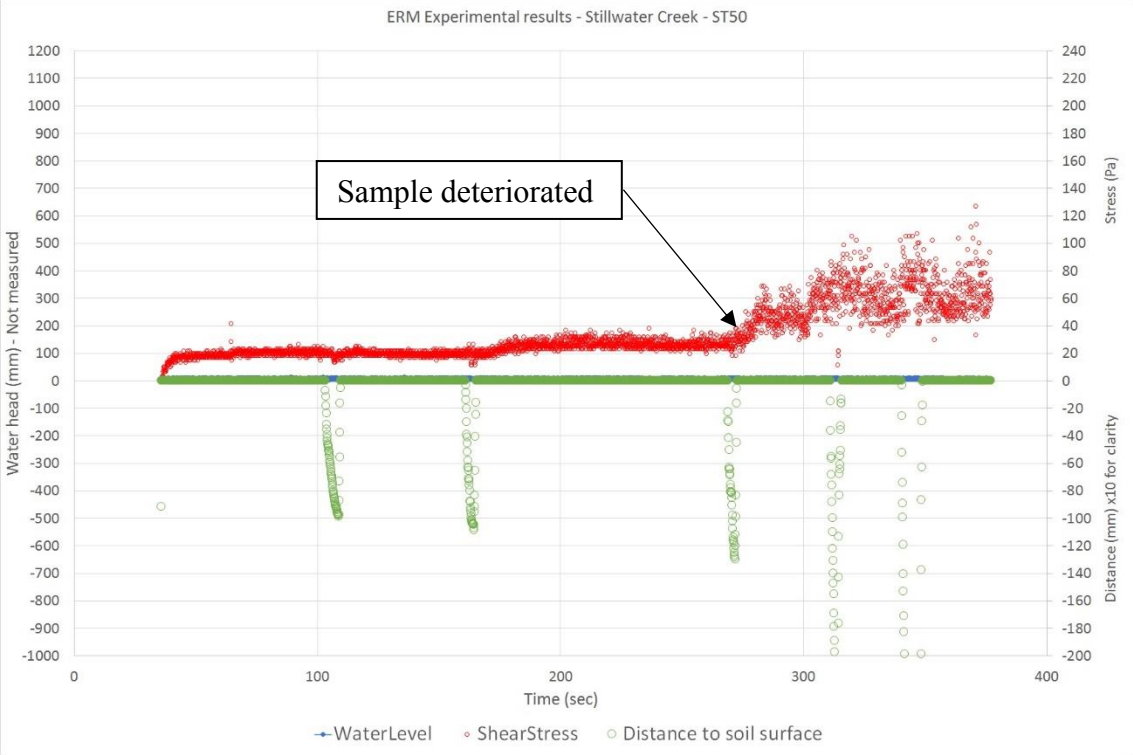

Figure 106. ST50, shear stress and distance measurements.

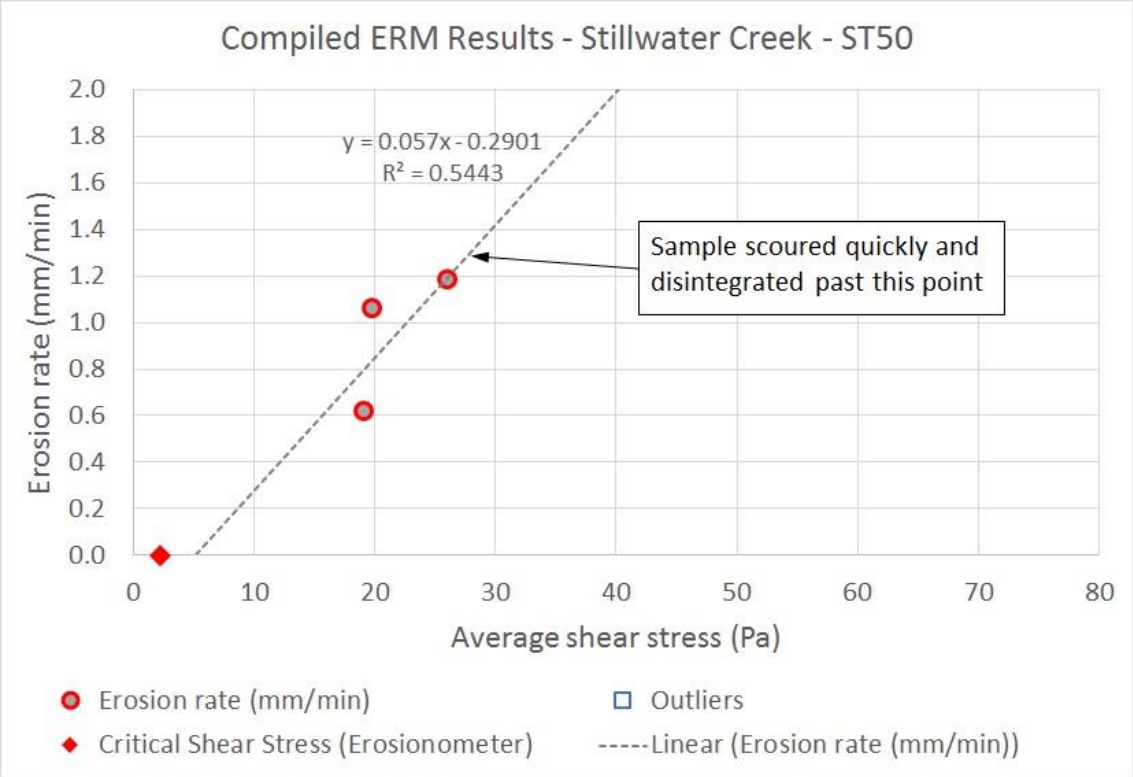

Figure 107. ST50, compiled ERM results with additional eliminated outliers

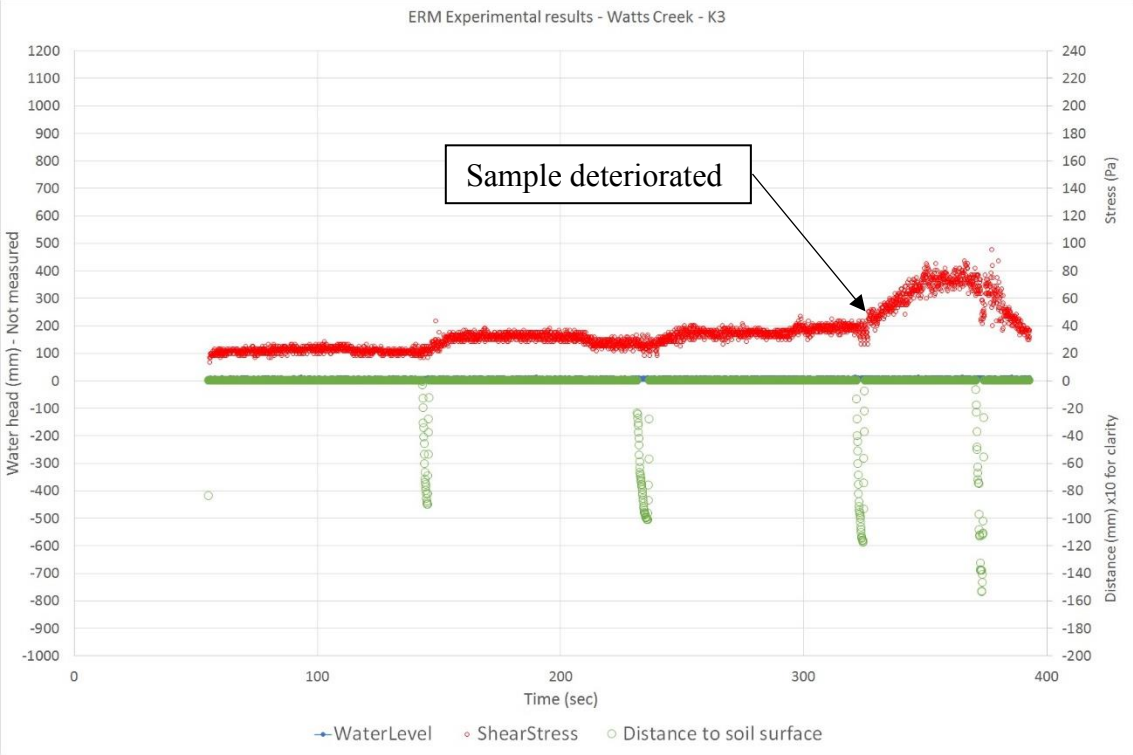

Figure 108. K3, shear stress and distance measurements.

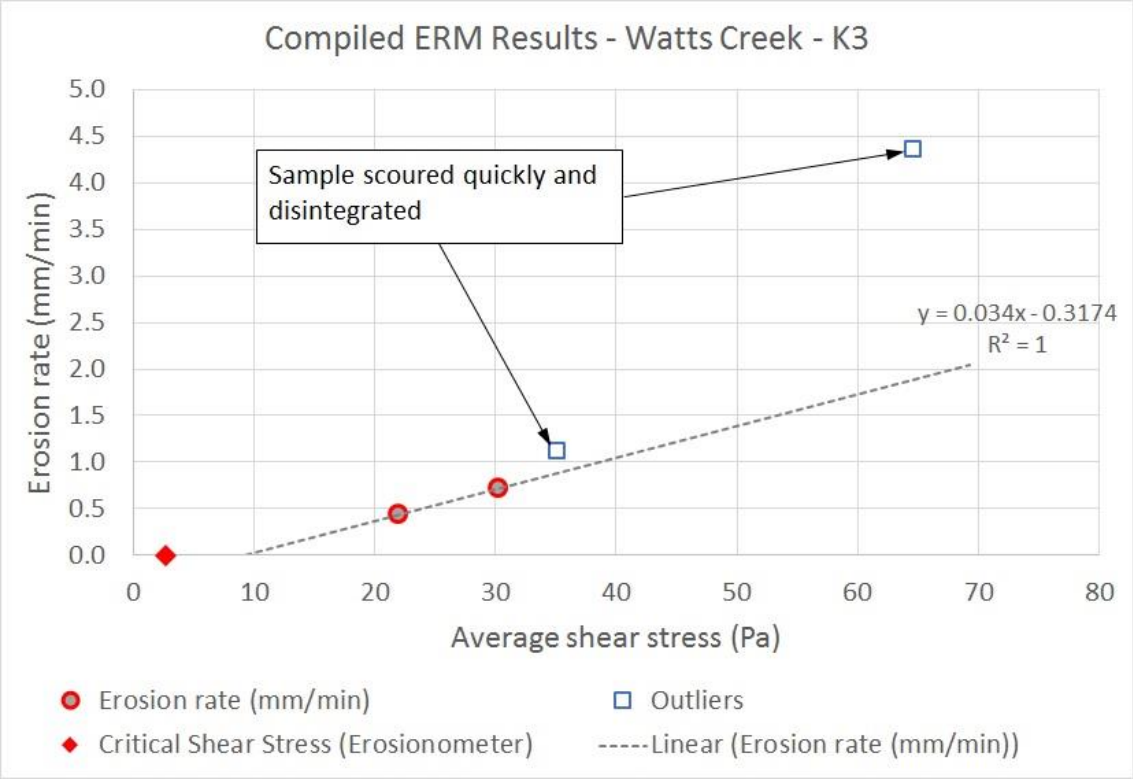

Figure 109. K3, compiled ERM results with additional eliminated outliers

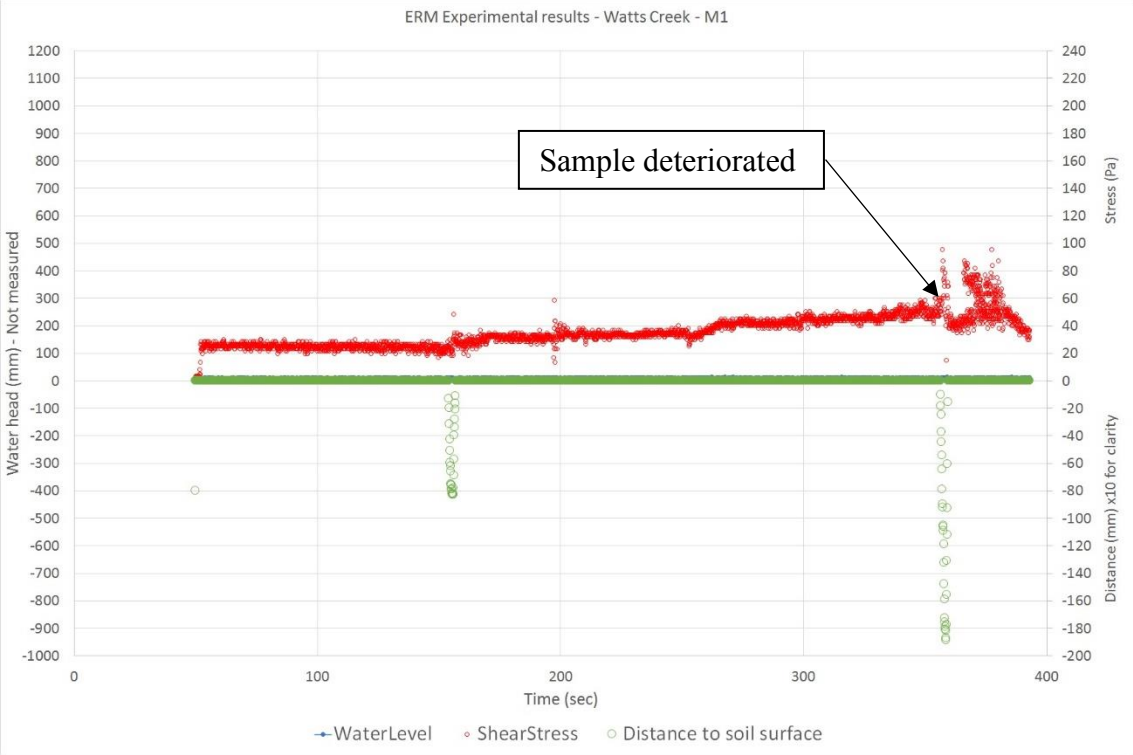

Figure 110. M1, shear stress and distance measurements.

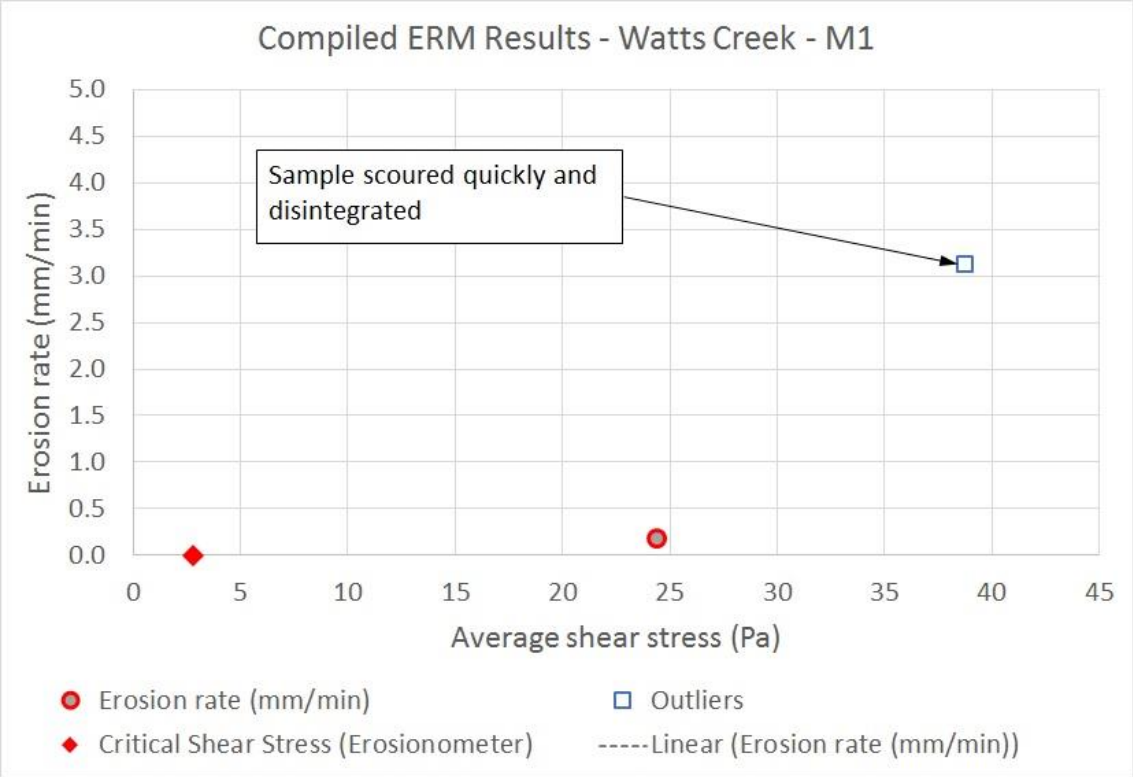

Figure 111. M1, compiled ERM results with additional eliminated outliers

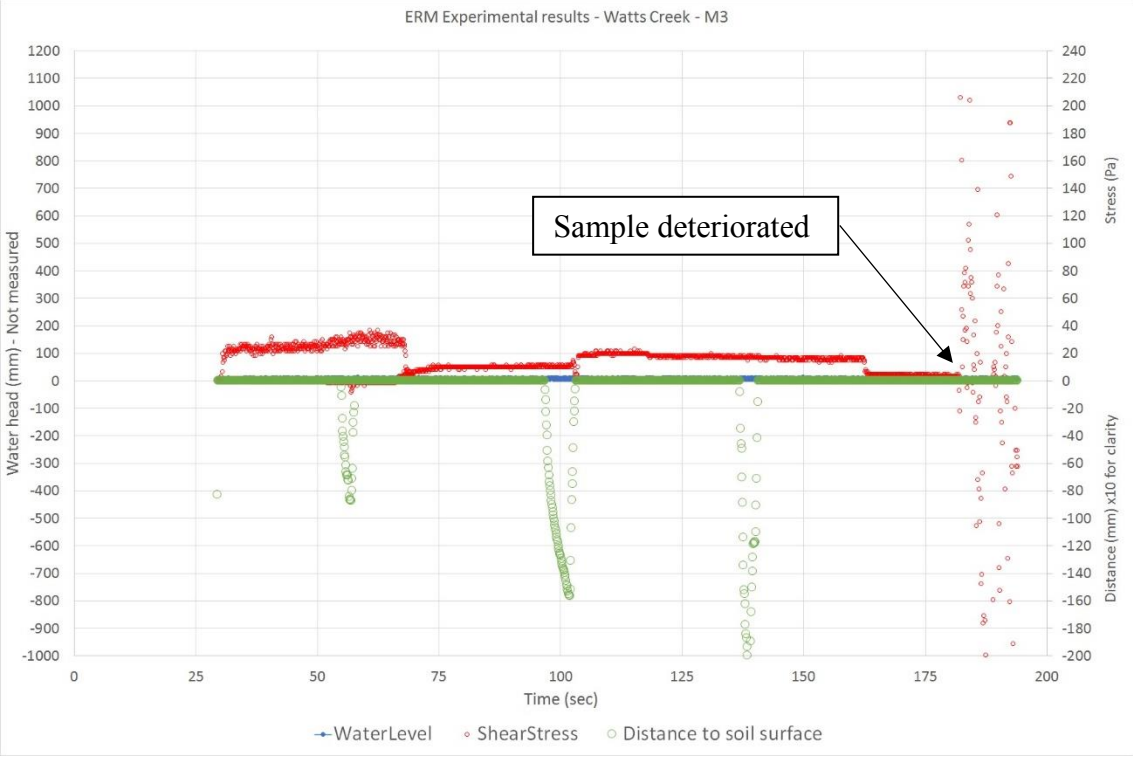

Figure 112. M3, shear stress and distance measurements.

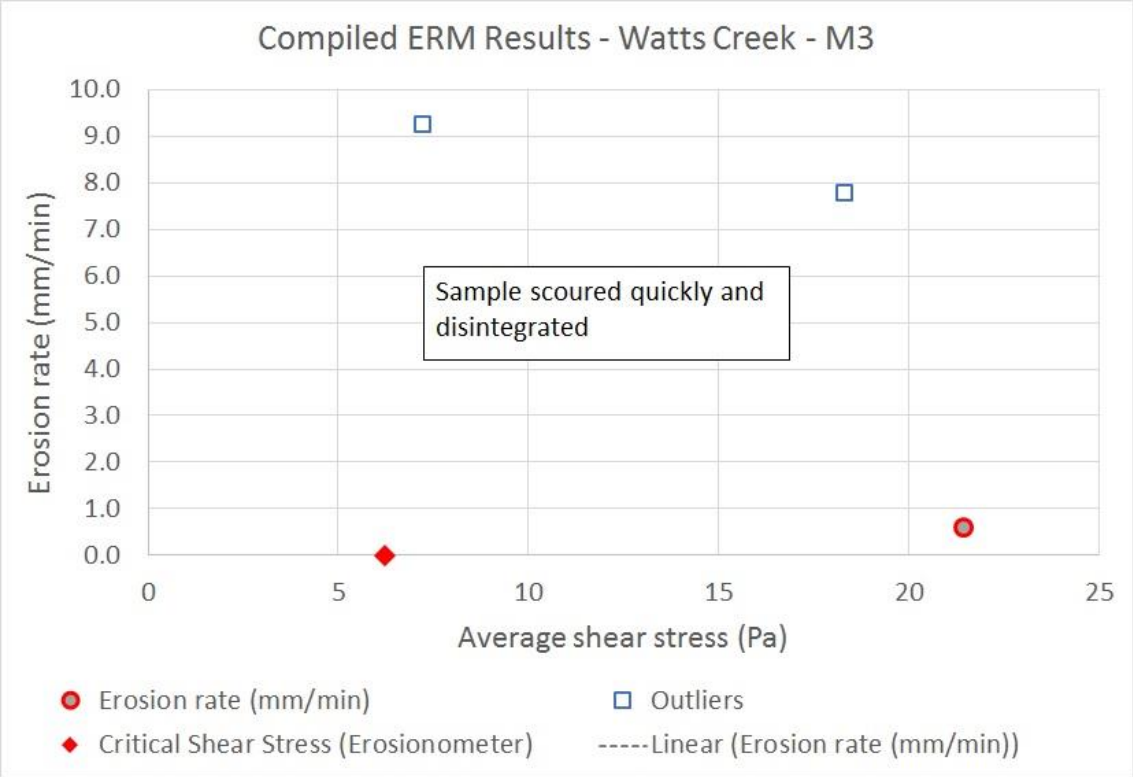

Figure 113. M3, compiled ERM results with additional eliminated outliers

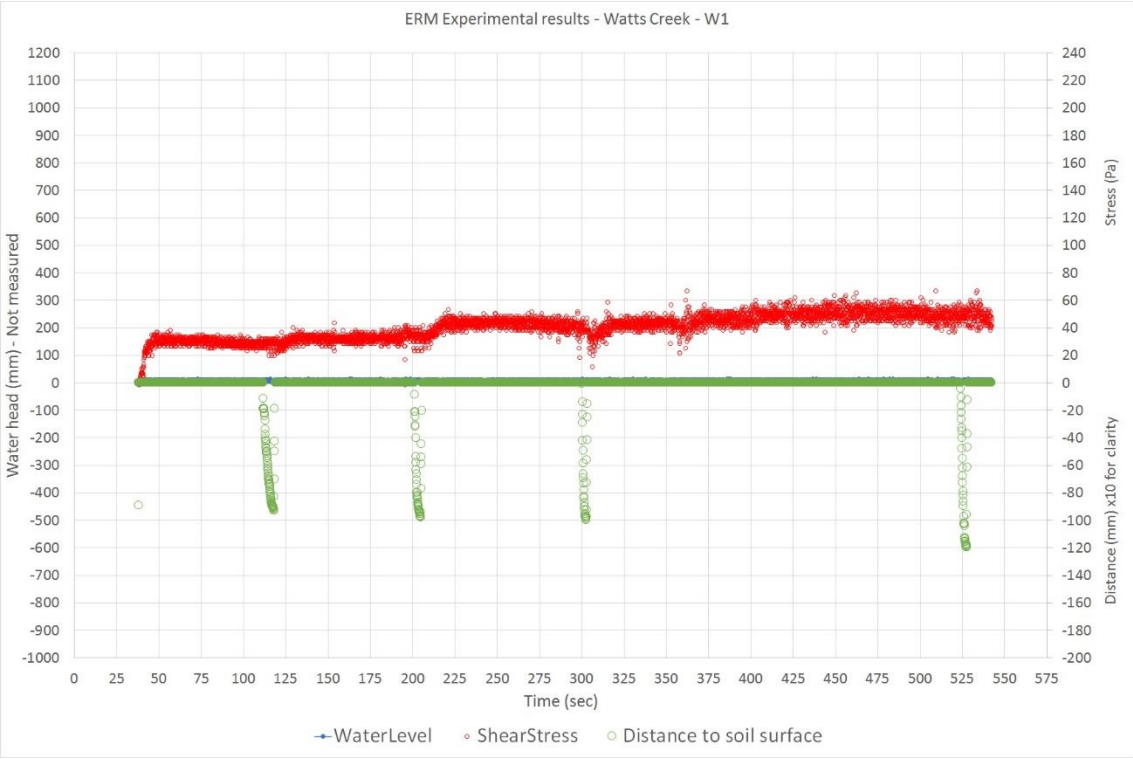

Figure 114. W1, shear stress and distance measurements.

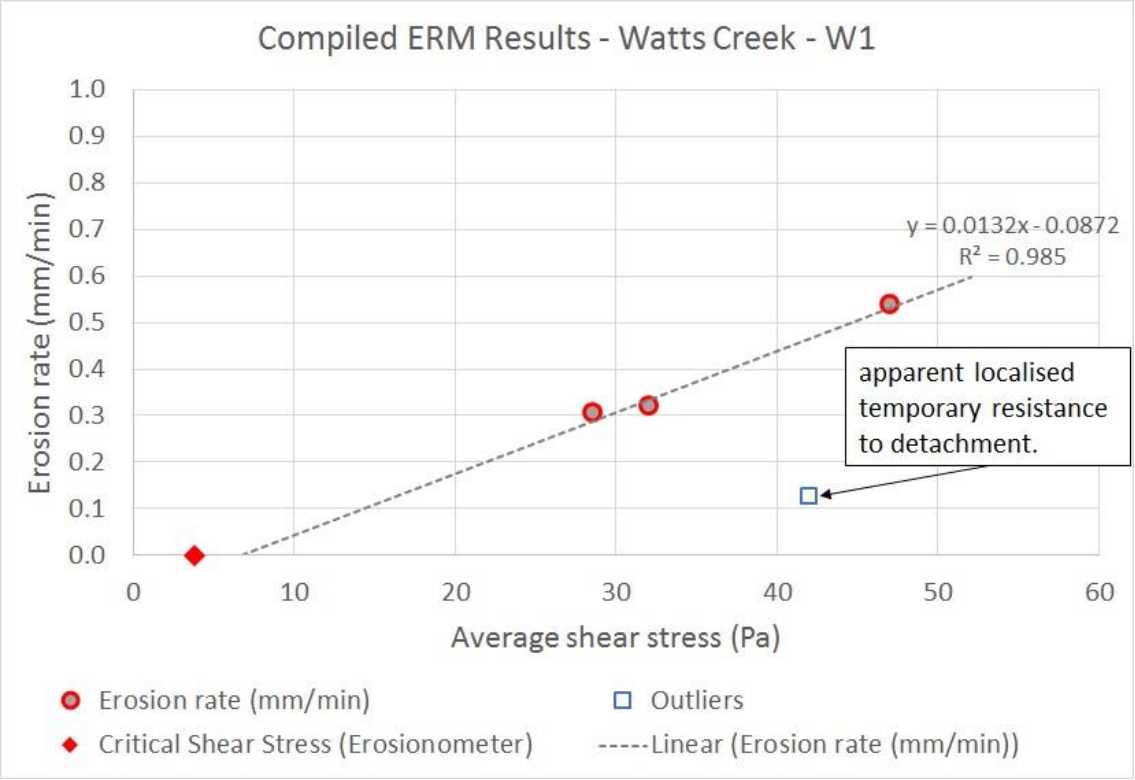

Figure 115. W1, compiled ERM results with additional eliminated outliers

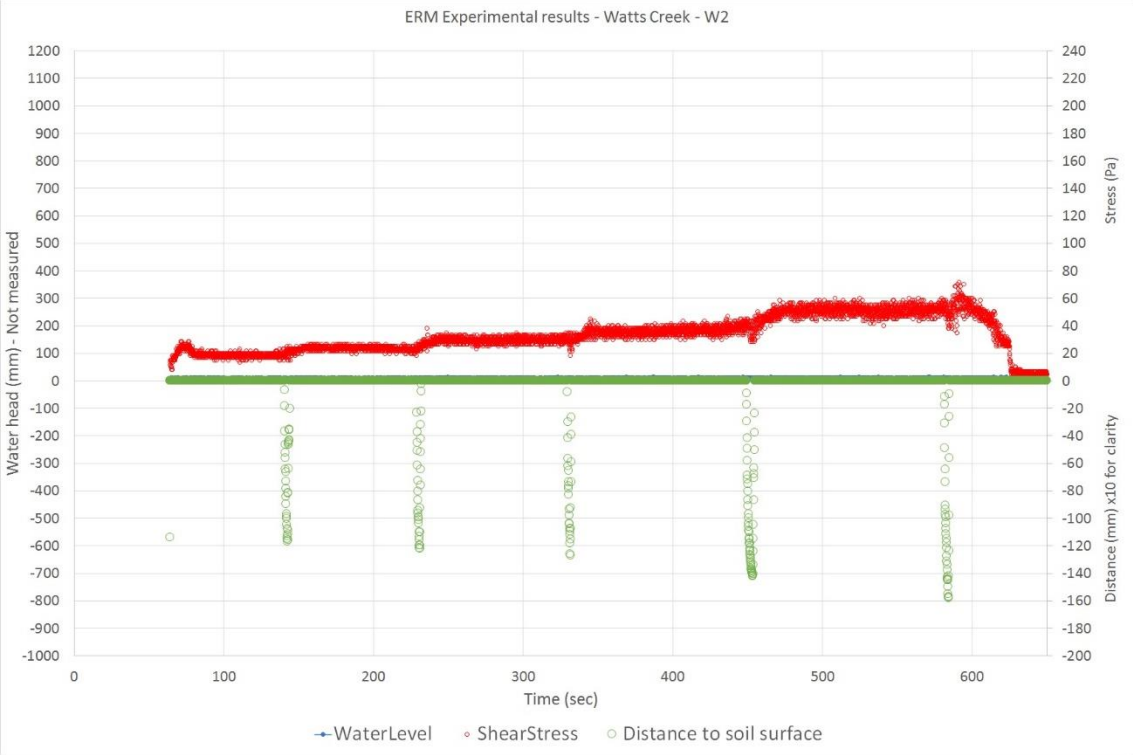

Figure 116. W2, shear stress and distance measurements.

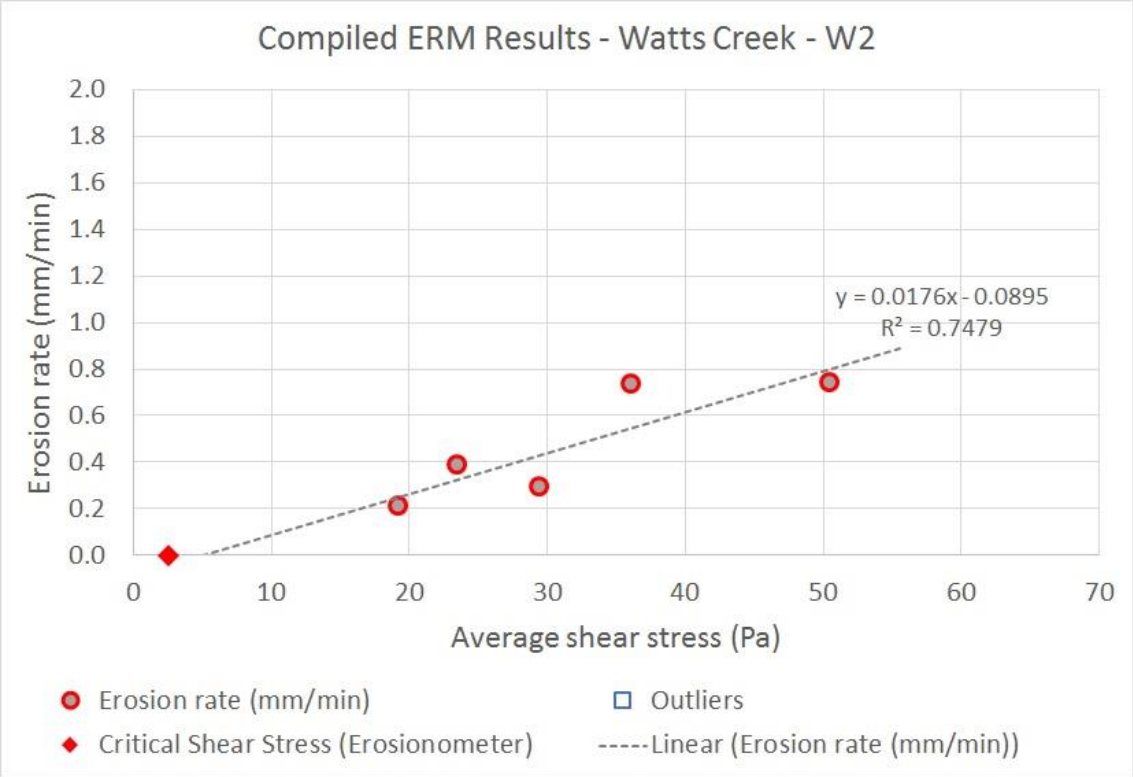

Figure 117. W2, compiled ERM results with additional eliminated outliers

As can be seen from plotted results, all but two of the tested soils (samples M1 and M3 from Stillwater Creek) showed a linear relationship between erosion rate and measured shear, consistent with the common excess shear model with an exponent m = 1. Samples M1 and M3 could not sustain the excess shear imposed by the ERM and disintegrated before any meaningful measurements could be made.

Data from all ERM tests are compiled in Table 8 and the parameters of the excess shear model are calculated for each soil. The critical shear stress is computed as the regression line value at y = 0 (intersection with the x-axis), and the slope of the regression line represents the k-value in the excess shear model (Equation 1), with the exponent m = 1.

Based on the ERM test results, the excess shear linear model can be adopted as a simple representative model for erosion rate. Looking at the summary in Table 8, the k-value for these soils seems to range roughly between 0.003 and 0.07.

The linear relationships from all tests are shown in Figure 118. While some soils showed some similarities in behaviour, the overall results show a significant diversity in response to excess shear.

Table 8. Summary of linear erosion model parameter calculated from test data

Sample number	Slope K	Intercept	R^2	τ_c	Erosion rate E (mm/min.) Excess Shear Model
BB2	0.0712	-0.8082	0.58	11.35	E = 0.0712 x (τ - 11.35)
BR1	0.0072	-0.0617	0.79	8.57	E = 0.0072 x (τ - 8.57)
GC1	0.008	-0.0738	0.69	9.23	E = 0.008 x (τ - 9.23)
MC1	0.0056	-0.0214	0.89	3.82	E = 0.0056 x (τ - 3.82)
O1	0.0048	-0.0548	0.61	11.42	E = 0.0048 x (τ - 11.42)
WBSR2	0.0078	-0.1039	0.71	13.32	E = 0.0078 x (τ - 13.32)
ST15	0.0049	-0.028	0.63	5.71	E = 0.0049 x (τ - 5.71)
ST19	0.0069	-0.0498	0.83	7.22	E = 0.0069 x (τ - 7.22)
ST40	0.0034	-0.05	0.71	14.71	E = 0.0034 x (τ - 14.71)
ST48	0.0111	-0.1141	0.81	10.28	E = 0.0111 x (τ - 10.28)
ST50	0.057	-0.2901	0.54	5.09	E = 0.057 x (τ - 5.09)
K3	0.034	-0.3174	1.00	9.34	E = 0.034 x (τ - 9.34)
M1	-	-	-	-	-
M3	-	-	-	-	-
W1	0.0132	-0.0872	0.99	6.61	E = 0.0132 x (τ - 6.61)
W2	0.0176	-0.0895	0.75	5.09	E = 0.0176 x (τ - 5.09)

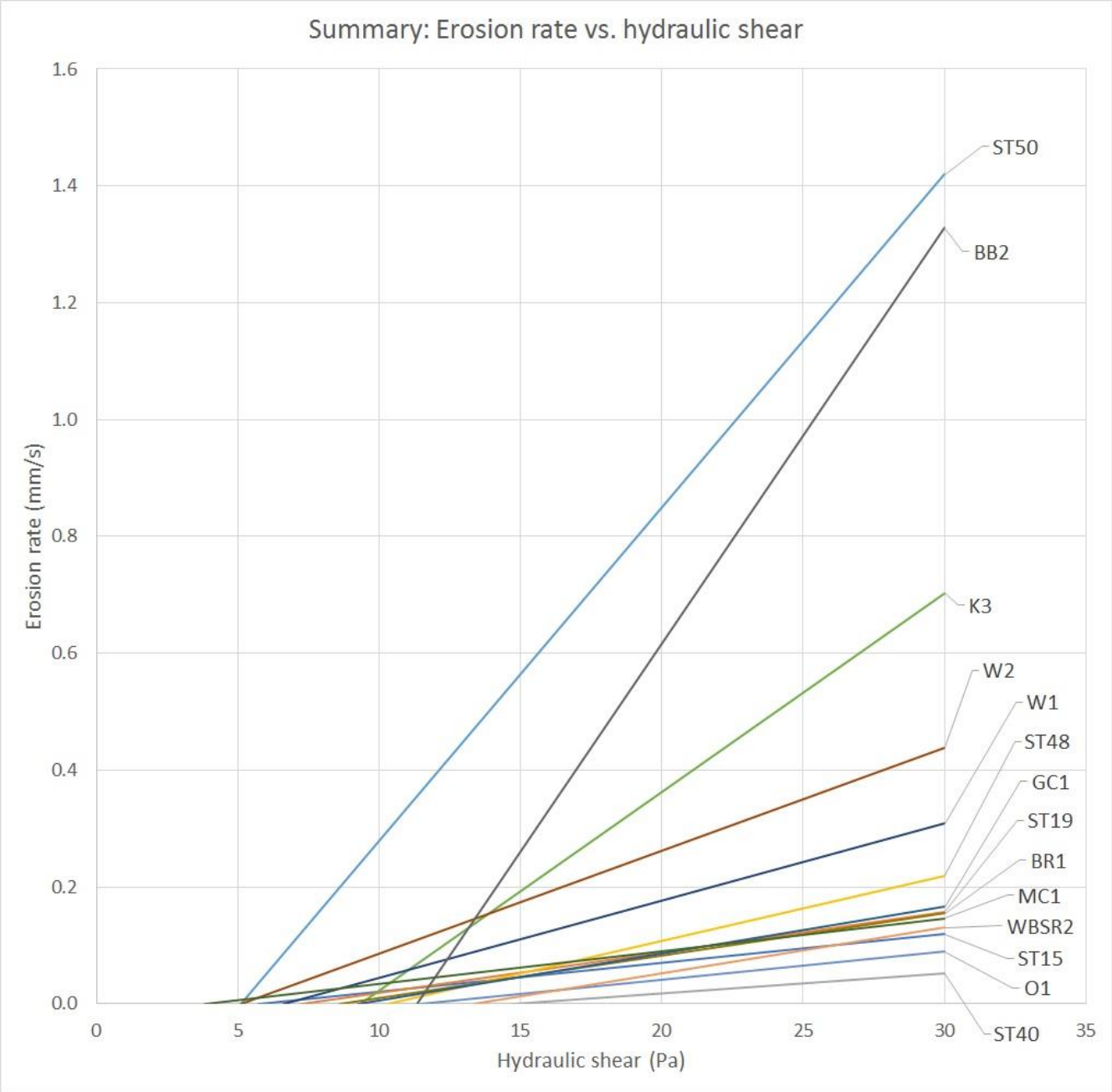

Figure 118. Erosion rate vs. hydraulic shear from all tests

5.3.7. **Discussion**

Based on the results of the initial tests reported in Section 5.3.5, it is clear that the same flow, driven by the same constant hydraulic gradient, over the same soil induced a much higher shear stress when the soil was subjected to entrainment for a longer period of time. This confirms that hydraulic flow characteristics alone are not sufficient to determine the shear stress on an isolated soil surface (sample) that differs from its surroundings, as postulated in Section 5.3.2. On the other hand, it is also possible for entrainment to reduce the bed shear in circumstances where bed shapes, deposited or formed at low

flow, draw high shear stresses when subjected to higher flows and eventually get entrained resulting in a smoother bed, drawing less shear stresses, and thus resisting entrainment.

Most existing erosion rate tests do not account for the change in the shear drawn by the sample at high erosion rate, namely:

- Flumes which are not equipped for direct shear measurement on the sample itself. As the characteristics of the flume bed and walls do not change, the high shear values associated with the measured entrainment may not be accurate.
- The Impinging Jet test, where the shear is computed from the jet intensity and distance to the soil surface. Any change in the soil surface characteristics, including the slope of the soil around the jet impact, do not influence the calculation of the applied shear

Furthermore, in the test results reported in Section 5.3.6 (Erosion measurements), the correlation between the erosion rate and the bed shear appears to be linear, which is in line with the linear excess shear entrainment model (see Section 4.2.1) used by many researchers (Partheniades, 1965; Hanson and Cook, 1997; etc.). Other researchers, such as Walder (2016), suggested an exponential excess shear model (see Section 4.2.1) based on data from Detroit River by Jepsen et al. (1997). Walder suggested an exponential relationship with an exponent m = 1.72 to match the data, as shown in Figure 119. It is important to note in this case that Jepsen et al. used the Sedflume (McNeil et al, 1996) to acquire the data in Figure 119. The shear for the Sedflume is determined as a function of flow rate from standard pipe flow theory, and completely independent of the characteristics of the soil in the piston sample. It is therefore expected, as demonstrated in the initial ERM test results, that the assumed shear stress at the soil-water interface is underestimated in the higher shear range. This would be applicable at a transport stage (T) higher than 4, which translates to an assumed shear stress higher than 5 times the critical shear stress of the soil ($T = \tau/\tau_c - 1$, see Equation 3 in Section 4.2.1).

As the data in Figure 119 appear to follow a linear correlation for $T < 4$ ($\tau < 5 \times \tau_c$), it is possible that the data continue to follow a linear trend at higher transport stage following an adequate shear stress correction.

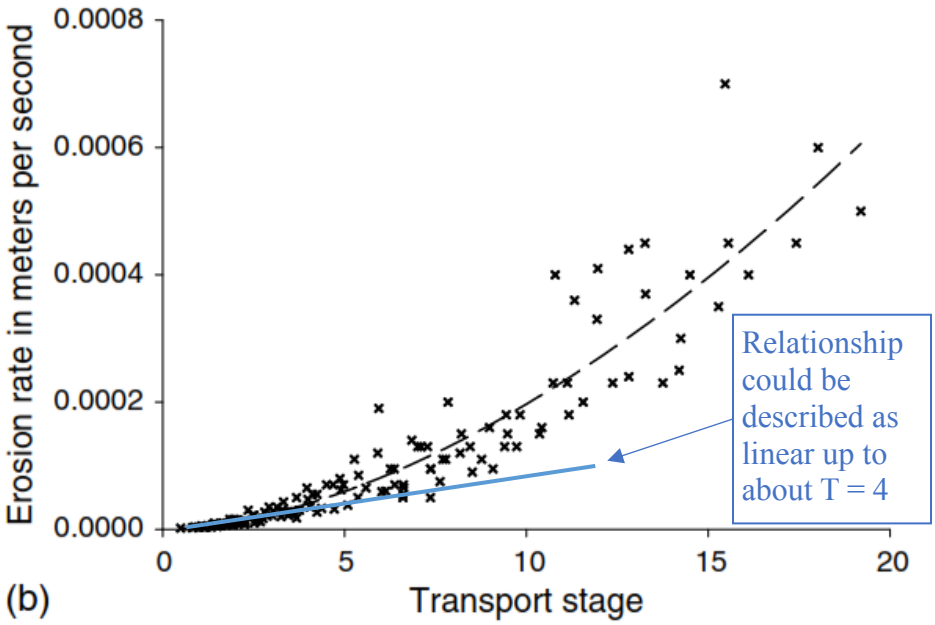

Figure 119. Exponential model proposed by Walder (2016) - Data by Jepsen et al. (1997), with added annotations by Salem, H. (in blue)

The data and discussions provided herein lead to an important question: what if the flow test used in the erosion experiments, inducing a shear stress well above the critical shear of the soil, is continued for an extended duration? The soil sample in this case would be subjected to a constant morphological change by losing soil clusters, and therefore, as shown in Section 5.3.5, the actual shear stress on the soil will continue to increase, leading to an exponential growth in erosion rate until complete blowout of the sample, or, in the case of full-scale field observations, a natural change in roughness and/or geometry, reducing the shear stress on the bed by reducing the flow intensity. What this means is that behavioral observations drawn from experimenting with shear stresses above the critical shear of the soil have temporal limitations; in other words, they can be applied to relatively short-term flows, and the higher the shear stress above the critical level, the shorter the validity time of the proposed behavior. Based on crude observations from examining published data (Jepsen et al., 1997; Elliot et al., 1989), it is apparent that for stress exceedances of up to 2 to 3 times the critical shear stress it may be reasonable to assume that the erosion-stress relation holds over the long-term. Under these relatively low transport stage conditions many cohesive soils would erode by losing individual grains or small clusters as wash-load while maintaining their surface texture and constant shear stress from interacting with a steady flow. Higher stresses will result in an ever-changing texture of the soil surface due to large-cluster erosion, which in turn increases the bed shear stress (under constant flow condition) causing an exponential deterioration of the sample. Such behavior can be treated as a piece-wise linear relationship between shear and entrainment if a dynamic measurement of the shear stress is feasible.

5.3.8. **Limitations of the ERM**

In its current design, the ERM suffers some limitations:

- The sample dimensions of the sample are small and require precise measurement of the distance to the soil surface which requires skill and practice. Another consequence of the sample size is that some soils with relatively large structure sizes cannot be adequately tested
- The flow is too strong for some soils that cannot sustain such shear for too long without rapid deterioration
- Setting up the soil sample in the probe requires some manipulation of the soil

The following improvements are recommended to increase the accuracy and versatility of the ERM:

1. A more precise fabrication of the prototype. This could include more precise machining of the essential parts such as the nozzle and the sample pod, including a special access to insert the sample from the bottom of the pod to reduce the disturbance of the sample surface.
2. A wider nozzle and a larger sample pod allowing deeper erosion would also be excellent improvements that would allow for testing soils with larger features and allowing deeper erosion to increase the tolerance on distance measurements
3. Another valuable addition would be a mechanism to reduce the flow intensity out of the nozzle without creating turbulent bursts; such improvement would facilitate the testing of low cohesion and granular soil samples which can only sustain a lower range of fluid shear without disintegrating.

6. CORRELATION WITH MATERIALS TEST DATA

One of the questions raised in this research work is whether the erodibility of cohesive soils or any of its elements (critical shear or erosion rate) can be linked or correlated to any of the physical characteristics of the soil, specifically, any of its strength parameters determined through traditional geotechnical laboratory testing. There are ample data determined for the ten core soils to investigate such relationships. The summarised results for the core soils shown in Appendix 3, Table A3-1, are examined for this purpose and plotted as follows:

- The critical shear τ_c determined from the flume and Erosionometer tests on the first set of samples, and from the Erosionometer tests on the second core set of samples are plotted against the effective cohesion c' in Figure 120, against the effective angle of internal friction ϕ' in Figure 121, and against the undrained shear strength τ_u in Figure 122.
- Similarly, the coefficient of erodibility K (Excess shear model with exponent $m = 1$) determined from ERM measurements for the second set of samples of core soils are plotted against the effective cohesion c' in Figure 123, against the effective angle of internal friction ϕ' in Figure 124, and against the undrained shear strength τ_u in Figure 125.

After a quick examination of the plots in Figure 120 through Figure 125, no discernable trend or correlation could be identified. This is consistent with the findings of other researchers exploring such relationships (Raudkivi, 1976, and others).

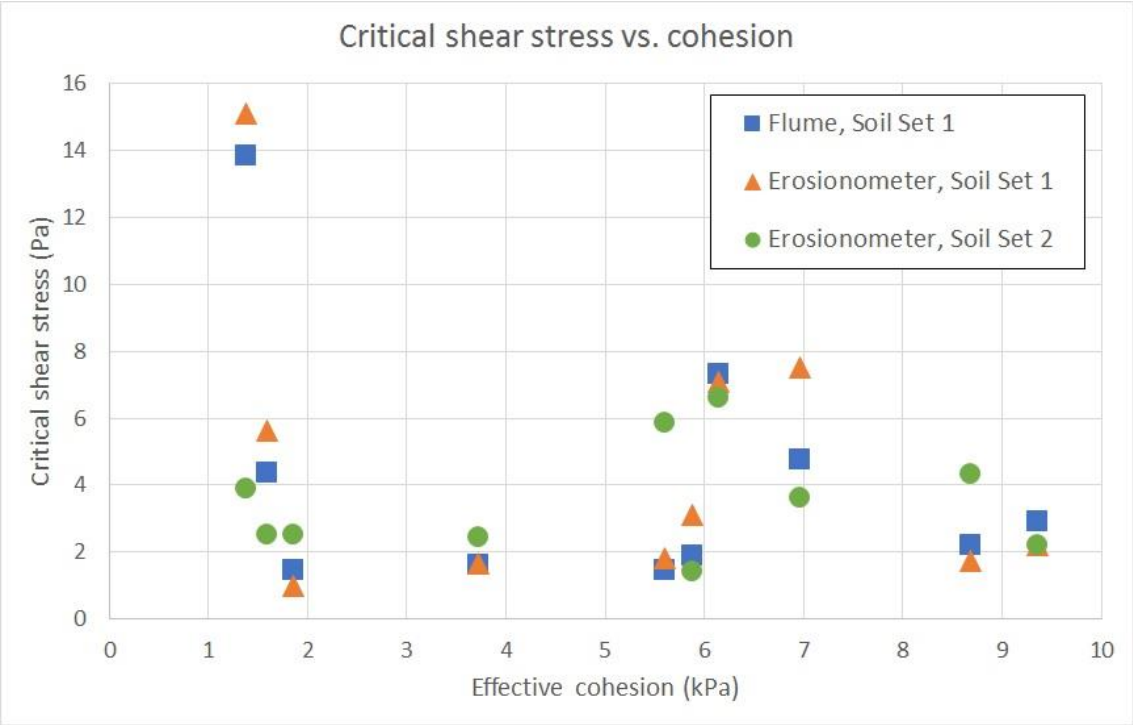

Figure 120. Critical shear stress τ_c vs. effective cohesion c'

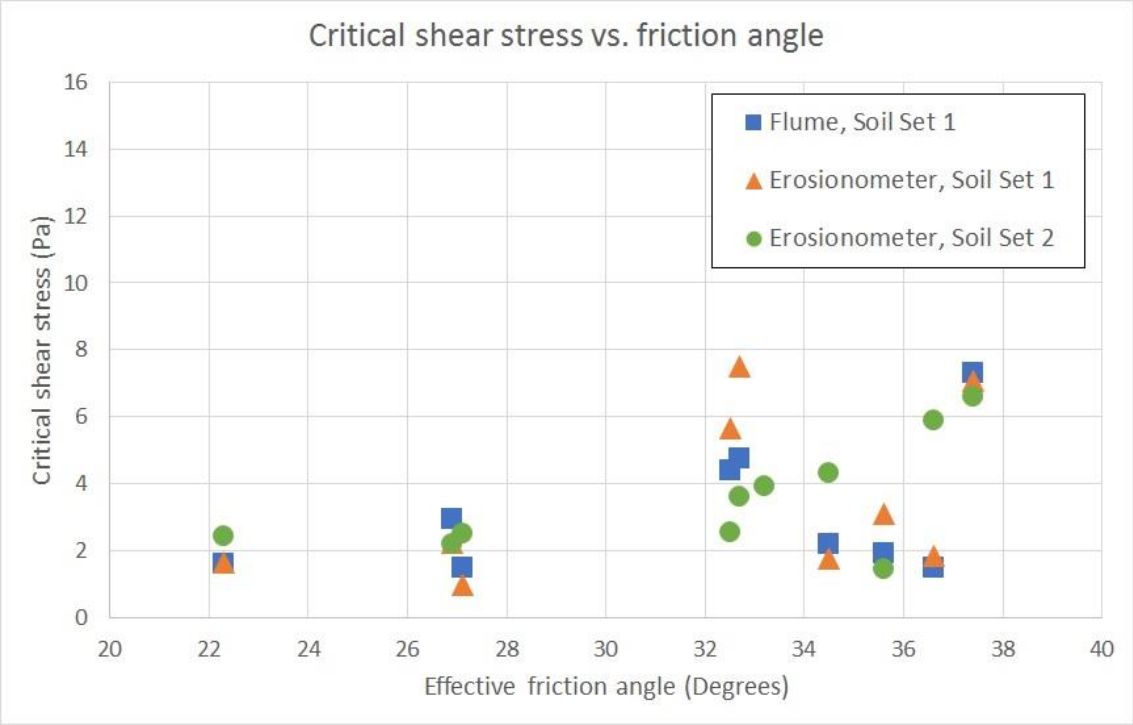

Figure 121. Critical shear stress τ_c vs. effective angle of internal friction ϕ'

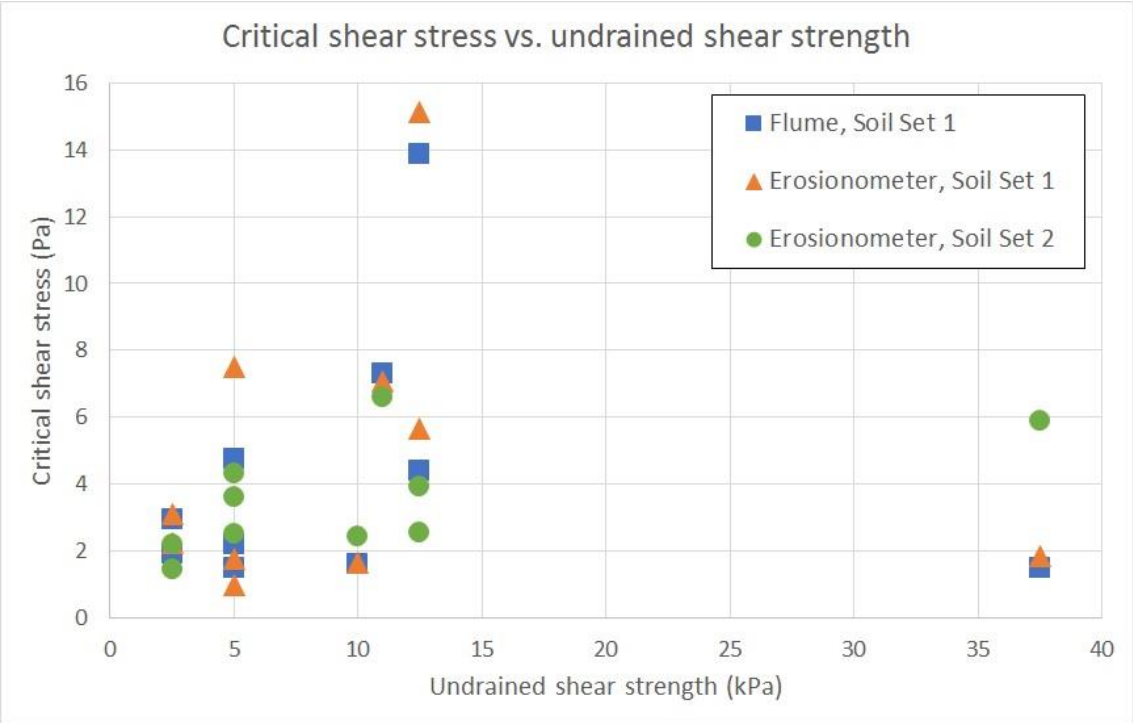

Figure 122. Critical shear stress τ_c vs. undrained shear strength τ_u

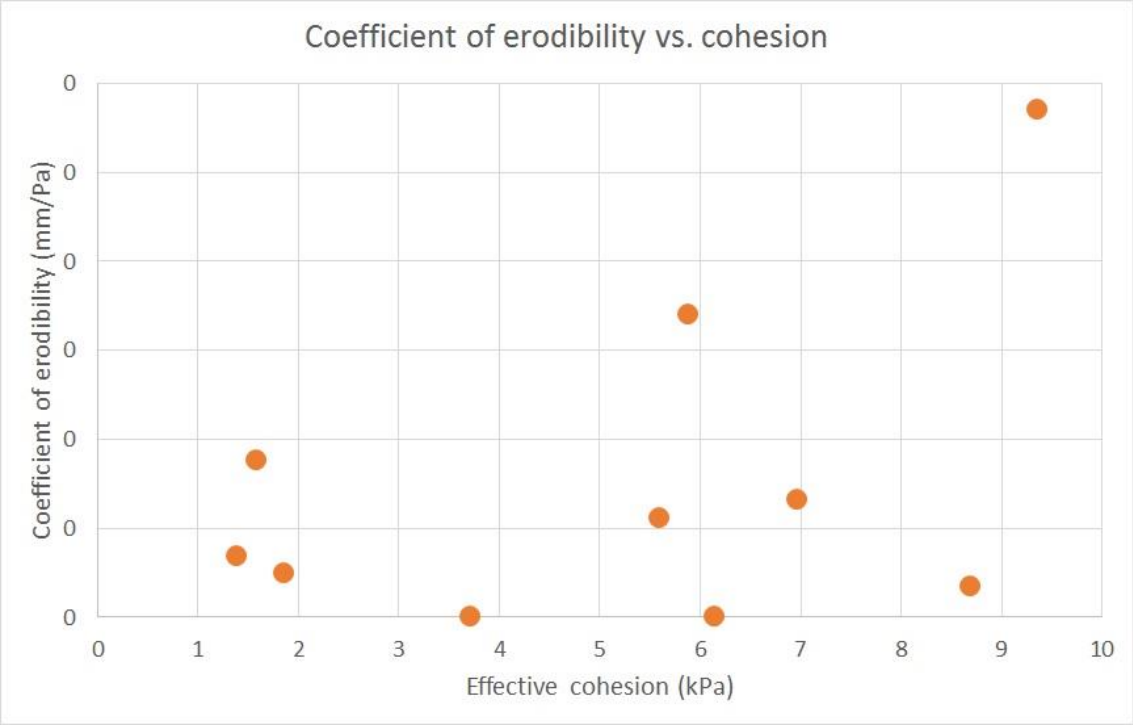

Figure 123. Coefficient of erodibility *K* vs. effective cohesion *c*'

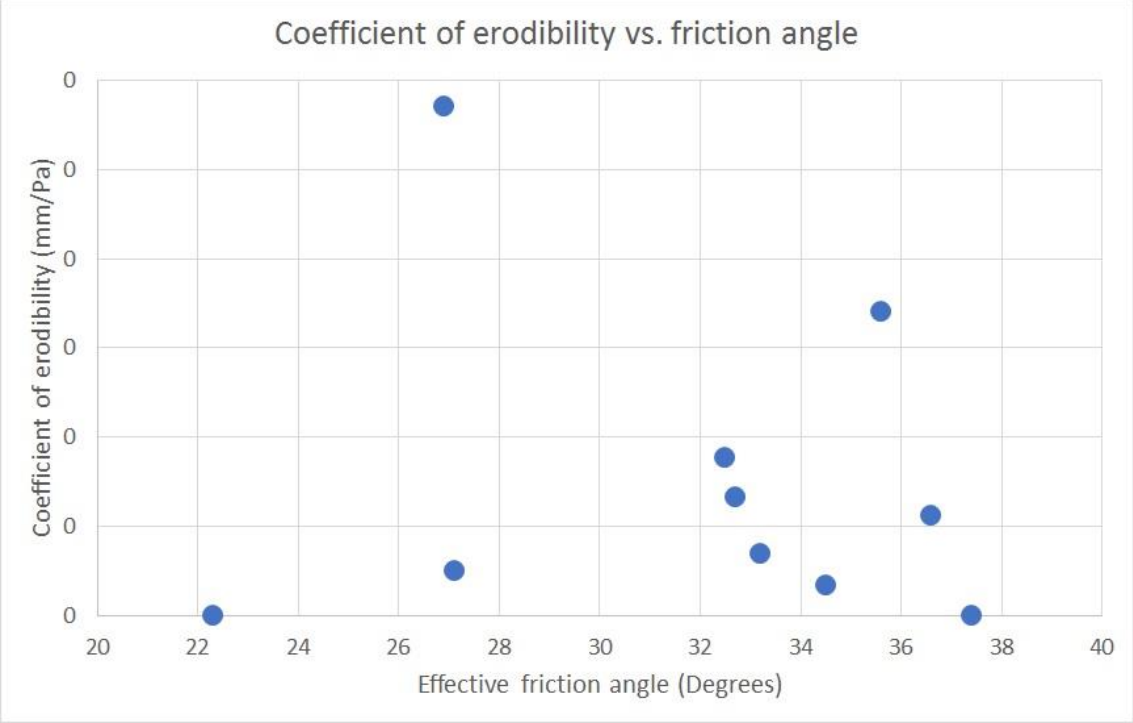

Figure 124. Coefficient of erodibility *K* vs. effective angle of internal friction ϕ'

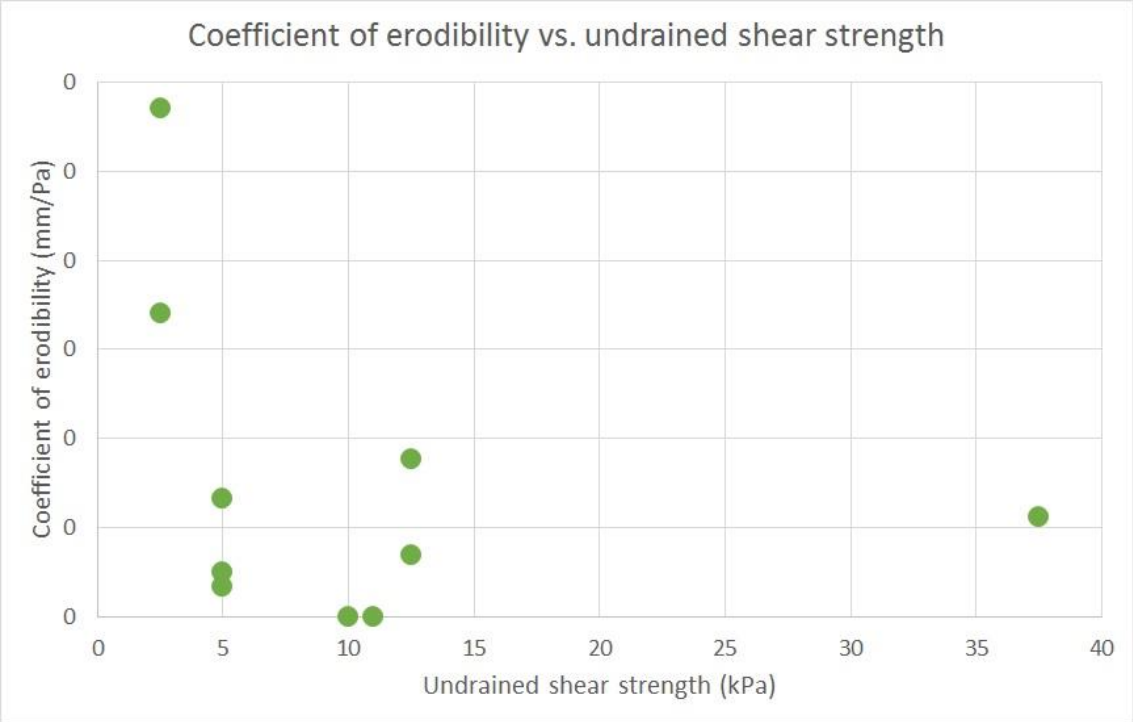

Figure 125. Coefficient of erodibility K vs. undrained shear strength τ_u

7. DISCUSSION AND CONCLUSIONS

It was highlighted throughout this research that the interaction between cohesive soils and turbulent flow is extremely complex and practically unpredictable. This complexity arises from the fact that the virtually weightless microscopic grains, which act as the matrix and binder of cohesive soils in general, can behave as much heavier particles due to the electro-chemical bonds between them. These bonds dwarf the gravity effects dominant in cohesionless granular soils. These stable cohesive particles of many different denominations (kaolinite, illite, montmorillonite, etc.), are deposited in many different environments (marine, glacial, lacustrine, etc.), and more importantly, combined with a variety of other particles (silts and sands). It is therefore natural to encounter unlimited variations of cohesive soils in terms of composition and behavior under fluid shear (see Appendix 1). As such, it is highly unlikely that the erodibility characteristics of a cohesive soil can be determined from its description, class, or gradation. Some researchers try to relate the erodibility of cohesive soils to their mechanical properties established through geotechnical testing techniques, which makes sense in principle; however, it was shown that the cohesion and shear resistance potential at the free surface of the soil and in the deeper confined continuum differ by orders of magnitude. This was best expressed by Raudkivi (1976), in his book "Loose boundary hydraulics":

"The angle. of friction in cohesive soils has so far eluded a definition. Even in sands the definition of the angle of friction in terms of grain size has met with little success because of the effects of variation of grain shape and structure of packing. Two clays with identical grain size distribution can differ in all

other respects, in soil mechanics the intercept of the t-line on the t-s plane is called the cohesion, but this is not necessarily the strength of the unconfined saturated clays. The various shear strength test procedures are described in texts on soil mechanics. In general, the shear strength of a soil has little bearing on its erodibility. Critical shear stresses have been found to be orders of magnitude lower than corresponding soil shear strength and the same flow conditions may initiate erosion in cohesive soils which differ in shear strength by orders of magnitude."

In this research, some of the cohesive soil erosion theories and methods used by researchers and the industry were examined. As a result, the following issues were identified:

- Testing methods and devices being used for assessing the erodibility of cohesive soils suffer from many drawbacks and misconceptions
- There is no consensus in the research community on adequate testing methods, representative erosion models, etc.

Regarding erosion testing, issues with determining the bed shear stress during the test were identified. Consequently, a wide range of models have been proposed as researchers looked for trends in uncertain data with high scatter.

With respect to the engineering aspects, reliable data and models are required within reasonable time and cost to resolve issues like stability, loss of property and habitat, scour, sediment accumulation, drainage design, etc. Still, a reliable assessment for the erodibility of a cohesive soil bed requires a research-level investigation at a relatively high cost.

It is in the Author's opinion that existing means and methods of assessing the erosion potential and rate are not adequate, and further work is needed. The broad objective of this research was to develop a set of solutions to the cohesive soil erosion problem. The targeted solutions would be a suite of practical testing devices and procedures combined with confirming a practical mathematical model for cohesive soil erosion. Such solutions would help establish the study of cohesive soil erosion as a standalone discipline.

A first device, the Erosionometer, was developed to perform a quick and reliable test to determine the critical shear stress of soils. This device is portable, easy to deploy in the field and in the laboratory and allows engineers and researchers to cover a sizeable terrain by performing many tests in a short timeframe, with immediate results. In engineering practice, the erosion threshold or critical shear stress is one of the most important erosion parameters for stable designs of slopes, submerged structures, drainage waterways, and other project classes as the objective is to avoid the long-term deterioration of such structures. This makes the Erosionometer a versatile tool for designers and researchers.

In addition to the demonstrated versatility of the Erosionometer, a simple modification allowing the application of different pressures on each side of the soil sample provided the capability to study the effect of subsurface hydrology on soil erosion. This capability was proven by replicating through simple

and fast experiments the results of complex and extensive research in this domain. As a result, a simple linear relationship was developed to quantify the effect of downward (drainage) hydraulic gradient on the critical shear of cohesive soils. This is similar to test results reported by Nouwakpo et al. (2010) using a large-scale hillside model (see Section 4.3.1). Further modifications to the Erosionometer device added the capability of introducing an upward pressure gradient on the sample; however, this was not tested at this stage and may be a subject for continued research work.

A second device, the Erosion Rate Meter, or ERM, was developed to test cohesive soil samples to determine the rate of erosion under various levels of bed shear stress. This device, while being portable and fast to setup and use, is a very realistic simulation of the flow-bed interaction and allows for a direct measurement of bed shear stress on the soil sample and a precise measurement of the erosion rate. In addition, the ERM allows for a fast and controlled variation of flow intensity, therefore the resulting bed shear stress. In projects or cases where a controlled exceedance of the erosion threshold is required or expected, the ERM can be used to assess the impact of such exceedance for a safe and economical design. An obvious outcome of using the ERM is the easy development of erosion rate vs. bed shear stress relationships or models to characterize different soils for design projects or further research.

Based on ERM tests performed on several cohesive soil samples collected from different sites in Ontario, the erosion rate appears to be proportional to the bed shear stress (linear model), which suggests that other, more elaborate models proposed in literature may not justify the added effort. A thorough review of a popular deterministic model (Wilson, B. N., 1993a and 1993b), as part of this research, revealed multiple inconsistencies, especially when it comes to using physical soil description as input to determine its erodibility. In the Author's opinion, it is clear from the review that, while the curve-fitting version of the model can still be used when fitted to test data, the simpler linear excess shear model is more representative of soil behavior.

The testing systems and methods developed in this research provide a comprehensive solution to the erodibility of cohesive soils from investigation to design. Significant improvements are achieved in the speed, reliability, accuracy, and cost of modelling the erodibility of cohesive soils over existing systems. In addition, further improvements and automation can be introduced to upgrade the prototypes. More testing may be performed on a range of different soils to reinforce the findings and develop valuable databases on the behavior of regional soils. Such additional work is beyond the scope of this research.

It should be added that, while the devices presented in this research were developed for cohesive soils, they may also be applicable to slightly cohesive mixes or even some granular soils, which are outside the scope of this research and may be pursued as a separate undertaking.

8. REFERENCES

Aberle, J., Nikora, V., McLean, S., Doscher, C., McEwan, I., Green, M., Goring, D., and Walsh, J. (2003).

"Straight Benthic Flow-Through Flume for In Situ Measurement of Cohesive Sediment

Dynamics.", J. Hydraul. Eng., 10.1061/(ASCE)0733-9429(2003)129:1(63)

Ade, F., and Rajaratnam, N. (1998). "Generalized study of erosion by circular horizontal turbulent jets.", Journal of Hydraulic Research, 36(4), 613-636. doi:10.1080/00221689809498612

Afzalimehr, H., Rennie, C.D. (2009). "Determination of bed shear stress using boundary layer parameters in a gravel-bed river." Hydrological Sciences Journal, 54(1):147-159, 2009

Al-Dahlaki, M. H., and Al-Sharify, G. A. (2008). "A proposed approach for plastic limit determination using the drop-cone penetrometer device." J. Eng. Dev., 12(1), 107–117.

Al-Madhhachi, A. T., Hanson, G. J., Fox, G. A., Tyagi, A. K., & Bulut, R. (2013). "Deriving Parameters of a Fundamental Detachment Model for Cohesive Soils from Flume and Jet Erosion Tests." Transactions of the ASABE, 56(2), 489-504. doi:10.13031/2013.42669.

Al-Madhhachi, A., Fox, G., Hanson, G., Tyagi, A., and Bulut, R. (2014a). "Mechanistic Detachment Rate Model to Predict Soil Erodibility Due to Fluvial and Seepage Forces." J. Hydraul. Eng., 10.1061/(ASCE)HY.1943-7900.0000836, 04014010.

Al-Madhhachi, A. T., Fox, G. and J. Hanson, G. (2014b). "Quantifying the erodibility of streambanks and hillslopes due to surface and subsurface forces." Transactions of the ASABE, Vol. 57, No. 4, pp. 1057-1069, DOI: 10.13031/trans.57.10416.

Amos, C.L., Daborn, G.R., Christian, H.A., et al. (1992). "Insitu erosion measurement on fine-grained sediments from the Bay of Fundy." Marine Geology, Vol. 108, Issue 2, pp. 175-196.

Anthony, D. J. (2001). "*Applying Geomorphology to Environmental Management*." Water Resources Publication.

Barnes, Matthew P., and Tom E. Baldock, 2007. "Direct Bed Shear Stress Measurements in Bore-Driven Swash and Swash Interactions." Coastal Sediments '07. doi:10.1061/40926(239)153.

Beltaos S., Rajaratnam N. (1974). "Impinging circular turbulent jets." J Hydraul Div, Vol. 100, pp. 1313–1328

Briaud, J. L., Ting, F. C. K., Chen, H. C., Gudavalli, R., Perugu, S., and Wei, G. (1999). "Sricos: Prediction of Scour Rate in Cohesive Soils at Bridge Piers." J. Geotech. Geoenviron. Eng., Vol. 125, No. 4, pp. 237–246.

Briaud, Jean-Louis, Govindasamy, Anand V., and Shafii, Iman, 2017. "Erosion Charts for Selected Geomaterials." Journal of Geotechnical and Geoenvironmental Engineering 143, no. 10 (2017), 04017072. doi:10.1061/(asce)gt.1943-5606.0001771.

Campbell, D. J. (1976). "Plastic Limit Determination Using A Drop-Cone Penetrometer." Journal of Soil Science, 27(3), 295-300. doi:10.1111/j.1365-2389.1976.tb01999.x.

Chapman, L.J. and D.F. Putnam. 1984. "The Physiog- raphy of Southern Ontario, Third Edition" Ontario Geological Survey, Special Volume 2, Ontario Ministry of Natural Resources.

Chepil, W. S. (1959). "Equilibrium of soil grains at the threshold of movement by wind.", Soil Science Society America Proceedings 23(6):422-428.

Chu-Agor, M.L., G.A. Fox, R.M. Cancienne, and G.V. Wilson, (2008). "Seepage caused tension failures and erosion undercutting of hillslopes." Journal of Hydrology 359, no. 3-4 (2008), 247-259. doi:10.1016/j.jhydrol.2008.07.005.

Coles, D. (1956). "The law of the wake in the turbulent boundary layer." J. Fluid Mech., Cambridge, U.K., I, 191-226.

Collins, K., and Mcgown, A. (1974). "The form and function of microfabric features in a variety of natural soils.", Géotechnique, 24(2), 223-254. doi:10.1680/geot.1974.24.2.223.

Crowley, R., Robeck, C., and Thieke, R. (2014). "Computational Modeling of Bed Material Shear Stresses in Piston-Type Erosion Rate Testing Devices." J. Hydraul. Eng., 10.1061/(ASCE)HY.1943-7900.0000797

Dey, S., and Sarkar, A. (2006). "Response of velocity and turbulence in submerged wall jets to abrupt changes from smooth to rough beds and its application to scour downstream of an apron.", Journal

of Fluid Mechanics, 556, 387. doi:10.1017/s0022112006009530

Debnath, K., Nikora, V., Aberle, J., Westrich, B., and Muste, M. (2007). "Erosion of Cohesive Sediments: Resuspension, Bed Load, and Erosion Patterns from Field Experiments.", J. Hydraul. Eng., 10.1061/(ASCE)0733-9429(2007)133:5(508).

Einstein, H. A. and El-Samni,E. A. (1949). "Hydrodynamic forces acting on a rough wall.", Reviews Modern Physics 21(3):520524.

Elliot, W. J., Liebenow, A. M., Laflen, J. M., and Kohl, K. D. (1989). "A compendium of soil erodibility data from WEPP cropland soil field erodibility experiments 1987 and 1988." NSERL ASCE, Report No. 3. Columbus, OH: Ohio State University and USDA Agricultural Research Service.

Fox, Garey A., Glenn V. Wilson, Andrew Simon, Eddy J. Langendoen, Onur Akay, and John W. Fuchs, (2007). "Measuring streambank erosion due to ground water seepage: correlation to bank pore water pressure, precipitation and stream stage." Earth Surface Processes and Landforms 32, no. 10, 1558-1573. doi:10.1002/esp.1490.

Gaskin, S.J., Pieterse, J., Al Shafie, A., and Lepage, S. (2003). "Erosion of undisturbed clay samples from the banks of the St. Lawrence River." Canadian Journal of Civil Engineering, Vol. 30, pp. 585-595.

Ghaneeizad, S.M., Atkinson, J.F. (2015). "Effect of flow confinement on the hydrodynamics of circular impinging jets: implications for erosion assessment." Environ Fluid Mech, Vol. 15, pp. 1–25

Grabowski, R.C., Droppo, I.G., and Wharton, G., 2012, "Estimation of critical shear stress from cohesive strength meter-derived erosion thresholds", Limnol. Oceanogr.: Methods, DOI 10.4319/lom.2010.8.678–685.

Hanson, G. J. (1991). "Development of a jet index to characterize erosion resistance of soils in earthen spillways." Transactions of the ASAE, Vol. 34, Issue 5, pp. 2015-2020.

Hanson, G. J. and Cook, K. R. (2004). "Apparatus, test procedures, and analytical methods to measure soil erodibility in situ." American Society of Agricultural Engineers, Vol. 20, Issue 4, pp. 455-462.

Haralampides, K., Rodgriguez, A. (2006) Erosional properties of the sediments in the Petitcodiac River estuary at Moncton, New Brunswick, Canadian J. Civil Engineering, 33:1209-1216.

Hollick, M. (1976). "Towards a routine test for the assessment of critical tractive forces of cohesive soils." Transactions of the ASAE, Vol. 19, Issue 6, pp. 1076-1081.

Holtz, R. D., and Kovacs, W. D. (1981). "An Introduction to geotechnical engineering.", Englewood Cliffs, NJ: Prentice Hall.

Huang, C., and Laflen, J. (1996). Seepage and soil erosion for a clay loam soil. Soil Science Society of America Journal 60: 408-416.

Inderbitzen, A. L. (1961). "An Erosion Test for Soils." Mater. Res. Stand, Vol. 1, No. 7, pp. 553-554.

Jepsen, R., Roberts, J., and Lick, W. (1997). “Effects of bulk density on sediment erosion rates.” Water Air Soil Pollut., 99, 21–31

Julian, J. P. and Torres, R. (2006). "Hydraulic erosion of cohesive riverbanks." Geomorphology, Vol. 76, pp. 193–206.

Kamphuis, J. W. (1983). "On the erosion of consolidated clay material by a fluid containing sand." Canadian Journal of Civil Engineering, 10(2), 223-231. doi:10.1139/l83-038

Kamphuis, J.W., and Hall, K.R., (1983). Initiation of erosion of consolidated cohesive materials by unidirection current. ASCE Journal of the Water Resources Planning and Management Division, 109: 49-61

Kamphuis, J. W., Gaskin, P. N., and Hoogendoorn, E. (1990). "Erosion Tests on Four Intact Ontario Clays." Can. Geotech. J., 27, No. 5, pp. 692–696.

Kassif, G., D. Zaslavsky, and J. Zeitlin (1965). "Analysis of Filter Requirements for Compacted Clays." Proceedings, Sixth International Conference Soil Mechanics and Foundation Engineering, Montreal, Canada, Vol. 2, pp. 495-499.

Kemper, W. D., and R. C. Rosenau, (1984). "Soil Cohesion as Affected by Time and Water Content."

Soil Science Society of America Journal 48, no. 5 (1984), 1001. doi:10.2136/sssaj1984.03615995004800050009x.

Kemper, W.D., Rosenau, R.C., Dexter, A.R., (1987). "Cohesion development in disrupted soils as affected by clay and organic matter content and temperature." Soil Sci Soc Am J. 1987;51:860-7. doi:10.2136/sssaj1987.03615995005100040004x

Khan I. and Kostaschuk, R. (2011). "Erodibility of cohesive glacial till bed sediments in urban stream channel systems." Canadian Journal of Civil Engineering, Vol. 38, pp. 1363 – 1372.

Kirkgöz, M. S., & Ardiçlioğlu, M. (1997). "Velocity Profiles of Developing and Developed Open Channel Flow." Journal of Hydraulic Engineering, 123(12), 1099-1105. doi:10.1061/(asce)0733-9429(1997)123:12(1099)

Knighton, David. Fluvial Forms and Processes: A New Perspective. Xv, 383 p: Ill, 1998.

Lim, Seok San; Khalili, Nasser (2009). "An Improved Rotating Cylinder Test Design for Laboratory Measurement of Erosion in Clayey Soils." Geotechnical Testing Journal, Vol. 32, Issue 3, pp. 232-238.

Locat, Ariane, Pascal Locat, Denis Demers, Serge Leroueil, Denis Robitaille, and Guy Lefebvre, 2017. "The Saint-Jude landslide of 10 May 2010, Quebec, Canada: Investigation and characterization of the landslide and its failure mechanism." Canadian Geotechnical Journal 54, no. 10 (2017), 1357-1374. doi:10.1139/cgj-2017-0085.

Lutz, J. F. (1934). The physico-chemical properties of soils affecting soil erosion, Univ. of Missouri, Columbia, MO.

Mazurek, K.A., Rajaratnam, N., and Sego, D. (2001). "Scour of Cohesive Soil by Submerged Circular Turbulent Impinging Jets." J. Hydraul. Eng., 10.1061/(ASCE)0733-9429(2001)127:7(598-606).

Mazurek, K.A., Rajaratnam, N., Sego, D.C. (2003). "Scour of a cohesive soil by submerged plane turbulent wall jets." J. Hydraul. Res., 41(2), pp. 195-206.

McNeil, J., Taylor, C., and Lick, W. (1996). "Measurements of erosion of undisturbed bottom sediments with depth.", Journal of Hydraulic Engineering, 122(6), 316-324

Moore, W. L. and Masch, F. D., Jr. (1962). "Experiments on the Scour Resistance of Cohesive Sediments." J. Geophys. Res., Vol. 67, No. 4, pp. 1437–1449.

Nadal-Romero, M.E., Verachtert, E., Maes, R., and Poesen, J. (2011). "Quantitative assessment of the piping erosion susceptibility of loess-derived soil horizons using the pinhole test." J. Geomorphology, Vol. 135, pp. 66–79.

Nouwakpo, Sayiro K., Chi-hua Huang, Laura Bowling, and Phillip Owens. (2010). "Impact of Vertical Hydraulic Gradient on Rill Erodibility and Critical Shear Stress." Soil Science Society of America Journal 74, no. 6 (2010), 1914. doi:10.2136/sssaj2009.0096.

Nouwakpo, S. K., and C. Huang. (2012). "The Role of Subsurface Hydrology in Soil Erosion and Channel Network Development on a Laboratory Hillslope." Soil Sci. Soc. Am. J. 76:1197-1211. doi:10.2136/sssaj2012.0013

Perez, M., Zech, W., Donald, W., and Fang, X. (2014). "Methodology for Evaluating Inlet Protection Practices Using Large-Scale Testing Techniques." J. Hydrol. Eng., 10.1061/(ASCE)HE.1943-5584.0001019

Pértile, Patricia, José M. Reichert, Paulo I. Gubiani, Dörthe Holthusen, and André D. Costa, (2016). "Rheological Parameters as Affected by Water Tension in Subtropical Soils." Revista Brasileira de Ciência do Solo 40, no. 0 (2016). doi:10.1590/18069657rbcs20150286.

Phares DJ, Smedley GT, Flagan RC (2000). "The wall shear stress produced by the normal impingement of a jet on a flat surface." J. Fluid Mech., Vol. 418, pp. 351–375.

Rankin, Kelly L., and Hires, Richard I., 2000. "Laboratory measurement of bottom shear stress on a movable bed." Journal of Geophysical Research: Oceans 105, no. C7, 17011-17019. doi:10.1029/2000jc900059.

Raudkivi, A. J. (1976). *Loose boundary hydraulics*. Oxford: Pergamon Press.

Raudkivi, A. J. (1998). Loose boundary hydraulics, 4th Edition, Rotterdam; Brookfield, VT.

Reddi, L. N., Lee, I. M., and Bonala, M. V. S. (2000). "Comparison of Internal and Surface Erosion Using Flow Pump Tests on a Sand-Kaolinite Mixture." Geotech. Test. J., Vol. 23, No. 1, pp. 116–122.

Richard, S.H., N.R . Gadd, and J.S. Vincent. (1977). "Surficial Materials and Terrain Features, Ottawa-Hull." Map 1425A. Scale 1:125,000. Geological Survey of Canada.

Salem, Hicham, Colin Rennie, and Carlo Zaro Custodio, 2014. "Influence of pore pressure on clay erosion." In River Flow 2014: Proceedings of the International Conference on Fluvial Hydraulics, (River Flow 2014), Lausanne, Switzerland, 3-5 September 2014, edited by Anton Schleiss International Conference on Fluvial Hydraulics, Giovanni De Cesare, Mário J. Franca, and Michael Pfister, 1553-1560. CRC Press, 2014.

Schut, L. W., Wilson, E. A., Ontario. Ministry of Agriculture and Food, Pedology, O. I., & Centre, L. R. (1987). The Soils of the Regional Municipality of Ottawa-Carleton.

Simon, A., and S.E. Darby. 1999. The nature and significance of incised river channels. p. 3–18. In S.E. Darby and A. Simon (ed.) Incised river channels: Processes, forms, engineering and management. John Wiley & Sons, New York.

Simon, Andrew, and Collison., Andrew J., 2001. "Pore-water pressure effects on the detachment of cohesive streambeds: seepage forces and matric suction." Earth Surface Processes and Landforms 26, no. 13, 1421-1442. doi:10.1002/esp.287.

Sherard, J. L., Dunnigan, L. P., Decker, R. S., and Steele, E. F. (1976). "Pinhole Test for Identifying Dispersive Soils." J. Geotech. Engrg. Div., Vol. 102, No. GT1, pp. 69–85.

Smerdon, D. B., and Beasley, M. L. (1959). Tractive force theory applied to stability of open channels in cohesive soils, Univ. of Missouri, Columbia, MO.

Southard, John, (2006). *12.090 Introduction to Fluid Motions, Sediment Transport, and Current-*

Generated Sedimentary Structures. Fall 2006. Massachusetts Institute of Technology: MIT OpenCourseWare, https://ocw.mit.edu. License: Creative Commons BY-NC-SA.

Ternat, F., Boyer, P., Anselmet, F., and Amielh, M. (2008). "Erosion threshold of saturated natural cohesive sediments: Modeling and experiments." Water Resour. Res., Vol. 44, W11434, pp. 1-18.

Terwindt, J.H.J., Breusers, H.N.C., and Svasek, J.N. (1968). "Experimental investigation on the erosion-sensitivity of a sand-clay lamination." Sedimentology, Vol. 11, pp. 105-114.

USDA-NRCS, (2012). "Part 650 - Engineering Field Handbook." H_210_NEH_650 - Amend. 48 - January 2012, Ch.3

UNESCO, (2017). "Water management curricula using ecohydrology and integrated water resources management." First edition, April 2017.

Valentin, C., J. Poesen, and Y. Li, (2005). "Gully erosion: Impacts, factors and control." Catena 63:132–153. doi:10.1016/j.catena.2005.06.001

van Rijn, L. (1984). "Sediment Transport, Part I: Bed Load Transport." J. Hydraul. Eng., 10.1061/(ASCE)0733-9429(1984)110:10(1431), 1431-1456.

Walder, Joseph S. (2016). "Dimensionless Erosion Laws for Cohesive Sediment." J. Hydraul. Eng., 10.1061/(ASCE)HY.1943-7900.0001068, 142(2): 04015047-1-13.

Wilson, B. N. (1993a). "Development of a fundamental based detachment model." T. ASAE, 36(4), 1105–1114.

Wilson, B. N. (1993b). "Evaluation of a fundamental based detachment model." T. ASAE, 36(4), 1115–1122.

Winterwerp, J. C., Kesteren, W. G., Prooijen, B. V., & Jacobs, W. (2012). "A conceptual framework for shear flow-induced erosion of soft cohesive sediment beds." Journal of Geophysical Research: Oceans, 117(C10). doi:10.1029/2012jc008072

Yalin, M.S. (1992), River mechanics, Pergamon Press, New York.

Zheng, F., Huang, C., and Norton, L.D., (2000). "Vertical Hydraulic Gradient and Run-On Water and Sediment Effects on Erosion Processes and Sediment Regimes." Soil Science Society of America Journal 64: 4-11.

Appendix 1:
In-depth review of
Wilson's Fundamentally based detachment model

9. FUNDAMENTALLY BASED DETACHMENT MODEL

In this study, the model proposed in Wilson (1993a and 1993b) (the Wilson model), which was briefly introduced in Section 4.2.1, will be closely examined. In order to keep track of the inherent uncertainties in the formulation, the introduction of proposed factors and coefficients will be underlined throughout the description of the model and derivations for quick future reference and clarity.

9.1 Framework of the Wilson model

This section of the study will examine the fundamental structure of the proposed model. For further details, the reader is directed to the actual references (Wilson, 1993a and 1993b). Using the illustration shown in Figure 126, Wilson formulated a moment balance at which the incipient motion of a particle of diameter *d* occurs.

$$l_1 W_s \sin\alpha + l_3 F_d + l_4 F_L = l_2 W_s \cos\alpha + M_c \qquad 30$$

The terms on the left-hand side of Equation 30 represent the dislodging moments while the right-hand terms represent the resisting or stabilizing moments. Keeping in mind that the moment balance is applied for one grain size at a time, the terms in Equation 30 from left to right represent the following moments of forces causing rotation of the particle around the lee point of contact with the adjacent grain; l_1 through l_4 being the length of the corresponding moment arm of each force:

1. Component of the buoyant weight (W_s) of the particle parallel to the flow direction where α is the incline of the bed with respect to the horizontal.
2. Drag force (F_d) in the flow direction
3. Lift force (F_L) perpendicular to the flow direction (upward)
4. Component of the buoyant weight of the particle perpendicular to the flow direction (downward)
5. Sum of all moments (M_c) of friction and cohesion forces resisting detachment.

Using a proportionality between drag and lift forces proposed by Chepil (1959), Wilson proceeds to rewrite Equation 30 into a shorter form:

$$F_d = W_s \, (K_{ls} + f_c) \qquad 31$$

He defines K_{ls} and f_c as:

$$K_{ls} = [\cos\alpha \, (l_2 - l_1 \, S_0)] \, / \, \left[l_3 + l_4 \, K_L / k_f\right] \qquad 32$$

$$f_c = \left[M_c \, / \, \left(l_3 + l_4 \, K_L / k_f\right)\right] / \, W_s$$

Where S_o is the slope of the sediment bed (slope of the flow direction), K_L is the proportional constant between drag and lift coefficients and their respective velocities (Chepil, 1959), and k_f is the ratio of projected area for drag to that of lift forces.

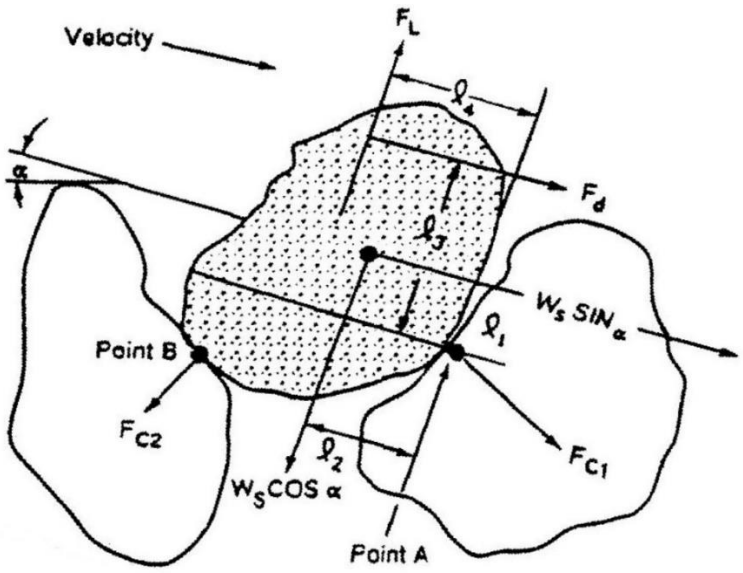

Figure 126. Illustration of moments acting on sediment grain, Wilson (1993a)

Before moving on to explore the formulation of the model, it is important to validate the basic principles on which the model is founded.

To begin, the basic assumption is that the model will be developed for a specific grain size and adding the computed detachment rates for all grain sizes in the mix, proportionally, to obtain the total detachment rate (Wilson, 1993b). It is the Author's opinion that such an assumption is not valid for cohesive soils, and even for well-graded non-cohesive granular soils. To illustrate, let us consider an actual representation of a cohesive soil matrix as shown in Figure 127, after Colins and Mcgown (1974). The infinite possibilities of soil matrix arrangement imply that the ideal representation in Figure 126is not realistic. The photos of various soil assemblages taken through an electron microscope, as presented by Colins and Mcgown (1974), are shown in Figure 128, and they further demonstrate the difficulty of a simple 2-D representation of surface grains. Therefore, looking at the 2-D representation in Figure 129, which is a modified and more realistic version of Wilson's illustration (Figure 126), we can conclude the following:

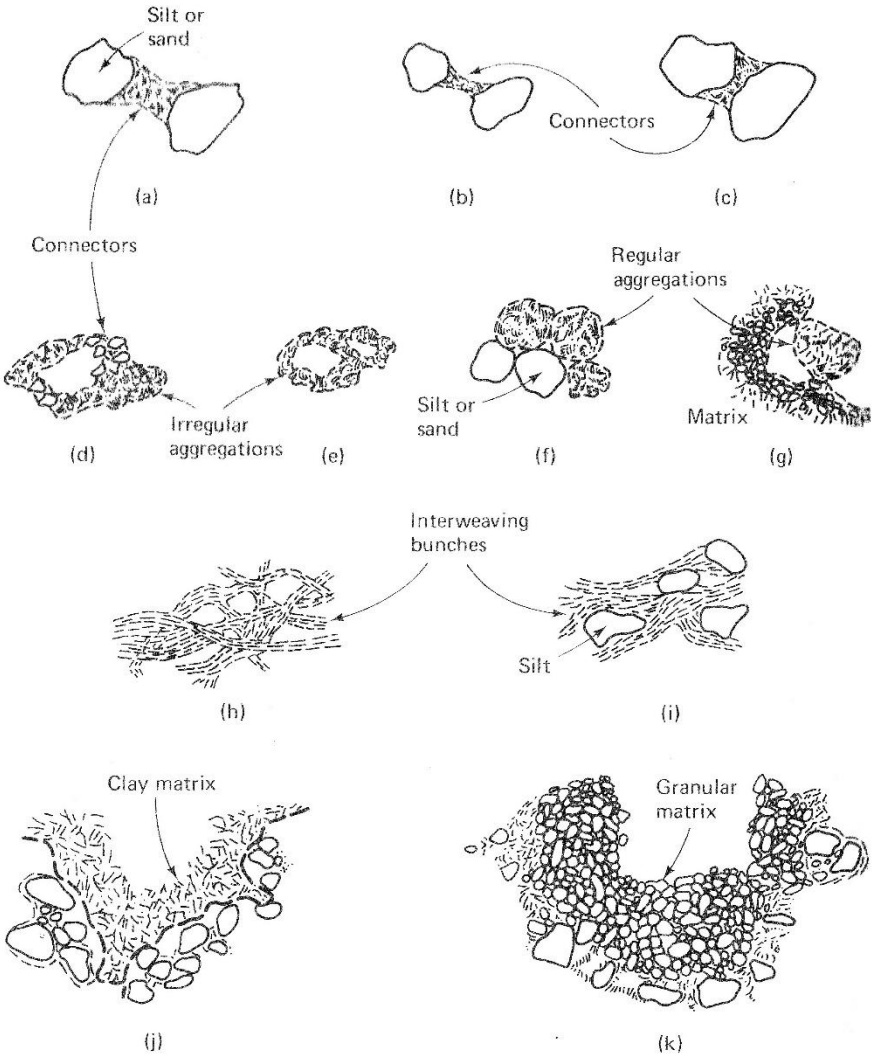

Figure 127. Schematic representations of particle assemblages, Collins and McGown (1974): (a), (b). and (c) connectors: (d) Irregular aggregations linked by connector assemblages: (e) Irregular aggregations forming a honeycomb arrangement; (f) regular aggregations Interacting with silt or sand grains: (g) regular aggregation Interacting with particle matrix: (h) interweaving bunches of clay; (I) Interweaving bunches of clay with silt inclusions; (j) clay particle matrix; (k) granular particle matrix.

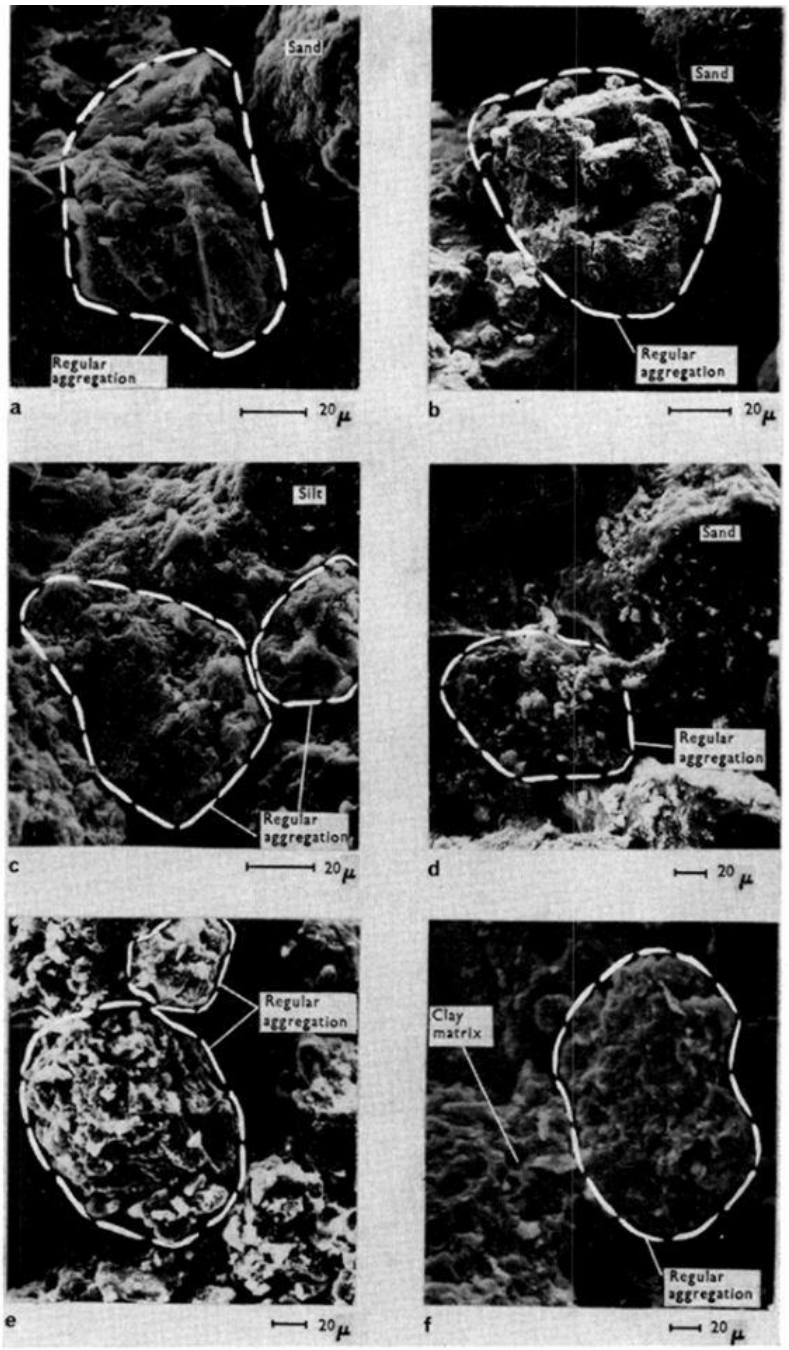

Figure 128. Regular aggregation assemblages, Collins and McGown (1974): (a) Lydda silty clay-Israel-freshwater alluvial deposit (consisting of connector assemblages and interacting with silt and sand); (b) Transvaal sand-South Africa-aeolian deposit (consisting of connector assemblages and interacting whth sand-; (c) Holon silty clay-Israel-freshwater alluvial deposit (consisting of elementary particle arrangements and interacting with each other and silt); (d) Reeks sandy till-Eire-glacial ablation deposit (consisting of elementary particle arrangements and interacting with sand); (e) Tucson silty clay-USA-freshwater alluvial deposit (consists of elementary particle arrangements interacting with silt and sand); (f) Holon silty clay-Israel-freshwater alluvial deposit (consisting of elementary particle arrangements interacting with clay particle matrix).

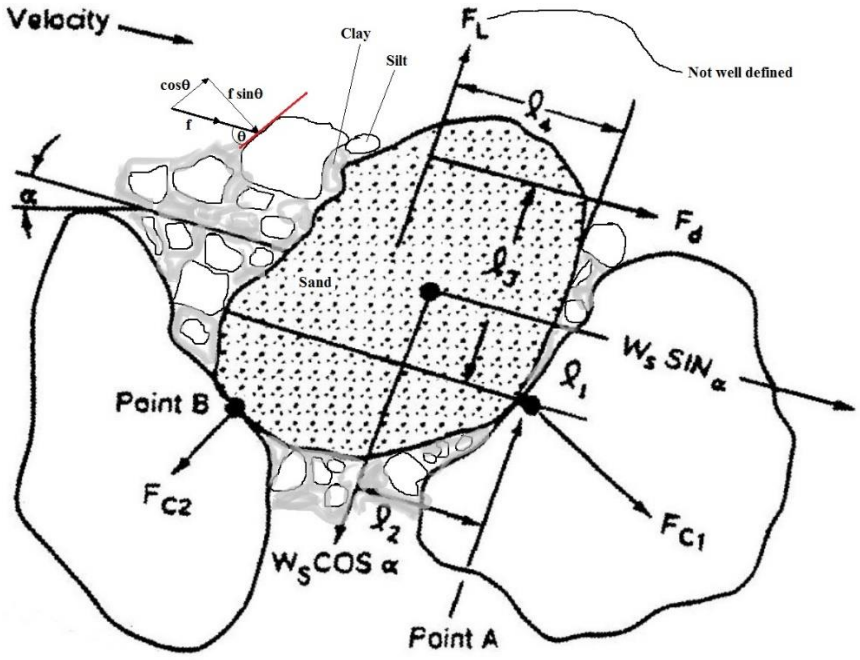

Figure 129. Modified illustration of the Wilson (1993a) concept for moments acting on sediment grain

- In addition to the resisting forces of friction and cohesion, a significant amount of bearing resistance exists between adjacent particles as the single point of contact between grains is not a realistic assumption in cohesive soils.
- At any point of impact of the moving fluid, unless the impacted particle face is perfectly perpendicular to the flow direction, which is statistically rare, the fluid impact force, f, which is represented in part by Wilson as a pure drag force (F_d) in the direction of the flow, can be resolved into two distinct components: tangent to the grain and perpendicular to the grain surface. While it could be argued that these components are partially accounted for in the drag and lift forces considered by Wilson, omitting the effect of the normal component is also not realistic as it could have a significant effect on particle stability by increasing the interparticle friction.

Furthermore, it is in the Author's opinion that adopting the proportionality of drag and uplift forces reported by Chepil (1959), is not appropriate in this case. The experiment conducted by Chepil involved near uniformly graded gravel under dry conditions in a wind tunnel (see Figure 130). Wind flow in this case can access the underside of the near spherical gravel grain and create a more or less consistent pressure differential between the underside and the top of the grain in accordance with Bernoulli's law. This is similar to the airfoil effect whereby a low-pressure pocket is created by the flow at the lee side of the particle while a high pressure is created underneath the particle. That said, in this case, as can be seen in Figure 129, the soil matrix in a cohesive soil mix does not allow the moving fluid to traverse underneath the grain, and while there is still a low pressure pocket behind the grain compared to the quasi-hydrostatic pore pressure in the soil matrix, the principle of proportionality with the drag force, at least the one stated by Chepil, cannot be adopted in this case.

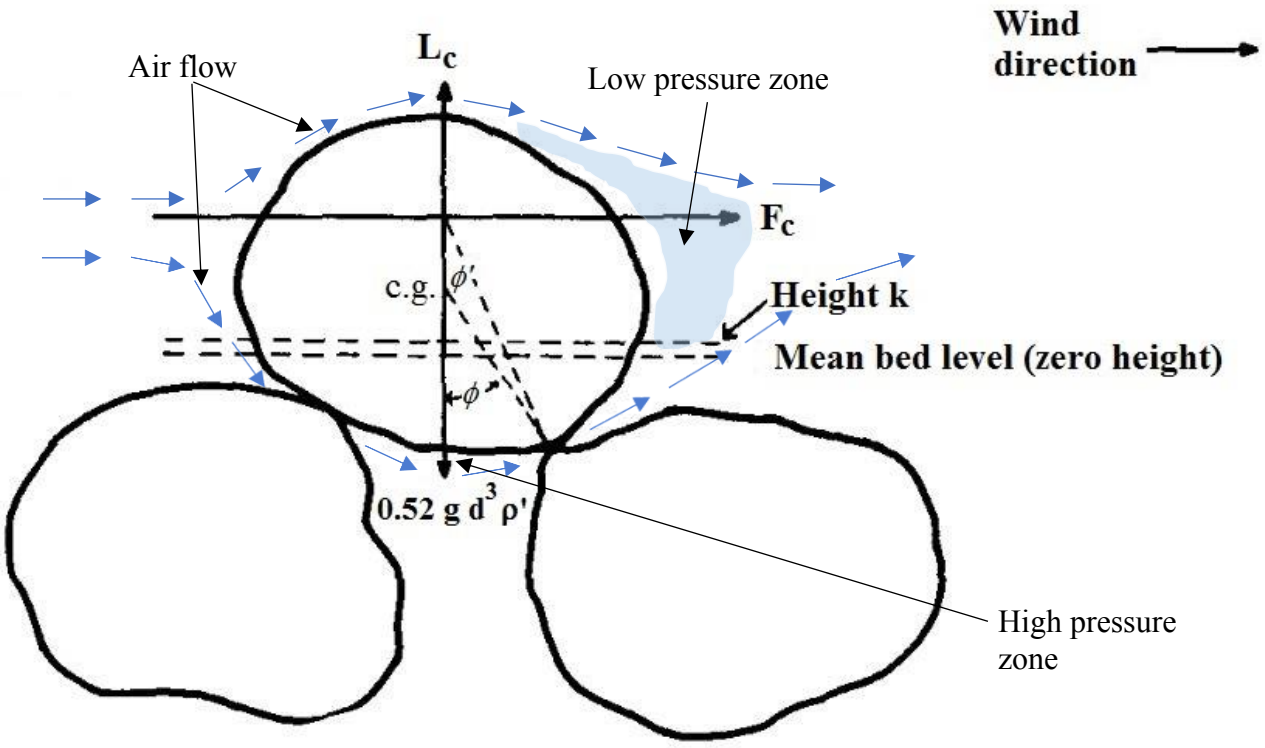

Figure 130. Illustration of forces and moments, uniform gravel in windtunnel, Chepil (1959)

9.2 Time-averaged dislodging forces

Einstein and El-Samni (1949), based on an experiment with turbulent flow over plastic half-spheres of diameter $K_s = 69\ mm$, glued to the base of the flume, reported that uplift pressure on the hemispheres can be related to time-averaged flow velocity close to the rough bed:

$$\Delta p = C_L\ (\rho/2) U_d^2$$

34

Where Δp is equivalent to the uplift pressure, C_L is the lift coefficient, ρ is the fluid density, and U_d is the time-averaged drag velocity measured at a specific height above a theoretical wall datum. The datum is defined by Einstein and El-Samni as $0.2 \times K_s$ below the top of the hemispheres (roughness). They further stated that the coefficient C_L is a constant "if and only if the velocity is measured at a distance of $0.35 \times K_s$ above the theoretical wall".

By assuming that the entire cross-section of the exposed grain ($k_a\ d^2$) is subject to the drag force, and using the previous assumption that the ratio of projected area of drag force to that of lift force is a constant k_f, Wilson rewrote the relationship in Equation 34 as:

$$\bar{F}_d = C_d\ k_f\ k_a\ d^2\ \frac{\rho U_d^2}{2}$$

35

Where $\bar{F}_d$ is time-averaged drag force, C_d is the drag coefficient, k_a is the area constant, and the remaining terms are as previously defined.

Before going further into the model, it is important to recall that Einstein and El-Samni stated at the start of their experiment that "any convenient size particle could be used to find the desired statistical pressure distributions as long as it is sufficiently large to make the surface hydraulically rough". Cohesive soils do not generally conform to such a criterion, and therefore, the relationships developed by Einstein and El-Samni should not have been adopted by Wilson for his model derivation.

Using the log-law and the definition of shear velocity, Equation 35 was evaluated as:

$$\bar{F}_d = K_d \, k_a \, d^2 \, \bar{\tau}$$

36

With the dimensionless hydraulic drag parameter K_d defined as:

$$K_d = \left[C_d \, k_f \, (ln(\varphi) \, / \, \kappa \, + B)^2\right] / \, 2$$

37

Where $\bar{\tau}$ is the average bed shear stress, φ is the ratio of the height where the drag velocity is measured (z) to the roughness height (K_s), κ is the Von Karman constant (about 4.0), and B is a dimensionless log-velocity factor dependent on the shear Reynolds number.

Another discrepancy is introduced by Wilson when using the log-law while measuring the height z from the base of the wall rather than from the theoretical wall datum defined by Einstein and El-Samni, which constitutes a deviation from the stated conditions. Therefore, C_L in Equation 34 cannot be taken as a constant, but rather varies with the flow characteristics.

Wilson then expresses the critical shear stress leading to incipient motion of the particle ($\tau_c = \bar{\tau}$) by equating the limit drag force expressed in Equation 31 to the time-averaged drag force in Equation 36 and using the following definitions:

$$k_r \, = \, k_v \, / \, k_a \; and$$
$$W_s = \, g \, (\rho_s - \rho) k_v \, d^3$$

38

Where k_v is the volume constant, k_r is the ratio of volume to area constants, g is the gravity acceleration, ρ_s is the density of the particle, and ρ is the density of the fluid. Therefore:

$$\tau_c = \frac{k_r}{K_d}\, g\, (\rho_s - \rho) d (K_{ls} + f_c)$$

39

Or in dimensionless form (τ_c^*) as

$$\tau_c^* = \frac{\tau_c}{g\, (\rho_s - \rho) d} = \frac{k_r}{K_d}\, (K_{ls} + f_c)$$

40

9.3 Turbulent dislodging forces

While the math in the previous section is quite rigorous, not withstanding the fundamental discrepancies listed in Section 9.2 , the biggest challenges to Wilson's model lie in the probabilistic approach discussed in this section.

Wilson defines the term P as the probability within a fixed duration that the instantaneous drag force exceeds the limit drag force provided in Equation 31. He then proceeds to equate this probability to a fraction of the total bed area subjected to drag forces beyond the incipient motion level. While this may be a valid assumption when applied to a large study area, it is not an obvious analogy when observing a limited test spot of the same general bed composition, especially when observations from the test zone are used to determine model parameters to be applied to the general bed area. This translates into an expression for the number of particles of diameter *d* per unit bed area that could potentially be detached within the set duration:

$$n_{di} = n_i\, P = \frac{\Delta FF_i P}{k_a\, d^2}$$

41

Where n_{di} is the number of particles of diameter *d* for potential detachment per unit bed area, n_i is the total number of particles of diameter *d* per unit bed area, ΔFF_i is the mass fraction finer than *d*, which is also assumed to be the fraction of bed area covered with particles of size *d*. Other elements are as defined earlier.

To address the rate of detachment, a time element is needed, and the proposed rate of detachment is:

$$n_{ri} = \frac{\Delta FF_i P}{k_a\, d^2 (K_e\, t_e)}$$

42

Where n_{ri} is the rate of detachment of particles of size *d*, t_e is the exchange time of a particle, and $\underline{K_e}$ is a parameter to account for the additional time to remove the surrounding particles such that the underlying particles are no longer protected from the flow. It is unclear at this point how this parameter will be determined, and no suggested value or range of values are provided in Wilson (1993b), but from

subsequent formulation, it appears that it will be lumped with other uncertainty factors to be determined experimentally.

Mass detachment rate (e_i) can be obtained instead by multiplying Equation 42 by the particle unit weight

$$e_i = n_{ri}\,\rho_s\,k_v\,d^3 = \frac{\Delta FF_i\,P\,\rho_s\,k_r\,d}{(K_e\,t_e)}$$

43

Linking the exchange time to particle exit velocity, Wilson defines the time-averaged net force acting in the direction of movement as $\bar{F}_n$ and assumes that cohesive forces are negligible after initial movement and simplifies the problem by considering the primary motion is sliding and rolling, thus simplifying the problem to the difference between drag and horizontal resistance forces in the form:

$$\bar{F}_n = K_t\,\bar{F}_d - \mu_f\,g(\rho_s - \rho)\,k_v\,d^3$$

44

The first term on the right-hand side of Equation 44 applies a factor K_t to the drag force to account for "the cumulation of instantaneous fluid forces" for which Wilson adopts a value of 2.5 reported by Chepil (1959), from wind experiments on dry gravel. The second term on the right-hand side of Equation 44 is the weight of the particle multiplied by a friction coefficient μ_f

Using Newton's second law, integrating the time-dependent particle acceleration ($\gamma = F_n/m$) over the exit time duration (t_e), with the particle mass as defined in Equation 43, the exit velocity becomes:

$$v_e = \frac{\bar{F}_n}{m}\,t_e = t_e\left(\frac{K_n\,\bar{\tau}}{(\rho_s-\rho)\,d} - \mu_f\,g\right)$$

45

With $K_n = K_t\,K_d\,k_r$ defined as a "combination of particle and fluid factors" which were introduced earlier.

Wilson then assumes that the movement required for exit consideration is proportional to the particle diameter and defines another proportionality coefficient k_d (not to be confused with K_d defined in Equation 37), such that:

$$t_e = \frac{k_d\,d}{v_e}$$

46

Invoking the dimensionless shear definition in Equation 40, replacing v_e in Equation 46 by Equation 45, and solving for t_e, Wilson obtains the exit time expression:

$$t_e = d\sqrt{\frac{k_d}{g\,d\,(K_n\,\tau^* - \mu_f)}}$$

47

Provided $K_n\,\tau^* > \mu_f$

To assess the detachment rate based on the probability of exceedance of the limit drag force defined in Equation 31, Wilson selected the Extreme Value Type 1 (EVT1) distribution.

By definition, the probability of the drag force exceeding the resisting moments given in Equation 31 can be written as:

$$P = 1 - F = 1 - \int_{-\infty}^{W_s\,(K_{ls} + f_c)} f(F_d)\,d(F_d)$$

48

Where F_d is the instantaneous drag force, P is the probability of the drag force to exceed the incipient motion threshold, F is the probability of the drag force to be below the incipient motion threshold, and f is the probability density function of the EVT1 distribution.

By definition, the probability of exceedance for this distribution is:

$$P = 1 - e^{-e^{-\mathcal{U}_e}}$$

49

Where $\mathcal{U}_e$ is the upper limit of integration for the EVT1 and is given by (see Wilson, 1993a, Appendix A):

$$\mathcal{U}_e = \left(\frac{\pi}{\mathcal{C}_v\sqrt{6}}\right)\left[\frac{k_r(K_{ls}+f_c)}{K_d\tau^*} - \left(1 - \frac{1.365\mathcal{C}_v}{\pi}\right)\right]$$

50

Where $\mathcal{C}_v$ is the coefficient of variation, and other terms are as previously defined.

By replacing the value of t_e and P in Equation 43 by the expressions given in Equation 47 and Equation 49, respectively, and assuming that the coefficient of friction μ_f is small relative to $K_n\,\tau^*$ (assumes negligible friction forces against detachment), the mass detachment model is given as:

$$e_i = \chi_1\,\rho_s\,\sqrt{gd\tau^*}\;\times\left[1 - e^{-e^{\left(\frac{1.28}{\mathcal{C}_v} - 0.5572 - \frac{\chi_2}{\mathcal{C}_v\tau^*}\right)}}\right]$$

51

With

$$\chi_1 = \frac{k_r}{K_e}\Delta F F_i\sqrt{\frac{K_n}{k_d}}$$

52

$$\chi_2 = \frac{\pi}{\sqrt{6}} \frac{k_r(K_{ls}+f_c)}{K_d}$$

53

As stated earlier, this detachment model must be applied to each particle size separately, then adding the different values to obtain a total detachment rate of the mix. That said, Wilson cautions about adding the rates of detachment of various particle sizes, rightfully stating that this concept would overlook the interaction between particles of different sizes, i.e. larger particles shielding smaller particles must be entrained first, and vice versa ("selective detachment"). Therefore, additional coefficients may have to be added to the model to compensate for such interaction. Wilson (1993b), then proposes a simplified version of the model that would be applied to the sediment mix, lumping selective detachment effects with all other coefficients and parameters as part of the "calibration procedures". He then proposes a modified form consisting of a two-parameter model that is a direct function of the average bed shear. The modified form of the model is obtained by assuming that C_v is 0.36 only in part of Equation 51 (citing Einstein and El-Samni, 1949). It is not clear to the Author how the inference was made from the citation; based on the EVT1 general formulation, C_v should be a parameter proportional to the scale of the distribution.

The resulting model is presented as:

$$e = b_0 \sqrt{\bar{\tau}} \times \left[1 - e^{-e^{\left(3.0 - \frac{b_1}{\bar{\tau}}\right)}}\right]$$

54

With

$$b_0 = \rho_s \frac{k_r}{K_e} \sqrt{\frac{K_n}{k_d(\rho_s - \rho)}}$$

55

$$b_1 = \frac{\pi}{C_v \sqrt{6}} \frac{k_r(K_{ls}+f_c)}{K_d} g\,(\rho_s - \rho)\,d$$

56

It is important to note that the term d in the above expression of the combined model is a "representative diameter" of the sediment mix, which is hard to define for cohesive soils.

At this point, parameters b_0 and b_1 become merely empirical parameters determined by curve-fitting techniques to match experimental data of bed shear versus erosion rate.

9.4 Discussion

There is no doubt that the formulation of the fundamental model (Wilson 1993a and 1993b), reviewed herein, is an elaborate and advanced exercise in forging a relationship between the sediment detachment phenomenon and various soil and fluid flow characteristics. Throughout the review, however, obvious potential sources of uncertainty were pointed out. One of the most important anomalies being the geometric representation of the fundamental model itself. The fundamental assumption that the entrainment of a cohesive sediment base can be modeled separately for each grain size and the resulting formula generalized with a corrective factor for interaction between grain sizes is, in the Author's opinion, invalid. It was shown in Section 9.1 that a cohesive soil structure is extremely complex. In fact, in many cases, even in most cases, grains belonging to the granular content in cohesive soils are immersed in the fine-grained material matrix and not readily exposed to the flow the way Wilson's representation suggests (see Figure 126).

Moving past the geometric representation, several key elements, instrumental to the formulation of the model, were adopted from published findings by others without making the case for the applicability of such findings to the situation at hand. One obvious example is the adoption of the proportionality between drag and lift forces from Chepil (1959), in which uniform, near rounded gravel, in excess of 3 mm in diameter, was tested in a wind tunnel. The fact that the grains considered in the model formulation are embedded in a closed structure, impervious to the flow, was not discussed. Another example is adopting a relationship between the uplift forces and flow velocity from Einstein and Al-Samni (1949), which was determined from water flow over hemispheres of plastic balls, about 70 mm in diameter, glued to the base of the flume (see Equation 34). No discussion about the differences in scale, shape, orientation, or exposure of the grains between the two cases was provided. In addition, critical initial conditions for Einstein and El-Samni's derivations are not satisfied by cohesive soils in general, as stated earlier, which casts major doubts on adopting their findings to derive this model.

Furthermore, the most important drawback to Wilson's model, in the Author's opinion, is the massive accumulation of correction factors, relationship coefficients, and theoretical uncertainty factors to account for the unpredictable nature of sediment mixes and base soils, especially cohesive mixes, as well as the shortcomings of available test methods in accurately capturing soil behavior. It is common in erosion studies to represent scattered data with a trend equation with one or more empirical constants or factors, be it erosion rate measurements, flow measurements, typical grain size, etc. Adopting values for such factors determined directly from the data is generally acceptable, even with uncertainties of ±50%. The problem arises when multiple expressions with such empirical factors are collected from literature, whether applicable to the study at hand or not, and combined into complex mathematical equations to produce a new dependant quantity; the compounded uncertainty may not be within acceptable levels. Several such combined approximations were underlined throughout the review. With such elaborate formulation, it is imperative to perform a thorough study tracking the uncertainty carried forward with

the introduction of each empirical coefficient to prove that the resulting combined uncertainty is reasonable. Thus, it is in the Author's opinion that, without such proof, the parameters listed in the model presented in Equations 54, 55, and 56 cannot be considered to represent actual sediment and fluid characteristics, but rather empirical curve-fitting parameters, similar to the factors used in the excess shear stress models (see Section 4.2.1). In other words, determining the model parameters from sediment and flow characteristics without calibration by actual test data is not realistic.

That said, a comparison between the Wilson model, and the simple excess shear model using actual test data is necessary to assess the versatility of the model and advantages, if any, for using a more demanding curve-fitting procedure. For this purpose, we can examine the comparison done by Wilson (1993b). Four sets of rill erosion data from two sites are reported: Lincoln, NE (Sharpsburg silty clay) and Big Spring, TX (Amarillo loamy sand). The data used in the comparison is out of the Water Erosion Prediction Project (WEPP) initiated by the USDA Agricultural Research Service (ARS) in 1985 (Elliot et al., 1989). The four sets of data are:

- Sharpsburg silty clay, Lincoln, NE, Rill 1, with rainfall
- Amarillo loamy sand, Big Spring, TX, Rill 1, with rainfall
- Sharpsburg silty clay, Lincoln, NE, Rill 1, without rainfall
- Amarillo loamy sand, Big Spring, TX, Rill 1, without rainfall

To briefly describe the tests, the flow was induced in rills made by a tractor specifically for the tests and a rainfall simulator nozzle was used to simulate rain at a rate of 60 mm/h. Some datasets were obtained with rated water flow only without applying simulated rainwater (without rainfall) and others were collected while both rated flow and simulated rain were applied simultaneously (with rainfall).

The four comparisons are shown in Figure 131 through Figure 134, respectively. It should be stressed here that, while Wilson referred to the linear fit in the comparison as "excess shear" model, it is in fact a linear correlation between applied shear and erosion rate; no critical shear value was subtracted from the data. The term "excess shear" will be carried for this data only in this section of the study to maintain consistency between the actual article and this review. The comparisons of datasets 1 and 2 (with rainfall) are reconstructed to match Wilson (1993b), and the proposed fundamental detachment model appears to be comparable to the excess shear model for all practical purposes (see Figure 131 and Figure 132).

The comparisons of datasets 3 and 4, as presented by Wilson (1993b), appear to have some inconsistencies. As shown in Figure 135, an outlier in the erosion data (Dataset 3) was included in the curve fitting which caused the fundamental model to underestimate the detachment rate at moderate bed shear while causing the excess shear model to overestimate the detachment rate, albeit to a lesser degree within the same bed shear range. It is also important to note that data points representing zero observed detachment were also included in the curve fitting of the excess shear model. Any data taken at a bed

shear below the critical shear level can erroneously skew the regression, leading to unwarranted error in the model calibration. An alternate comparison is presented in Figure 133 by eliminating the high-detachment rate outlier from the curve fitting procedure, and by eliminating the effects of the zero erosion points on the excess shear model calibration. The resulting comparison is consistent with that of Datasets 1 and 2, and both models are comparable.

The comparison provided by Wilson (1993b), for Dataset 4, is shown in Figure 136. Note that both models were erroneously fitted to the data and both appear to overestimate the detachment rate. It is possible that the curve fitting was again skewed by a data outlier outside the plotted range. An alternate curve fitting is proposed in Figure 134, also showing both models as comparable.

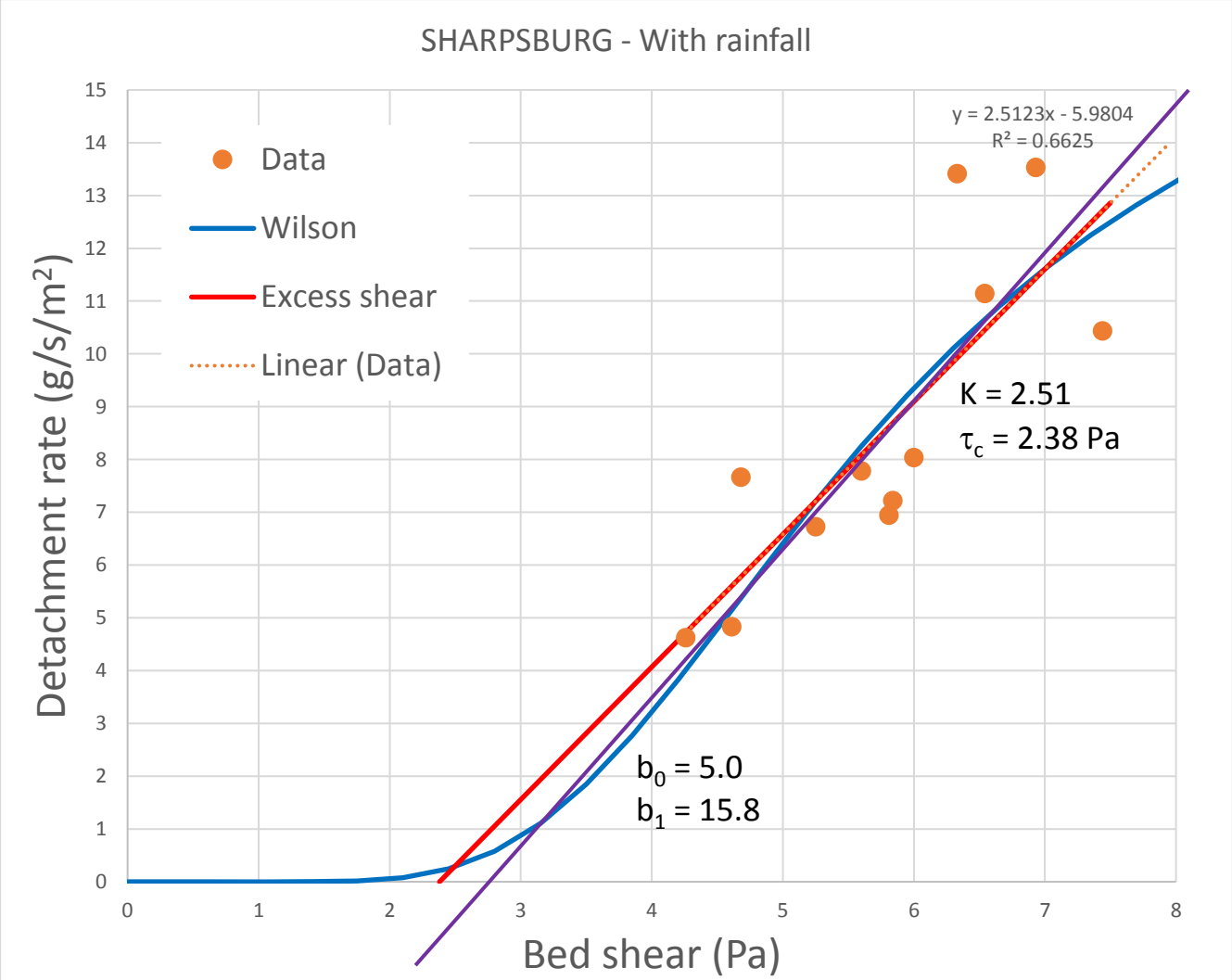

Figure 131. Erosion data with fitted model curves, Sharpsburg silty clay, Rill 1, with rainfall. (Elliot et al., 1989; Wilson, 1993b)

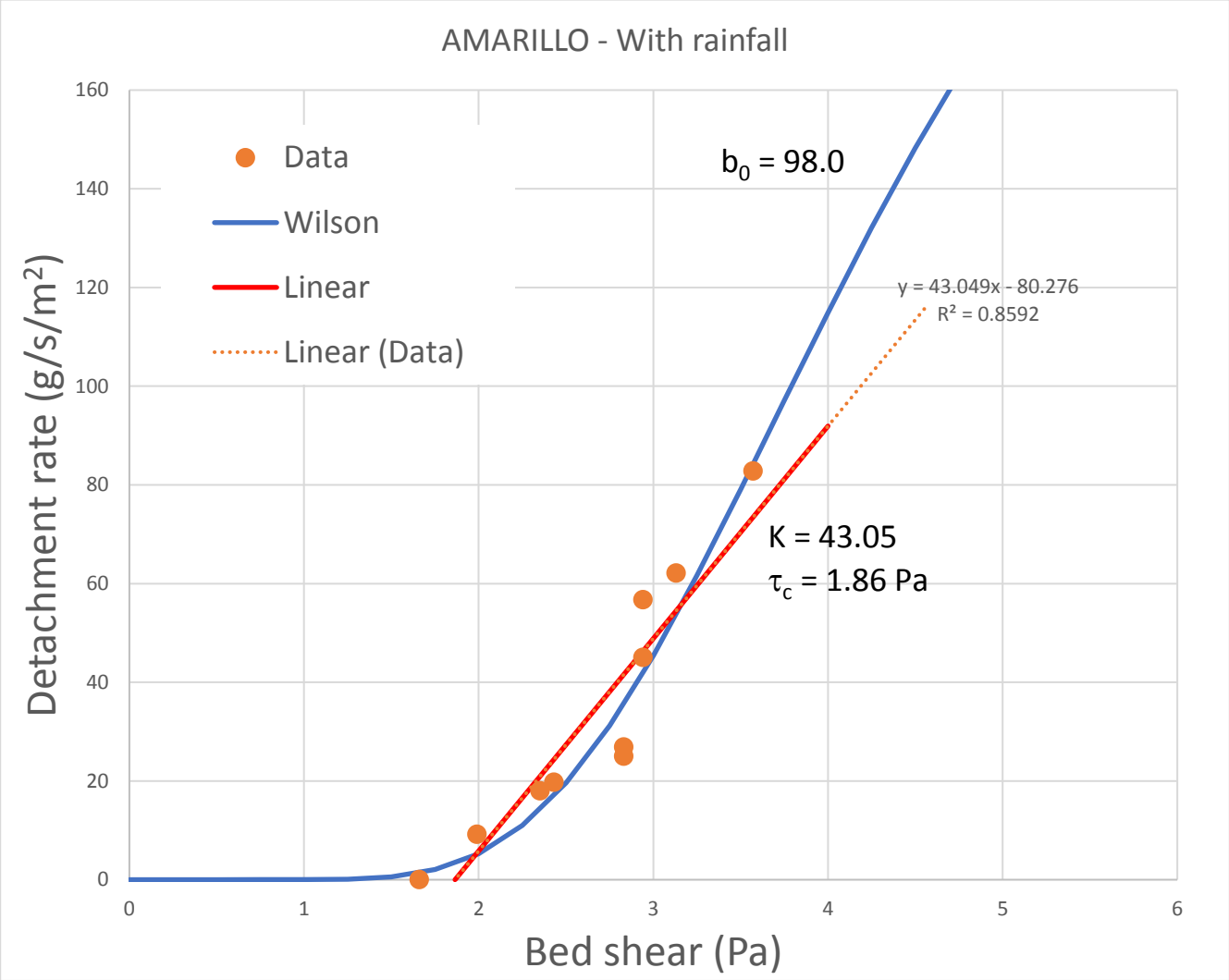

Figure 132. Erosion data with fitted model curves, Amarillo loamy sand, Rill 1, with rainfall. (Elliot et al., 1989; Wilson, 1993b)

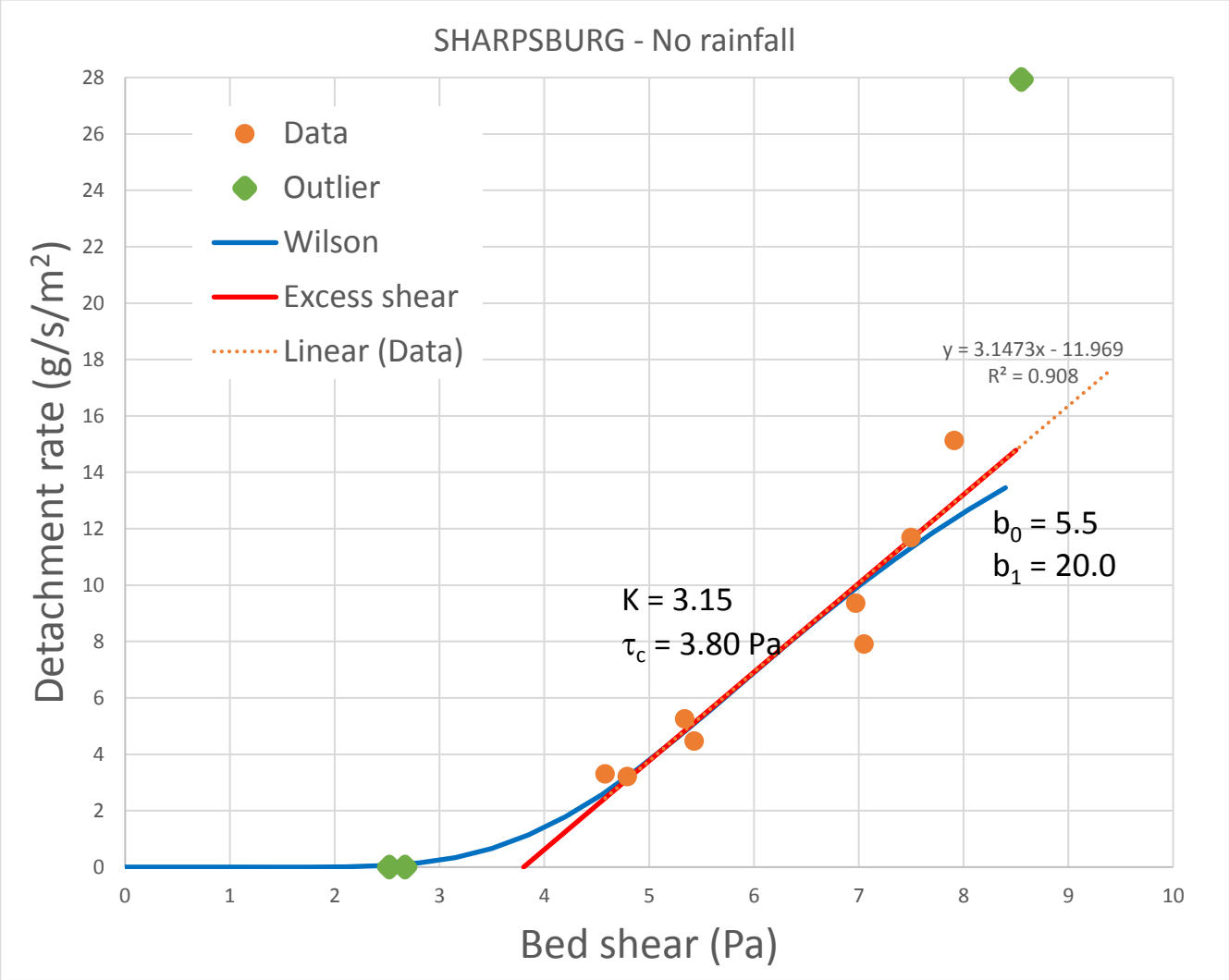

Figure 133. Erosion data with fitted model curves, Sharpsburg silty clay, Rill 1, without rainfall. (Elliot et al., 1989; Wilson, 1993b)

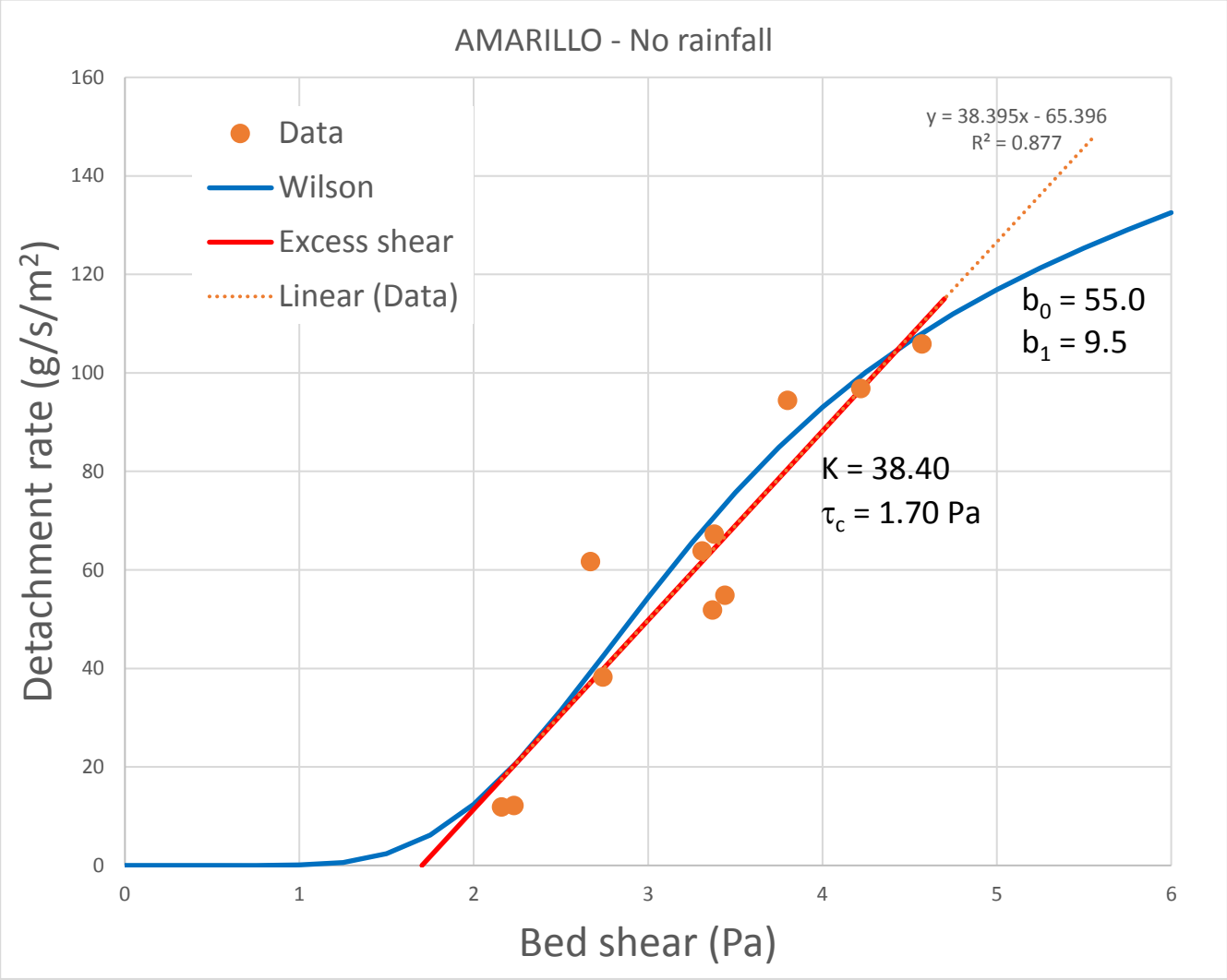

Figure 134. Erosion data with fitted model curves, Amarillo loamy sand, Rill 1, without rainfall. (Elliot et al., 1989; Wilson, 1993b)

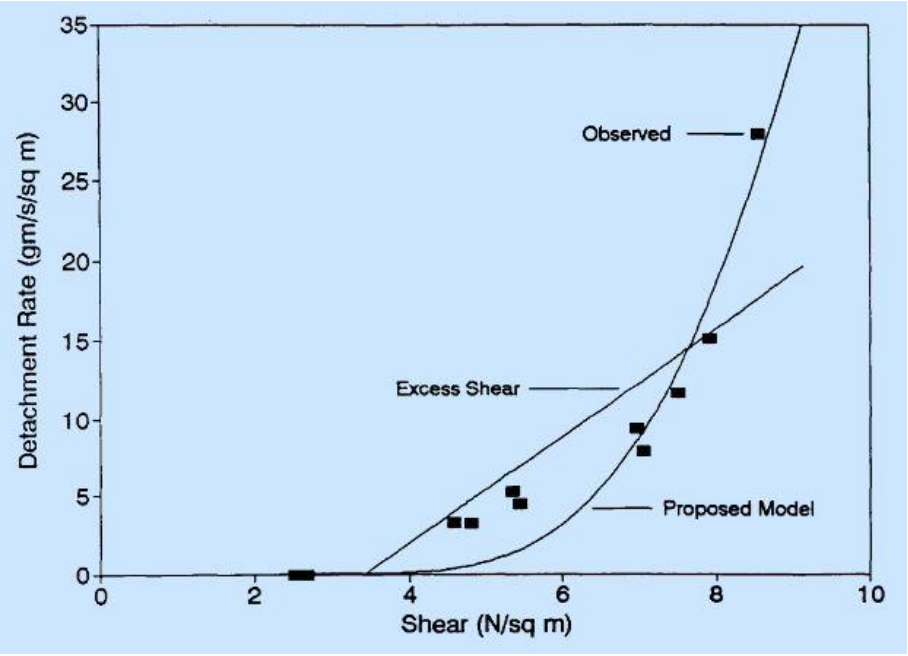

Figure 135. Comparison presented by Wilson (1993b): Sharpsburg silty clay, without rainfall

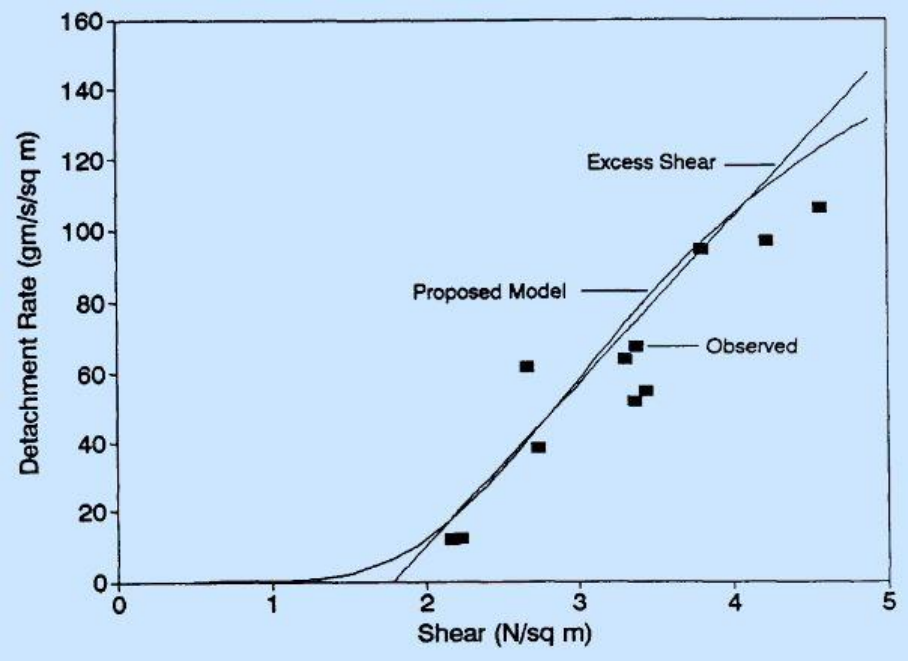

Figure 136. Comparison presented by Wilson (1993b): Amarillo loamy sand, without rainfall

To test the claim that Wilson's model better represents the erosion data, the linear fit and Wilson's fit were subjected to a statistical fit test using the method of least squares. The square of the difference between the measured detachment rate and the ordinate of each fitted curve at the corresponding shear

value was calculated. The squares were added for all plotted data points and tabulated as shown in Table 9.

Table 9. Least Squares test: Wilson v. Excess Shear model

Test data	Wilson	Excess Shear
Amarillo - With rainfall	533	869
Amarillo - No rainfall	8567	7331
Sharpsburg - With rainfall	13371	13360
Sharpsburg - No rainfall	16657	16577

It is clear in Table 9 that Wilson's model offers no advantage over the simple linear correlation in representing detachment rate data; in fact, only one out of the four datasets shows a lower sum of least squares attributed to Wilson's fit.

This review shows that the proposed fundamental detachment model, while intended as an elaborate attempt to predict the erodibility of cohesive soils based on their physical characteristics, is practically a two-parameter curvilinear representation of the bed shear-detachment rate relationship, which must be calibrated by curve fitting to representative erosion test data, same as the linear excess shear model. The field data selected by Wilson for demonstrating the model application seems to lend itself to a linear trend with relatively high coefficient of determination (R2) and the comparisons provided did not show any advantage for using the proposed fundamental model over the commonly used excess shear model in terms of representing actual detachment rate data.

It is in the Author's opinion that the complexities of the fundamental model proposed by Wilson are unnecessary and the model itself provides no real advantages over the simpler excess shear model. One of the main objectives of this research, is to develop new tools for fast and accurate assessment of the erosion rate of cohesive soils under varying shear levels. It is therefore anticipated that the excess shear model, or an improved version of it, will be used throughout the continuation of this study.

Appendix 2:
Maps of sampling site locations

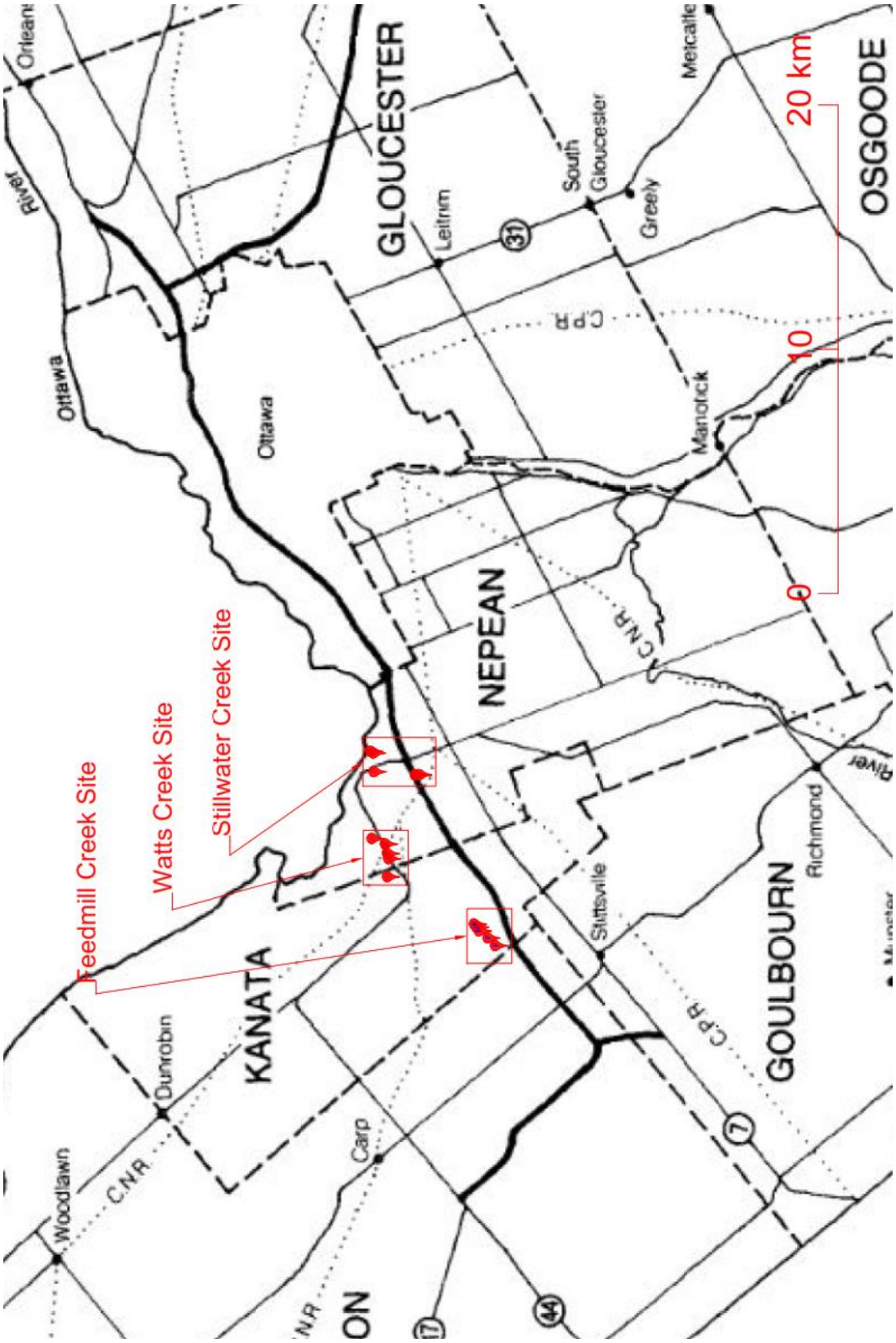

Main soil sampling locations referenced to municipal boundaries, after Schut and Wilson (1987).

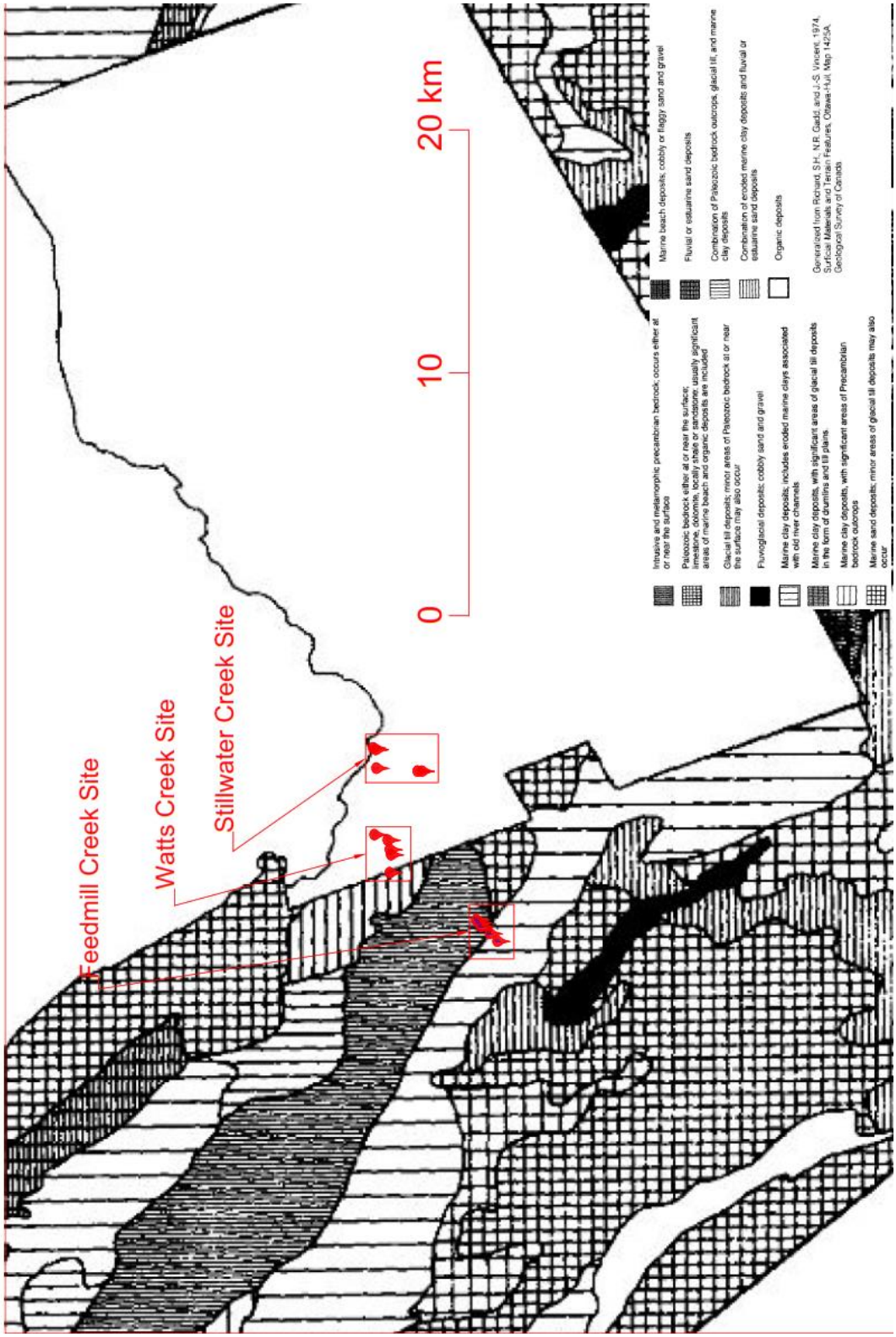

Main soil sampling locations referenced to surficial geology, after Schut and Wilson (1987).

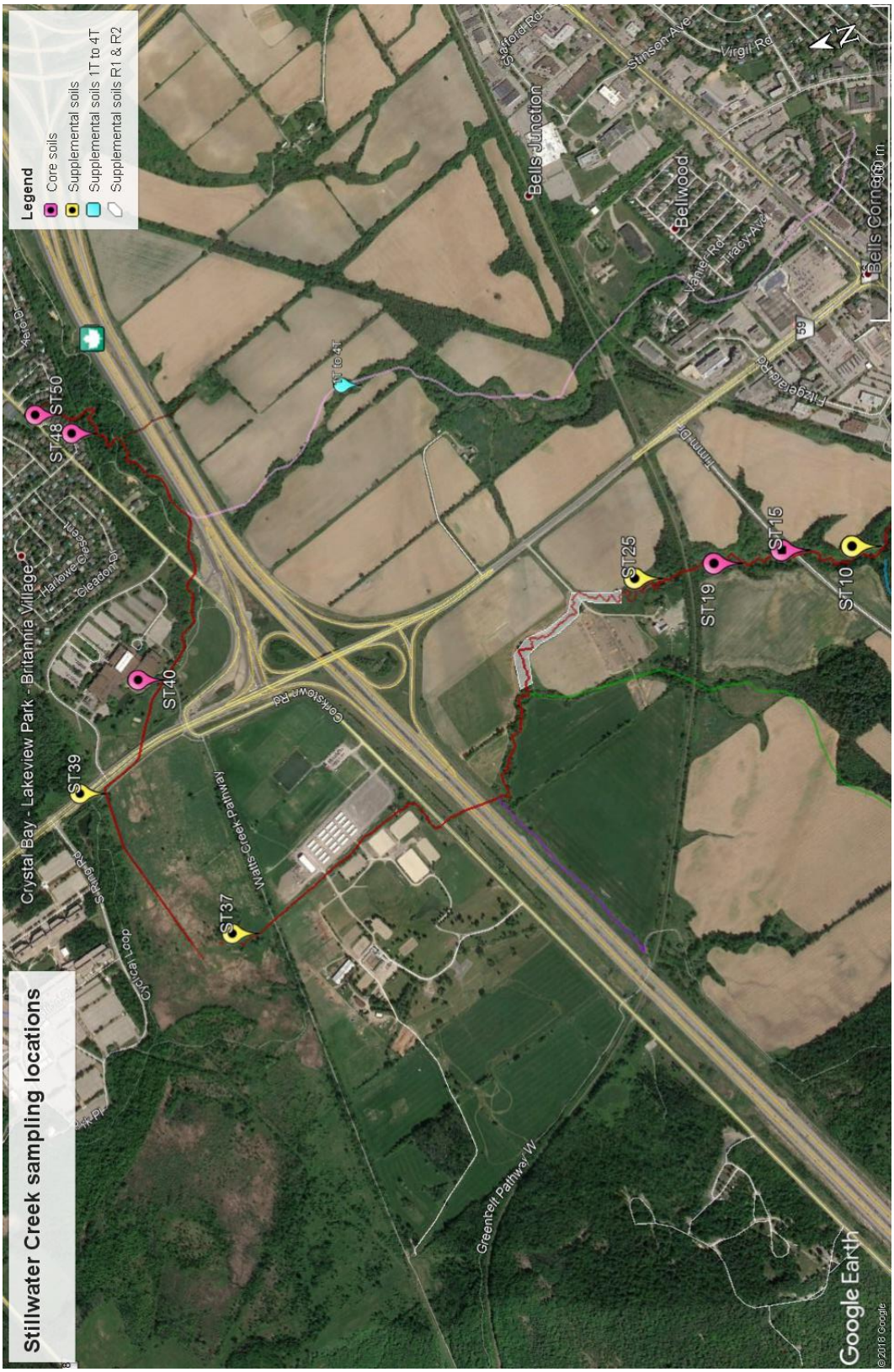
Stillwater Creek sampling locations
Legend
Core soils
Supplemental soils
Supplemental soils 1T to 4T
Supplemental soils R1 & R2
ST50
ST48
ST40
ST39
ST37
ST25
ST19
ST15
ST10
1T to 4T
Crystal Bay - Lakeview Park - Britannia Village
Bells Junction
Bellwood
Bells Corners
Greenbelt Pathway W
Google Earth


Watts Creek sampling locations
Main reach and Watts reach
Legend
Sampling locations
M1
M3
W1
W2
K3
Greenbelt Pathway W
Watts Creek Pathway
Shaw Dr
38
400 m
N
Google Earth

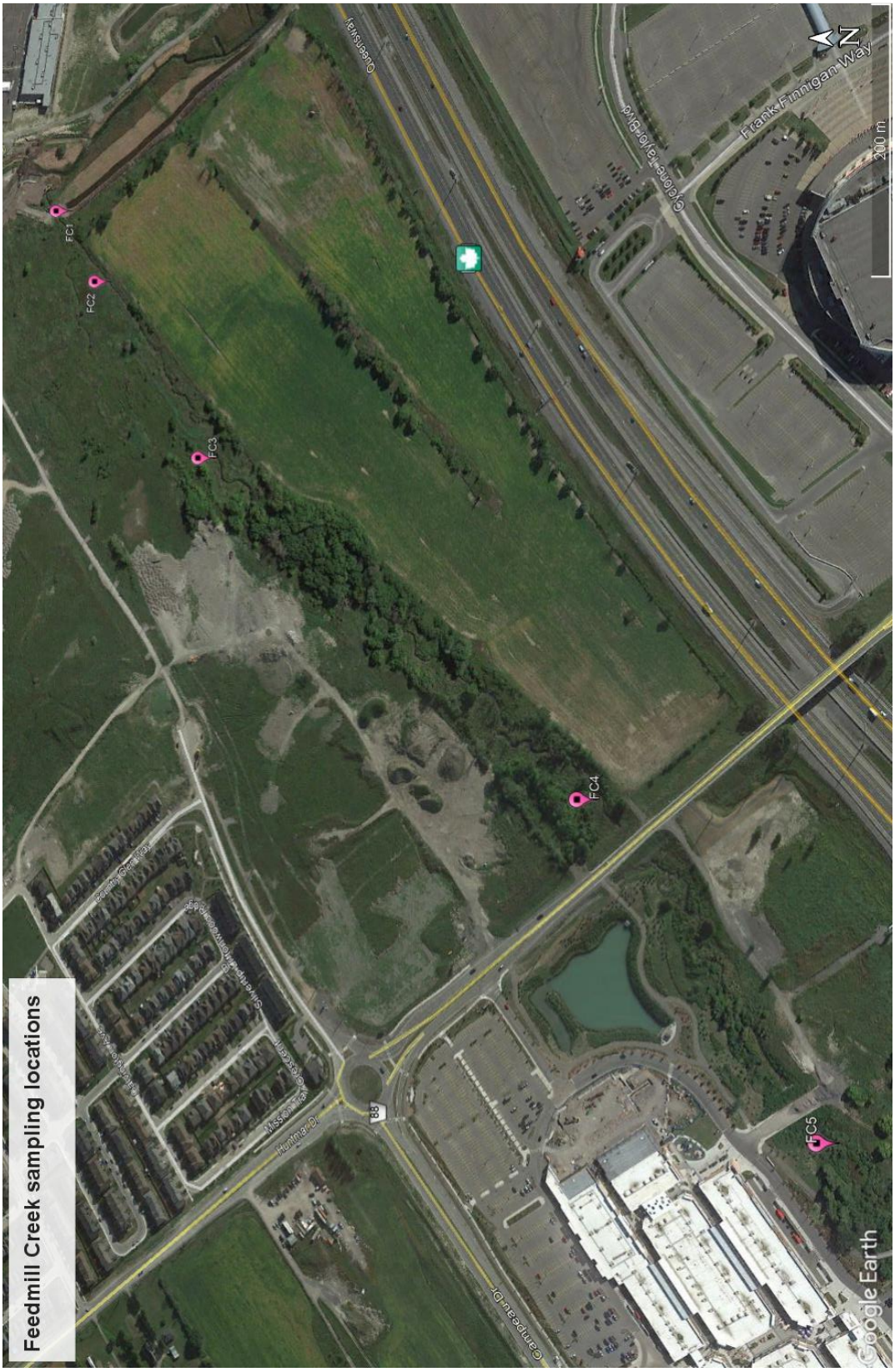
Feedmill Creek sampling locations
FC1
FC2
FC3
FC4
FC5
Frank Finnigan Way
Google Earth

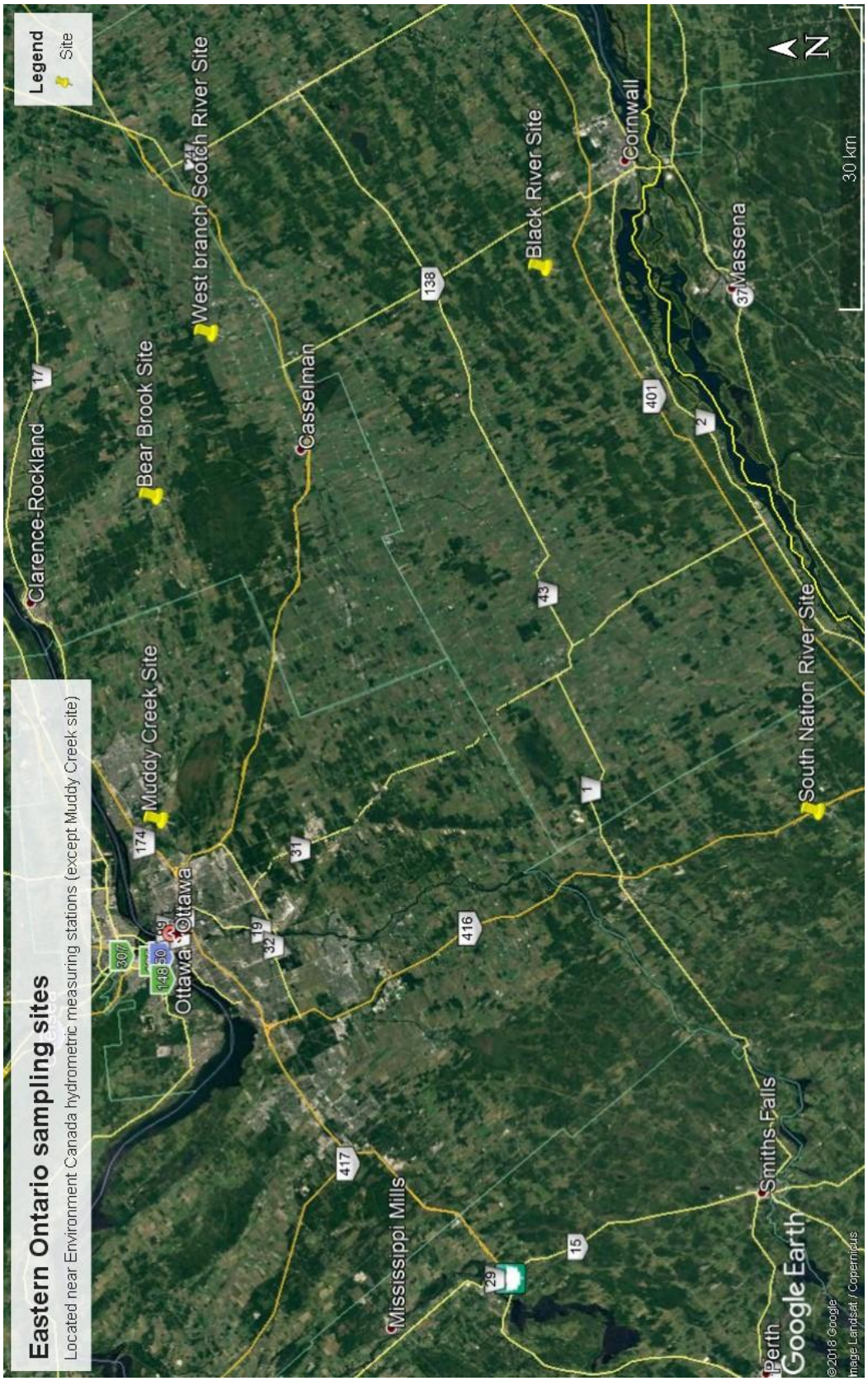
Eastern Ontario sampling sites
Located near Environment Canada hydrometric measuring stations (except Muddy Creek site)
Legend
Site
Clarence-Rockland
Bear Brook Site
West branch Scotch River Site
Casselman
Muddy Creek Site
Ottawa
Black River Site
Cornwall
Massena
South Nation River Site
Smiths Falls
Mississippi Mills
Perth
N
30 km
Google Earth
©2018 Google
Image Landsat / Copernicus

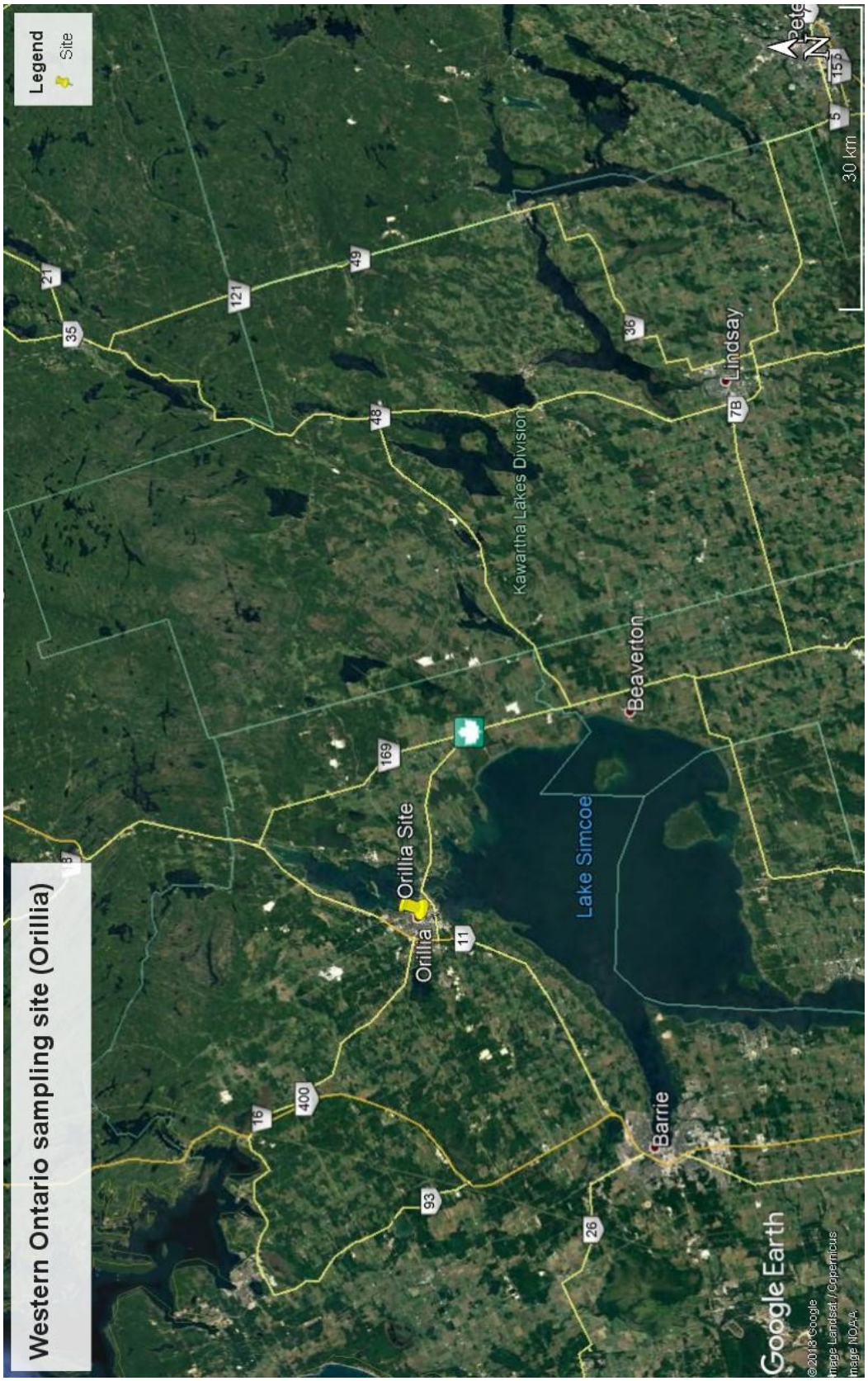
Western Ontario sampling site (Orillia)
Legend
Site
Orillia Site
Orillia
Lake Simcoe
Beaverton
Kawartha Lakes Division
Lindsay
Barrie
30 km
Google Earth

Appendix 3:
Laboratory and field test results:
summary and details

Raw data and analyses filed separately

Table A3-1. Summary of test results - Core soils

Site	Index	Sample No.	Description	Geodetic coordinates		Grain size distribution			Atterberg limits				Strength tests				Erosionometer yield force Y (N)	Critical shear, τ_c (Pa)		Seepage test results		ERM test results	
				Latitude	Longitude	Sand (%)	Silt (%)	Clay (%)	Plastic limit, PL (%)	Water content, WC (%)	Liquid limit, LL (%)	Plasticity index, PI	Effective cohesion c' (kPa)	Effective friction angle, ϕ' (Deg.)	Pocket penetrometer* UC (kPa)	Undrained shear strength τ_u (kPa)		Erosionometer	Flume	Intercept (Pa)	slope (Pa)	X-Intercept (Pa)	Coefficient of erodibility k (mm/Pa)
Stillwater Creek	1	ST15	Grey Leda clay, small structures (up to 5 mm), silty	45°19'31.51"N	75°50'32.55"W	25	47	28	31.1	65.7	73.3	42.2	1.86	27.1	10	5	3.26	0.98	1.46	2.5042	0.0318	5.714	0.0049
	2	ST19	Brownish grey organic clayey sandy silt, decomposed roots	45°19'37.76"N	75°50'31.79"W	4	21	75	22.1	36.4	42.1	20.0	1.38	33.2	25	12.5	28.07	15.12	13.87	3.913	0.3287	7.217	0.0069
	3	ST40	Grey silty sandy clay with dense roots, soft	45°20'35.57"N	75°50'25.15"W	23	30	47	34.5	31.7	53.0	18.5	8.69	34.5	10	5	4.59	1.74	2.19	4.3224	0.2849	14.706	0.0034
	4	ST48	Grey silty clay w/ sand, stiff	45°20'35.74"N	75°49'47.93"W	19	26	55	27.1	33.3	43.4	16.3	5.60	36.6	75	37.5	4.74	1.82	1.46	5.8809	0.1052	10.279	0.0111
	5	ST50	Greyish brown clayey silty sand, soft, roots	45°20'39.01"N	75°49'43.66"W	43	28	29	26.1	42.1	48.4	22.2	9.36	26.9	5	2.5	5.43	2.22	2.92	2.1844	0.1003	5.089	0.057
Watts Creek	6	K3	Bluish grey clayey silt, black organics and roots	45°20'24.46"N	75°53'37.36"W	9	48	43	40.2	73.0	94.0	53.8	5.88	35.6	5	2.5	6.98	3.10	1.90	1.4356	0.2088	9.335	0.034
	7	M1	Yellowish brown soft clay and silt loam, roots and black organics (peat)	45°20'44.40"N	75°52'21.66"W	1	49	50	25.8	42.1	48.4	22.6	3.72	22.3	20	10	4.44	1.65	1.61	2.4354	0.2683	-	-
	8	M3	Dark grey clayey silty sand, black hue, strong organic odour, soft	45°20'25.91"N	75°52'32.54"W	50	22	28	26.5	45.4	50.6	24.1	6.14	37.4	22	11	13.96	7.07	7.30	6.6067	0.1889	-	-
	9	W1	Brownish grey organic silt, clay, sand loam, very soft	45°20'23.59"N	75°52'51.07"W	33	34	33	20.9	37.0	43.1	22.2	6.97	32.7	10	5	14.70	7.50	4.75	3.6081	0.3111	6.606	0.0132
	10	W2	Sand, clay and silt loam, very soft	45°20'22.44"N	75°53'1.67"W	36	28	36	17.1	34.3	35.1	18.0	1.59	32.5	25	12.5	11.43	5.64	4.38	2.5348	0.0359	5.085	0.0176

*: Measures the unconfined compressive strength at the surface of the soil sample

Table A3-2. Summary of test results - Supplemental soils

				Geodetic coordinates		Grain size distribution			Atterberg limits				Strength tests					Critical shear, τ_c (Pa)		Seepage test results		ERM test results	
Site	Index	Sample No.	Description	Latitude	Longitude	Sand (%)	Silt (%)	Clay (%)	Plastic limit, PL (%)	Water content, WC (%)	Liquid limit, LL (%)	Plasticity index, PI	Effective cohesion c' (kPa)	Effective friction angle, ϕ' (Deg.)	Pocket penetrometer* UC (kPa)	Undrained shear strength τ_u (kPa)	Erosionometer yield force Y (N)	Erosionometer	Flume	Intercept (Pa)	slope (Pa)	X-Intercept (Pa)	Coefficient of erodibility k (mm/Pa)
Stillwater Creek	11	1T	Firm clayey silt w/ organics	45°20'8.21"N	75°49'52.98"W	-	-	-	-	-	-	-	-	-	-	-	6.23	2.67	2.56	-	-	-	-
	12	2T	Firm clayey silt w/ organics	45°20'8.21"N	75°49'52.98"W	-	-	-	-	-	-	-	-	-	-	-	3.85	1.31	1.83	-	-	-	-
	13	3T	Stiff silty clay, organics	45°20'8.21"N	75°49'52.98"W	-	-	-	-	-	-	-	-	-	-	-	15.74	8.09	10.59	-	-	-	-
	14	4T	Stiff silty clay, organics	45°20'8.21"N	75°49'52.98"W	-	-	-	-	-	-	-	-	-	-	-	21.09	11.14	14.60	-	-	-	-
	15	R2-02	Low-plasticity organic silty clay	45°19'55.16"N	75°50'32.61"W	-	-	-	22.7	31.3	38.6	15.9	-	-	-	-	10.75	5.25	3.29	-	-	-	-
	16	R1-02	Low-plasticity organic silty clay	45°19'55.16"N	75°50'32.61"W	-	-	-	23.6	31.7	39.5	15.9	-	-	-	-	5.34	2.16	4.02	-	-	-	-
	17	R1-01	Low-plasticity organic silty and clay loam	45°19'55.16"N	75°50'32.61"W	-	-	-	25.8	28.3	38.3	12.5	-	-	-	-	13.06	6.56	7.67	-	-	-	-
	18	R2-03	High-plasticity organic clayey silt	45°19'55.16"N	75°50'32.61"W	-	-	-	46.0	62.2	80.9	35.0	-	-	-	-	15.14	7.75	12.41	-	-	-	-
	19	ST10	Clay, sand and silt loam, firm	45°19'25.36"N	75°50'34.60"W	37	24	39	-	-	-	-	-	-	-	-	8.11	3.74	2.19	-	-	-	-
	20	ST25	Silty clay, some sand, stiff	45°19'45.19"N	75°50'30.80"W	7	18	75	-	-	-	-	-	-	-	-	24.19	12.91	10.22	-	-	-	-
	21	ST37	Silty clay w/ sand, high plasticity	45°20'32.79"N	75°51'3.70"W	15	35	50	30.0	45.9	57.3	27.3	-	-	-	-	6.62	2.90	2.19	-	-	-	-
	22	ST39	Silty sandy clay, high plasticity	45°20'44.66"N	75°50'38.69"W	20	25	55	53.4	79.5	100.1	46.7	-	-	-	-	8.41	3.91	1.46	-	-	-	-
	23	S1	Sand, clay and silt loam	45°20'44.39"N	75°50'38.06"W	37	28	35	62.4	57.6	84.7	22.3	-	-	-	-	-	-	-	-	-	-	-
	24	S2	Clayey silty sand, organics	45°20'29.44"N	75°50'7.20"W	57	24	19	61.6	90.5	114.5	52.9	-	-	-	-	-	-	-	-	-	-	-
	25	S3	Silty clay, high plasticity	45°19'49.79"N	75°50'31.90"W	5	24	71	32.6	50.4	62.7	30.1	-	-	-	-	-	-	-	-	-	-	-
	26	S4	Silty clay, low plasticity	45°20'35.78"N	75°49'47.95"W	0	28	72	43.3	36.1	54.5	11.1	-	-	-	-	-	-	-	-	-	-	-
	27	S5	Clayey, silty sand	45°20'29.44"N	75°50'11.05"W	60	18	22	35.1	58.8	71.2	36.1	-	-	-	-	-	-	-	-	-	-	-
Feedmill Creek	28	FC1-S1	Brown silty clay, organics	45°18'15.40"N	75°55'29.66"W	-	-	-	19.4	38.2	40.2	20.9	-	-	-	-	9.21	4.37	3.20	-	-	-	-
	29	FC1-S2	Brown silty clay, organics	45°18'15.40"N	75°55'29.66"W	-	-	-	17.6	33.4	36.0	18.4	-	-	-	-	5.35	2.17	3.20	-	-	-	-
	30	FC2-N1	Silty clay, brown, organics and roots	45°18'13.67"N	75°55'33.42"W	-	-	-	21.5	40.1	43.6	22.1	-	-	-	-	7.43	3.36	3.20	-	-	-	-
	31	FC2-N1'	Silty clay, brown, organics and roots	45°18'13.67"N	75°55'33.42"W	-	-	-					-	-	-	-	7.13	3.18	3.20	-	-	-	-
	32	FC2-S1	Clayey silt, brown, organics and roots	45°18'13.67"N	75°55'33.42"W	-	-	-	31.4	39.7	52.8	21.4	-	-	-	-	7.72	3.52	3.20	-	-	-	-
	33	FC3-N1	Silty and clay loam, brown, organics	45°18'9.35"N	75°55'42.23"W	-	-	-	28.3	40.6	51.8	23.5	-	-	-	-	14.56	7.42	6.40	-	-	-	-
	34	FC4-N1	Greyish brown clayey silt	45°17'56.69"N	75°55'56.58"W	-	-	-	33.3	49.9	62.7	29.4	-	-	-	-	6.84	3.02	2.24	-	-	-	-
	35	FC4-S1	Structured grey Champlain sea clay	45°17'56.69"N	75°55'56.58"W	-	-	-	32.8	52.4	64.5	31.7	-	-	-	-	14.26	7.25	27.20	-	-	-	-

Table A3-2. Summary of test results - Supplemental soils

				Geodetic coordinates		Grain size distribution			Atterberg limits				Strength tests					Critical shear, τ_c (Pa)		Seepage test results		ERM test results	
Site	Index	Sample No.	Description	Latitude	Longitude	Sand (%)	Silt (%)	Clay (%)	Plastic limit, PL (%)	Water content, WC (%)	Liquid limit, LL (%)	Plasticity index, PI	Effective cohesion c' (kPa)	Effective friction angle, ϕ' (Deg.)	Pocket penetrometer* UC (kPa)	Undrained shear strength τ_u (kPa)	Erosionometer yield force Y (N)	Erosionometer	Flume	Intercept (Pa)	slope (Pa)	X-Intercept (Pa)	Coefficient of erodibility k (mm/Pa)
	36	FC5-N1	Grey silty clay, firm	45°17'50.57"N	75°56'7.87"W	-	-	-	22.5	42.2	45.8	23.3	-	-	-	-	8.61	4.03	3.20	-	-	-	-
	37	FC5-N1'	Grey silty clay, firm	45°17'50.57"N	75°56'7.87"W	-	-	-					-	-	-	-	5.35	2.17	2.56	-	-	-	-
	38	FC5-S1	Grey silty clay, firm	45°17'50.57"N	75°56'7.87"W	-	-	-	22.1	42.8	45.7	23.6	-	-	-	-	14.86	7.59	9.60	-	-	-	-
	39	FC5-S1'	Grey silty clay, firm	45°17'50.57"N	75°56'7.87"W	-	-	-					-	-	-	-	13.07	6.57	9.60	-	-	-	-
Bear Brook	40	BB2	Grey clayey sand, some organics (wood)	45°25'32.43"N	75°9'9.48"W	-	-	-	20.8	30.3	36.5	15.7	-	-	-	-	-	11.35	-	-	-	11.35	0.0712
Black River	41	BR1	Grey sensitive clay (Champlain Sea), stiff	45°4'46.70"N	74°52'10.20"W	-	-	-	46.1	91.2	104.8	58.6	-	-	-	-	-	8.57	-	-	-	8.57	0.0072
Green's Creek	42	GC1	Bluish grey soft silty clayey fine sand, medium plasticity	45°27'7.83"N	75°34'43.13"W	55	18	27	20.4	30.9	36.7	16.3	-	-	-	-	-	9.23	-	-	-	9.23	0.008
	43	GC2		45°27'7.83"N	75°34'43.13"W	-	-	-					-	-	-	-	-	3.03	-	3.03	0.3628		
Muddy Creek	44	MC1	Champlain sea clay, soft, grey, structured, high plasticity	45°25'21.41"N	75°33'36.39"W	-	-	-	50.7	70.0	90.4	39.7	-	-	-	-	-	3.82	-	-	-	3.82	0.0056
	45	MC2		45°25'21.41"N	75°33'36.39"W	28.5	18.5	53	24.6	60.0	64.2	39.6	-	-	-	-	-	3.95	-	3.95	0.2621	-	-
Orillia WWTP	46	O1	Grey silty clay, soft	44°35'27.37"N	79°24'52.57"W	-	-	-	41.6	53.3	70.7	29.0	-	-	-	-	-	11.42	-	-	-	11.42	0.0048
South Nation River	47	SNR1	Greyish brown clayey sand, fine, compact	44°50'29.20"N	75°33'2.50"W	61	22	17	-	-	-	-	-	-	-	-	-	3.46	-	3.46	0.1072	-	-
West Branch Scotch River	48	WBSR1	Greyish brown silty clay, stiff, black organic content, high plasticity	45°22'33.13"N	74°56'51.06"W	-	-	-	-	-	-	-	-	-	-	-	-	6.90	-	6.9	0.1502	-	-
	49	WBSR2		45°22'33.13"N	74°56'51.06"W	-	-	-	46.1	57.1	76.5	30.4	-	-	-	-	-	13.32	-	-	-	13.32	0.0078

*: Measures the unconfined compressive strength at the surface of the soil sample

Graphical results of undrained direct shear tests

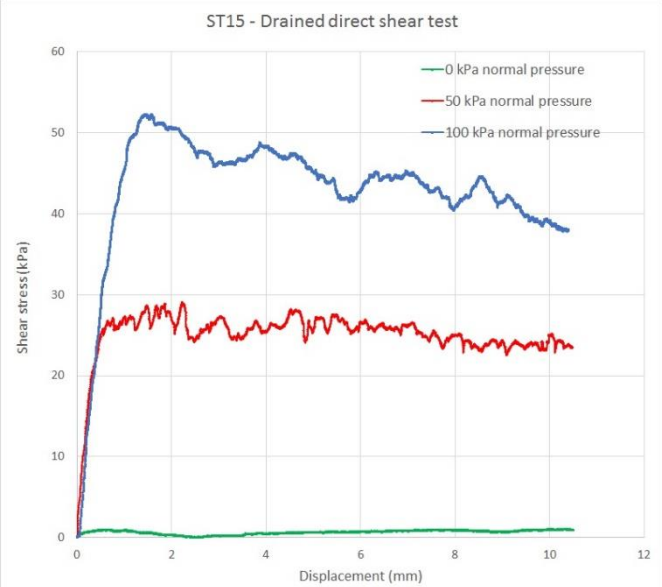

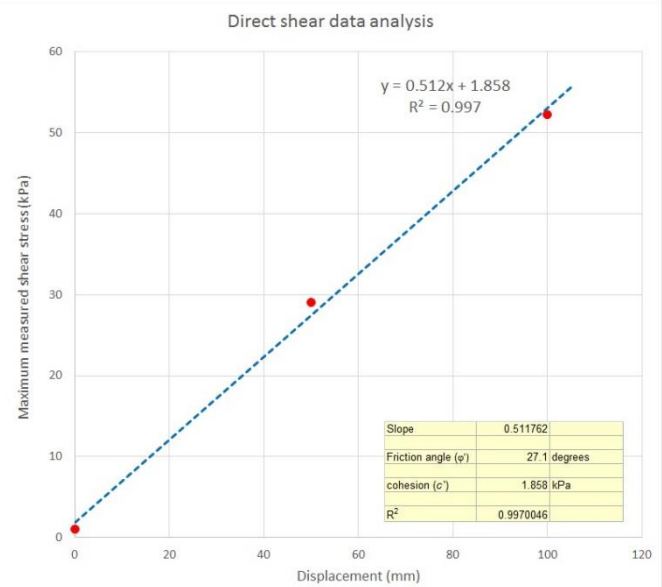

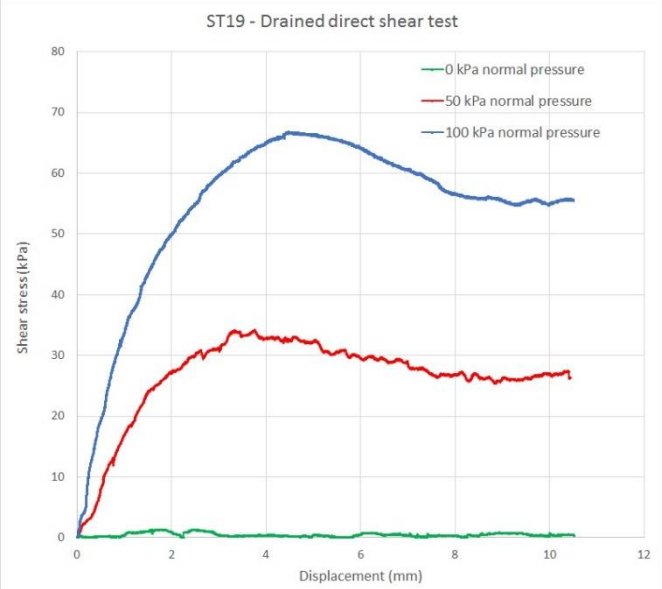

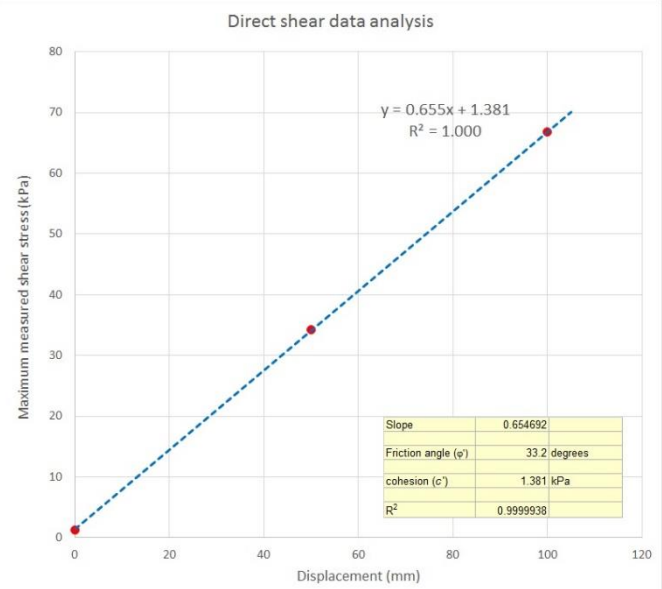

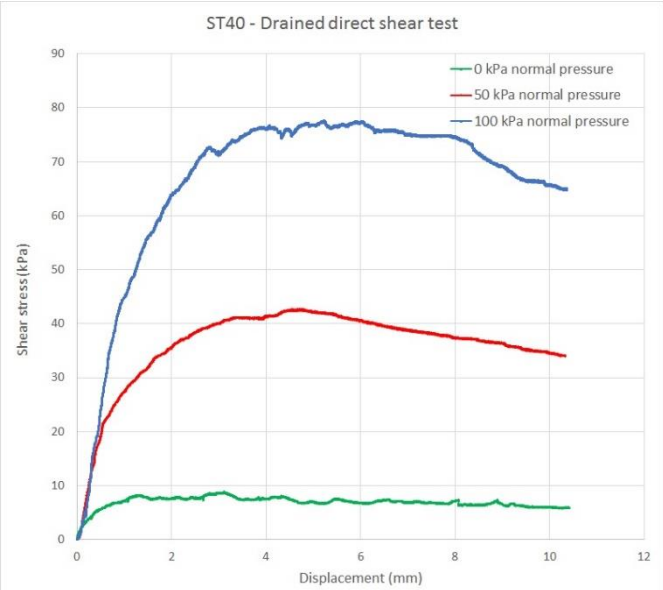
ST40 - Drained direct shear test
0 kPa normal pressure
50 kPa normal pressure
100 kPa normal pressure
Shear stress (kPa)
Displacement (mm)

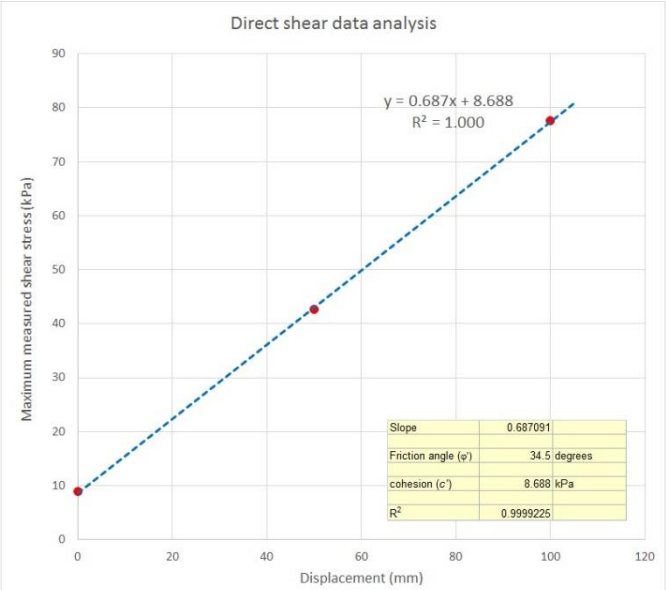
Direct shear data analysis
y = 0.687x + 8.688
R² = 1.000
Maximum measured shear stress (kPa)
Displacement (mm)
Slope 0.687091
Friction angle (φ') 34.5 degrees
cohesion (c') 8.688 kPa
R² 0.9999225

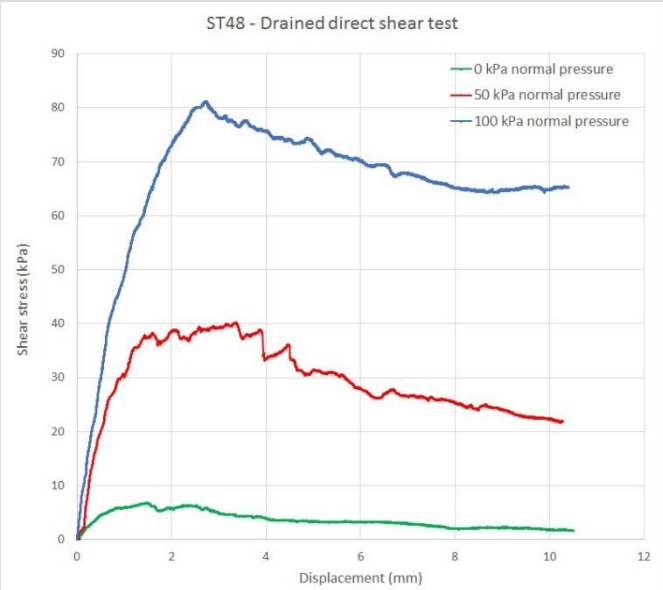
ST48 - Drained direct shear test
0 kPa normal pressure
50 kPa normal pressure
100 kPa normal pressure
Shear stress (kPa)
Displacement (mm)

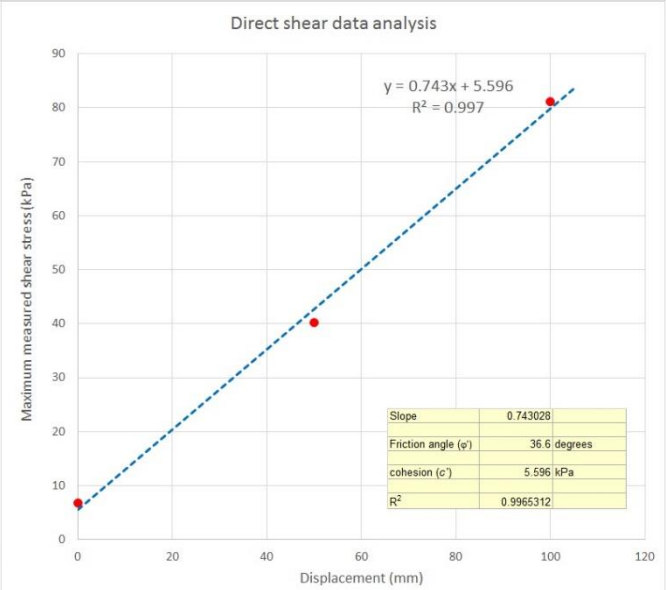
Direct shear data analysis
y = 0.743x + 5.596
R² = 0.997
Maximum measured shear stress (kPa)
Displacement (mm)
Slope 0.743028
Friction angle (φ') 36.6 degrees
cohesion (c') 5.596 kPa
R² 0.9965312

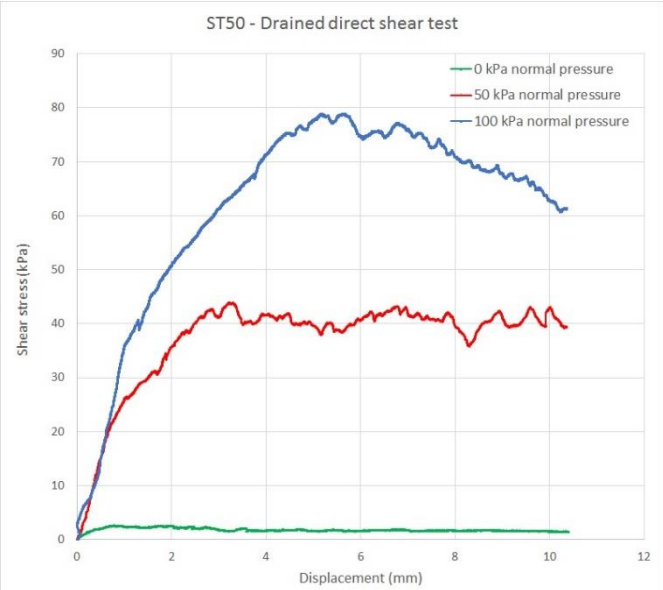
ST50 - Drained direct shear test
0 kPa normal pressure
50 kPa normal pressure
100 kPa normal pressure
Shear stress (kPa)
Displacement (mm)

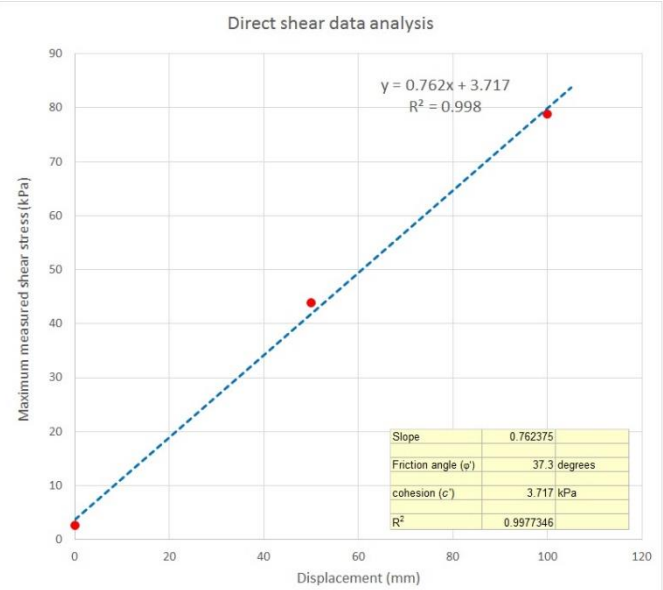
Direct shear data analysis
y = 0.762x + 3.717
R² = 0.998
Maximum measured shear stress (kPa)
Displacement (mm)
Slope 0.762375
Friction angle (φ') 37.3 degrees
cohesion (c') 3.717 kPa
R² 0.9977346

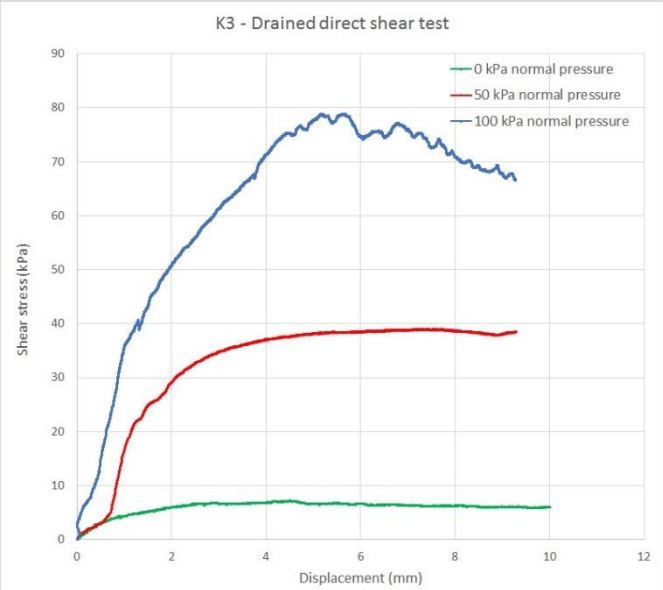
K3 - Drained direct shear test
0 kPa normal pressure
50 kPa normal pressure
100 kPa normal pressure
Shear stress (kPa)
Displacement (mm)

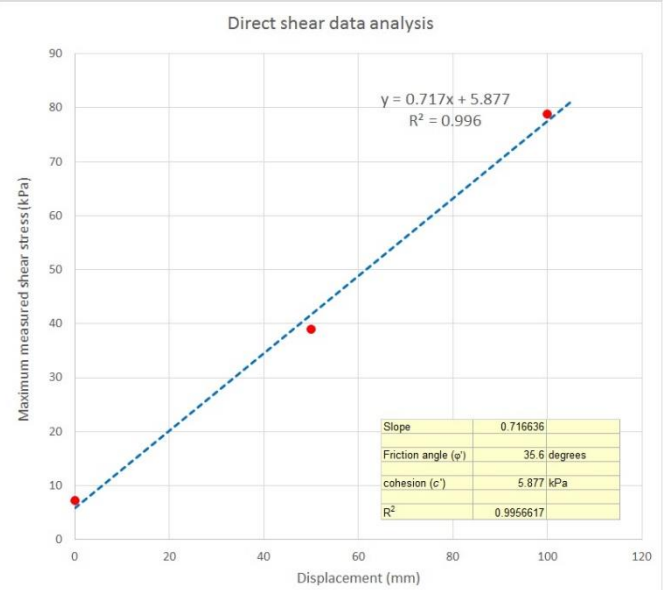
Direct shear data analysis
y = 0.717x + 5.877
R² = 0.996
Maximum measured shear stress (kPa)
Displacement (mm)
Slope 0.716636
Friction angle (φ') 35.6 degrees
cohesion (c') 5.877 kPa
R² 0.9956617

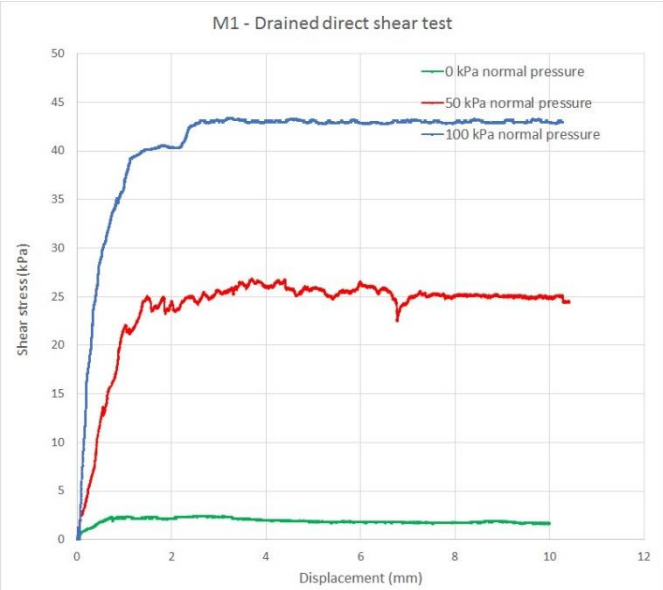
M1 - Drained direct shear test
0 kPa normal pressure
50 kPa normal pressure
100 kPa normal pressure
Shear stress (kPa)
Displacement (mm)

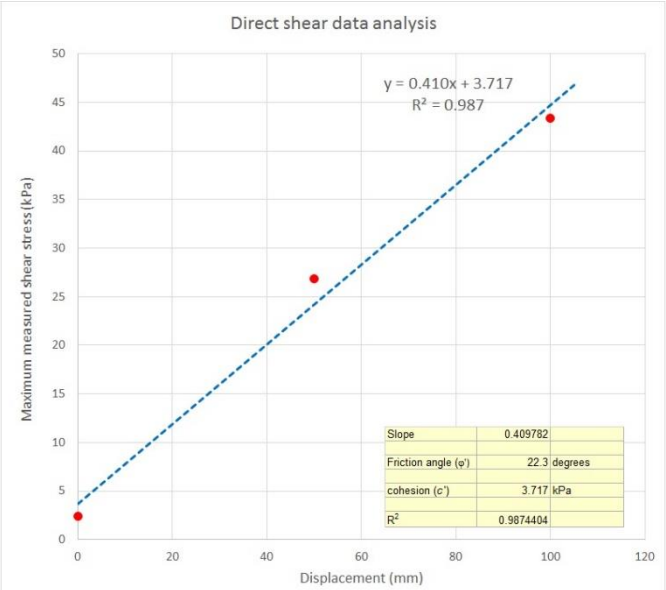
Direct shear data analysis
y = 0.410x + 3.717
R² = 0.987
Maximum measured shear stress (kPa)
Displacement (mm)
Slope 0.409782
Friction angle (φ') 22.3 degrees
cohesion (c') 3.717 kPa
R² 0.9874404

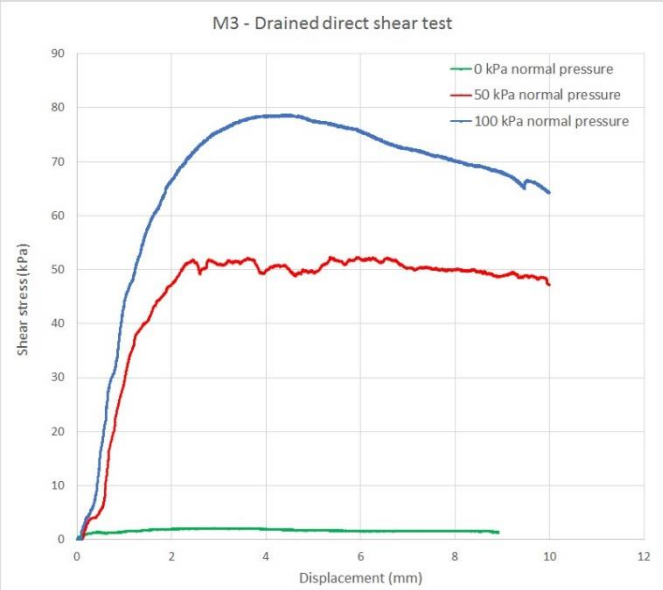
M3 - Drained direct shear test
0 kPa normal pressure
50 kPa normal pressure
100 kPa normal pressure
Shear stress (kPa)
Displacement (mm)

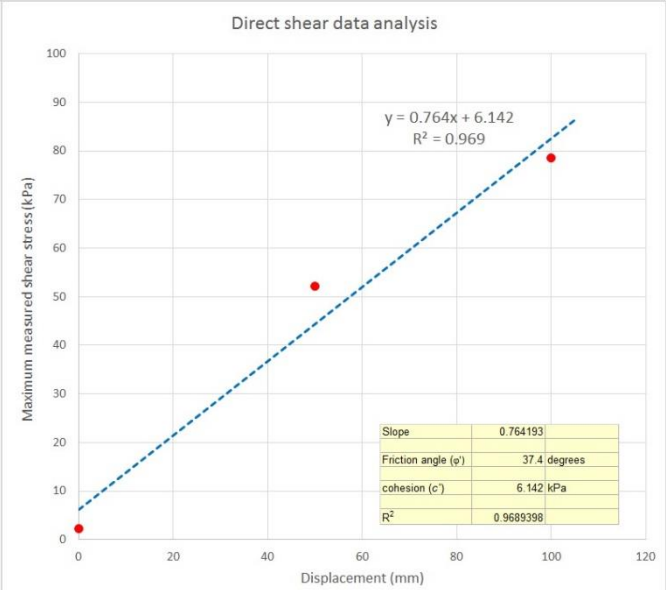
Direct shear data analysis
y = 0.764x + 6.142
R² = 0.969
Maximum measured shear stress (kPa)
Displacement (mm)
Slope 0.764193
Friction angle (φ') 37.4 degrees
cohesion (c') 6.142 kPa
R² 0.9689398

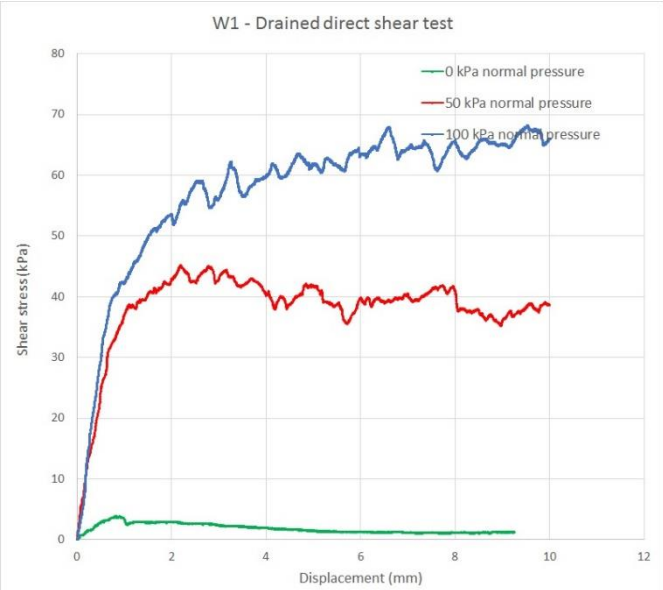
W1 - Drained direct shear test
0 kPa normal pressure
50 kPa normal pressure
100 kPa normal pressure
Shear stress (kPa)
Displacement (mm)

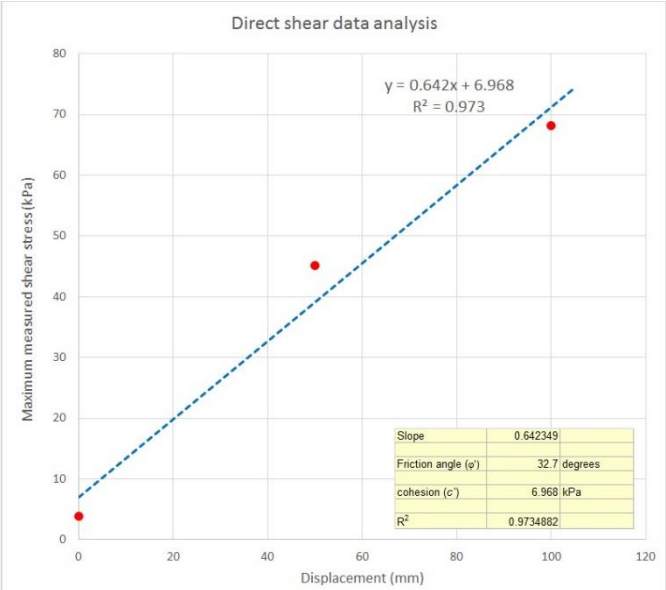
Direct shear data analysis
y = 0.642x + 6.968
R² = 0.973
Maximum measured shear stress (kPa)
Displacement (mm)
Slope 0.642349
Friction angle (φ') 32.7 degrees
cohesion (c') 6.968 kPa
R² 0.9734882

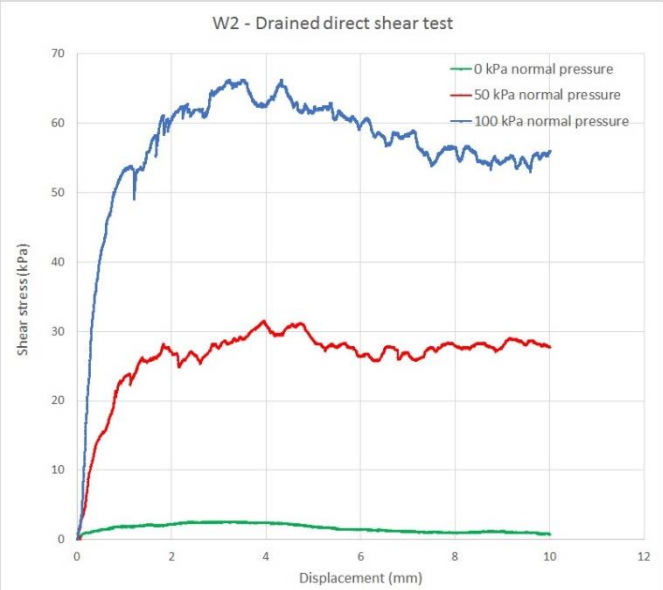
W2 - Drained direct shear test
0 kPa normal pressure
50 kPa normal pressure
100 kPa normal pressure
Shear stress (kPa)
Displacement (mm)

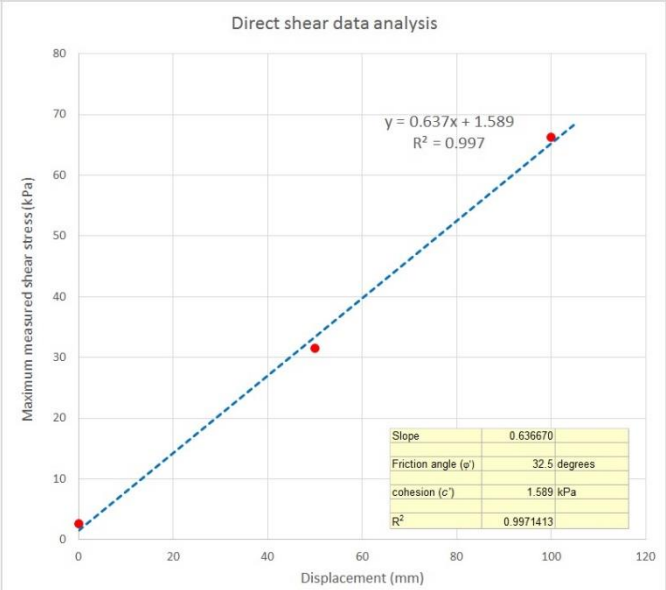
Direct shear data analysis
y = 0.637x + 1.589
R² = 0.997
Maximum measured shear stress (kPa)
Displacement (mm)
Slope 0.636670
Friction angle (φ') 32.5 degrees
cohesion (c') 1.589 kPa
R² 0.9971413

Results of hydraulic conductivity tests

Soil description:	Grey silty clay, soft, high moisture content, high plasticity	
Sample diameter	5.6	cm
Sample cross-section (A)	24.630	cm2
Sample height	10	cm
Header above soil in sample tube	4	cm
Head tube diameter	1.00	cm
Head tube cross-section (a)	0.79	cm2
Downstream tube diameter	14.6	cm

Time	Reading (cm)	H_u (cm)	H_L (cm)	Δt (s)	K (cm/s)
2018-06-03 17:35	181.0				
2018-06-03 17:57	180.5	185.0	184.5	1320	6.5E-07
2018-06-03 18:28	180.2	184.5	184.2	1860	2.8E-07
2018-06-03 18:46	179.9	184.2	183.9	1080	4.8E-07
2018-06-03 19:35	179.4	183.9	183.4	2940	2.9E-07
2018-06-03 20:30	178.4	183.4	182.4	3300	5.3E-07
2018-06-03 21:09	177.8	182.4	181.8	2340	4.5E-07
2018-06-03 22:48	176.6	181.8	180.6	5940	3.6E-07
2018-06-03 23:36	175.9	180.6	179.9	2880	4.3E-07
2018-06-04 17:25	143.6	179.9	147.6	64140	9.8E-07
			Hydraulic conductivity =		9.8E-07

On the basis of the test results, the permeability of the sample can be calculated as

$$K=[2.3\ a\ L\ /\ (A\ \Delta t)]\ Log(h\_U\ /\ h\_L)$$

in which we have

L: the height of the soil sample column
A: the sample cross section
a: the cross section of the standpipe
Δt: the recorded time for the water column to flow though the sample
h_U and h_L : the upper and lower water level in the standpipe measured using the same water head reference

Soil description:	Bluish grey Champlain sea clay, relatively small structures (smaller than 1 cm), high plas	
Sample diameter	5.6	cm
Sample cross-section (A)	24.630	cm2
Sample height	10	cm
Header above soil in sample tube	4	cm
Head tube diameter	1.00	cm
Head tube cross-section (a)	0.79	cm2
Downstream tube diameter	14.6	cm

Time	Reading (cm)	H_u (cm)	H_L (cm)	Δt (s)	K (cm/s)
2018-06-06 18:55	179.5				
2018-06-06 21:44	177.7	183.5	181.7	10140	3.1E-07
2018-06-07 10:55	170.9	181.7	174.9	47460	2.6E-07
2018-06-10 9:32	137.9	174.9	141.9	81420	8.2E-07
2018-06-11 20:03	124.7	141.9	128.7	37860	8.2E-07
				Hydraulic conductivity =	8.2E-07

Soil description:	Grey silty clay, some fine sand, low to medium plasticity	
Sample diameter	5.6	cm
Sample cross-section (A)	24.630	cm2
Sample height	9	cm
Header above soil in sample tube	5	cm
Head tube diameter	1.00	cm
Head tube cross-section (a)	0.79	cm2
Downstream tube diameter	14.6	cm

Time	Reading (cm)	H_u (cm)	H_L (cm)	Δt (s)	K (cm/s)
2018-06-05 18:30	181.0				
2018-06-06 9:53	180.5	186.0	185.5	55380	1.4E-08
2018-06-06 18:06	180.2	185.5	185.2	29580	1.6E-08
				Hydraulic conductivity =	1.5E-08

Results of hydrometer tests - core soils

Total mass of air-dried sample	50.06	g
Mass retained on the No. 10 Sieve	0.00	g
Mass passing the No. 10 Sieve	50.06	g
% passing the No. 10 Sieve	100.00	%

Hygroscopic moisture

Mass of dish	3.50	g
Mass of dish plus air-dry soil	18.50	g
Mass of dish oven-dry soil	18.50	g
Hygroscopic moisture correction	1.000	

Hydrometer test

Mass of air-dry soil for Hydrometer test	50.06	g
Equivalent oven-dry mass of Hydrometer soil	50.06	g
Equivalent oven-dry mass passing No. 10 sieve (W)	50.06	g

Hydrometer test: Sample: Stillwater Creek, ST15

Time	Hydrometer Reading	Suspension Temperature	Corrected Reading	Soil in suspension P (%)	Effective length L (cm)	Particle diameter D (mm)	
% finer than 2 mm (passing No.10 sieve) >>				100.00	-	2.000	
1	35	22	35.10	70.12	10.5	0.0432	70.1
2	29.5	22	29.60	59.13	11.4	0.0319	
5	23	22	23.10	46.14	12.5	0.0211	
15	20	21	20.05	40.05	13.0	0.0126	
30	17	21	17.05	34.06	13.5	0.0090	
60	15	21	15.05	30.06	13.8	0.0065	
250	12	20	12.00	23.97	14.3	0.0033	
1440	10	20	10.00	19.98	14.7	0.0014	20.0

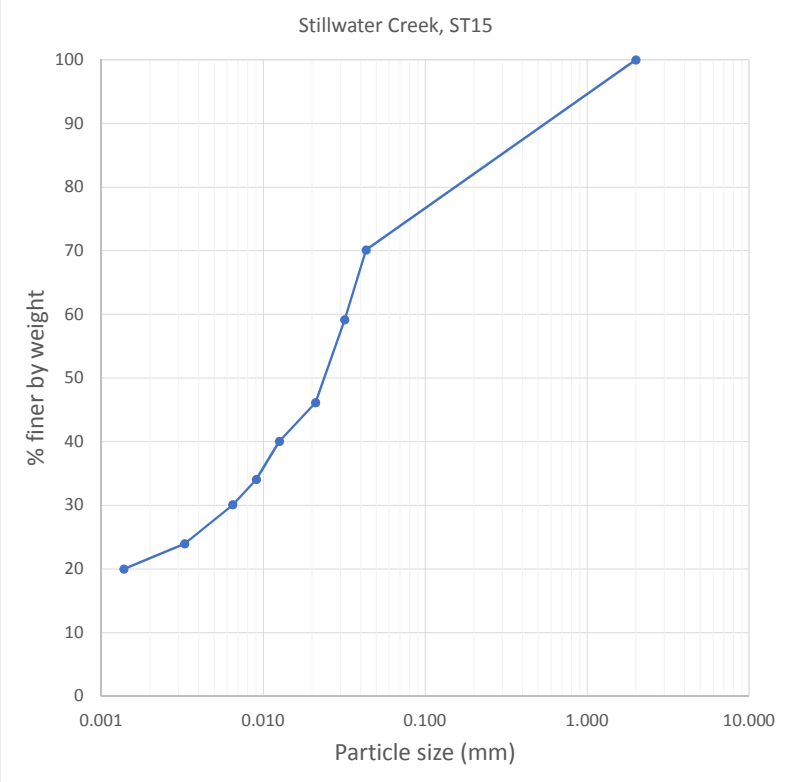

Total mass of air-dried sample	50.44	g
Mass retained on the No. 10 Sieve	0.00	g
Mass passing the No. 10 Sieve	50.44	g
% passing the No. 10 Sieve	100.00	%

Hygroscopic moisture

Mass of dish	3.50	g
Mass of dish plus air-dry soil	18.50	g
Mass of dish oven-dry soil	18.50	g
Hygroscopic moisture correction	1.000	

Hydrometer test

Mass of air-dry soil for Hydrometer test	50.44	g
Equivalent oven-dry mass of Hydrometer soil	50.44	g
Equivalent oven-dry mass passing No. 10 sieve (W)	50.44	g

Hydrometer test: Sample: Stillwater Creek, ST19.1

Time	Hydrometer Reading	Suspension Temperature	Corrected Reading	Soil in suspension P (%)	Effective length L (cm)	Particle diameter D (mm)	
% finer than 2 mm (passing No.10 sieve) >>				100.00	-	2.000	
1	48	22	48.10	95.36	8.4	0.0386	95.4
2	45	22	45.10	89.41	8.9	0.0281	
5	44	21	44.05	87.33	9.1	0.0182	
15	41	21	41.05	81.38	9.6	0.0108	
30	39	21	39.05	77.42	9.9	0.0077	
60	38	20	38.00	75.34	10.1	0.0056	
250	32	20	32.00	63.44	11.0	0.0029	
1440	23	20	23.00	45.60	12.5	0.0013	45.6

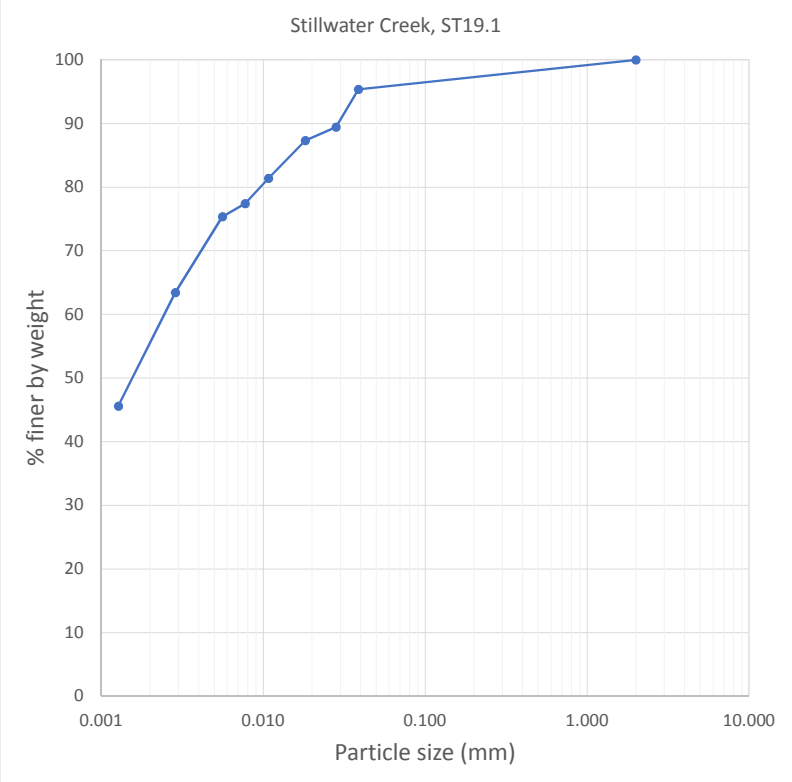

Total mass of air-dried sample	50.54 g
Mass retained on the No. 10 Sieve	0.00 g
Mass passing the No. 10 Sieve	50.54 g
% passing the No. 10 Sieve	100.00 %

Hygroscopic moisture

Mass of dish	3.50 g
Mass of dish plus air-dry soil	18.50 g
Mass of dish oven-dry soil	18.50 g
Hygroscopic moisture correction	1.000

Hydrometer test

Mass of air-dry soil for Hydrometer test	50.54 g
Equivalent oven-dry mass of Hydrometer soil	50.54 g
Equivalent oven-dry mass passing No. 10 sieve (W)	50.54 g

Hydrometer test: Sample: Stillwater Creek, ST40.1

Time	Hydrometer Reading	Suspension Temperature	Corrected Reading	Soil in suspension P (%)	Effective length L (cm)	Particle diameter D (mm)	
% finer than 2 mm (passing No.10 sieve) >>				100.00	-	2.000	
1	37	22	37.10	73.41	10.2	0.0426	73.4
2	33	22	33.10	65.49	10.9	0.0310	
5	30	21	30.05	59.46	11.4	0.0203	
15	27	21	27.05	53.52	11.9	0.0120	
30	26	20	26.00	51.44	12.0	0.0086	
60	24	20	24.00	47.49	12.4	0.0062	
250	21	20	21.00	41.55	12.9	0.0031	
1440	16	19	15.95	31.56	13.7	0.0013	31.6

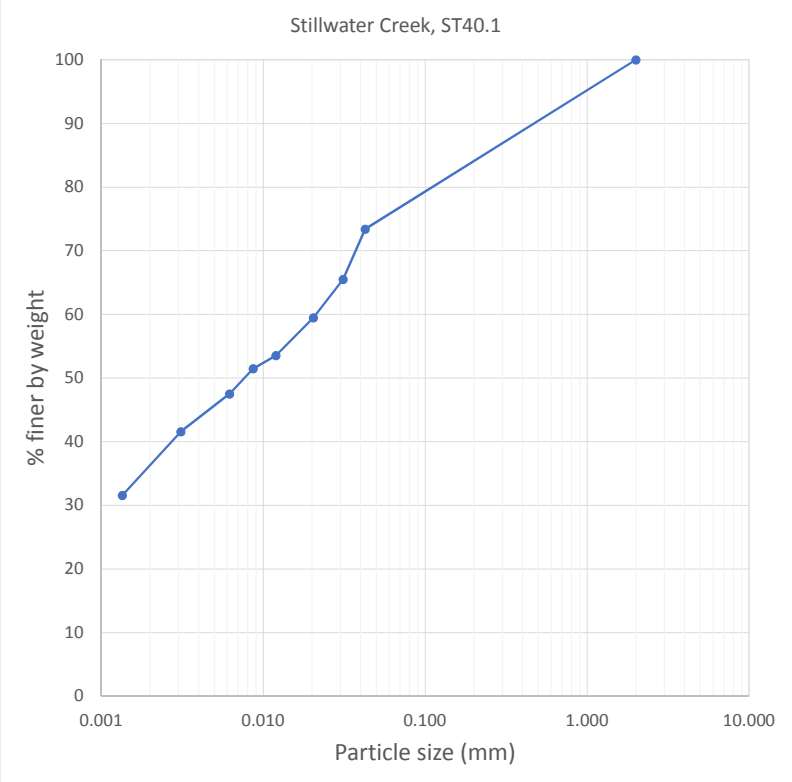

Total mass of air-dried sample	50.69 g
Mass retained on the No. 10 Sieve	0.00 g
Mass passing the No. 10 Sieve	50.69 g
% passing the No. 10 Sieve	100.00 %

Hygroscopic moisture

Mass of dish	3.50 g
Mass of dish plus air-dry soil	18.50 g
Mass of dish oven-dry soil	18.50 g
Hygroscopic moisture correction	1.000

Hydrometer test

Mass of air-dry soil for Hydrometer test	50.69 g
Equivalent oven-dry mass of Hydrometer soil	50.69 g
Equivalent oven-dry mass passing No. 10 sieve (W)	50.69 g

Hydrometer test: Sample: Stillwater Creek, ST48.2

Time	Hydrometer Reading	Suspension Temperature	Corrected Reading	Soil in suspension P (%)	Effective length L (cm)	Particle diameter D (mm)
% finer than 2 mm (passing No.10 sieve) >>				100.00	-	2.000
1	0	0	0.00	0.00	16.3	#N/A
2	38	22	38.10	75.16	10.0	0.0299
5	35	22	35.10	69.24	10.5	0.0193
15	32	22	32.10	63.33	11.0	0.0114
30	30	22	30.10	59.38	11.4	0.0082
60	28	22	28.10	55.43	11.7	0.0059
250	23	21	23.05	45.47	12.5	0.0030
2780	16	20	16.00	31.56	13.7	0.0010

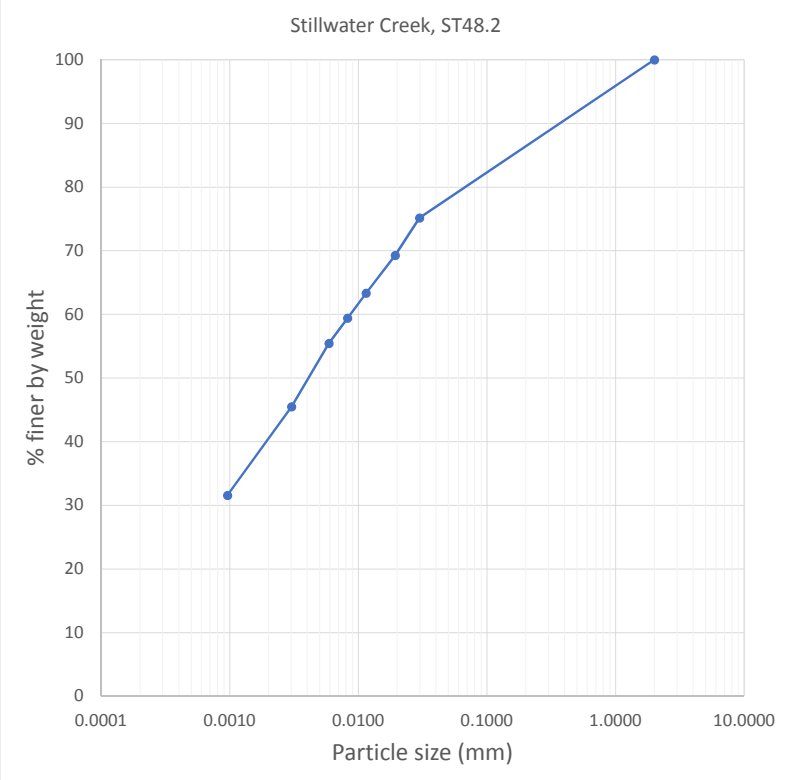

Total mass of air-dried sample	50.51 g
Mass retained on the No. 10 Sieve	0.00 g
Mass passing the No. 10 Sieve	50.51 g
% passing the No. 10 Sieve	100.00 %

Hygroscopic moisture

Mass of dish	3.50 g
Mass of dish plus air-dry soil	18.50 g
Mass of dish oven-dry soil	18.50 g
Hygroscopic moisture correction	1.000

Hydrometer test

Mass of air-dry soil for Hydrometer test	50.51 g
Equivalent oven-dry mass of Hydrometer soil	50.51 g
Equivalent oven-dry mass passing No. 10 sieve (W)	50.51 g

Hydrometer test: Sample: Stillwater Creek, ST50.3

Time	Hydrometer Reading	Suspension Temperature	Corrected Reading	Soil in suspension P (%)	Effective length L (cm)	Particle diameter D (mm)	
% finer than 2 mm (passing No.10 sieve) >>				100.00	-	2.000	
1	25	23	25.15	49.79	12.2	0.0459	49.8
2	22	23	22.15	43.85	12.7	0.0331	
5	20	23	20.15	39.89	13.0	0.0212	
15	18	22	18.10	35.83	13.3	0.0126	
30	16	22	16.10	31.87	13.7	0.0090	
60	15.5	21	15.55	30.79	13.7	0.0065	
250	13	20	13.00	25.74	14.2	0.0032	
1440	10	20	10.00	19.80	14.7	0.0014	19.8

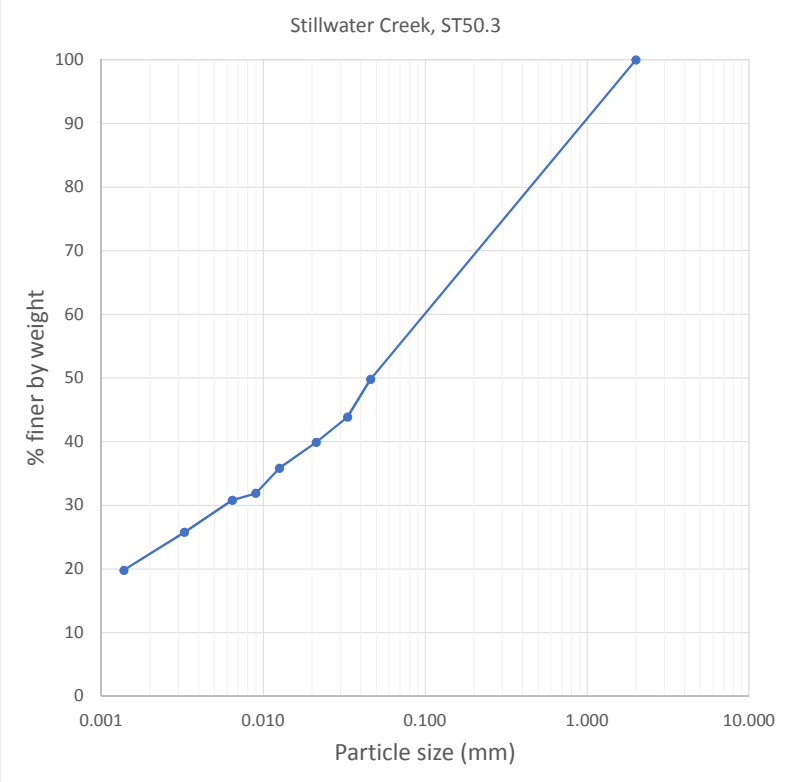

Hydrometer test data
Watts creek

Time (min)	Temp(*C)	Hydrometer Reading	% Finer	Effective Length (L)	L/t	Sqrt(L/t)	K	Diameter
1	24	47	91.08527	8.6	8.6	2.932576	0.01282	0.037596
2	24	47	91.08527	8.6	4.3	2.073644	0.01282	0.026584
3	24	47	91.08527	8.6	2.866667	1.693123	0.01282	0.021706
5	24	46	89.14729	8.8	1.76	1.32665	0.01282	0.017008
10	24	46	89.14729	8.8	0.88	0.938083	0.01282	0.012026
15	24	45.2	87.5969	8.9	0.593333	0.770281	0.01282	0.009875
30	24	43.5	84.30233	9.15	0.305	0.552268	0.01282	0.00708
60	24	42	81.39535	9.4	0.156667	0.395811	0.01282	0.005074
240	24	37	71.70543	10.2	0.0425	0.206155	0.01282	0.002643
349	24	35.5	68.79845	10.5	0.030086	0.173453	0.01282	0.002224
4800	24	22	42.63566	12.7	0.002646	0.051438	0.01282	0.000659

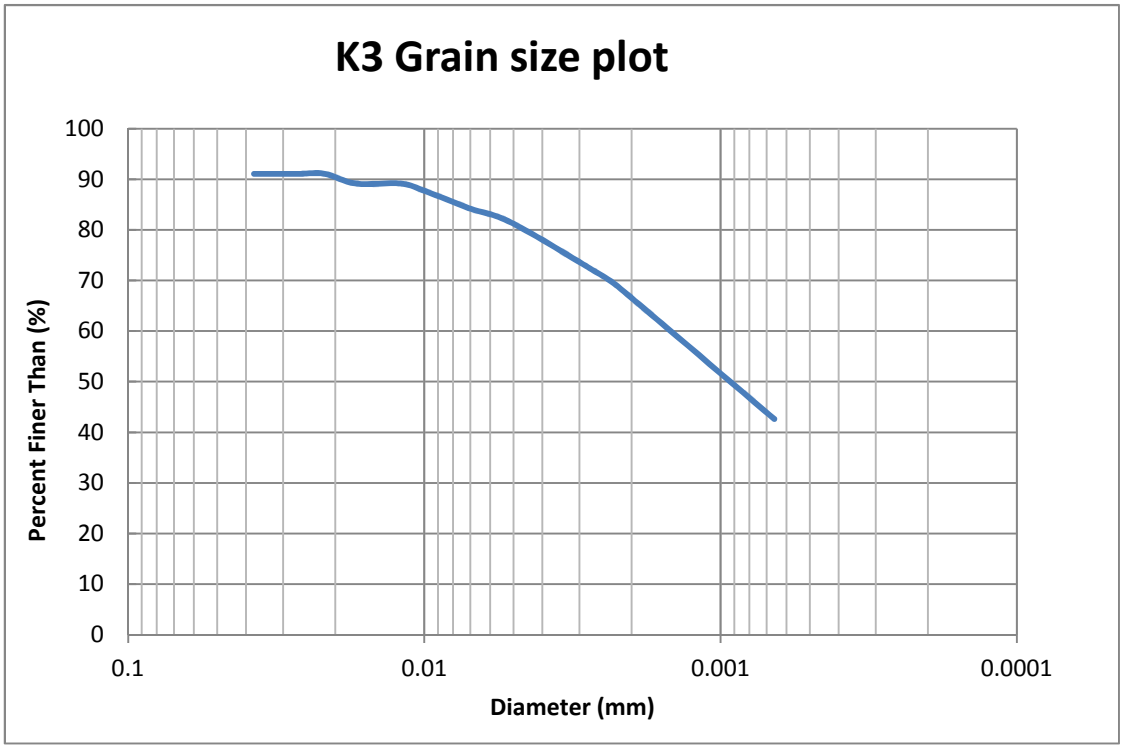

Hydrometer test data
Watts creek

Time (min)	Temp(*C)	Hydrometer Reading	% Finer	Effective Length (L)	L/t	Sqrt(L/t)	K	Diameter
1	24	50	98.81423	8.1	8.1	2.84605	0.01282	0.036486
2	24	49	96.83794	8.3	4.15	2.037155	0.01282	0.026116
3	24	48	94.86166	8.4	2.8	1.67332	0.01282	0.021452
5	24	46	90.90909	8.8	1.76	1.32665	0.01282	0.017008
10	24	45	88.93281	8.9	0.89	0.943398	0.01282	0.012094
15	24	44	86.95652	9.1	0.606667	0.778888	0.01282	0.009985
30	24	43	84.98024	9.2	0.306667	0.553775	0.01282	0.007099
60	24	41.5	82.01581	9.5	0.158333	0.397911	0.01282	0.005101
240	24	36.5	72.13439	10.3	0.042917	0.207163	0.01282	0.002656
349	24	35.5	70.1581	10.5	0.030086	0.173453	0.01282	0.002224
4800	24	25.5	50.39526	12.1	0.002521	0.050208	0.01282	0.000644

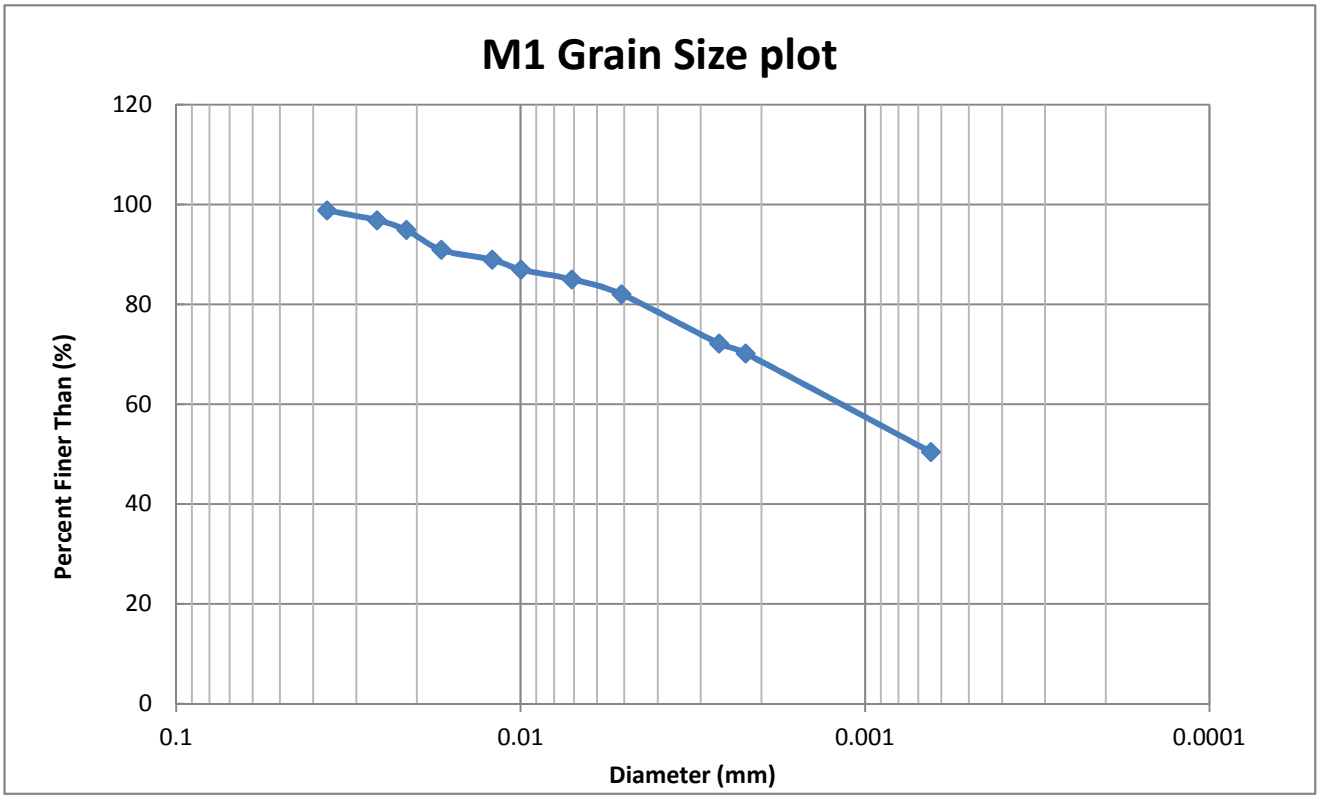

Hydrometer test data
Watts creek

Time (min)	Temp(*C)	Hydrometer Reading	% Finer	Effective Length (L)	L/t	Sqrt(L/t)	K	Diameter
1	24	25	49.91016	12.2	12.2	3.49285	0.01282	0.044778
2	24	24	47.91376	12.4	6.2	2.48998	0.01282	0.031922
3	24	22	43.92094	12.7	4.233333	2.057507	0.01282	0.026377
4	24	21	41.92454	12.9	3.225	1.795828	0.01282	0.023023
5	24	20.5	40.92633	13	2.6	1.612452	0.01282	0.020672
10	24	19.5	38.92993	13.1	1.31	1.144552	0.01282	0.014673
15	24	18.5	36.93352	13.25	0.883333	0.939858	0.01282	0.012049
30	24	18	35.93532	13.3	0.443333	0.665833	0.01282	0.008536
60	24	17.2	34.33819	13.4	0.223333	0.472582	0.01282	0.006058
95	24	17	33.93891	13.5	0.142105	0.376969	0.01282	0.004833
120	24	16.5	32.94071	13.6	0.113333	0.33665	0.01282	0.004316
165	24	16.3	32.54143	13.7	0.08303	0.28815	0.01282	0.003694
250	24	16.1	32.14214	13.7	0.0548	0.234094	0.01282	0.003001
1302	24	14	27.94969	14	0.010753	0.103695	0.01282	0.001329
10080	24	12	23.95688	14.3	0.001419	0.037665	0.01282	0.000483

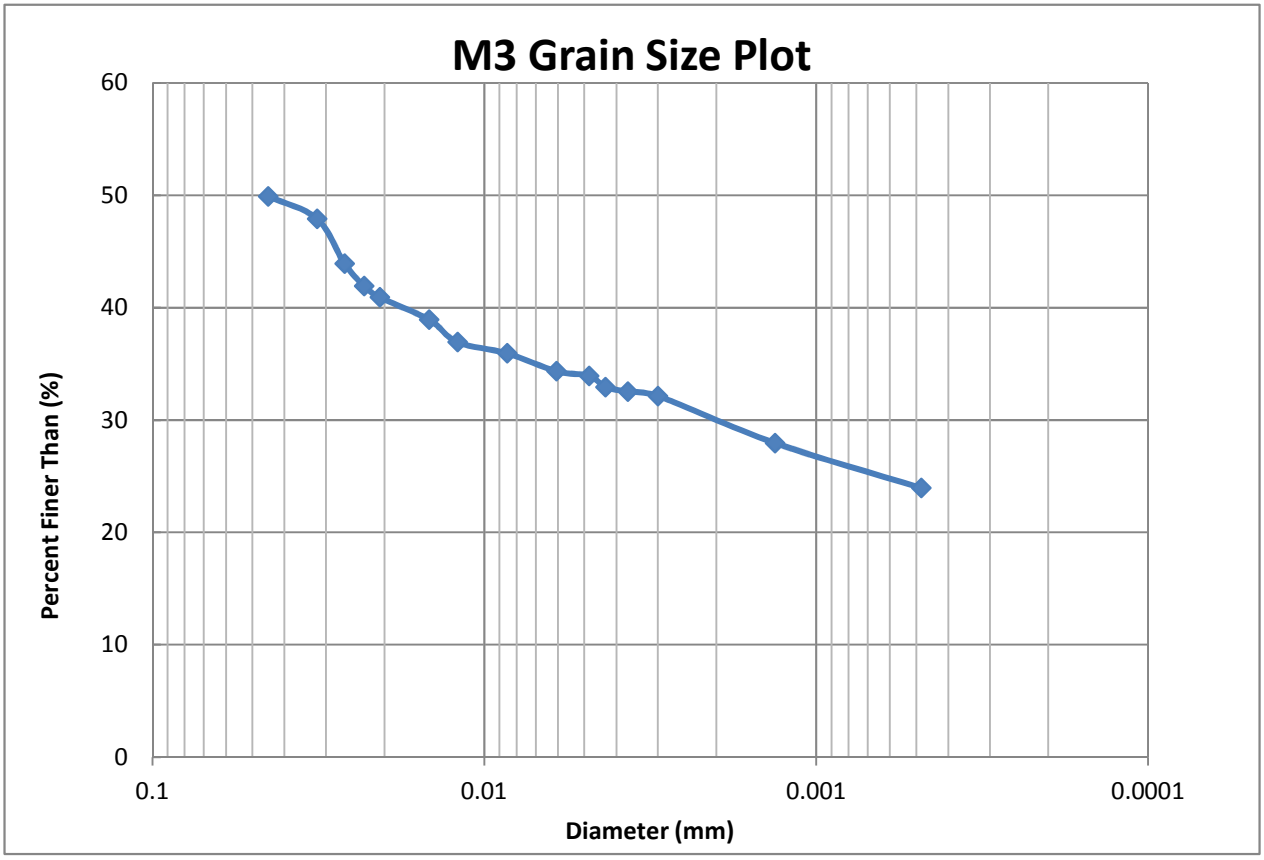

Total mass of air-dried sample	57.42	g
Mass retained on the No. 10 Sieve	0.00	g
Mass passing the No. 10 Sieve	57.42	g
% passing the No. 10 Sieve	100.00	%

Hygroscopic moisture

Mass of dish	0.00	g
Mass of dish plus air-dry soil	31.58	g
Mass of dish oven-dry soil	25.57	g
Hygroscopic moisture correction	0.810	

Hydrometer test

Mass of air-dry soil for Hydrometer test	57.42	g
Equivalent oven-dry mass of Hydrometer soil	46.50	g
Equivalent oven-dry mass passing No. 10 sieve (W)	46.50	g

Hydrometer test: Sample: W1

Time	Hydrometer Reading	Suspension Temperature	Corrected Reading	Soil in suspension P (%)	Effective length L (cm)	Particle diameter D (mm)
% finer than 2 mm (passing No.10 sieve) >>				100.00	-	2.000
1	28	26	28.30	60.86	11.7	0.0434
2	27	26	27.30	58.71	11.8	0.0309
5	24	26	24.30	52.26	12.3	0.0200
15	21	26	21.30	45.81	12.8	0.0118
30	20	26	20.30	43.66	13.0	0.0084
60	19	26	19.30	41.51	13.1	0.0060
250	16	25	16.25	34.95	13.6	0.0030
1440	14	25	14.25	30.65	14.0	0.0013

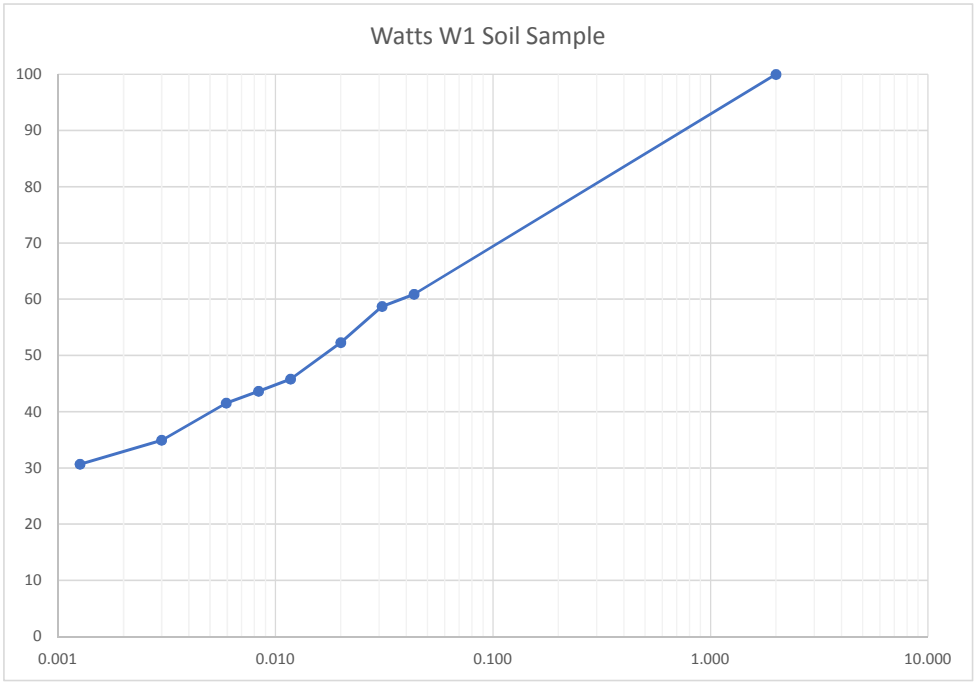

Hydrometer test data

Watts creek

Time (min)	Temp(*C)	Hydrometer Reading	% Finer	Effective Length (L)	L/t	Sqrt(L/t)	K	Diameter
1	24	33	64.13	10.9	10.9	3.301514804	0.01411	0.046584
2	24	30.5	59.27	11.3	5.65	2.376972865	0.01411	0.033539
3	24	29	56.35	11.5	3.833333333	1.957890021	0.01411	0.027626
5	24	26.8	52.08	11.9	2.38	1.542724862	0.01411	0.021768
10	24	25	48.58	12.2	1.22	1.104536102	0.01411	0.015585
15	24	24	46.64	12.4	0.826666667	0.909212113	0.01411	0.012829
30	24	23	44.69	12.5	0.416666667	0.645497224	0.01411	0.009108
60	24	22	42.75	12.7	0.211666667	0.460072458	0.01411	0.006492
120	24	21	40.81	12.9	0.1075	0.327871926	0.01411	0.004626
314	24	20.5	39.84	12.95	0.041242038	0.203081359	0.01411	0.002865
1394	24	18.5	35.95	13.25	0.009505022	0.0974937	0.01411	0.001376
2256	24	17	33.04	13.5	0.005984043	0.077356593	0.01411	0.001092
2652	24	16	31.09	13.7	0.005165913	0.071874283	0.01411	0.001014

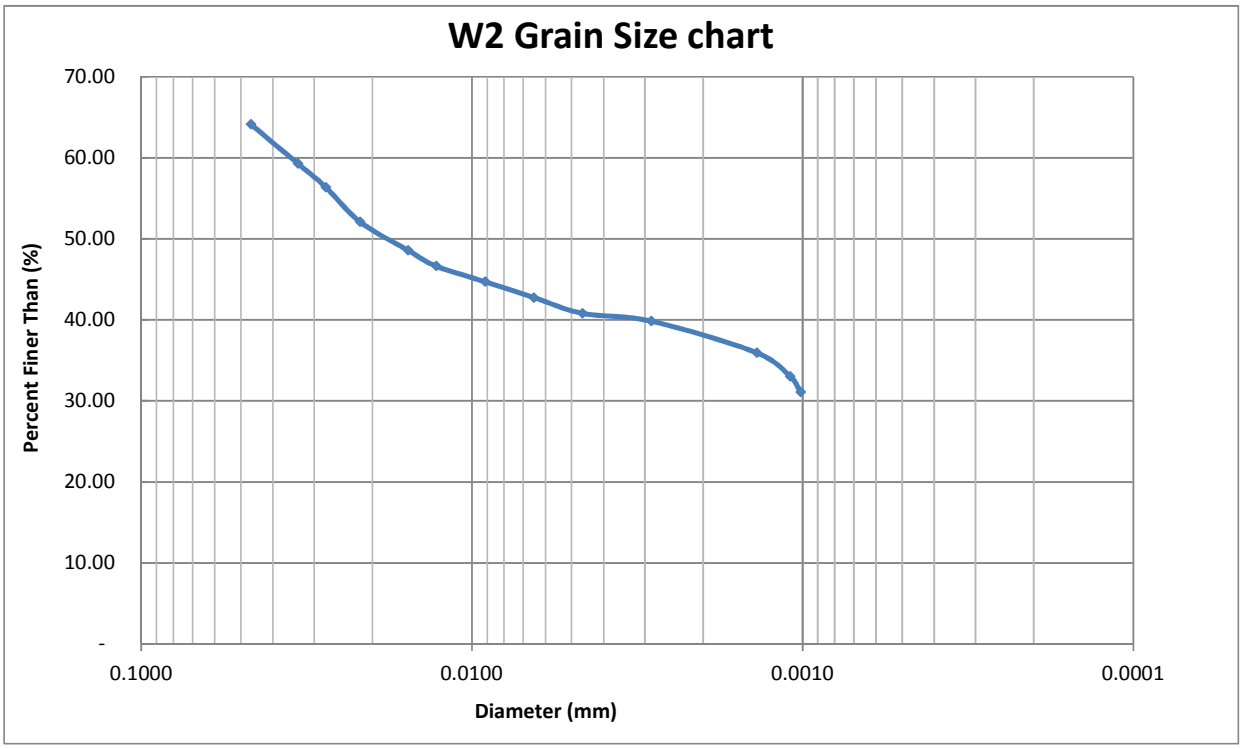

Results of hydrometer tests - Supplemental soils

Total mass of air-dried sample	60.71 g
Mass retained on the No. 10 Sieve	0.00 g
Mass passing the No. 10 Sieve	60.71 g
% passing the No. 10 Sieve	100.00 %

Hygroscopic moisture

Mass of dish	3.50 g
Mass of dish plus air-dry soil	18.50 g
Mass of dish oven-dry soil	18.50 g
Hygroscopic moisture correction	1.000

Hydrometer test

Mass of air-dry soil for Hydrometer test	60.71 g
Equivalent oven-dry mass of Hydrometer soil	60.71 g
Equivalent oven-dry mass passing No. 10 sieve (W)	60.71 g

Hydrometer test: Sample: Stillwater Creek, ST10

Time	Hydrometer Reading	Suspension Temperature	Corrected Reading	Soil in suspension P (%)	Effective length L (cm)	Particle diameter D (mm)
% finer than 2 mm (passing No.10 sieve) >>				100.00	-	2.000
1	34	23	34.15	56.25	10.7	0.0431
2	30	23	30.15	49.66	11.4	0.0314
5	27	23	27.15	44.72	11.8	0.0203
15	27	23	27.15	44.72	11.8	0.0117
30	25	21	25.05	41.26	12.2	0.0086
60	24	21	24.05	39.61	12.4	0.0061
250	22	20	22.00	36.24	12.7	0.0031
1440	0	0	0.00	0.00	16.3	#N/A

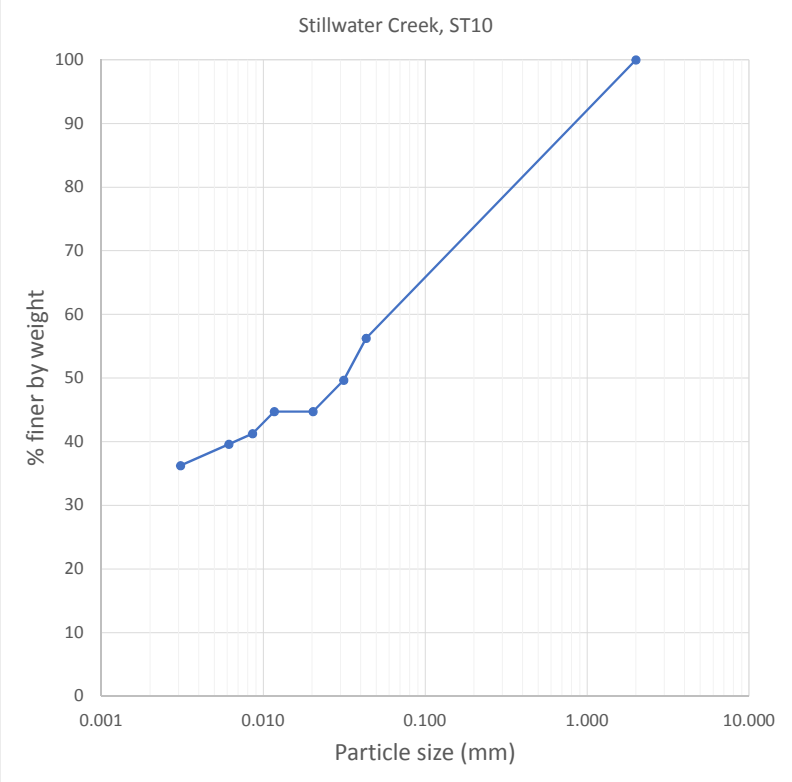

Total mass of air-dried sample	52.71	g
Mass retained on the No. 10 Sieve	0.00	g
Mass passing the No. 10 Sieve	52.71	g
% passing the No. 10 Sieve	100.00	%

Hygroscopic moisture

Mass of dish	3.50	g
Mass of dish plus air-dry soil	18.50	g
Mass of dish oven-dry soil	18.50	g
Hygroscopic moisture correction	1.000	

Hydrometer test

Mass of air-dry soil for Hydrometer test	52.71	g
Equivalent oven-dry mass of Hydrometer soil	52.71	g
Equivalent oven-dry mass passing No. 10 sieve (W)	52.71	g

Hydrometer test: Sample: Stillwater Creek, ST25.2

Time	Hydrometer Reading	Suspension Temperature	Corrected Reading	Soil in suspension P (%)	Effective length L (cm)	Particle diameter D (mm)
% finer than 2 mm (passing No.10 sieve) >>				100.00	-	2.000
1	0	0	0.00	0.00	16.3	#N/A
2	48	22	48.10	91.25	8.4	0.0273
5	46	22	46.10	87.46	8.7	0.0176
15	45	22	45.10	85.56	8.9	0.0103
30	42	21	42.05	79.78	9.4	0.0075
60	40	21	40.05	75.98	9.7	0.0054
250	36	20	36.00	68.30	10.4	0.0028
1440	0	0	0.00	0.00	16.3	#N/A

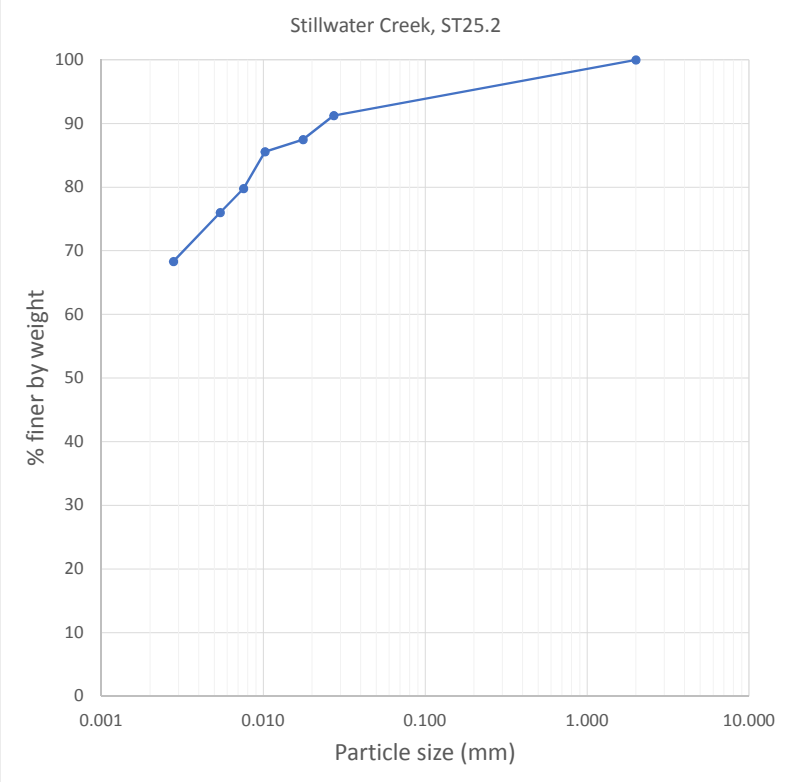

Total mass of air-dried sample	52.41 g
Mass retained on the No. 10 Sieve	0.00 g
Mass passing the No. 10 Sieve	52.41 g
% passing the No. 10 Sieve	100.00 %

Hygroscopic moisture

Mass of dish	3.50 g
Mass of dish plus air-dry soil	18.50 g
Mass of dish oven-dry soil	18.50 g
Hygroscopic moisture correction	1.000

Hydrometer test

Mass of air-dry soil for Hydrometer test	52.41 g
Equivalent oven-dry mass of Hydrometer soil	52.41 g
Equivalent oven-dry mass passing No. 10 sieve (W)	52.41 g

Hydrometer test: Sample: Stillwater Creek, ST37

Time	Hydrometer Reading	Suspension Temperature	Corrected Reading	Soil in suspension P (%)	Effective length L (cm)	Particle diameter D (mm)	
% finer than 2 mm (passing No.10 sieve) >>				100.00	-	2.000	
1	43	21	43.05	82.14	9.2	0.0410	82.1
2	41	21	41.05	78.32	9.6	0.0295	
5	39	20	39.00	74.41	9.9	0.0192	
15	36	20	36.00	68.69	10.4	0.0114	
30	31	20	31.00	59.15	11.2	0.0083	
60	27	20	27.00	51.52	11.9	0.0061	
250	21	20	21.00	40.07	12.9	0.0031	
1440	16	20	16.00	30.53	13.7	0.0013	30.5

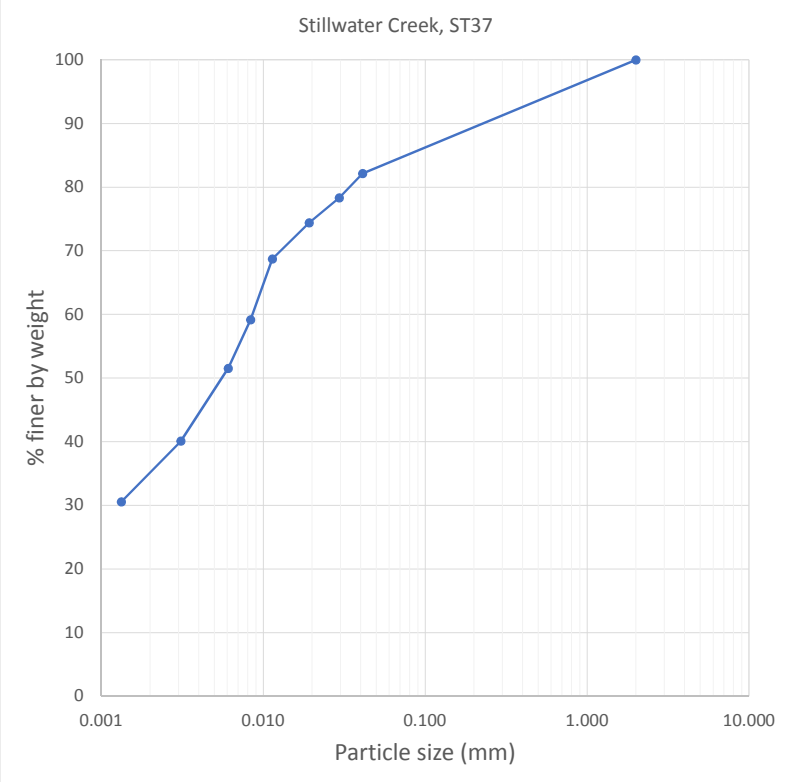

Total mass of air-dried sample	55.11 g
Mass retained on the No. 10 Sieve	0.00 g
Mass passing the No. 10 Sieve	55.11 g
% passing the No. 10 Sieve	100.00 %

Hygroscopic moisture

Mass of dish	3.50 g
Mass of dish plus air-dry soil	18.50 g
Mass of dish oven-dry soil	18.50 g
Hygroscopic moisture correction	1.000

Hydrometer test

Mass of air-dry soil for Hydrometer test	55.11 g
Equivalent oven-dry mass of Hydrometer soil	55.11 g
Equivalent oven-dry mass passing No. 10 sieve (W)	55.11 g

Hydrometer test: Sample: Stillwater Creek, ST39

Time	Hydrometer Reading	Suspension Temperature	Corrected Reading	Soil in suspension P (%)	Effective length L (cm)	Particle diameter D (mm)	
% finer than 2 mm (passing No.10 sieve) >>				100.00	-	2.000	
1	42	22	42.10	76.39	9.4	0.0408	76.4
2	40	22	40.10	72.76	9.7	0.0294	
5	38	21	38.05	69.04	10.1	0.0191	
15	35	21	35.05	63.60	10.5	0.0113	
30	33	21	33.05	59.97	10.9	0.0081	
60	31	20	31.00	56.25	11.2	0.0059	
250	26	20	26.00	47.18	12.0	0.0030	
1440	20	20	20.00	36.29	13.0	0.0013	36.3

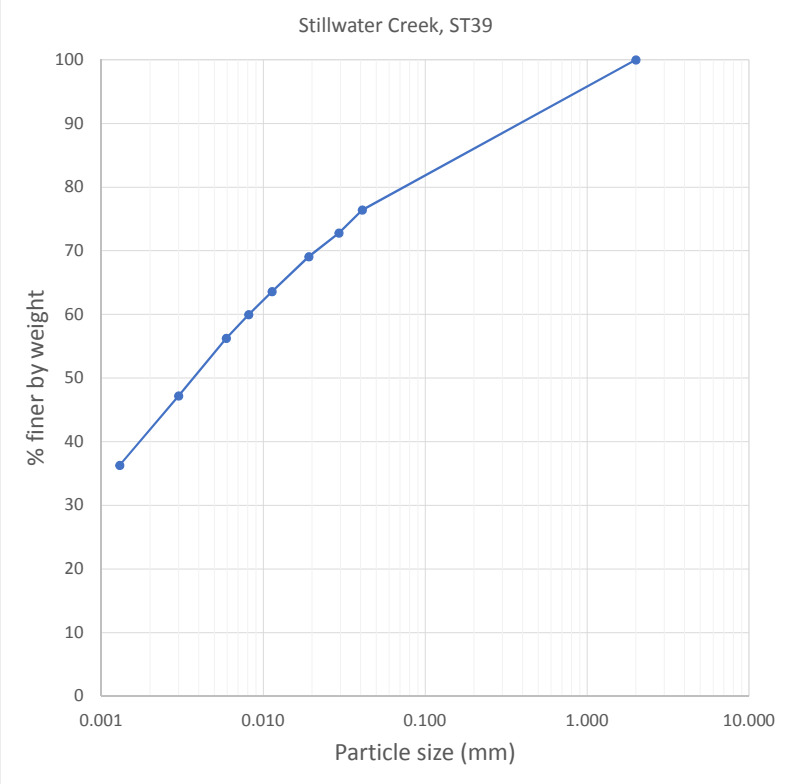

Total mass of air-dried sample	57.00 g
Mass retained on the No. 10 Sieve	0.00 g
Mass passing the No. 10 Sieve	57.00 g
% passing the No. 10 Sieve	100.00 %

Hygroscopic moisture

Mass of dish	3.50 g
Mass of dish plus air-dry soil	18.50 g
Mass of dish oven-dry soil	18.50 g
Hygroscopic moisture correction	1.000

Hydrometer test

Mass of air-dry soil for Hydrometer test	57.00 g
Equivalent oven-dry mass of Hydrometer soil	57.00 g
Equivalent oven-dry mass passing No. 10 sieve (W)	57.00 g

Hydrometer test: Sample: Stillwater Creek, S1

Time	Hydrometer Reading	Suspension Temperature	Corrected Reading	Soil in suspension P (%)	Effective length L (cm)	Particle diameter D (mm)
% finer than 2 mm (passing No.10 sieve) >>				100.00	-	2.000
2	30	23	30.15	52.89	11.4	0.0314
5	26	23	26.15	45.88	12.0	0.0204
15	22	23	22.15	38.86	12.7	0.0121
30	21	22	21.10	37.02	12.8	0.0087
60	20	22	20.10	35.26	13.0	0.0062
250	18	22	18.10	31.75	13.3	0.0031
1350	14	21	14.05	24.65	14.0	0.0014
1440	13	20	13.00	22.81	14.2	0.0014

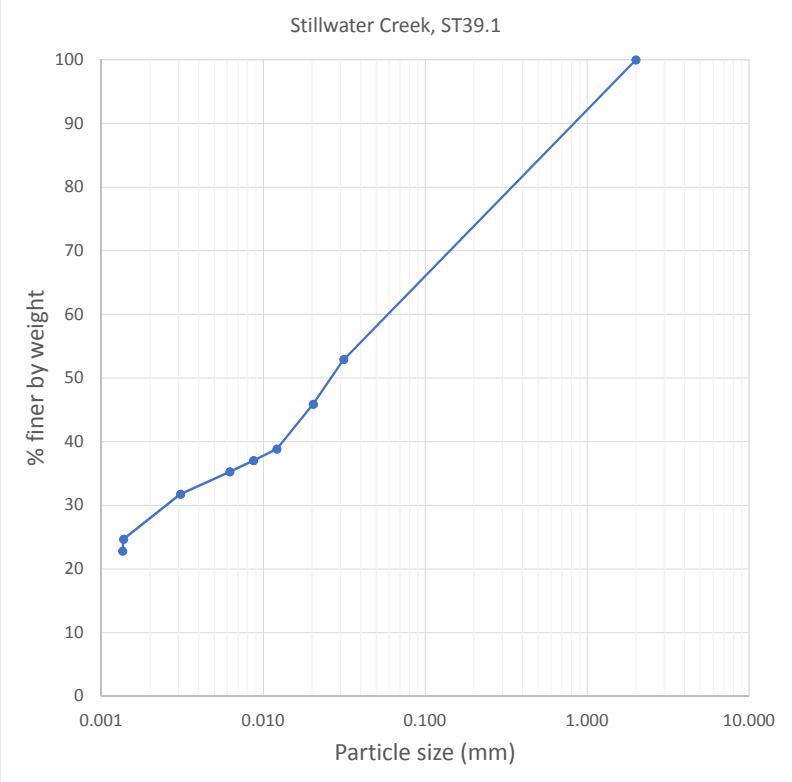

Total mass of air-dried sample	50.52 g
Mass retained on the No. 10 Sieve	0.00 g
Mass passing the No. 10 Sieve	50.52 g
% passing the No. 10 Sieve	100.00 %

Hygroscopic moisture

Mass of dish	3.50 g
Mass of dish plus air-dry soil	18.50 g
Mass of dish oven-dry soil	18.50 g
Hygroscopic moisture correction	1.000

Hydrometer test

Mass of air-dry soil for Hydrometer test	50.52 g
Equivalent oven-dry mass of Hydrometer soil	50.52 g
Equivalent oven-dry mass passing No. 10 sieve (W)	50.52 g

Hydrometer test: Sample: Stillwater Creek, S2

Time	Hydrometer Reading	Suspension Temperature	Corrected Reading	Soil in suspension P (%)	Effective length L (cm)	Particle diameter D (mm)
% finer than 2 mm (passing No.10 sieve) >>				100.00	-	2.000
1	0	0	0.00	0.00	16.3	#N/A
2	15	23	15.15	29.99	13.8	0.0346
5	14	23	14.15	28.01	14.0	0.0220
15	12	23	12.15	24.05	14.3	0.0129
30	10.5	22	10.60	20.98	14.6	0.0093
60	10	22	10.10	19.99	14.6	0.0066
250	8	21	8.05	15.93	15.0	0.0033
1440	7	20	7.00	13.86	15.1	0.0014

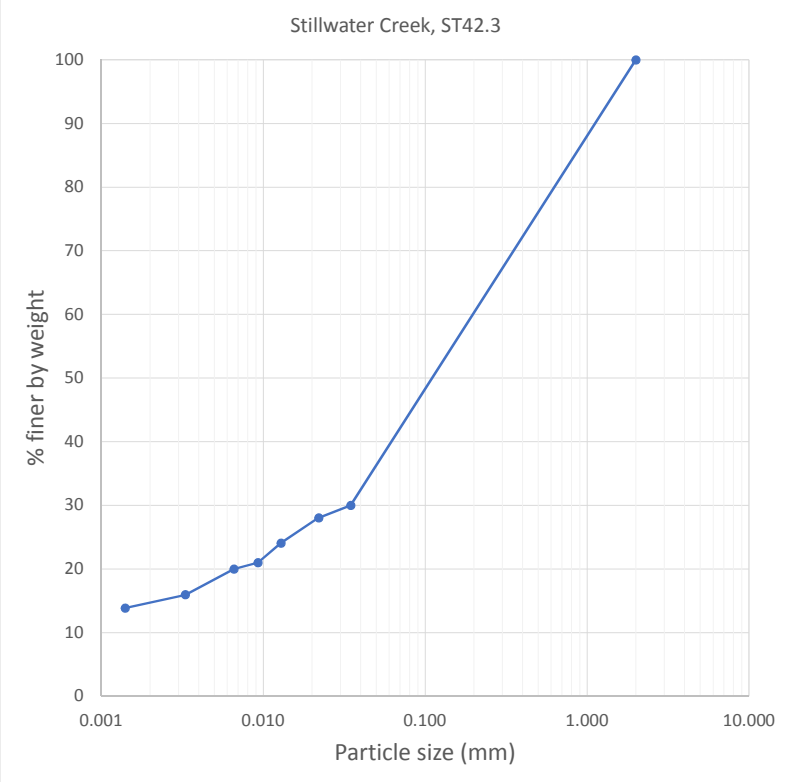

Total mass of air-dried sample	50.13 g
Mass retained on the No. 10 Sieve	0.00 g
Mass passing the No. 10 Sieve	50.13 g
% passing the No. 10 Sieve	100.00 %

Hygroscopic moisture

Mass of dish	3.50 g
Mass of dish plus air-dry soil	18.50 g
Mass of dish oven-dry soil	18.50 g
Hygroscopic moisture correction	1.000

Hydrometer test

Mass of air-dry soil for Hydrometer test	50.13 g
Equivalent oven-dry mass of Hydrometer soil	50.13 g
Equivalent oven-dry mass passing No. 10 sieve (W)	50.13 g

Hydrometer test: Sample: Stillwater Creek, S3

Time	Hydrometer Reading	Suspension Temperature	Corrected Reading	Soil in suspension P (%)	Effective length L (cm)	Particle diameter D (mm)
% finer than 2 mm (passing No.10 sieve) >>				100.00	-	2.000
1	47	22	47.10	93.96	8.6	0.0390
2	44	22	44.10	87.97	9.1	0.0284
5	42	22	42.10	83.98	9.4	0.0183
15	38	21	38.05	75.90	10.1	0.0110
30	36	21	36.05	71.91	10.4	0.0079
60	36	21	36.05	71.91	10.4	0.0056
250	32	21	32.05	63.93	11.0	0.0028
2880	25	20	25.00	49.87	12.2	0.0009

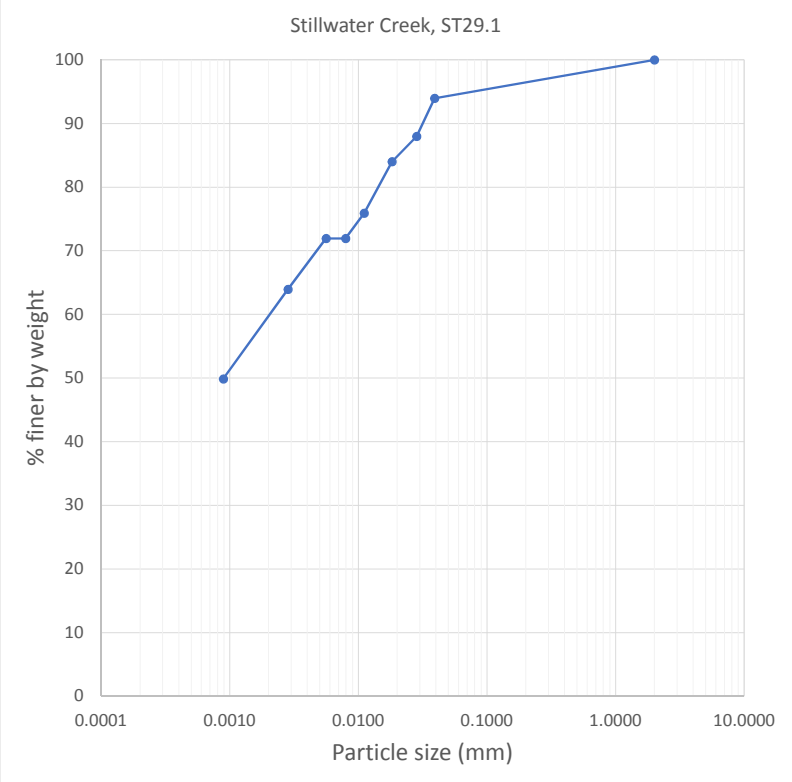

Total mass of air-dried sample	57.19 g
Mass retained on the No. 10 Sieve	0.00 g
Mass passing the No. 10 Sieve	57.19 g
% passing the No. 10 Sieve	100.00 %

Hygroscopic moisture

Mass of dish	3.50 g
Mass of dish plus air-dry soil	18.50 g
Mass of dish oven-dry soil	18.50 g
Hygroscopic moisture correction	1.000

Hydrometer test

Mass of air-dry soil for Hydrometer test	57.19 g
Equivalent oven-dry mass of Hydrometer soil	57.19 g
Equivalent oven-dry mass passing No. 10 sieve (W)	57.19 g

Hydrometer test: Sample: Stillwater Creek, S4

Time	Hydrometer Reading	Suspension Temperature	Corrected Reading	Soil in suspension P (%)	Effective length L (cm)	Particle diameter D (mm)
% finer than 2 mm (passing No.10 sieve) >>				100.00	-	2.000
1	57	22	57.10	99.84	6.9	0.0351
2	55	22	55.10	96.35	7.3	0.0254
5	51	21	51.05	89.26	7.9	0.0170
15	47	21	47.05	82.27	8.6	0.0102
30	45	20	45.00	78.69	8.9	0.0074
60	42	20	42.00	73.44	9.4	0.0054
250	35	20	35.00	61.20	10.6	0.0028
1440	27	20	27.00	47.21	11.9	0.0012

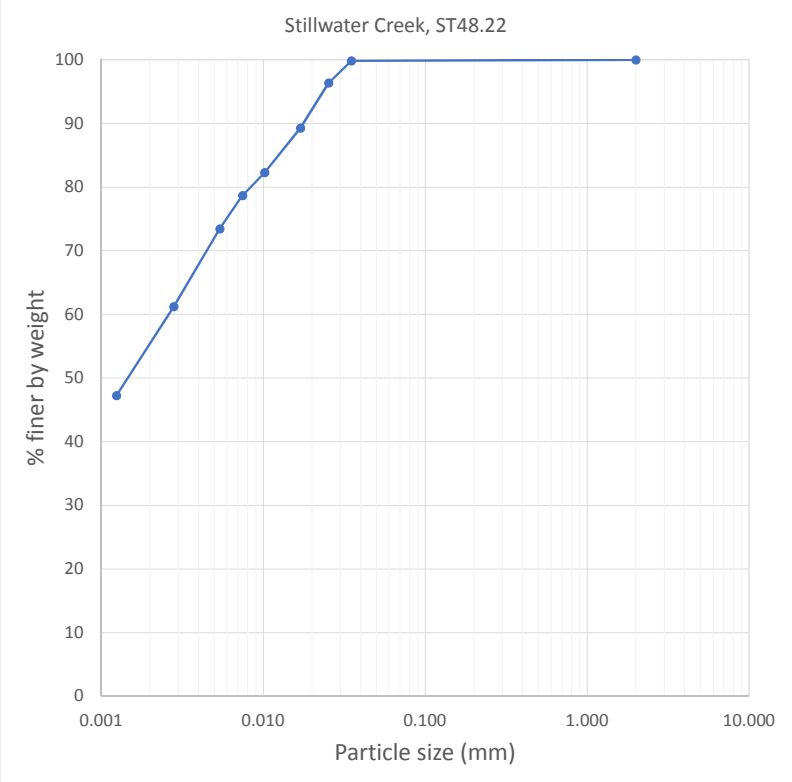

Total mass of air-dried sample	57.19 g
Mass retained on the No. 10 Sieve	0.00 g
Mass passing the No. 10 Sieve	57.19 g
% passing the No. 10 Sieve	100.00 %

Hygroscopic moisture

Mass of dish	3.50 g
Mass of dish plus air-dry soil	18.50 g
Mass of dish oven-dry soil	18.50 g
Hygroscopic moisture correction	1.000

Hydrometer test

Mass of air-dry soil for Hydrometer test	57.19 g
Equivalent oven-dry mass of Hydrometer soil	57.19 g
Equivalent oven-dry mass passing No. 10 sieve (W)	57.19 g

Hydrometer test: Sample: Stillwater Creek, S5

Time	Hydrometer Reading	Suspension Temperature	Corrected Reading	Soil in suspension P (%)	Effective length L (cm)	Particle diameter D (mm)
% finer than 2 mm (passing No.10 sieve) >>				100.00	-	2.000
1	18	22	18.10	31.65	13.3	0.0486
2	16	21	16.05	28.06	13.7	0.0352
5	15	21	15.05	26.32	13.8	0.0224
15	14	21	14.05	24.57	14.0	0.0130
30	14	21	14.05	24.57	14.0	0.0092
60	13	20	13.00	22.73	14.2	0.0066
250	12	20	12.00	20.98	14.3	0.0033
1440	0	0	0.00	0.00	16.3	#N/A

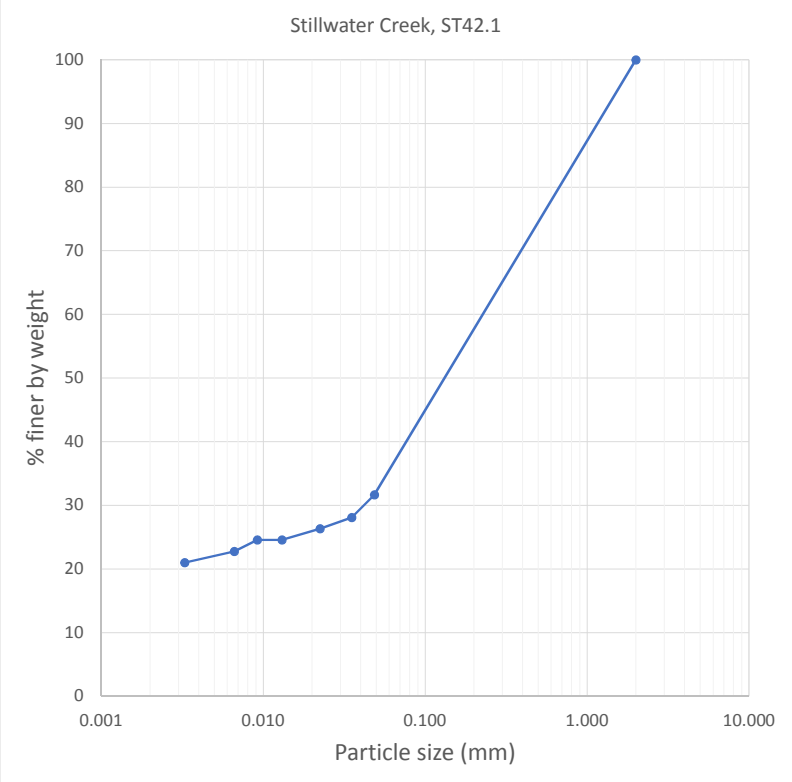

Total mass of air-dried sample	55.11	g
Mass retained on the No. 10 Sieve	0.00	g
Mass passing the No. 10 Sieve	55.11	g
% passing the No. 10 Sieve	100.00	%

Hygroscopic moisture

Mass of dish	3.64	g
Mass of dish plus air-dry soil	35.27	g
Mass of dish oven-dry soil	34.70	g
Hygroscopic moisture correction	0.982	

Hydrometer test

Mass of air-dry soil for Hydrometer test	50.25	g
Equivalent oven-dry mass of Hydrometer soil	49.34	g
Equivalent oven-dry mass passing No. 10 sieve (W)	49.34	g

Hydrometer test: Sample: Muddy Creek 2

	Time	Hydrometer Reading	Suspension Temperature	Corrected Reading	Soil in suspension P (%)	Effective length L (cm)	Particle diameter D (mm)
	% finer than 2 mm (passing No.10 sieve) >>				100.00	-	2.000
15:21	1	33	18	32.90	66.67	10.9	0.0462
15:22	2	33	18	32.90	66.67	10.9	0.0327
15:25	5	33	18	32.90	66.67	10.9	0.0207
15:35	15	33	18	32.90	66.67	10.9	0.0119
15:50	30	32	18	31.90	64.65	11.1	0.0085
16:20	60	31	18	30.90	62.62	11.2	0.0061
19:30	250	28	18	27.90	56.54	11.7	0.0030
14:49	1440	23	18	22.90	46.41	12.5	0.0013

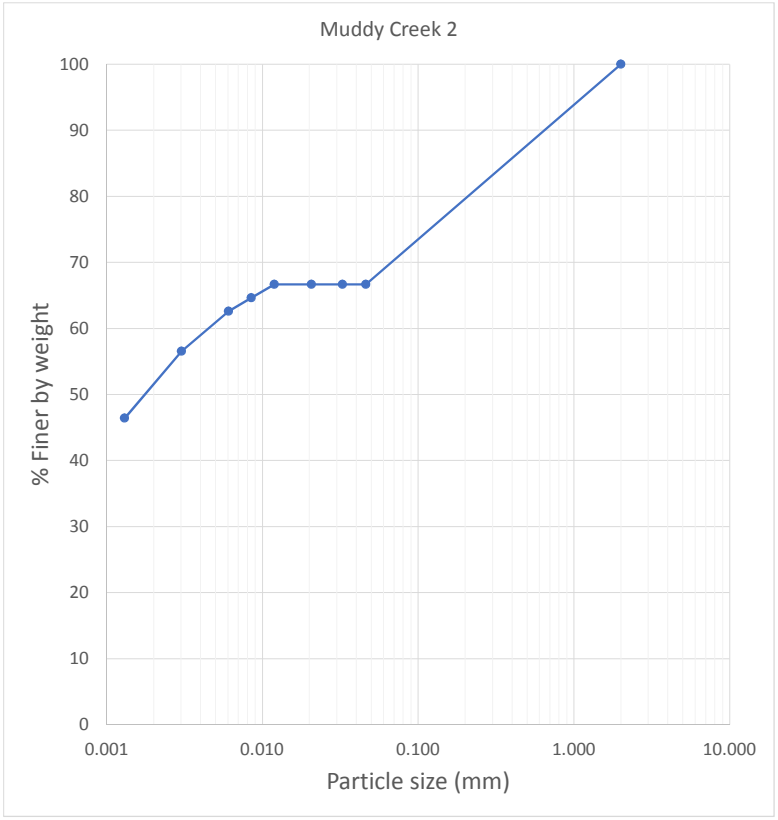

Total mass of air-dried sample	5055.11	g
Mass retained on the No. 10 Sieve	0.00	g
Mass passing the No. 10 Sieve	5055.11	g
% passing the No. 10 Sieve	100.00	%

Hygroscopic moisture

Mass of dish	3.74	g
Mass of dish plus air-dry soil	18.50	g
Mass of dish oven-dry soil	18.50	g
Hygroscopic moisture correction	1.000	

Hydrometer test

Mass of air-dry soil for Hydrometer test	50.78	g
Equivalent oven-dry mass of Hydrometer soil	50.78	g
Equivalent oven-dry mass passing No. 10 sieve (W)	50.78	g

Hydrometer test: Sample: Green's Creek 2

	Time	Hydrometer Reading	Suspension Temperature	Corrected Reading	Soil in suspension P (%)	Effective length L (cm)	Particle diameter D (mm)
	% finer than 2 mm (passing No.10 sieve) >>				100.00	-	2.000
14:31	1	20	18	19.90	39.19	13.0	0.0505
14:32	2	20	18	19.90	39.19	13.0	0.0357
14:35	5	19	18	18.90	37.22	13.2	0.0227
14:45	15	17	18	16.90	33.28	13.5	0.0133
15:00	30	16	18	15.90	31.31	13.7	0.0094
15:30	60	16	18	15.90	31.31	13.7	0.0067
18:40	250	15	18	14.90	29.34	13.9	0.0033
14:47	1457	13	18	12.90	25.40	14.2	0.0014

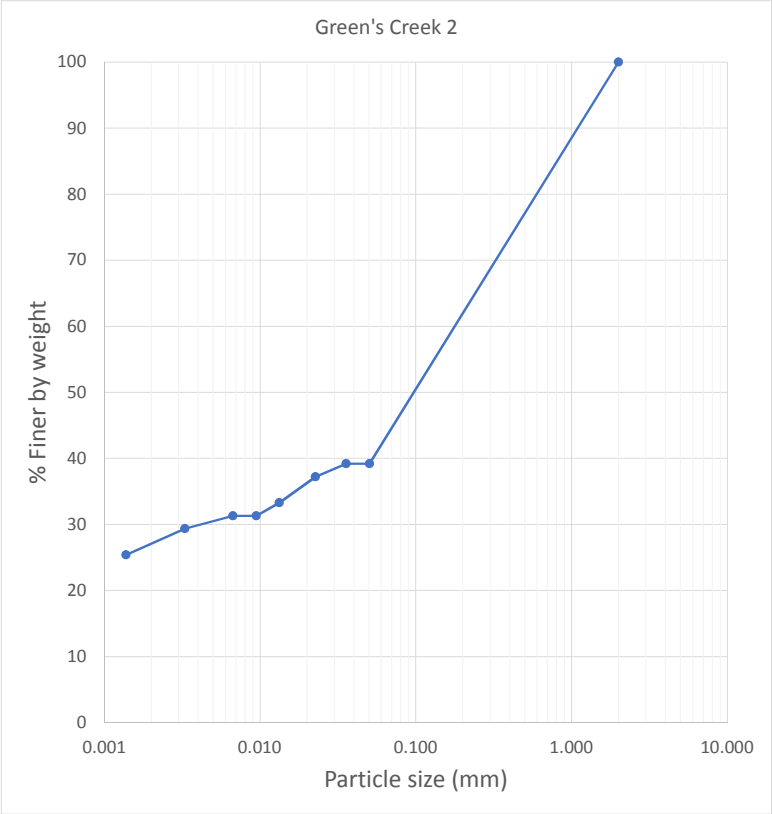

Total mass of air-dried sample	55.11	g
Mass retained on the No. 10 Sieve	0.00	g
Mass passing the No. 10 Sieve	55.11	g
% passing the No. 10 Sieve	100.00	%

Hygroscopic moisture

Mass of dish	3.67	g
Mass of dish plus air-dry soil	49.40	g
Mass of dish oven-dry soil	48.86	g
Hygroscopic moisture correction	0.988	

Hydrometer test

Mass of air-dry soil for Hydrometer test	50.34	g
Equivalent oven-dry mass of Hydrometer soil	49.75	g
Equivalent oven-dry mass passing No. 10 sieve (W)	49.75	g

Hydrometer test: Sample: South Nation River 1

	Time	Hydrometer Reading	Suspension Temperature	Corrected Reading	Soil in suspension P (%)	Effective length L (cm)	Particle diameter D (mm)
	% finer than 2 mm (passing No.10 sieve) >>				100.00	-	2.000
14:56	1	16	18	15.90	31.96	13.7	0.0518
14:57	2	13	18	12.90	25.93	14.2	0.0373
15:00	5	12	18	11.90	23.92	14.3	0.0237
15:10	15	11	18	10.90	21.91	14.5	0.0138
15:25	30	10	18	9.90	19.90	14.7	0.0098
15:55	60	10	18	9.90	19.90	14.7	0.0069
19:05	250	9	18	8.90	17.89	14.8	0.0034
14:48	1433	8	18	7.90	15.88	15.0	0.0014

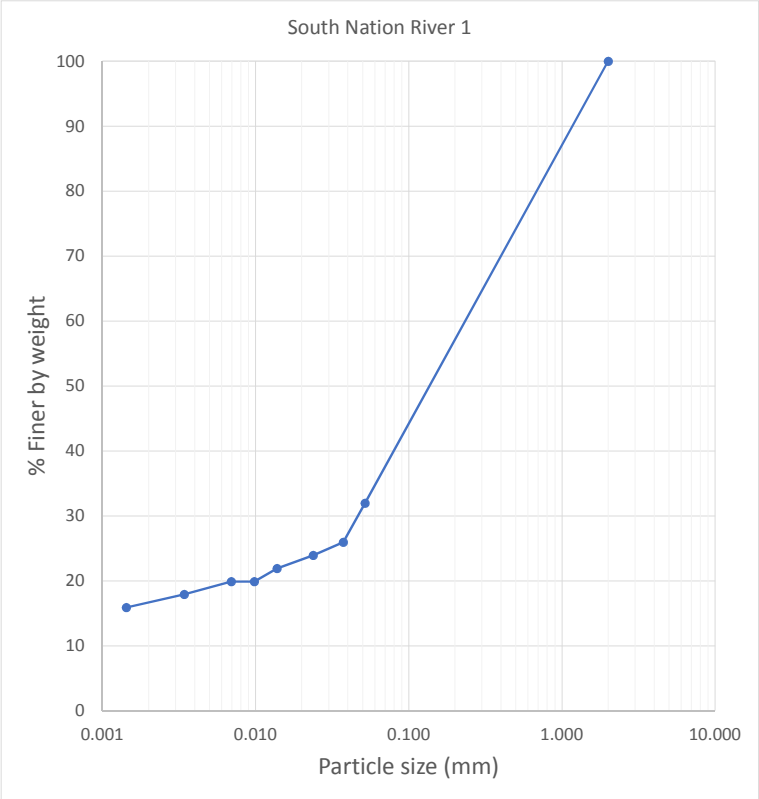

Appendix 4:
Publication 1
Influence of Pore Pressure on Clay Erosion

Salem H.(S.), Rennie, C.D., Custodio, C.Z. (2014) Influence of Pore Pressure on Clay Erosion, River Flow 2014, Lausanne, Switzerland, Sep. 3-5, 2014.

Abstract title: Influence of Pore Pressure on Clay Erosion

H. (Sam) Salem
University of Ottawa, Ottawa, Ontario, Canada

Colin D. Rennie
University of Ottawa, Ottawa, Ontario, Canada

Carlo Zaro Custodio
Exchange Student, University of Ottawa, Ottawa, Ontario, Canada

ABSTRACT: In comparison to sand and gravel, cohesive soils, and clays in particular, present significant challenges when critical entrainment thresholds and erosion rates are to be modeled in the laboratory. When modeling sand beds for example, buoyant weights of individual particles can be quantified. The water below the bed surface can be reasonably considered an extension of the water flowing above the surface in the sense that a hydrostatic pressure distribution can be assumed throughout. Therefore, aside from facilitating particle buoyancy, and possibly bed sediment dilation, it can be assumed that pore water has relatively little influence on erosion and transport mechanisms in non-cohesive sediments. The objective of this paper is to highlight important principles to consider when modeling actual field conditions involving the erosion of cohesive soils such as clayey sands. A specialized device presented herein was designed specifically to examine the influence of positive or negative pore water pressure on critical entrainment thresholds. Initial calibration of the device showed a very close correlation with critical shear values measured in the laboratory flume. Subsequent testing showed an increase in critical shear following a rise in pressure head applied to the surface of the sample.

1 INTRODUCTION

The erosion potential (erodibility) of cohesive soils is not yet well understood. Extensive flume tests and measurements have been done on cohesive samples, be it clayey silty sands or silty clays; however, erosion simulations on such soils have proven very difficult.

Part of the difficulty in simulating the effect of water flow on cohesive samples is the near impossibility to replicate field conditions, namely, the constantly varying pore water pressure within the soils in response to changing flow depth, changing groundwater conditions and resulting seepage pressures, and other variations both in space and time at study sites. Unlike granular soils, which adopt the new conditions almost instantly, cohesive soils tend to take significant time to reach steady state under new imposed conditions, and often take longer than the duration of the changed conditions. Julian et. al., 2006, enumerated a multitude of difficulties as such and used statistical methods to relate the entrainment of cohesive riverbanks to peak flow intensity, duration and silt-clay content of the soils, which in a way reflects the cyclic variation in pore pressure within the bed and bank materials.

In addition, the slow rate of erosion and the fact that cohesive soils erode mainly in clusters of random size and shape, as opposed to individual grains in the case of granular soils, adds another layer of difficulty to the research.

In this study, a different approach to the potential of cohesive soil erosion is explored. Consider a drainage channel or creek where cyclic flash flows occur following major precipitation events. It is traditionally expected that flash flows are associated with the bulk of observed erosion of the channel bed. While this may be true for the upper-level banks near the flow surface, it is not the case for the bed and lower-level banks where the new pressure differential contributes to the stability of the bed. Figure 1 below illustrates the bed condition following the relatively fast rise in water level. While the soil structure within a transition zone supports the bulk of the added weight, the pressure differential causes a temporary downward gradient that maintains the coherence of the bed surface much like a synthetic liner. It should be noted that this scenario may not apply in large scale

cases where the added water load approaches the strength of the soil in the bed, though the occurrence of such cases is not common.

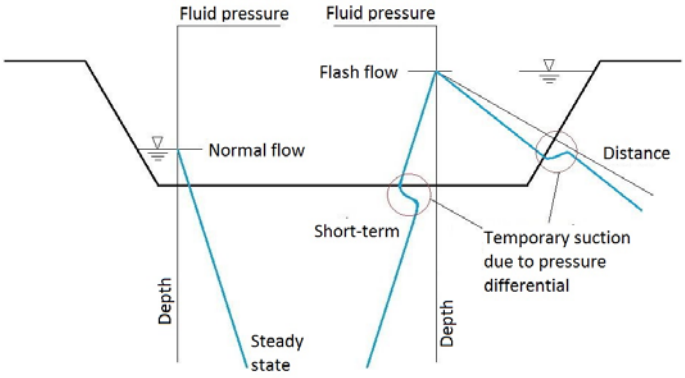

Figure 1: Pore pressure profile at flash flow

Now consider the case where the creek is situated in a ravine and drains the watershed composed of the steep eroded slopes on both sides of the ravine. In such cases, a significant change in groundwater conditions around and below the bed is expected between dry and wet seasons. These changes are magnified in cases where layers and lenses of permeable soils are sandwiched within the hillside soil profile. As the hillside gets saturated from infiltrated precipitation and rising water table, and the clay forming the slope face acts as a practically impervious barrier, it is common to find non-hydrostatic pressures below the surface near the bottom of the slope and under the stream bed. These conditions are illustrated in Figure 2 below.

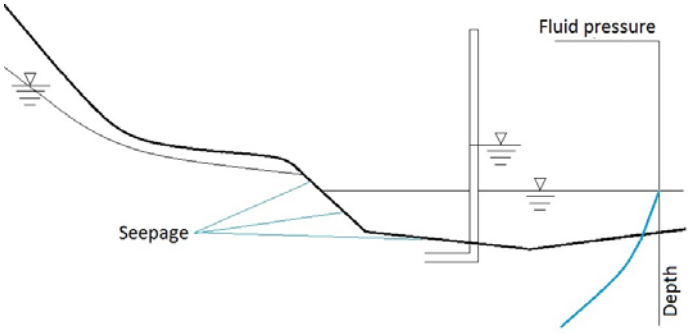

Figure 2: Pore pressure in ravine

Similar conditions, to a lesser extent, can be observed where flash flows of a relatively long duration recede back to steady state conditions (reversal of conditions illustrated in Figure 1)

It is apparent from the above-illustrated conditions that pore pressure differential at the interface between the flowing water and the channel bed must be considered in order to simulate the erosion in laboratory experiments. Tonkin et. al., 2003, showed that short-term rise in pore pressure behind receding surf caused accelerated scour in sand, despite the lower fluid shear. Some experiments conducted at the hydraulics laboratory at the University of Ottawa, which further illustrate the effect of pressure differential on the erosion of cohesive soils, are presented herein.

2 POSITIVE PORE WATER PRESSURE DIFFERENTIAL

In this study, the main objective was to assess, at least qualitatively, the effect of artesian pore water conditions on the erodibility of the clay surface.

A three-dimensional compacted clay soil block was placed in a specially constructed aluminum box. A metal screen and geotextile separated the water compartment at the bottom from the clay soil at the top. A water inlet through the side of the box allowed the transfer of water pressure from an elevated reservoir into the bottom of the soil box. The water pressure applied against the bottom of the soil created an upward gradient (I) which can be quantified as

$$I = H/t \quad (1)$$

Where H is the imposed water head at the bottom of the soil block (elevation of water in reservoir minus elevation of the base of soil sample), and t is the thickness of the soil block.

The surface of the clay soil was leveled flush with the top rim of the box. Two channels, 75 mm in width, were created at the surface of the soil block using stainless steel strips to contain the flow of water, thereby creating small erodible flumes at the clay surface. The two flume channels were located where no visible distress was noticeable at the surface of the soil block to ensure consistency in surface conditions in both flumes.

Two vibrating wire piezometers were inserted through the clay surface near the centre of the soil block to monitor the change in pressure: Piezometer 1 was inserted to 75 mm below the clay surface, and Piezometer 2 was inserted to 125 mm (i.e. to the bottom of the clay). Figure 3 illustrates the experimental setup.

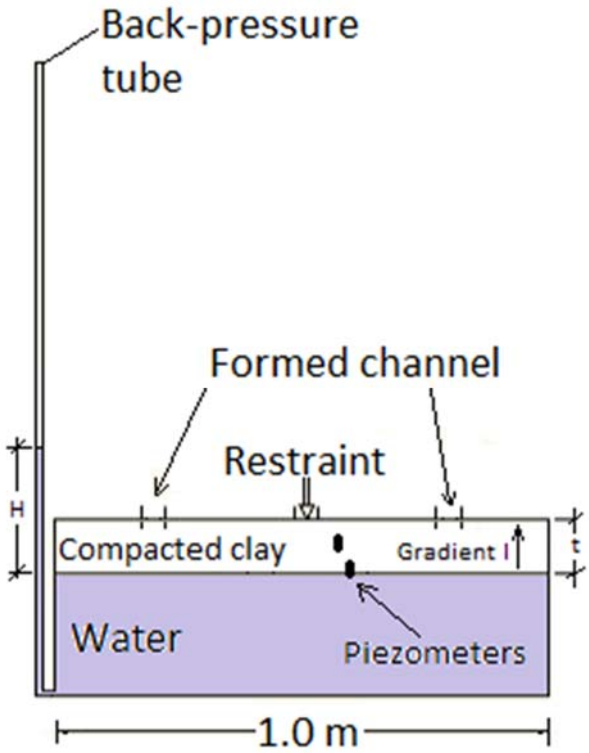

Figure 3: Schematic of pressure box setup

The soil box was inclined at 5% in the direction of the flow. A total of two runs (tests) were performed in this experiment: one run (Test 1) was performed while the water head was about half-way into the clay thickness (below the clay surface); the second run (Test 2) was performed after the reservoir applying the water head was raised to about 500 mm above the clay base and maintained at a more or less constant water level for about 35 minutes before the second run was performed. It should be noted, as indicated by the piezometer readings (see Figure 4 below), that the actual water head had dropped to about 350 mm above the base of the clay at the time Test 2 was performed. The declining head is due to a constantly increasing seepage that developed through the surface of the soil block at various locations, even though the head in the elevated reservoir was maintained more or less constant.

A constant volume of water (20 L) was used for each run to create a flow of water through each of the channels delimited at the surface of the soil block. The corresponding pressure head was applied about 30 minutes before each test was performed. As pointed out earlier, a constant flow velocity and total flow volume were used for both tests. The flow velocity was approximated at about 0.7 m/s.

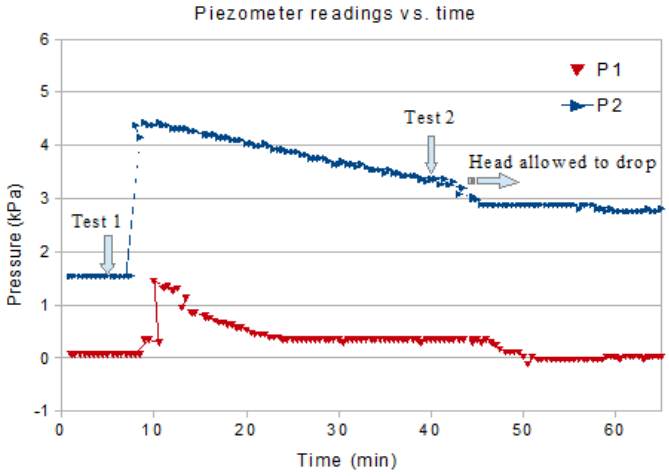

Figure 4: Back-pressure measurement

From simple visual inspection of the clay surface and the collected water samples, it was obvious that some sediments were entrained during Test 1 from the clay surface; however, during the flow in Test 2, large chunks of clay were entrained as shown in Figure 5, which was also evident in the collected water sample. Figure 5(a) shows the flow test (similar in both cases), while 5(b) and 5(c) show the resulting erosion from Test 1 and Test 2, respectively. For the purpose of this study, qualitative assessment of the sediment entrainment is deemed sufficient as the effect of the back-pressure on the entrainment can be confirmed by simple visual observations.

(a) (b) (c)

Figure 5: (a) Test flow, (b) Erosion at low back-pressure, (c) Erosion at high back-pressure

3 NEGATIVE PORE WATER PRESSURE DIFFERENTIAL

The erosion mechanism in cohesive soils involves drag forces imposed by fluid shear on exposed clusters across a rough irregular soil surface. It should be not-

ed that, even in soils with low cohesion, such as clayey sands and silts with low clay content, the cohesive forces preventing the separation of surface clusters from the rest of the soil are significant, and cannot be overcome exclusively by fluid shear force. In fact, the main contribution of the fluid shear force is to drag the detached clusters and transport them, same as it does with non-cohesive granular soils (Mazurek et. Al, 2001, Moore & Masch, 1962).

It remains to be explained how clusters of cohesive particles are separated from the soil in the bed or banks against a cohesion ranging from 200 Pa (or N/m2) to over 10,000 Pa, where in most cases, fluid shear is estimated at below 100 Pa. The following theory is the Authors' interpretation of the mechanisms acting to separate individual clusters from the cohesive soil mass.

Where the eroded surface is irregular and relatively rough, the fluid exerts large dynamic forces against out-of-plane soil features (protrusions or depressions), as illustrated in Figure 6. The detail in Figure 7 (enlarged from Figure 6) shows the mechanism by which the different forces interact to dislodge a cluster of cohesive soil particles, which will eventually be transported by the fluid. As the horizontal force against the upstream face of the protruding cluster creates an uplifting moment, the base of the cluster on the upstream side becomes subjected to a tension stress concentration, which is the weakness of soils in general, including cohesive soils. The tension forces cause the initiation of a void as loose particles under tension get washed out as cyclic oscillations from turbulent shear continuously degrade the base of the cluster. The resulting void facing the flow hosts a pocket of fluid at high pressure and in turn increases the uplift pressure on the cluster until the rupture of the cluster along the weakest path. This shows that relating fluid shear to the erodibility of cohesive soils is not a straightforward undertaking.

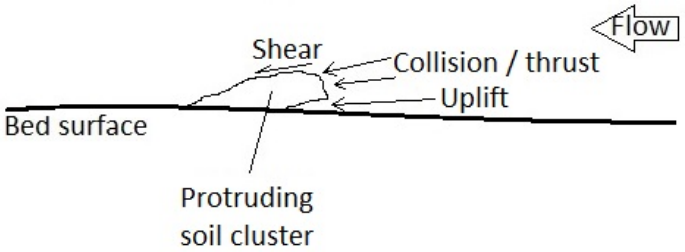

Figure 6: Flow forces

It follows then, that under hydrostatic pressure conditions, a well-polished soil surface, with high clay content and relatively fine grains in the mix is practically immune to erosion, which can be observed in natural streams. Yet the same soil under different circumstances still shows signs of erosion, which highlights the significant role of pore pressure balance in the erosion of cohesive soil mixes.

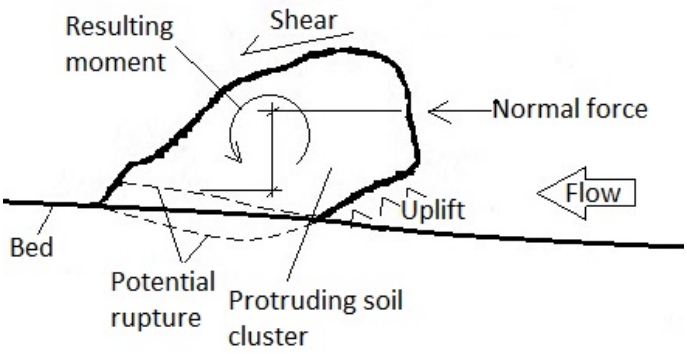

Figure 7: Forces on protruding cluster

Consider a case where a smooth channel bed is subjected to cyclic variation in flow depth, such as a natural or artificial channel that drains an agricultural watershed. As the level of water rises rapidly, the low permeability of the bed and banks causes the pore water pressure in the soil to lag behind the pressure head in the adjacent water within the channel. Until a reasonable equilibrium is achieved, a pressure gradient through the soil-water interface causes seepage forces to stabilize particle clusters at the surface. This is done by supplementing the cohesive forces and increasing the friction forces due to added normal force, as illustrated in Figure 8.

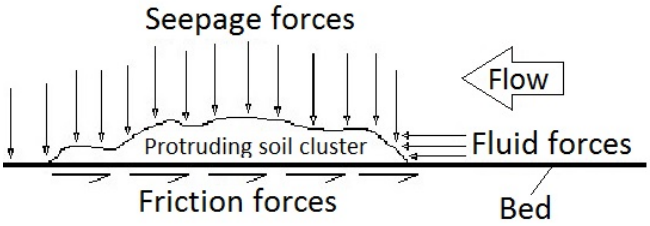

Figure 8: Seepage forces, rising water level

As the level of water recedes back to the original level, a reverse gradient (from the soil to the channel) forms. For a period of time, the pore water pressure in the soil is higher than the adjacent water head in the channel, and seepage forces use the paths of least resistance to return water to the channel and restore the pressure head equilibrium. This transition weakens the coherence of the surface soil clusters due to the uplifting seepage forces, and the development of micropaths cut out by seeping water. Furthermore, as the surface clusters are subjected to uplift forces, friction resistance to their movement is significantly reduced. Figure 9 illustrates these transition effects.

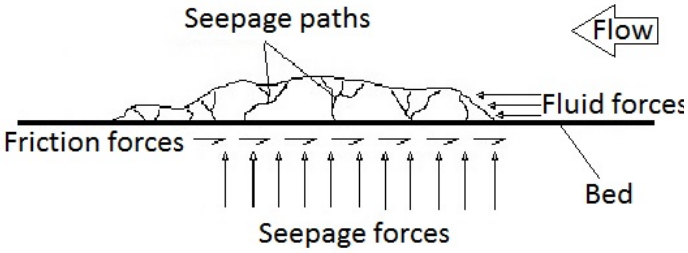

Figure 9: Seepage forces, receding water

Depending on the nature of the soil mix, especially its vertical hydraulic conductivity, and the characteristics of the flow depth cycles, the effect on the pore water pressure within the bed material near the surface can be illustrated as shown in Figure 10 below.

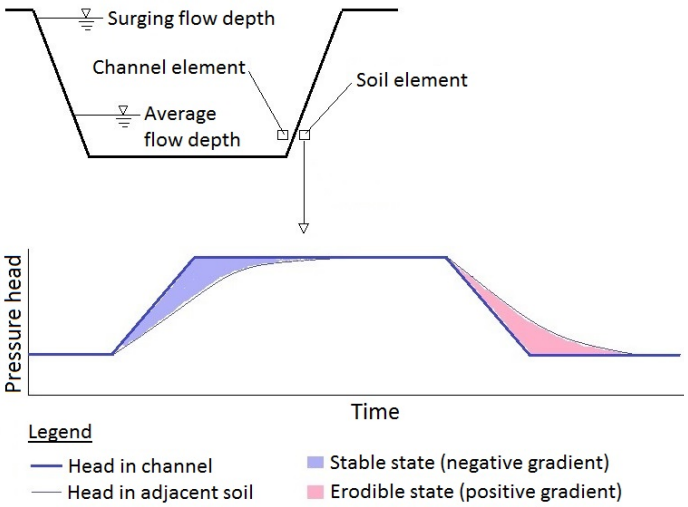

Figure 10: Pore pressure transition

In light of the complexity of these interactions between pore pressure and erosion potential, it was necessary to develop a testing device that can replicate the transition gradients while simulating the erosion mechanisms.

3.1 *Proposed apparatus*

The main requirement is to develop a critical shear stress test device where water pressure can be controlled and cycled as needed to replicate field conditions. Once the pressure head control is achieved, an indicator test is necessary to provide a measure of the soil's resistance to entrainment under the imposed pressure head conditions. As water flow forces are difficult to measure within a limited experimental space, it was decided to adopt a special probe that will be calibrated to provide a specific relationship between the soil's resistance to surface shear by the probe and its resistance to entrainment by water flow bed shear stress.

A somewhat similar approach was published by Khan & Kostaschuk, 2011, whereby the critical shear was estimated by an "Impinging Jet" apparatus (Hanson & Cook, 2004), and correlated with strength and bulk properties obtained from conventional soil testing (Shear vane, penetrometer, etc...).

Figure 11 shows an illustration of the "Erosionometer" device and probe, as designed and built for the above-mentioned purposes.

The surface shear probe is applied to the soil by applying a steady pressure until a full penetration of the pins into the soil is observed. As the desired pressure cycling is applied, the surface shear probe is pulled at a set rate of displacement by a software-controlled step motor via a steel cable through the access tube and around a fixed pulley within the pressure cell. The applied force is constantly measured by a resistive inline load cell and the probe displacement is measured by a linear potentiometer. The resulting load-displacement relationship will be analyzed to determine the yield point

3.2 *Test procedure*

The first process is to calibrate the test apparatus. Using a piston flume (Crowley et. al., 2014), the critical shear (shear at initiation of erosion) will be determined for cohesive soil samples of various compositions, taken from different sites and locations. As the samples are tested in the flume they will be saturated with near zero pore pressure head. The head in the Erosionometer will be set at the depth of water in the flume at the critical shear. The rate of displacement of the probe will be set at 0.5 mm per second. The yield force determined from the Erosionometer test will be correlated with the flume results (critical shear). With a sufficient number of diversified samples and a wide range of determined critical shear, it is anticipated that a correlation function can be determined between the critical shear and Erosionometer yield values. Once the apparatus is calibrated, any sample can be tested in the Erosionometer to determine its critical shear under field conditions that cannot be easily simulated in the flume.

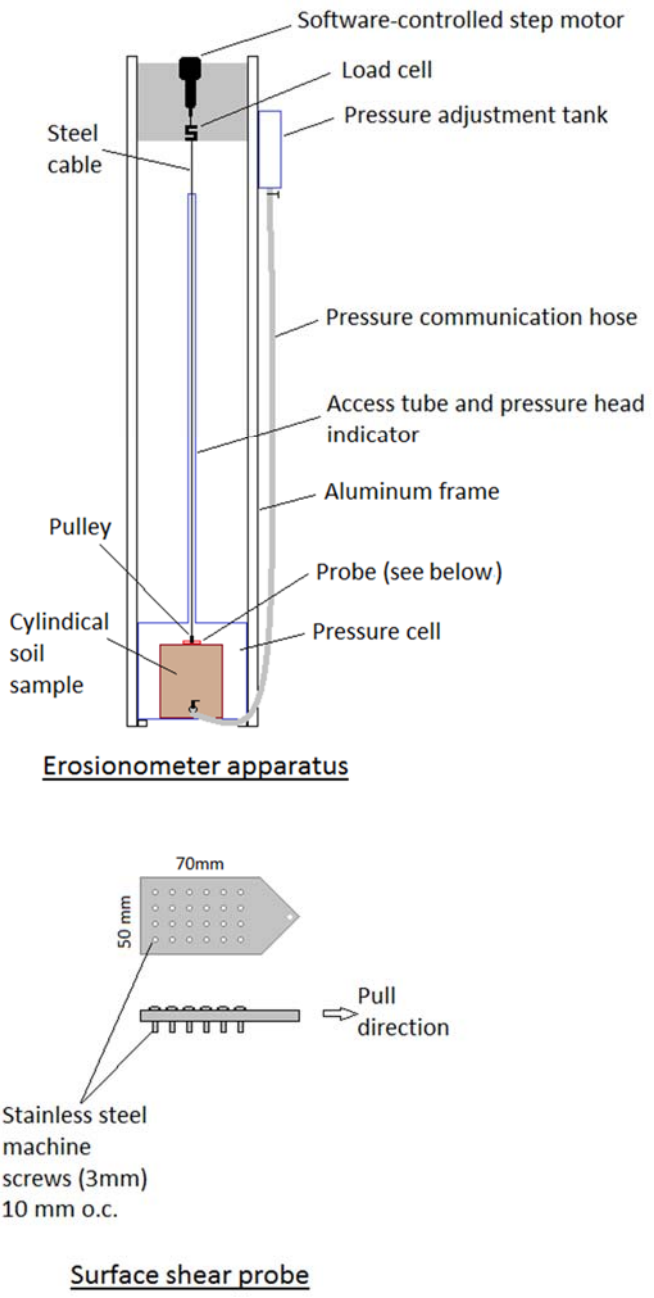

Figure 11: The Erosionometer - illustration

3.3 *Calibration*

At this stage, a total of eight samples from two different creeks were tested for calibrating the Erosionometer. The samples consisted of silty clayey sand with varying levels of fines content. The samples were collected by pushing steel cylinders into the ground surface near or within the stream banks, and extracting them with as little disturbance as possible. The samples were first inserted into a specially constructed piston flume at the University of Ottawa hydraulic laboratory as shown in Figure 12, and subjected to a water flow while visually observing the surface of the sample to identify the initiation of erosion. Although the cylindrical samples were extracted with minimal disturbance, some of them had to be sliced flush with the base of the flume. The slicing was done as clean as possible and the resulting loose particle were allowed to wash out before the actual test was started.

Figure 12: Specialized piston flume

The flume is 30 cm wide by 20 cm height, made of stainless steel channel sections. The total length of the flume is 4.86 m, 3.6 m to sample location. The flume slope was set at 1% throughout the testing and the flow intensity was increased gradually until signs of erosion were observed. Near uniform flow conditions were maintained by judicious operation of the tail gate. For the purpose of this study, the fluid shear was computed using the following relationship:

$$\tau = \rho \times Rh \times S \qquad (2)$$

Where:

τ = fluid shear (N/m^2)

ρ = specific weight of water = 9789 N/m^3

Rh = Hydraulic radius (m)

S = Flume slope (0.01)

The eight samples available for this study were tested in the flume where the flow characteristics at

first signs of erosion were used to determine an estimate of the fluid shear. The same samples were then subjected to Erosionometer testing under similar pressure head condition to obtain a yield force. A typical Erosionometer test result is shown graphically in Figure 13. The peak force shown in the figure is considered the yield force (Ye) of the Erosionometer test. A system friction effect of 1.5 N (as determined experimentally) is subtracted from all yield values.

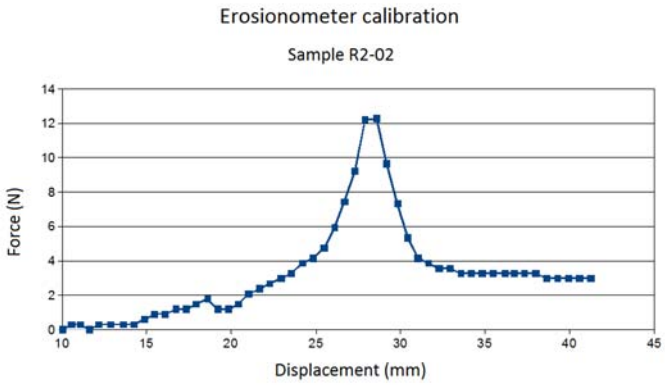

Figure 13: Typical Erosionometer test results

Test results from both flume and Erosionometer testing for all eight samples are summarized numerically in Table 1 below.

Sample No.	Flow depth (cm)	τ (N/m2)	Erosionometer Yield (N)
1T	1.75	1.53	6.23
2T	1.25	1.13	3.85
3T	7.25	4.78	15.74
4T	10.00	5.87	21.09
R2-02	2.25	1.92	10.75
R1-02	2.75	2.27	5.34
R1-01	5.25	3.81	13.06
R2-03	8.50	5.31	15.14

Table 1: Compilation of flume and Erosionometer test data

A graphical correlation between flume shear results and Erosionometer yield values for all eight samples is presented in Figure 14.

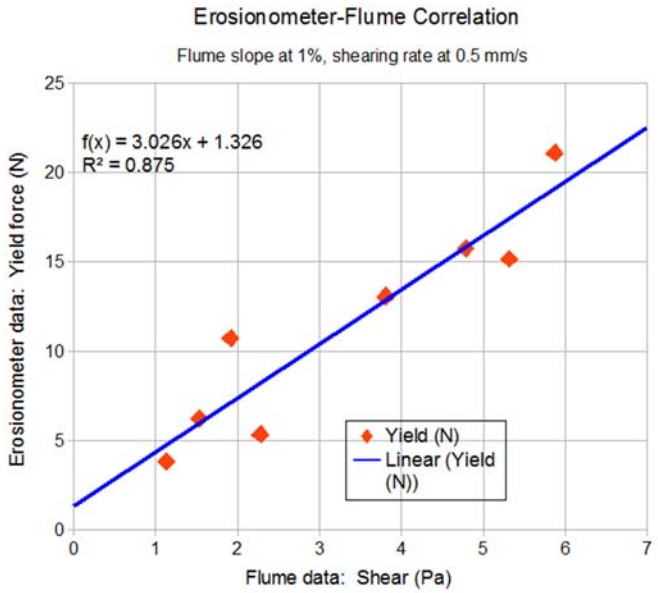

Figure 14: Linear correlation - all samples

The same correlation is shown in Figure 15 excluding the outlier values from Sample R2-02.

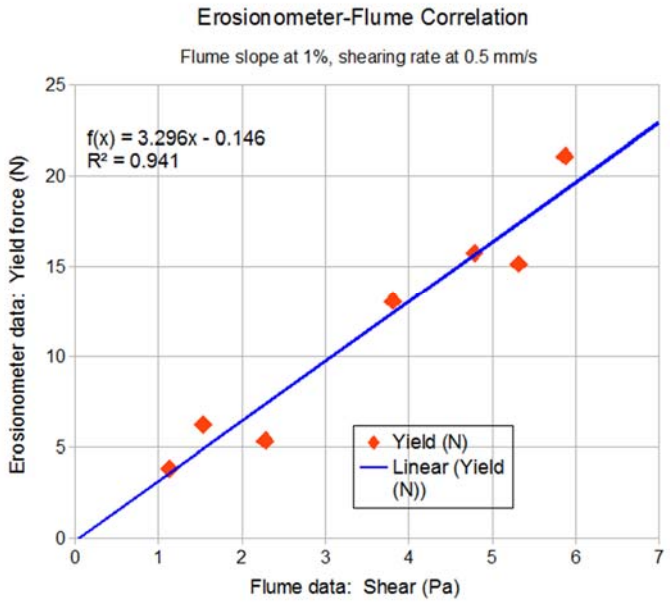

Figure 15: Linear correlation - Excluding R2-02

As can be seen from the linear regression data, a reliable linear relationship can be established, relating the Erosionometer yield values to the critical shear of a particular soil (correlation index close to unity). A larger number of samples may further improve the correlation. A zero intercept can be reasonably adopted based on the data, which indicates that the critical shear is directly proportional to the Erosionometer yield values. With the limited number and composition of tested samples, a proposed relation based on the data provided herein would be:

$\tau_c = 0.3\ Y_e$ (3)

Where:

τ_c = Critical shear (N/m^2)

Y_e = Erosionometer yield force

3.4 *Pressure head effect*

To investigate the effect of a water pressure head on the erodibility of cohesive soils, The Erosionometer test was repeated for Samples 1T through 4T, with a water pressure head of 50 cm applied to the surface of the sample just before shearing it.

The results of the Erosionometer tests at 50 cm head are compared to those obtained at a near zero head as shown in Table 2. Note that Sample 2T, which is mostly sand, with very little cohesive content showed no effect of the pressure head on the yield value. The remaining three samples with higher cohesive content showed an increase in the yield force of about 15% to 38%.

Sample #	zero head Yield (N)	50 cm head Yield (N)	% Change
1T	6.23	8.60	38.0
2T	3.85	3.55	-7.8
3T	15.74	18.12	15.1
4T	21.09	29.11	38.0

Table 2: Erosionometer yield vs. Pressure

4 CONCLUSION

Although this research is in its infancy, the early testing presented in this manuscript is very promising, and clearly demonstrates the effect of fluctuating seepage forces on the erodibility of cohesive soils.

Of special importance is the significant effect of negative gradient which tends to stabilize cohesive channel beds and banks. This effect should be incorporated in studying the erodibility of drainage channels where flash flows are a frequent occurrence.

Another important outcome of this study is the development of the Erosionometer as a calibrated probe system for quick determination of the critical shear of various soils. This system will be further developed into an in-situ test apparatus for determining characteristic critical shear in the field without the need for extracting and transporting samples. It should be noted that the calibration of the Erosionometer is so far considered absolute (does not need to be calibrated for each site to be tested), since samples from two different sites showed an agreement with a single linear relationship. This will have to be verified by testing a larger number of samples with varying sources and characteristics.

Although the Erosionometer, in its current design, showed an effect of the water head increase on erodibility, it is not yet suitable to accurately quantify that effect for design purposes. Further studies are needed to develop relationships governing the time-dependent effect of fluctuating gradients on the erodibility of cohesive soils. Incorporating such relationships into constitutive models is also a challenging objective.

5 ACKNOWLEDGEMENTS

The authors would like to thank Mr. Mark Lapointe for his valuable assistance in the fabrication of the experimental equipment, and Mr. Derek Eden for his assistance in conducting laboratory experiments.

6 REFERENCES

Khan I. and Kostaschuk, R., 2011. Erodibility of cohesive glacial till bed sediments in urban stream channel systems. Canadian Journal of Civil Engineering, Vol. 38, pp. 1363 – 1372.

Hanson, G. J. and Cook, K. R., 2004. Apparatus, test procedures, and analytical methods to measure soil erodibility in-situ. American Society of Agricultural Engineers, ISSN 0883-8542.

Crowley, R. W., Robeck, C., and Thieke R. J., 2014. Computational Modeling of Bed Material Shear Stresses in Piston-Type Erosion Rate Testing Devices. Journal of Hydraulic Engineering Jan 2014, Vol. 140, No. 1, pp. 24-34.

Julian, J. P. and Torres, R, 2006. Hydraulic erosion of cohesive riverbanks. Geomorphology 76 (2006) 193–206

Tonkin, S., Harry, Y., Kato F., and Sato, S., 2003. Tsunami scour around a cylinder. Journal of Fluid Mechanics (2003), vol. 496, pp. 165–192.

Moore, W. L., and Masch, F. D. Jr., 1962. Experiments on the scour resistance of cohesive sediments. Journal of Geophysical Research, 67(4), 1437–1449.

Mazurek, K., Rajaratnam, N., and Sego, D., 2001. Scour of Cohesive Soil by Submerged Circular Turbulent Impinging Jets. Journal of Hydraulic Engineering, 127(7), 598–606.

Appendix 5:
Publication 2

Practical Determination of Critical Shear in Cohesive Soils

Salem, H., Rennie, C.D. Practical determination of critical shear in cohesive soils. J. Hydraulic Engineering (ASCE), 143(10): 04017045, 2017.

Note that content from this paper is included in Section 5.2 of this thesis.

Practical Determination of Critical Shear Stress in Cohesive Soils

Hicham (Sam) Salem, P.Eng., M.ASCE[1]; and Colin D. Rennie, Ph.D., M.ASCE[2]

Abstract: In comparison to sand and gravel, cohesive soils, and clays in particular, present significant challenges when critical entrainment thresholds and erosion rates are to be determined for a particular basin or modeled in the laboratory. A wide variation in cohesive soil characteristics and behavior is usually encountered, even within relatively short reaches of river and creek beds. It is, therefore, evident that assessing the erodibility of such beds requires analysis of a large number of locations within reach, resulting in a costly and time-consuming undertaking. The objective of this paper is to introduce a practical procedure and test device designed to allow a fast and accurate determination of the critical shear stress of cohesive (and some noncohesive) soils, both in laboratory samples and in the field. The device, herein referred to as the erosionometer, is based on physical shearing of the soil surface. Initial calibration of the device showed a very good correlation with critical shear stress values for particle entrainment measured in a laboratory flume. **DOI: 10.1061/(ASCE)HY.1943-7900.0001363.**

Introduction

The erosion potential (erodibility) of cohesive soils is not yet well understood. Extensive flume tests and measurements have been done on cohesive samples, be it clay, silt, and sand mixtures in varying proportions, yet erosion modeling of such soils has proven difficult and time consuming. The erosion rate of cohesive soils is widely computed using excess shear stress models (Partheniades 1965; Hanson and Cook 1997), which involves the determination of the critical shear stress characteristic of the soil, although some fundamental and probabilistic models (Wilson 1993a, b) have been gaining ground in recent years.

There are many variables affecting the erodibility of cohesive soils, including mineral composition, grain size and shape, cohesion, shear strength, porosity, water content, roughness, and consolidation (Raudkivi 1998; Ternat et al. 2008; and others). As such, the determination of cohesive soil erodibility has been mainly empirical and approximate. The need arises for a practical method to map soil characteristics such as critical shear stress, hereafter abbreviated as "critical shear," with a reasonable duration and effort in order to model accurately the morphodynamics of a watercourse. There are several methods in the literature that are frequently used for testing the erodibility of cohesive soils; most of them are laboratory based and require sample extraction. A new device for directly measuring the critical shear of soils in situ and in laboratory samples is presented herein, along with its calibration against flume test results. It is important to note that test results presented herein are for the sole purpose of calibrating the device and not for evaluating the effect of soil properties on its critical shear characteristic.

Existing Methods

Flume tests are the most direct method for determining the erodibility of cohesive soils (Kamphuis et al. 1990; Amos et al. 1992; McNeil et al. 1996; Briaud et al. 1999; Gaskin et al. 2003; Crowley et al. 2014). Specialized piston-type flumes were specifically built for cohesive soil erosion testing in the laboratory, such as the erosion function apparatus (EFA) (Briaud et al. 1999), the SEDFLUME (McNeil et al. 1996), and others. In such flumes, the sample is introduced into a special opening at the base of the flume through a piston-like conduit, and it is pushed in to maintain its upper surface flush with the base while being eroded by the flow.

Building a flume test in situ is a significant undertaking and impractical when it comes to testing multiple locations across a watercourse. Some portable flumes have also been developed for in situ testing, such as the National Institute of Water and Atmospheric Research (NIWA) benthic in situ flume (Aberle et al. 2003; Debnath et al. 2007), and the Sea Carousel (Amos et al. 1992), but these can be complicated and difficult to deploy. Laboratory flume tests are more practical but require extensive work and preparation to provide reliable results, as will be discussed further later in this article.

A pinhole test (Sherard et al. 1976; Nadal-Romero et al. 2011) and a similar one known as the flow pump test (Reddi et al. 2000) are used for quantifying the erodibility of cohesive soils. These tests consist mainly in running a distilled water flow at a gradually varying hydraulic gradient through a small hole made into a soil sample until dispersive sediments are observed in the discharged water. Although this test is fairly simple, the eroding surface can be significantly affected by the hole punching and may not represent the actual soil surface in the field.

A permeameter test (Kassif et al. 1965) is used to determine the hydraulic head necessary to cause a piping failure through a soil sample placed on a perforated base. Although the tested failure is due to soil erosion, this test may not be suitable as a direct indication of the critical shear of the soil under surface flow.

The rotating cylinder test (RCT) is used for determining the critical shear and the rate of erosion of cohesive soil samples. The

[1]Director, AATech Scientific, Inc., 589 Rideau St. #212, Ottawa, ON, Canada K1N 6A1; Ph.D. Candidate, Dept. of Civil Engineering, Univ. of Ottawa, 161 Louis Pasteur, Ottawa, ON, Canada K1N 6N5 (corresponding author). ORCID: https://orcid.org/0000-0003-3392-5029. E-mail: [redacted]

[2]Professor and Chair, Dept. of Civil Engineering, Univ. of Ottawa, 161 Louis Pasteur, Ottawa, ON, Canada K1N 6N5. E-mail: [redacted]

Note. This manuscript was submitted on May 26, 2016; approved on April 27, 2017; published online on August 7, 2017. Discussion period open until January 7, 2018; separate discussions must be submitted for individual papers. This paper is part of the ***Journal of Hydraulic Engineering***, © ASCE, ISSN 0733-9429.

RCT was first developed by Moore and Masch (1962) and was subjected to several improvements (Lim and Khalili 2009; and others). In this test, a cylindrical soil sample is mounted between two platens and suspended by a central shaft in a clear cylinder filled with water. The shear stress is applied to the lateral surface of the soil by spinning the outer cylinder relative to the soil cylinder. The shear is quantified by measuring the torque required to keep the soil sample stationary against the spinning water, and the resulting erosion is observed and measured. Although this device may provide a close simulation of actual water flow against the soil surface, it presents several limitations as the soil sample is subjected to significant manipulation during the preparation and setup, which may affect its behavior when sheared, and the test in itself is somewhat time consuming. In addition, some soft sediments cannot be formed and mounted as required in this test setup.

The most widely used test is the submerged jet test. This type of test was historically used by many researchers to assess the erodibility of cohesive soils (Hollick 1976; Hanson 1991; Mazurek et al. 2001). Hanson and Cook (2004) introduced, in detail, an improved version of a portable submerged jet test apparatus, which is currently widely used to determine the critical shear of cohesive soils both in situ and on extracted samples. They also introduced the mathematics required for interpreting the test results along with convenient software in spreadsheet form for simplifying the task.

The submerged jet device uses a constant head reservoir discharging through a standard size circular nozzle (6.4-mm diameter) mounted at its base. The jet nozzle is mounted such as to discharge vertically or at a slight incline inside an enclosed cylinder filled with water (submerging the jet), impinging onto the soil surface at the base of the cylinder. The thickness of soil scoured under the impinging jet is determined at regular time intervals using a point gauge, which temporarily blocks the jet flow during the measurement. The rate of erosion is determined based on the change in depth measurements of the scour hole. Jet impingement theory is then applied to determine the maximum tractive shear stress (parallel to the soil, also known as wall shear) on the soil surface as a decreasing function of the increasing distance between the jet and the soil, or indirectly, the depth of the scour hole. In theory, the critical shear is specifically defined as the calculated tractive shear stress when equilibrium is achieved, and no further scour is caused by the jet; however, such a point is rarely reached within a reasonable scour depth, and a method of extrapolation is provided (Hanson and Cook 2004) to determine a theoretical asymptotic value of the wall shear as the critical shear stress. It should be noted that the soil must be assumed homogeneous throughout the scour depth and beyond, with the only variable being the wall shear for such theory to be valid.

The Jet apparatus has provided significant advantages in terms of reducing the time and the effort required to determine the erosion rate and the critical shear of cohesive soils, especially in situ; however, as explained in detail in the discussion later in this article, it is in the authors' opinion that there are significant drawbacks to the Jet test method with respect to critical shear determination, which led to the development of the new system.

Another device, operating on similar principles to the Jet tester, is commercially available as the cohesive strength meter (CSM). The CSM is more portable than the Jet apparatus and has been calibrated by researchers (Grabowski et al. 2012); however, it is also based on an impinging jet perpendicular to the eroding surface and hence subject to the same limitations as the Jet tester.

In looking to conduct intensive studies on the erodibility of cohesive soils, and to assess the common erosion models, one of the objectives of this research was, therefore, to develop an alternative method that can be adapted for use in the field to determine quickly the critical shear of soils with good accuracy. The erosionometer was developed by the authors at the University of Ottawa to fulfill these needs and will be presented herein. It should be noted that, as the Jet test system is the closest device to the erosionometer in terms of portability and speed, it will be the only system discussed in detail later in this article in comparison with the erosionometer in order to illustrate the advantages of the new system.

Description of the Apparatus

The erosionometer was developed to measure the critical shear by measuring the soil's resistance to surface shear induced by a special probe. The surface shear probe is a specially fabricated stainless steel plate equipped with protruding machine screws in a grid formation, 10 mm on the center: Six rows along the direction of shearing and four across. The screws protrude 5 mm past the face of the plate.

The probe is positioned on the soil by applying a steady normal pressure until a full penetration of the pins into the soil is observed. The probe is then pulled at a set rate of displacement by a software-controlled step motor. The current tests and calibration presented herein were performed using a set rate of probe displacement of 0.5 mm/s. A braided flexible steel wire diverted around a fixed pulley close to the soil surface level pulls the probe horizontally along the surface of the test soil. For laboratory applications, a Plexiglass submerging cell is added at the base of the device where a soil sample contained in a cylindrical steel tube, 150 mm in diameter, can be inserted, submerged, and tested in the same manner. The applied force is constantly measured by a resistive inline load cell, and the probe displacement is measured by a linear potentiometer, while the thrust is maintained until a noticeable yielding of the soil surface is observed. The resulting load-displacement relationship is inspected to determine the yield point representing the peak tension force in the wire, which is in turn calibrated to indicate the critical shear of the tested soil surface.

Fig. 1 shows an illustration of the erosionometer device and probe, as designed and built for the abovementioned purposes. The photo in Fig. 2 shows the erosionometer as deployed in the field. Typical erosionometer data are shown in Fig. 3; the peak force reached during the test is calibrated to indicate the critical shear of the tested surface.

Calibration Process

As described in detail in the following section, a relatively large number of soil samples (18) were tested for critical shear in a piston flume and compared to the erosionometer results for calibration purposes. The same soil surface tested in the piston flume was sheared with the erosionometer for correlation. As mentioned earlier, the rate of displacement of the probe was set at 0.5 mm/s throughout this phase of the research, including calibration and verification. The yield force (peak force attained) determined from the erosionometer test was correlated with the flume results (critical shear). With a large number of diversified samples and a wide range of determined critical shear values, a reliable correlation function was determined between the critical shear and erosionometer yield values. Note that the correlation function is specific to the probe speed of 0.5 mm/s and may not apply if a different speed is used for testing. Once the apparatus is calibrated, any sample or in situ soil surface can be tested with the erosionometer to determine its critical shear. It should be emphasized that in addition to replacing the cumbersome and time-consuming flume tests, the calibrated erosionometer can be deployed in the field to run in situ tests, eliminating the effects of sample disturbance associated with

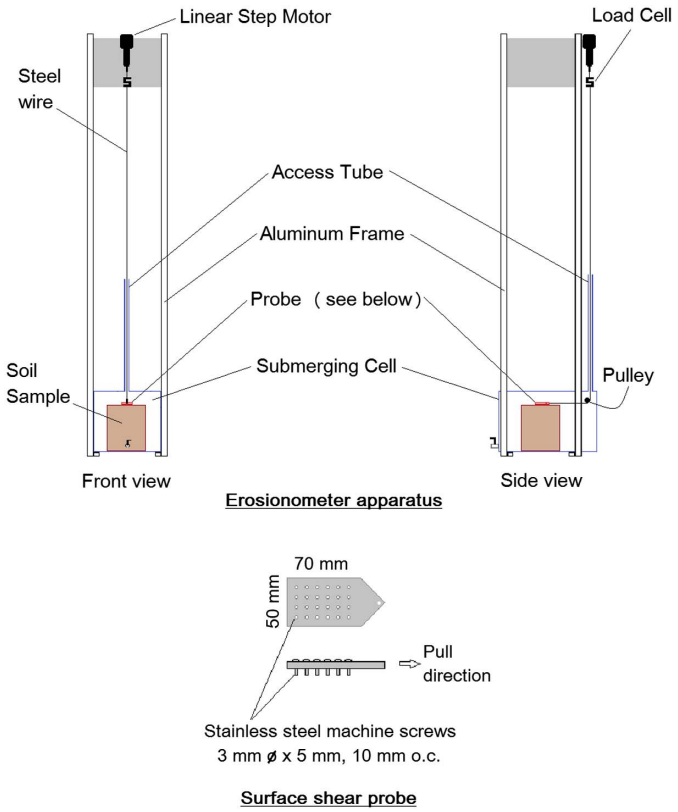

Fig. 1. Erosionometer device

Fig. 2. Erosionometer deployed in the field

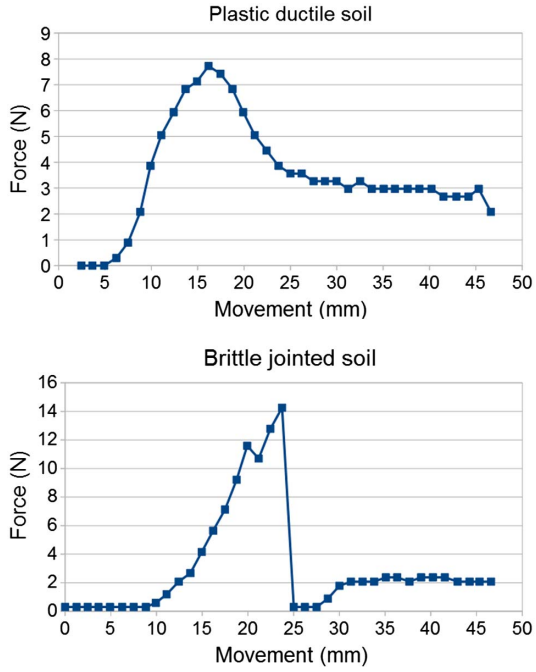

Fig. 3. Typical erosionometer data

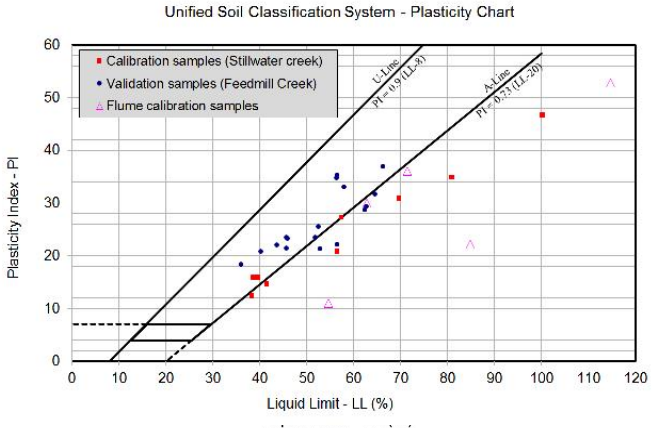

Fig. 4. Characterization of some of the soils used in the calibration of the erosionometer

extraction and transport. Furthermore, the erosionometer can test competent soils that cannot be easily eroded in a moderately sized piston flume.

Test Samples

A total of 18 samples from multiple locations along three different creek basins in Ottawa, Canada, were tested. The samples were extracted in 150-mm outer-diameter stainless steel cylinders, with a wall thickness of about 1.5 mm and a height of 150 mm. The samples were collected by pushing the thin-walled stainless steel cylinders into the ground surface near or within the stream banks and bed, extracting them with as little disturbance as possible. In many cases, the cylinders were easily inserted in the soft sediments with minimal effort. In some cases, where the flow had incised into virgin overconsolidated clayey strata, the cylinders had to be driven in by hammering on a special bulky steel bracket, distributing the impact on the entire rim of the sampling cylinder. Visual observation showed no appreciable effect of the sampling on the soil consistency beyond the interface with the inner surface of the sampling cylinders. One exception was observed when sampling one type of Champlain sea clay (from south bank of Site 4 of Feedmill Creek); this sample was characterized by an abundance of fissures and planes of weakness, which exhibited a brittle behavior when sampled.

The tested soil varied from silty clayey sand to silty clay and clay, with a wide variation in texture, organic content, and varying proportions of fines. Fig. 4 shows the classification of some of the soils tested for the calibration and verification of the erosionometer. The plasticity chart in Fig. 4 suggests a wide variation in soil characteristics between the samples (liquid limit). The authors should reiterate that the purpose of the testing is simply to calibrate the erosionometer and not to relate the critical shear to other soil properties. Note that the plastic limit (hence the plasticity index) of the soil samples was derived empirically from falling cone results using

relationships from literature (Campbell 1976; Al-Dahlaki and Al-Sharify 2008) and may not be suitable for further correlation; the main purpose of the liquid limit tests was to show the diversity of soil samples. The tested soils were generally organic silts and clays with varying sand content, and the high liquid limits of some samples suggest a high fibrous organic content. One sample also showed a high sand content.

Flume Measurements

A piston flume (e.g., McNeil et al. 1996; Briaud et al. 1999; Crowley et al. 2014), specially constructed at the University of Ottawa hydraulic laboratory, as shown in Fig. 5, was used to test for the critical shear of the samples. The flume is 30-cm wide by 20-cm high, made of aluminum channel sections. The total length of the flume is 4.86 and 3.6 m from the inlet to the sample location where a sleeve is provided for inserting the sample cylinder through the bottom. The flume slope was set at 1.5% for some of the early samples tested, then raised to 3% throughout the remainder of the testing to raise the limit on the available bed shear stress. The sample cylinder was inserted through the special opening at the bottom of the flume, then pushed up and trimmed flush with the flume base and subjected to a gradually increased flow. The trimming of the samples was done as clean as possible using a fine-tensioned steel wire, and any resulting loose particles were allowed to wash out before the actual test was started. In cases where the sample surfaces were not saturated, a gate at the end of the flume (discharge point) was raised to maintain a stagnant water level until surface saturation was achieved. The flume was then drained, and the gate was fully opened to allow for a free unrestricted discharge.

The soil surface was subsequently subjected to a gradually increasing water flow while visually observing the surface of the sample to identify the initiation of erosion. Initially, the fluid bed shear stress was computed using the depth-slope product, which is derived from the balance of forces on a free body of water on an inclined plane, using Newton's second law:

$$\tau = \rho \times g \times R_h \times S \tag{1}$$

where τ = fluid bed shear stress (N/m^2); ρ = water density = 998 kg/m^3; g = gravitational acceleration = 9.81 m/s^2; R_h = hydraulic radius (m); and S = flume slope (0.015 or 0.03). Eq. (1) assumes steady and uniform open-channel flow where boundary

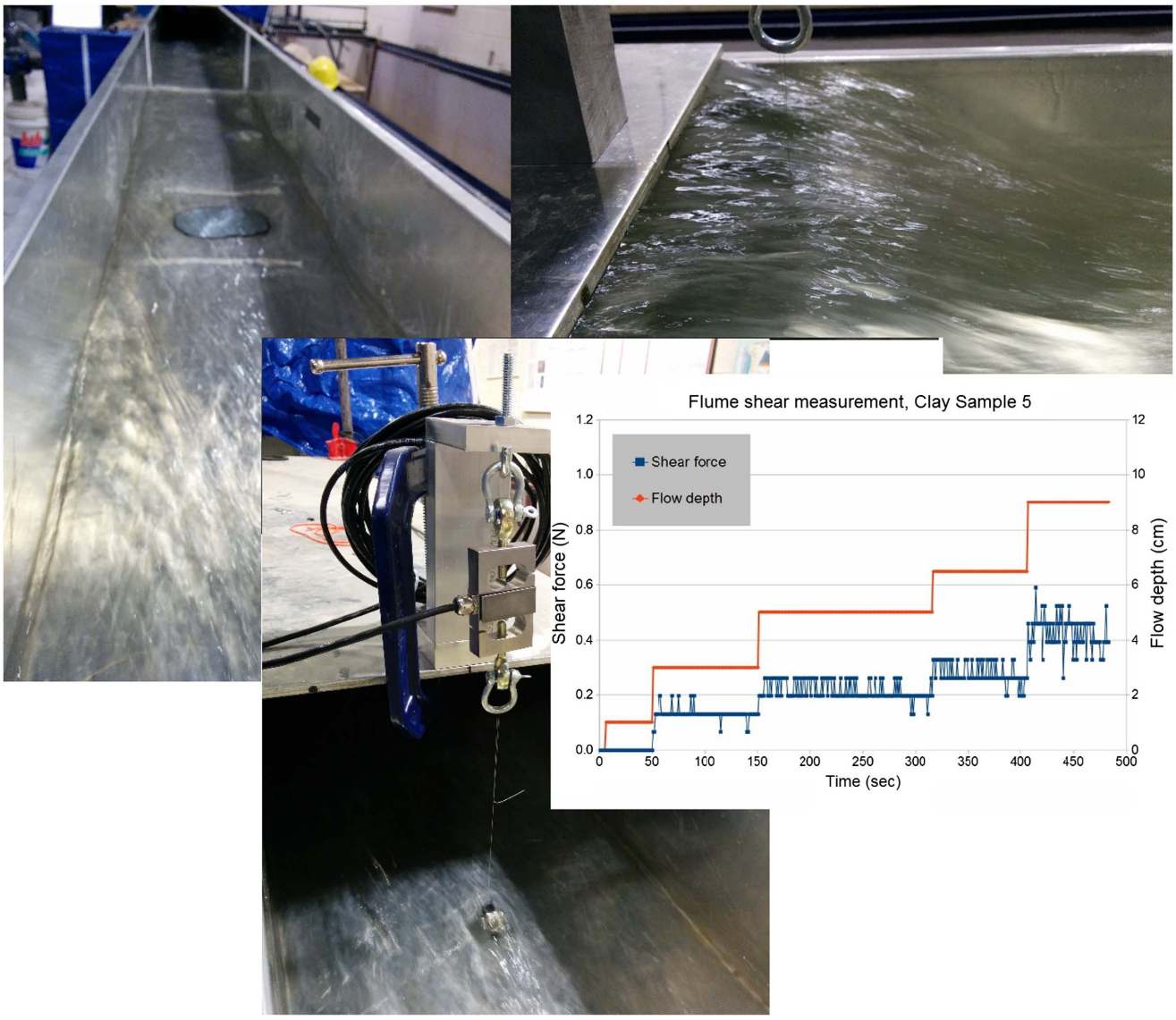

Fig. 5. Specially constructed piston flume, hydraulic laboratory, University of Ottawa

friction balances gravitational forcing and estimates the shear on a boundary surface similar in roughness to the typical channel boundary. Given that the sample surface had different roughness than the aluminum flume, the use of Eq. (1) induced an error in the shear estimation. Another issue to overcome was the short distance between the flume intake and the sample, which may prevent a fully developed open-channel flow at the sample location, especially at high flows where a hydraulic jump can be observed at the intake (Fig. 5). It was, therefore, necessary to derive a more accurate estimate of the flow shear that takes into consideration the contrast in roughness between the sample surface and the general flume surface, the proximity of the sample to the intake, in addition to the usual scaling issues. A shear plate apparatus (e.g., Klewicki et al. 2007) was then constructed to measure directly the shear stress across the sample surface and relate it to the depth of flow at the sample location. The shear plate measurement setup consisted of replacing the sample cylinder with a shallow circular dish mounted on a very flexible spring, allowing it to move freely in the direction of the flow. A thin steel wire connected to a small pin at the center of the dish was run upstream along the base of the flume and redirected vertically around a small bearing pulley to a load cell mounted above the flow inlet. The photos shown in Fig. 5 illustrate the setup and measurements. The sample dish was filled with a slice of a sample of cohesive soil, and the steel wire connecting it to the load cell was tensioned. As the flow depth was gradually increased in the flume, the additional tension in the wire was measured at 1 Hz frequency and recorded along with the measured flow depth. Each level of flow depth was maintained for about 1 min, and the recorded drag forces were averaged to capture the turbulent response. These measurements were repeated with five different soil samples, a sheet metal disk, and a 120-grit sandpaper disk in order to assess the sensitivity of the flow-shear relationship to the roughness of the soil sample. Subsequently, the dish was immobilized by a metal wedge downstream, and the flow was varied again to assess the drag forces on the wire and pulley system, which were subtracted from all the measurements. The shear measurements were performed at two different slopes of the flume: 1.5 and 3%. It should be noted that in all cases the flow intensity was increased beyond the critical shear of the soil to map the full range of flow depth-shear correlation, until large clusters of soil were eroded or the soil surface deviated from plane bed consistency.

The net shear results for individual samples at 1.5% flume inclination, including those of the sheet-metal and sandpaper disks, are shown in Fig. 6, along with the theoretical shear calculations [using Eq. (1)]. The results in Fig. 6 show a clear trend for each sample and suggest that the tested samples represent a wide range of surface roughness varying from that of a smooth sheet-metal surface to near that of 120-grit sandpaper. It is safe to conclude that such a range covers the cohesive soils of interest for the purpose of this research.

As the surface roughness of the cohesive soils of interest is relatively low, it is difficult to separate the effects of soil texture and surface quality of the sample on the resulting drag force. It was, therefore, decided to use all recorded points as one response space and obtain a single calibration relationship for the flume in terms of net shear stress versus flow depth. The final reduced net values of the shear stress versus flow depth, at a flume slope of 1.5 and 3.0%, are shown graphically in Figs. 7 and 8, respectively. A linear regression trend line computed from the lumped data from all tested soils yields the following relationships between the depth of water flow in the flume, measured in centimeters, and the induced shear on cohesive soil samples:

$$\tau = 1.42 \times D_{1.5} \tag{2}$$

$$\tau = 3.2 \times D_{3.0} \tag{3}$$

where τ = fluid shear (N/m^2); $D_{1.5}$ = depth of water flow in centimeters at 1.5% flume slope; and $D_{3.0}$ = depth of water flow in centimeters at 3% flume slope.

The displayed lines representing the −35 to 35% uncertainty range around the trend lines appear to encompass the bulk of the measured values. As such, for practical purposes, the critical shear estimate was simplified by lumping the response of all tested soils and textures and plotting a single best fit calibration curve (Figs. 7 and 8). The simplicity of this approach outweighed the required

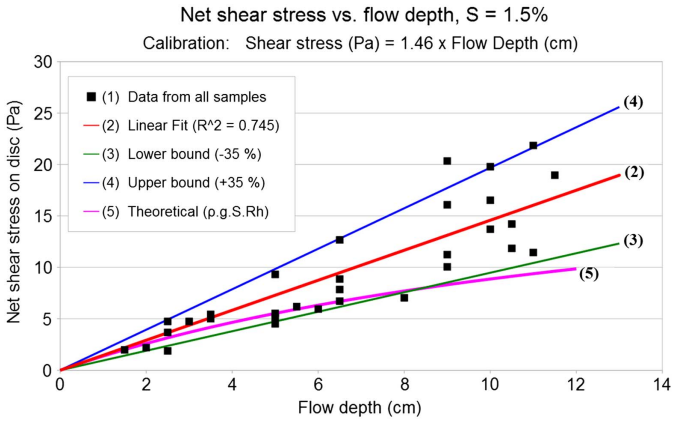

Fig. 7. Flume shear calibration data at 1.5% slope

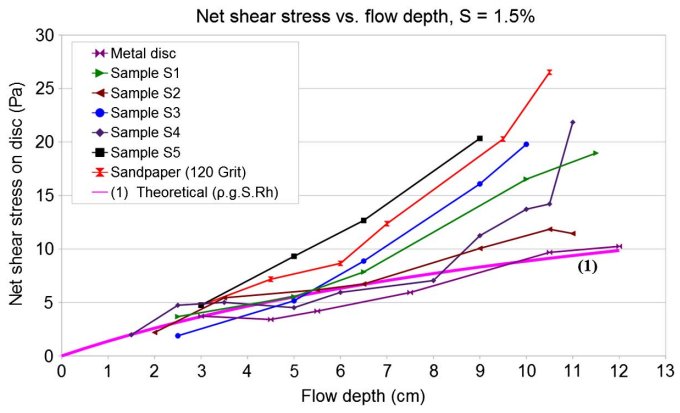

Fig. 6. Flume shear measurements for individual samples

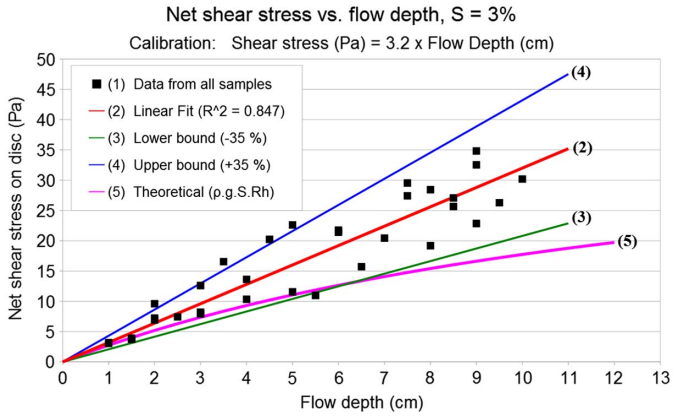

Fig. 8. Flume shear calibration data at 3.0% slope

effort and the uncertainty that would be induced by attempting to classify the texture and the roughness of the soil sample being tested. In other words, there is no guarantee that including the soil roughness as a flume calibration parameter and matching with a similar sample roughness from the erosionometer test would reduce uncertainty of the critical shear estimate.

Note that in all cases the measured shear is higher than the theoretical shear computed from the depth slope product [Eq. (1)]. This is particularly true at higher flows, which is expected since the flow is constantly accelerating between the flume intake and the free-falling discharge, including at the sample location.

Erosionometer Calibration

Eighteen soil samples from three different creek basins were tested in the piston flume, and the critical shear at the observed initial entrainment was computed using Eqs. (2) and (3) accordingly, based on the flume inclination at the time of testing. Subsequent erosionometer tests were performed on the same samples, and the yield values were plotted against the corresponding critical shear measured in the flume. The correlation appeared to be linear, and a regression analysis performed on the 18 points produced the following relationship with a coefficient of determination (r^2) of 0.83:

$$\tau_c = 0.57E_y - 0.65 \quad (4)$$

where τ_c = critical shear stress of the soil (N/m^2); and E_y = yield force (peak) measured by the erosionometer (N).

The calibrated relationship between the erosionometer yield force and the critical shear of the soil is shown graphically in Fig. 9.

The small negative intercept in Eq. (4) may represent a viscous drag resistance in soft sediments that are susceptible to suspension at any level of fluid motion (τ_c near zero). In other words, sediments already in suspension; that is, zero critical shear (light mud), would still exert some resistance to the moving probe by surface tension, viscous damping forces, etc.

It is important to mention that the calibration relationship provided previously is absolute and represents all cohesive soils with a roughness that can be compared to 120-grit sandpaper or smoother. No additional calibration is needed for using the erosionometer at different sites. That said, there is no reason to suspect that the calibration would not apply to coarser or less cohesive soils (even to noncohesive soils); however, such soils were not included in the calibration tests at this point and may be introduced in future work.

Validation

Following the calibration of the erosionometer, it was used to assess the critical shear of nine silty clay and clayey silt samples taken from five locations along the banks of Feedmill Creek, in the west end of Ottawa, Canada. The five locations covered a reach of about 1,150 m along the creek. The field and laboratory work was conducted from July 2015 to October 2015. The nine samples were extracted and tested following the exact same methodology described earlier, as applied to the 18 samples used in the calibration process. The measured yield force was plotted against the observed critical shear in the flume test and compared to the calibration line, as shown in Fig. 9. Three categories of verification tests are shown in the plot as stated in the legend:

1. Laboratory (lab) data representing flume tests and erosionometer tests performed on the same soil in the lab. The tests were performed on surfaces vertically located <5 mm from each other, as the sample surface was trimmed between the two tests the same way it was trimmed before the first test.
2. Field erosionometer versus lab flume test, whereby the in situ erosionometer tests were compared to the flume tests performed on samples extracted from the same location.
3. In situ erosionometer tests, which were additional tests performed at the same general areas as the other tests on site, were plotted along the calibration line with no comparison to flume data. These points were independent of any other testing and fall within the general range of critical shear level determined for the site, which illustrates the convenience of using the erosionometer for quickly mapping the critical shear of soils across the site.

All but one sample (from the south bank of Site 4) showed a close agreement with the established relationship. It is worth noting the range in measured critical shear (3–32 N/m^2) along this short reach, which demonstrates the need for a rapid testing device such as the erosionometer.

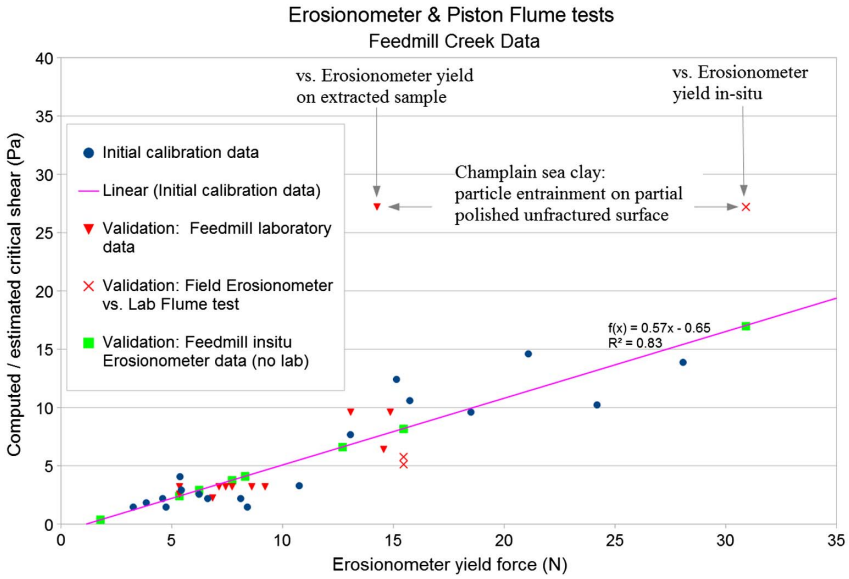

Fig. 9. Erosionometer calibration and verification data

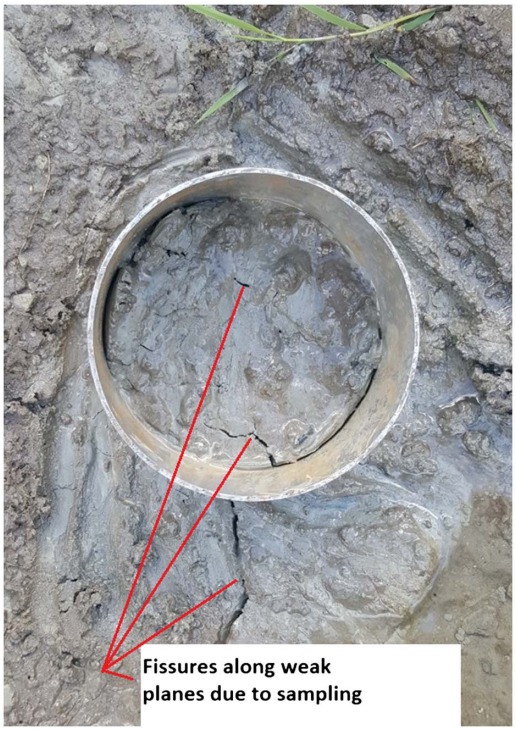

Fig. 10. Distressed brittle Champlain sea clay during sampling

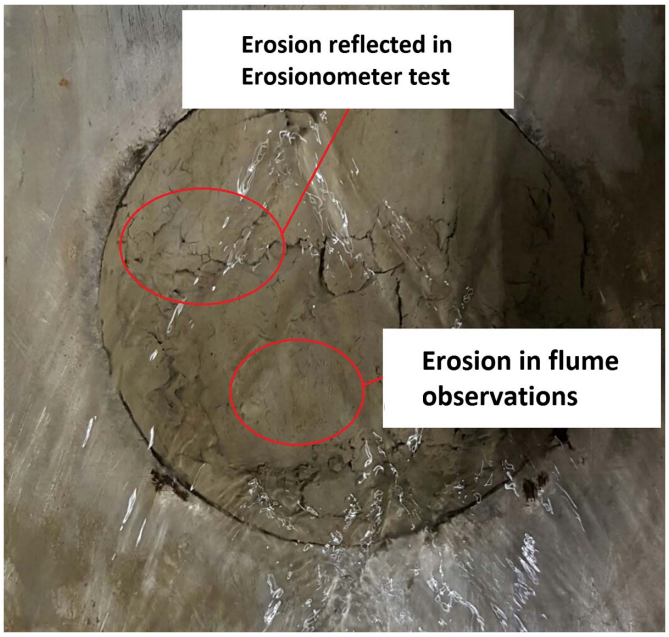

Fig. 11. Champlain sea clay in the flume

The material at the south bank of Site 4 is a brownish-gray Champlain sea clay, which, as mentioned earlier, is riddled with a dense web of fissures and weak planes. This clay exhibits a firm consistency with a brittle behavior, making it sensitive to manipulation. The wet surfaces appear polished and slick (oily-like surface), which blends the joints and gives the soil the appearance of a single homogeneous mass. Due to the brittle nature of this soil, it was obvious that the sampling process significantly affected the characteristics of the soil in terms of strength and integrity. This can be clearly seen in the photo shown in Fig. 10, taken during sampling. Consequently, in situ erosionometer tests were conducted for this site, which showed a yield force of more than twice the value measured for an extracted sample in the lab. Furthermore, the high value of critical shear was based on observed erosion of a polished partial surface of the sample, since it was not feasible to obtain a complete clean-cut flush with the flume base. Other parts of the sample surface, which showed a rugged texture as clusters of soil detached along the weak planes (Fig. 11), were eroded at a much lower flow/shear. This mode of erosion may be more representative of field conditions in such clays, as reported by Gaskin et al. (2003). The result of such erosion in clusters or blocks is often observed in the form of aggradation downstream by patches of rounded clay stones (Terwindt et al. 1968). It is the authors' opinion that the lower critical shear reflected by the erosionometer test on such clays is more realistic than particle-level erosion observed in the flume when partial patches of smooth horizontal planes are visually monitored to detect particle entrainment. This may represent a significant advantage of using the erosionometer as macroerosion of channel features made up of such clays, with underlying weakness zones, is very difficult to replicate in the laboratory. Furthermore, due to the sensitivity of this clay to manipulation, using a Jet test for several minutes at higher than critical shear may induce an error in prediction when extrapolating for the critical value.

Discussion

As stated earlier, the erosionometer was developed to improve the way critical shear is determined and to make it readily available for advancing research into soil erodibility. Following is a discussion of the improvements introduced by the new device in contrast with the leading methods currently in use.

While the Jet tester can be a great tool for assessing the erosion rate of soils, it suffers from several disadvantages when it comes to determining the critical shear characteristic:

- As stated earlier, the Jet test consists of collecting data points of wall shear versus eroded thickness as it impinges deeper into the soil, assuming the soil characteristics do not change throughout the scour depth. The critical shear is then estimated by fitting a hyperbolic trend to the data, with the asymptotic value representing the critical shear or projected equilibrium condition. There is an inherent uncertainty in the Jet test erosion rate data the way it is currently being used, which could deviate by as much as 100% from the rate determined in the flume (Hanson and Cook 2004; Al-Madhhachi et al. 2013, 2014). While such uncertainty in measured data is within the traditionally accepted margin in morphodynamics, extrapolating the data trend may not produce a reliable outcome. In contrast, the erosionometer measures the critical shear directly and within the top 5 mm of the surface. Furthermore, repeating the test at different depth intervals after carefully scraping the surface can produce a profile of the critical shear with depth as opposed to the Jet test, which produces a single value for the entire scour thickness assuming similar soil characteristics throughout.
- Many clays and silty clays are sensitive to shear and manipulation, as will be discussed. This implies that the physical characteristics, including strength and erodibility, will change when the soil is subjected to some level of antecedent shear. Since the Jet test, by its nature, starts with a high shear that gradually reduces towards the equilibrium value as the scour hole deepens, it mimics the reverse process of natural erosion, which may not be suitable for sensitive soils. The erosionometer probe, on the other hand, shears the soil along the tips of the pins with minimal prior disturbance.

- The tractive shear force developed from the impinging jet theory is based on a circular jet impinging on a horizontal flat surface. It is, therefore, implied that the impingement test should be limited to a wide and shallow scour hole to minimize the confinement effect; however, impingement scour holes as deep as 8 cm have been reported (Al-Madhhachi et al. 2014). Assuming the effect of gradually increasing confinement on the erosion rate is not excessive, extrapolating the data trend to simulate an even deeper scour condition may not represent the characteristics of the surface soil.
- Despite the significant improvement introduced by the Jet tester in terms of the effort and duration required to determine the critical shear, it is still somewhat time consuming to perform and interpret in the field. A further reduction in testing and interpretation time could be invaluable for advancing research.

Other researchers have also reported on issues with the Jet system. Ghaneeizad and Atkinson (2015), showed that the jet within the apparatus is significantly affected by the confinement imposed by the enclosed cylinder. Work by Phares et al. (2000) and Walder (2016) also highlighted the effect of the deepening depression at the impingement point on the validity of formulation used to interpret the results.

It is important to mention that it may be possible to improve the Jet test accuracy by modifying the test procedure. The depth of the scour hole can be limited to a couple of millimeters by moving the device and repeating the test at a fresh nearby spot with a higher nozzle each time. This way, every tested spot can be a new data point on the shear versus erosion rate chart, and the entire data set will be representative of the same surface soil, while the estimated wall shear from the water head will be more accurate as the impingement surface remains quasi-plane. Although the confining effect of the cylindrical enclosure remains, the resulting accuracy is expected to be improved significantly.

Conclusions

A new device is presented, referred to as the erosionometer, permitting fast and accurate determination of critical shear in cohesive and semicohesive soils. The device was rigorously calibrated and verified to produce unequivocally a realistic measure of the critical boundary shear stress of cohesive soils. The erosionometer is also portable and easy to deploy in the field for obtaining many data values across a reach of a water course. This device is proven to be an ideal tool for addressing the variability of soil conditions over short distances, typical of cohesive basins.

The erosionometer is used to shear the soil just below the surface by applying a horizontal pulling force to a special probe, moving it at a constant low speed. As such, the test replicates the effect of tractive water shear and, more importantly, along the same direction as the water drag, which results in a simple linear correlation, allowing researchers and users to determine the critical shear at the test spot immediately. The erosionometer device operation is not encumbered by the complexity and uncertainties associated with applying the impinging jet theory, and it reflects the characteristics of the surface it is testing rather than assuming constant soil characteristics with depth. In fact, the test can be repeated at different depths to investigate the change in erodibility with depth. As pointed out, while the Jet test may have revolutionized the erosion rate determination, it is subject to some drawbacks when it comes to determining the critical shear. These include the duration of the test, the complexity of the interpretation, and the necessity to extrapolate the value from other data points, which are already subject to precision limitations, as described earlier. In contrast, the erosionometer determines the critical shear directly without the need for extrapolation or lengthy interpretation procedure.

Furthermore, the erosionometer showed an additional advantage when it comes to soils with underlying weaknesses below the surface, including sensitive soils. The probe emulates the shear effect at a short distance below the surface, thus exposing potential cluster entrainment under flow intensities that would not normally erode the soil surface at particle level.

As the erosionometer test is conducted practically over a very short duration, it opens the door for further research related to soil behavior under fluid shear. The effect of physical soil characteristics such as degree of saturation, plasticity, etc., and the effect of pore pressure and other conditions on the erodibility of soils can be investigated with much more efficiency as the critical shear can be readily determined. Another important use of the erosionometer is to assess the merits of excess shear erosion models against other mechanistic or probabilistic models.

Acknowledgments

The authors offer many thanks to the City of Ottawa, and in particular Darlene Conway, for supporting the project; to Mr. Mark Lapointe for his valuable assistance in fabrication of lab and field setups; and to Nicholas Zorn, Benjamin Lambert, Alain Kayitaba, Andre Smith, Derek Eden, and Carlo Zaro Custodio for assisting in field and laboratory work.

References

Aberle, J., et al. (2003). "Straight benthic flow-through flume for in situ measurement of cohesive sediment dynamics." *J. Hydraul. Eng.*, 10.1061/(ASCE)0733-9429(2003)129:1(63), 63–67.

Al-Dahlaki, M. H., and Al-Sharify, G. A. (2008). "A proposed approach for plastic limit determination using the drop-cone penetrometer device." *J. Eng. Dev.*, 12(1), 107–117.

Al-Madhhachi, A., Fox, G., Hanson, G., Tyagi, A., and Bulut, R. (2014). "Mechanistic detachment rate model to predict soil erodibility due to fluvial and seepage forces." *J. Hydraul. Eng.*, 10.1061/(ASCE)HY.1943-7900.0000836, 04014010.

Al-Madhhachi, A. T., Hanson, G. J., Fox, G. A., Tyagi, A. K., and Bulut, R. (2013). "Deriving parameters of a fundamental detachment model for cohesive soils from flume and jet erosion tests." *Trans. ASABE*, 56(2), 489–504.

Amos, C. L., Daborn, G. R., Christian, H. A., Atkinson, A., and Robertson, A. N. D. A. (1992). "In situ erosion measurement on fine-grained sediments from the Bay of Fundy." *Mar. Geol.*, 108(2), 175–196.

Briaud, J. L., Ting, F. C. K., Chen, H. C., Gudavalli, R., Perugu, S., and Wei, G. (1999). "SRICOS: Prediction of scour rate in cohesive soils at bridge piers." *J. Geotech. Geoenviron. Eng.*, 10.1061/(ASCE)1090-0241(1999)125:4(237), 237–246.

Campbell, D. J. (1976). "Plastic limit determination using a drop-cone penetrometer." *Eur. J. Soil Sci.*, 27(3), 295–300.

Crowley, R., Robeck, C., and Thieke, R. (2014). "Computational modeling of bed material shear stresses in piston-type erosion rate testing devices." *J. Hydraul. Eng.*, 10.1061/(ASCE)HY.1943-7900.0000797, 24–34.

Debnath, K., Nikora, V., Aberle, J., Westrich, B., and Muste, M. (2007). "Erosion of cohesive sediments: Resuspension, bed load, and erosion patterns from field experiments." *J. Hydraul. Eng.*, 10.1061/(ASCE)0733-9429(2007)133:5(508), 508–520.

Gaskin, S. J., Pieterse, J., Al Shafie, A., and Lepage, S. (2003). "Erosion of undisturbed clay samples from the banks of the St. Lawrence River." *Can. J. Civ. Eng.*, 30(3), 585–595.

Ghaneeizad, S. M., and Atkinson, J. F. (2015). "Effect of flow confinement on the hydrodynamics of circular impinging jets: Implications for erosion assessment." *Environ. Fluid Mech.*, 15(1), 1–25.

Grabowski, R. C., Droppo, I. G., and Wharton, G. (2012). "Estimation of critical shear stress from cohesive strength meter-derived erosion thresholds." *Limnol. Oceanogr.: Methods*, 8(12), 678–685.
Hanson, G. J. (1991). "Development of a jet index to characterize erosion resistance of soils in earthen spillways." *Trans. ASAE*, 34(5), 2015–2020.
Hanson, G. J., and Cook, K. R. (1997). "Development of excess shear stress parameters for circular jet testing." *American Society of Agricultural Engineers Paper 972227*, ASAE, St. Joseph, MI.
Hanson, G. J., and Cook, K. R. (2004). "Apparatus, test procedures, and analytical methods to measure soil erodibility in situ." *Appl. Eng. Agric.*, 20(4), 455–462.
Hollick, M. (1976). "Towards a routine test for the assessment of critical tractive forces of cohesive soils." *Trans. ASAE*, 19(6), 1076–1081.
Kamphuis, J. W., Gaskin, P. N., and Hoogendoorn, E. (1990). "Erosion tests on four intact Ontario clays." *Can. Geotech. J.*, 27(5), 692–696.
Kassif, G., Zaslavsky, D., and Zeitlin, J. (1965). "Analysis of filter requirements for compacted clays." *Proc., 6th Int. Conf. Soil Mechanics and Foundation Engineering*, Vol. 2, University of Toronto Press, Toronto, 495–499.
Klewicki, J., Saric, W., Marusic, I., and Eaton, J. (2007). "Wall-bounded flows." *Springer handbook of experimental fluid mechanics*, Springer, Berlin, 871–907.
Lim, S. S., and Khalili, N. (2009). "An improved rotating cylinder test design for laboratory measurement of erosion in clayey soils." *Geotech. Test. J.*, 32(3), 232–238.
Mazurek, K., Rajaratnam, N., and Sego, D. (2001). "Scour of cohesive soil by submerged circular turbulent impinging jets." *J. Hydraul. Eng.*, 10.1061/(ASCE)0733-9429(2001)127:7(598-606), 598–606.
McNeil, J., Taylor, C., and Lick, W. (1996). "Measurements of erosion of undisturbed bottom sediments with depth." *J. Hydraul. Eng.*, 10.1061/(ASCE)0733-9429(1996)122:6(316), 316–324.
Moore, W. L., and Masch, F. D., Jr. (1962). "Experiments on the scour resistance of cohesive sediments." *J. Geophys. Res.*, 67(4), 1437–1446.
Nadal-Romero, M. E., Verachtert, E., Maes, R., and Poesen, J. (2011). "Quantitative assessment of the piping erosion susceptibility of loess-derived soil horizons using the pinhole test." *J. Geomorphol.*, 135(1), 66–79.
Partheniades, E. (1965). "Erosion and deposition of cohesive soils." *J. Hydraul. Div.*, 91(1), 105–139.
Phares, D. J., Smedley, G. T., and Flagan, R. C. (2000). "The wall shear stress produced by the normal impingement of a jet on a flat surface." *J. Fluid Mech.*, 418, 351–375.
Raudkivi, A. J. (1998). *Loose boundary hydraulics*, 4th Ed., A.A. Balkema, Rotterdam, Netherlands.
Reddi, L. N., Lee, I. M., and Bonala, M. V. S. (2000). "Comparison of internal and surface erosion using flow pump tests on a sand-kaolinite mixture." *Geotech. Test. J.*, 23(1), 116–122.
Sherard, J. L., Dunnigan, L. P., Decker, R. S., and Steele, E. F. (1976). "Pinhole test for identifying dispersive soils." *J. Geotech. Eng. Div.*, 102(1), 69–85.
Ternat, F., Boyer, P., Anselmet, F., and Amielh, M. (2008). "Erosion threshold of saturated natural cohesive sediments: Modeling and experiments." *Water Resour. Res.*, 44(11), W11434.
Terwindt, J. H. J., Breusers, H. N. C., and Svasek, J. N. (1968). "Experimental investigation on the erosion-sensitivity of a sand-clay lamination." *Sedimentology*, 11(1–2), 105–114.
Walder, J. S. (2016). "Dimensionless erosion laws for cohesive sediment." *J. Hydraul. Eng.*, 10.1061/(ASCE)HY.1943-7900.0001068, 04015047.
Wilson, B. N. (1993a). "Development of a fundamental based detachment model." *T. ASAE*, 36(4), 1105–1114.
Wilson, B. N. (1993b). "Evaluation of a fundamental based detachment model." *T. ASAE*, 36(4), 1115–1122.